Equilibrium dynamics of the Benguela system: a numerical modelling approach

Jennifer Veitch

A thesis presented for the degree of
Doctor of Philosophy
October, 2009

UNIVERSITY OF CAPE TOWN
IYUNIVESITHI YASEKAPA • UNIVERSITEIT VAN KAAPSTAD

Abstract

The Regional Ocean Modelling System (ROMS) is used to systematically investigate equilibrium conditions and seasonal variations of the Benguela system, including both the large-scale flow regime as well as the coastal upwelling regime. A shelf-edge poleward flow exists in the northern Benguela region and is driven primarily by the wind-stress curl via the Sverdrup relation. As such, it is strongly seasonal and is most intense during spring and summer when the wind-stress curl is most negative. The poleward flow deepens as it moves southward and between ~25-27°S much of it veers offshore due to the nature of the wind stress curl. In the mean state, the Benguela Current is characterized by two streams: the more inshore stream is topographically controlled and follows the run of the shelf-edge. The offshore stream is driven by nonlinear interactions of passing Agulhas rings and eddies and does not have a striking seasonal signal. The model simulates all seven of the major upwelling cells within its domain. Our results show that upwelling rates in the northern Benguela are inhibited by the convergence of geostrophic flow at the coast. The effect of topography on coastal upwelling was investigated by smoothing alongshore coastline and topography variations in the model, which showed that in all of the seven major upwelling cells, upwelling is enhanced on the downstream side of capes. Mesoscale variability of the Benguela system is dominated by Agulhas influx and instabilities associated with it. In constrast with the high offshore variability, the broad shelf of the southern Benguela harbours a region of low variability and relative quiescent. The role of Agulhas influx on the Benguela system is explicitly investigated by creating a dam in the model that induces an early diversion of the Agulhas Current so that it does not enter the Benguela system. We are thus able to identify regions of local generation of instabilities, such as in the central Benguela region, where large filaments are generated, with or without Agulhas influence. The Goodhope Jet is shown to be enhanced, but not entirely generated by Agulhas influx and the fact that the offshore extent of the upwelling front in the southern Benguela tends to be limited by the shelf-edge is not related to Agulhas influx.

Declaration

This thesis is a presentation of my original research work. Wherever contributions of others are involved, every effort is made to indicate this clearly, with due reference to the literature. Aside from guidance from my supervisors, I have received no assistance, except as acknowledged.

Supervisors:

Professor Frank Shillington: *Department of Oceanography, University of Cape Town, South Africa*

Dr. Pierrick Penven: *Institut de Recherche pour le Developpement, Laboratoire de Physique des Oceans (UMR 6523, CNRS, IFREMER, IRD, UBO), Centre IRD de Bretagne, France*

Publications based on this work:

- Lett, C., J.Veitch, C.van der Lingen and L.Hutchings, 2007: Assessment of an environmental barrier to transport of icthyoplankton from the southern to the northern Benguela ecosystems. *Mar. Ecol. Prog. Ser.*, **347**, 247-259.
- Veitch, J., P.Penven, and F.Shillington, 2009: The Benguela: a laboratory for comparative studies. *Prog. Oceanogr*, doi:10.1016/j.pocean.2009.08.008.
- Veitch, J., P.Penven, and F.Shillington, 2009: Modelling equilibrium dynamics of the Benguela Current system. submitted *to J. Phys. Oceanogr.*

Acknowledgements

I would like to thank both of my supervisors for, not only the opportunity of doing this PhD, but also the several invaluable opportunities I have had at attending international workshops, conferences and meetings during the course of it. I am grateful to Frank Shillington for always being available for discussion, encouragement when it was most needed and for always reminding me to take 'bite-sized' chunks. To Pierrick Penven, I am thankful for inspiring and animated discussions, for passing on some of his modelling expertise (may he continue to do so), for his constructively critical eye and most especially for making me derive every equation that appears in this thesis.

Discussions, both serious and not, with my colleagues and friends were integral in keeping me motivated and excited about a future in ocean science and for that I thank them.

I gratefully acknowledge the computing facilities that were available to me during the course of my PhD. These include: servers within the Department of Oceanography, UCT that were provided by BCLME funding, the high performance computing facilities (Caparmor) at Ifremer, Brest (France) and the Center for High Performance Computing (CHPC) in Rosebank, Cape Town. I am grateful also for funding from the National Research Foundation and a DSF bursary from the IRD (Institut de Recherche pour le développement).

An big, big 'thank-you' to my parents (all four of them!) for believing in me more than I ever have in myself. Finally, to Francis for joining me on this roller-coaster ride. His support during both the 'ups' and 'downs' is unfailing. Thank-you.

Contents

List of Figures

List of Tables

Chapter 1

Introduction

The Benguela system is the eastern boundary current system of the South Atlantic Ocean. It is situated off the west coast of Africa and is unique among the three other major eastern boundary upwelling systems of the worlds oceans in that both its northern and southern boundaries are dynamically linked to warm water current regimes, namely the Angola Current in the north and the western boundary Agulhas Current in the south (Shannon and Nelson (1996); Shillington (1998)). The northern and southern regions of the Benguela system are therefore subject to influence from the tropical Atlantic and Indian Oceans respectively. Low oxygen water (LOW), originating in the tropical Atlantic episodically advects far south into the northern Benguela upwelling regime and has, often catastophic, implications for the living marine resources there (Monteiro and van der Plas (2006); Monteiro et al. (2008)). In the south, the interaction of the north-westward path of Agulhas eddies with the upwelling front has been implicated in advective losses of fish larvae (Duncombe-Rae et al. (1992a)). Also unique to the Benguela upwelling regime is the juxtaposition of very low variability on the shelf with very high variability further offshore, particularly in the southern Benguela system where the offshore region has come to be known as the 'Cape Cauldron' due to its turbulent nature (Boebel et al. (2003)).

Another feature that might also be considered a boundary of significance is the so-called 'LUCORC' (Lüderitz Upwelling Cell Orange River Cone) barrier that has been described as separating the system into northern and southern regimes on the basis of their different biological and physical characteristics (Hutchings (2004)).

The LUCORC barrier is commensurate with the Lüderitz upwelling cell, that is often cited as the most vigorous upwelling cell in the world (Bakun (1996)) and is certainly the most vigorous in the Benguela upwelling system (Lutjeharms and Meeuwis (1987)).

The objective of this thesis is to take a comparative approach in systemtically investigating the disparate dynamics of the northern and southern Benguela regimes and the nature of the division between them. The focus is on the equilibrium dynamics so that the understanding of the mean state and seasonal cycle (which is dominant in the south Atlantic) may be improved and the 'bench-mark' from which we measure extreme events might be clarified. The importance of intrinsic, mesoscale variability in the system will be addressed in a general way. More specifically, the role of Agulhas influx (and mesoscale features associated with it) in the Benguela system will be investigated.

In order to study the northern and southern regimes in a systematic way, a modelling approach is employed in order to obtain data that is spatially, as well as temporally, cohesive. Until now, modelling in the Benguela has been limited to semi-analytical solutions (van Foreest and Brundrit (1985); Penven (2000); Fennel (1999)), fairly coarse resolution simulations (Skogen (1999)) or to only the southern part of the system (Penven (2000); Blanke et al. (2005)). The model simulation developed for this thesis is sufficiently high in order to capture the important mesoscale features of the system and it encompasses the Benguela system in its entirety, including the coastal upwelling regime as well as the large-scale circulation features further offshore.

A thorough literature review of the current knowledge of the Benguela system is presented in the next chapter. It encompasses work that has been done on both the large-scale flow regime as well as the nearshore upwelling system and allows us to identify the gaps in knowledge that we aim at addressing in this thesis. The objectives of this work are summarized at the end of the following chapter.

Chapter 3 describes the modelling system that is used in this work, namely: the Regional Ocean Modelling System (ROMS). The equations of motion are presented as is the prescription of the boundary conditions and the formulations of

the ocean-atmospheric feedback terms. The horizontal and vertical discretization, the advection and the turbulent closure shemes are described. The 2-way nesting scheme is outlined and benefits of it are briefly addressed. Details of the specific nested configuration of this simulation are included, i.e.: domain and resolution of the parent and child domains, time-stepping and lateral boundary conditions of each as well as the surface forcing of the nested configuration.

Based on the model simulation described in Chapter 3, the equilibrium dynamics of the Benguela system are described in Chapter 4 and, wherever possible, are compared with satellite and *in situ* data. The spatially, temporally and dynamically coherent model output allows us to investigate both the large-scale offshore regime as well as the nearshore upwelling domain in a systematic manner. In doing this we identify features salient to the disparate northern and southern Benguela regions as well as describing the dynamical basis of the transition between them. The role of the sudden narrowing of the shelf-edge in the central Benguela region in the transition between the northern and southern regions is explicitly investigated by straightening the shelf and the coastline in the model.

Chapter 5 focusses on mesoscale variability and the role of eddies in the Benguela system. Model-derived surface eddy kinetic energy (EKE) and offshore EKE propagation rates are compared with satellite products. The role of eddies in the system is quantitatively investigated by extracting terms of the vorticity balance and by separating the vorticity advection term into its mean and eddy components. Terms of the energy budget are analysed in order to investigate baroclinic and barotropic instabilities in the system.

Chapter 6 explicitly investigates the role of Agulhas influx, and associated mesoscale features, in the Benguela system by comparing the reference simulation with a model experiment that uses the same model configuration, but with an early diversion of the Agulhas Current so that it does not affect the Benguela system.

The last chapter summarises the results of the aforementioned chapters, suggests some applications and provides the scope for future work in the framework of this thesis.

In order to complement figures and text within this thesis, a CD of animations

is included (find it attached to the back cover). The animations give a good first impression of the nature of the Benguela system and provide the best reference of its highly dynamic nature. Animations included are:

- *sst.avi* (2-daily averaged sea surface temperatures). Note:
  - large filaments that are generated particularly off Lüderitz, but also northward of it
  - seasonal meridional movements of the Angola-Benguela Frontal Zone (ABFZ) at 14-16^{o}S
  - upwelling plumes off Cape Columbine and Cape Peninsula (at ~33^{o}S and ~34^{o}S respectively)
- *ssha.avi* (2-daily averaged sea surface height anomalies). Note:
  - distinct positive anomalies associated with anticyclonic Agulhas rings and their preferential path
  - negative anomalies associated with cyclonic eddies formed at the shelf-edge in the southern Benguela and their preferential path
- *salt_ currents_ surface.avi* (2-daily averaged surface salinity and currents). Note:
  - the high surface salinity signal associated with Agulhas rings
  - the intense meridional salinity gradient associated with the ABFZ and fluctuations of it
- *salt_ currents_ 60m.avi* (2-daily averaged salinity and currents at 60 m). Note:
  - the poleward advection of the high salinity signal associated with the tropical Atlantic along the coast in the northern Benguela region
- *current_ 0_ 100m.avi* (2-daily averaged current speed and direction, averaged from the surface to 100 m depth). Northward currents (i.e. 270^o-90^o) are shown as black arrows and southward (i.e. 90^o-270^o) are shown as white arrows. The colourbar represents the magnitude of the current. Note:

  - the weak, but persistent, poleward flow at the shelf-edge in the northern Benguela
  - the distinct offshore motion at ~30^{o}S
  - the perennial equatorward, coastal jet at Lüderitz
  - the generation of anticyclonic/cyclonic features at the narrowing of the shelf-edge near Lüderitz
  - the intense Goodhope Jet in the southern Benguela

- *current_200_1000m.avi* (as above, but averaged for the intermediate layer: 200-1000 m). Note:
  - the dominance of a poleward flow along the entire shelf
  - the anticyclonic Agulhas rings

- *eke_surface.avi* (2-daily averaged surface eddy kinetic energy). Note:
  - huge EKE associated with north-westward path of Agulhas rings in the southern Benguela
  - the generation of EKE off Lüderitz
  - the generation of EKE at the ABFZ and its subsequent poleward propagation

- *eddy_track_ssha.avi* (2-daily averaged ssha with locations of the centre of Agulhas rings). This animation is a demonstration of the eddy-tracking routine used to locate eddies (see Chapter 5).

Chapter 2

Literature Review

The Benguela can loosely be defined as the eastern boundary current system of the south Atlantic Ocean. More specifically, the Benguela system is defined as both the nearshore upwelling area and its associated shelf-circulation features as well as the large-scale Benguela Current. It is perhaps necessary at this point to explicitly define what is meant by the Benguela Current as there have been some inconsistencies in the nomenclature. The pioneering work of Hart and Currie (1960) used the term Benguela Current to refer only to the cool nearshore upwelling regime and this naming convention persisted for the next two decades. More recently, the eastern limb of the south Atlantic subtropical gyre is commonly referred to as the Benguela Current and the cool nearshore water simply as the Benguela upwelling regime. We use the latter, more recent naming convention.

2.1 Geographic location and geomorphology

The Benguela system is the eastern boundary current system of the South Atlantic Ocean and is situated off the west coast of Africa. As one of the worlds four major eastern boundary upwelling systems, the geographical location of the Benguela system is unique in that its southern boundary is coincident with the termination of both the African continent as well as the warm-water regime of the western boundary, Agulhas current. In this work the Benguela upwelling system is defined as the region extending northward from the southern tip of Africa to between 14-16^{o}S.

A prominent bathymetric feature of this region is the Walvis Ridge (refer to Figure 2.1), which extends offshore toward the southwest from ~20°S. It separates the abyssal Angola Basin in the north from the Cape Basin in the south. Other than the embayments of Walvis Bay, St Helena Bay and Table Bay, the NW-SE orientation of the coastline is relatively uniform until the Namibia/Angola border where the orientation tends toward NNE. The continental shelf is broadest at the Orange River mouth and narrows more abruptly to the north than to the south, resulting in a distinct discontinuity of the shelf-edge at ~28°S.

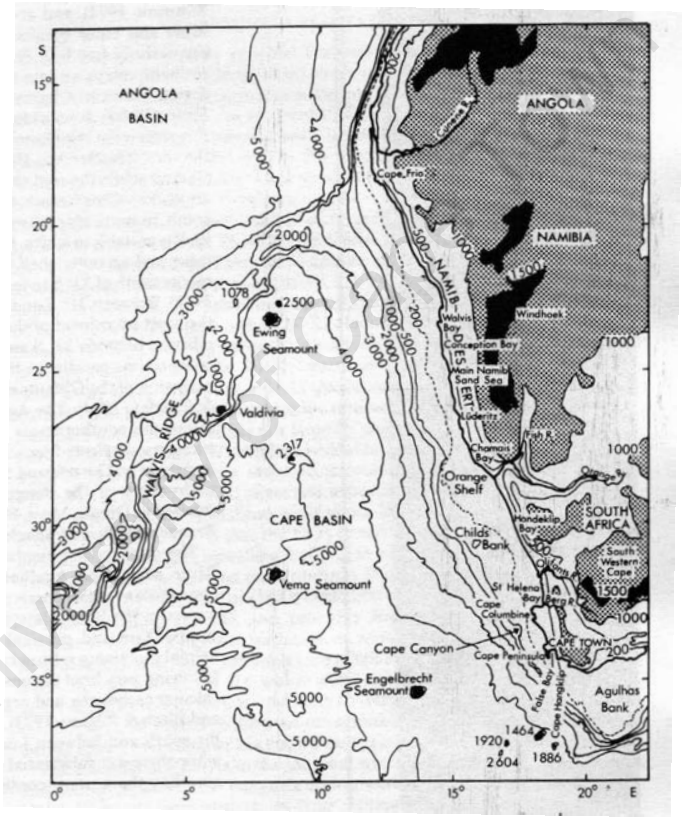

Figure 2.1: Bathymetry of the south-east Atlantic Ocean. From Shannon (1985)

2.2 Atmospheric forcing

Upwelling in the Benguela system is controlled by the anticyclonic winds of the South Atlantic Anticyclone (SAA), which are guided by the thermal barrier set-up by the coastline of the subcontinent, giving rise to the alongshore equatorward winds

on the west coast of Africa (Nelson and Hutchings (1983)). The prevalence of these upwelling favourable winds depends on the position of the SAA, the pressure systems over the continent and the eastward path of cyclones in the flow of the westerly wind belt south of the African continent. The SAA shifts seasonally and moves northwestward in autumn and southeastward in spring (Preston-Whyte and Tyson (1993)). The northward shift of the SAA in winter results in the dominance of a westerly wind regime in the southern Benguela, but does not affect the approximately perennial upwelling-favourable winds in the central Benguela. Satellite observations corroborate this and have shown that between 32-34° S the equatorward winds are highly seasonal but that between 24-32°S winds are upwelling favourable throughout the year and are most intense during summer months (Strub et al. (1998)). Refer to Figures 2.2g and 2.2h for the mean summer and winter windstress regimes in the Benguela system.

Upwelling favourable winds in the southern Benguela are modulated on timescales of 3-10 days by eastward travelling cyclones in the westerly wind belt between 35-45°S that form ahead of perturbations in the subtropical jet stream (Shannon and Nelson (1996)). The passage of cyclones can influence the wind field as far north as 30 °S by weakening or reversing the upwelling-favourable winds. The intensity of the cyclonic modulation of the SAA varies according to changes in the amplitude and configuration of Rossby waves in the subtropical jet stream (Nelson and Hutchings (1983)). In winter the timescale of modulation is of the order of a month and is associated with large waves in the jet stream, while smaller and faster moving waves are more common in summer and result in the higher frequency modulations (Jury et al. (1990)). Upwelling is suppressed by the so-called 'Berg' winds that occur in autumn and summer and are associated with a large continental high and strong offshore winds that lasts of the order of 4 days and can persist along the entire expanse of the Benguela upwelling area (Nelson and Hutchings (1983)).

2.2.1 Wind-stress curl

The curl of the wind stress is a fundamental forcing component of the ocean. It appears in the vorticity formulation of the momentum balance equations and defines

the divergence of Ekman transport and controls Ekman pumping. Ekman pumping is associated with upward (downward) velocities when there is a divergence (convergence) of Ekman transport that is driven by a negative (positive) wind-stress curl. In fact, it has been suggested by Enriquez and Friehe (1995) that upwelling induced by the process of Ekman pumping is similar in magnitude to that induced by coastal divergence so that the decrease in the latter due to the wind drop-off at the coast is compensated for by upwelling due to the former. However, a more recent modeling study (Capet et al. (2004)) shows that the wind drop-off at the coast diminishes upwelling and is therefore not compensated for by Ekman pumping, thus emphasizing the importance of an accurate description of the near-shore wind stress curl. Chelton (1984) raises the dynamic significance of wind-stress curl associated with the Sverdrup relation (Sverdrup (1947)), which describes a balance between wind-stress curl and the vertically integrated meridional transport to a depth of no-motion. Several ocean models of eastern boundary systems link poleward flows with the cyclonic wind stress curl that exists near the coast, based on the Sverdrup relation (e.g Pedlosky (1974); McCreary (1987); Marchesiello et al. (2003); Penven et al. (2005)).

The seasonal variability of the wind stress curl in eastern boundary current systems (California, Humboldt, Canary and Benguela) has been described by Bakun and Nelson (1991). Characteristic of all four of the major systems is a nearshore cyclonic curl that is associated with the wind drop-off at the coast and an anticyclonic curl offshore. In the Benguela system the region of cyclonic curl that extends, on average, to about 200-300 km offshore (Kamstra (1985); Bakun and Nelson (1991)) and is wedge-shaped; being narrowest toward the south (refer to Figures 2.2a-f). The seasonal signal of the wedge-shaped region of cyclonic curl is such that it extends furthest south in austral spring and is at its northward extreme in austral winter.

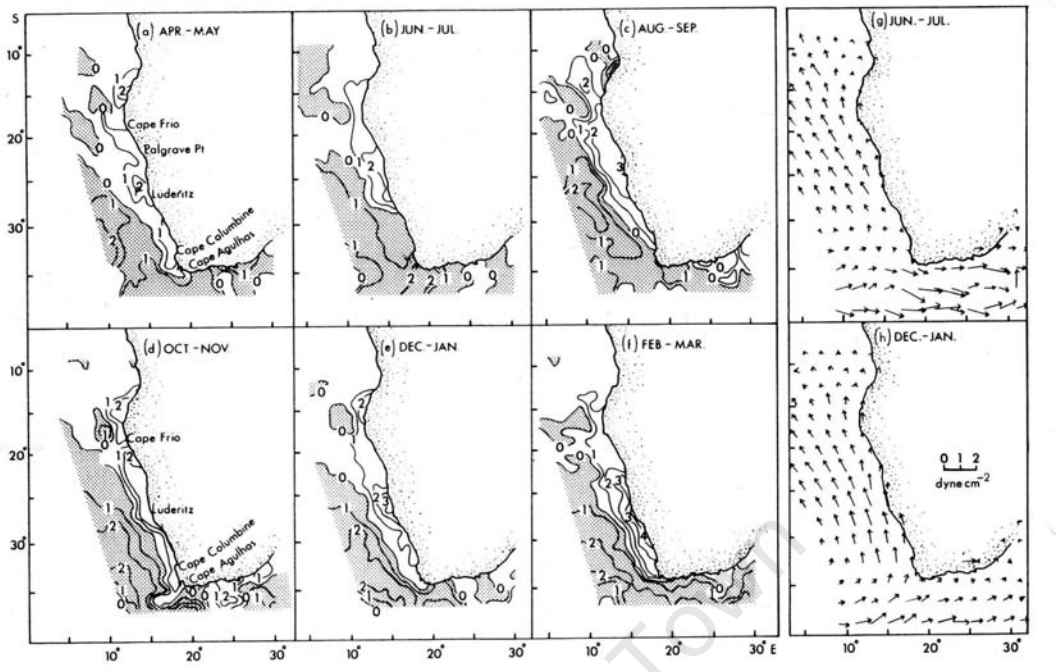

Figure 2.2: (a-f) Wind-stress curl (10^{-4}dyn.cm^{-3}) in the Benguela system (regions of anticyclonic windstress curl are shaded) and surface winds (g-h). From Shannon (1985).

2.3 Large-scale oceanographic setting

The Benguela Current lies offshore of the Benguela upwelling area and has been defined as the eastern boundary current of the anticyclonic South Atlantic subtropical gyre (Peterson and Stramma (1991)) and it is the definition that will be adopted in this work. For a schematic of the large-scale features of the system refer to Figure 2.3. A study of the geostrophic circulation of the south Atlantic by Reid (1989) revealed the path of the Benguela Current to be northward at ~34°S, tending increasingly northwestward toward the north and separating from the African coast near 30°S. Geostrophic flows derived by Reid (1989) show that by 1500 m depth, the flow is southward all along the coast of southern Africa, thus suggesting the fairly limited depth of the Benguela Current.

To the north of the Benguela system is the cyclonic Angola Gyre, which is of the order of 2000 km in diameter and extends from beneath a very thin surface wind-driven layer (~10-20 m) to approximately 300 m depth (Gordon and Bosley (1991)).

The eastern limb of the gyre is commensurate with the Angola Current, which carries water of equatorial origin poleward to approximately 15-18°S (Gordon and Bosley (1991)), which coincides with the northern extent of the Benguela upwelling regime. Observational evidence suggests that cyclonic Angola Gyre and the anticyclonic south Atlantic subtropical gyre have a confluence in the vicinity of the Luderitz upwelling cell (~26°S) (Mercier et al. (2003)), which is coherent with the finding of Stramma and Peterson (1989) who identify a westward transport at ~24°S.

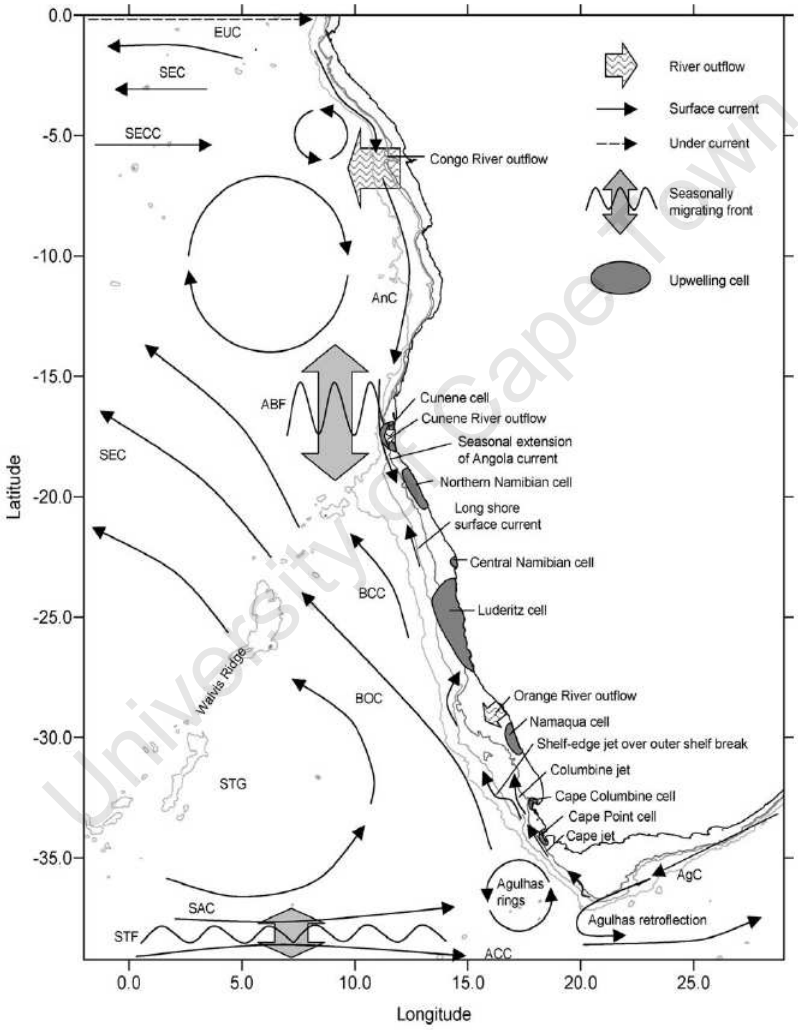

Figure 2.3: Schematic map of the salient large- and small-scale circulation features of the Benguela system. EUC: Equatorial Undercurrent, SEC: South Equatorial Current, SECC: South Equatorial Counter Current, AnC: Angola Current, BOC: Benguela Oceanic Current, BCC: Benguela Coastal Current, SAC: South Atlantic Current, AgC: Agulhas Current, ABF: Angola-Benguela front, STG: subtropical front, STG: subtropical gyre, ACC: Antarctic Circumpolar Current. From Hardman-Mountford and Villacastin (2003).

2.3.1 The Benguela Current: transports

As the eastern limb of the south Atlantic subtropical gyre (Stramma and Peterson (1990); Peterson and Stramma (1991)), it has been suggested that the 21 Sv (1 Sv = $10^6 m^3.s^{-1}$) (Peterson and Stramma (1991)) transport of the Benguela Current is primarily supplied by the southern limb of the gyre (i.e. the South Atlantic Current). However, the Benguela Current is also fed by south Indian Ocean waters via the Agulhas Current and can be influenced by Subantarctic Surface Water via perturbations in the Subtropical Front. In fact, geostrophic transports derived from observational data by Gordon et al. (1987) suggest that as much as 10 Sv of a total flow of 15 Sv into the upper 1500 m of the South Atlantic is fed by the Agulhas Current, the rest (5 Sv) being fed by the South Atlantic Current, this is supported by a more recent study by Gordon et al. (1992). Using altimetry data, van Ballegooyen et al. (1994) based their calculations of Indian Ocean input into the Benguela Current on the number of Agulhas eddies entering the south-east Atlantic and resolved an input of ~7 Sv. In order to investigate the origin and variabilty of Benguela transport, Garzoli and Gordon (1996) used data obtained from a series of cruises between 1992-1993 specifically designed to investigate Benguela Current transports (see their schematic in Figure 2.4). They calculated a 16-month mean northward geostrophic transport at 30°S in the upper 1000 m of 13 Sv. They divided this total volume flux into separate contributions: 50 % originating from the central Atlantic, 25 % from the Indian Ocean and the last portion a blend of Indian and tropical Atlantic water. This result is in agreement with the finding of Garzoli et al. (1997) who based their study on the same observational data merged with altimeter data. Though there are disparities in the absolute values of the volume flux of Indian Ocean water contributing to the Benguela Current, it is generally accepted as a significant contributor. Garzoli et al. (1996) found that a correlation exists between the strength of the Benguela Current and the salinity of the thermocline layers, suggesting that variations in the transport of the Benguela Current are related to variations of Agulhas input.

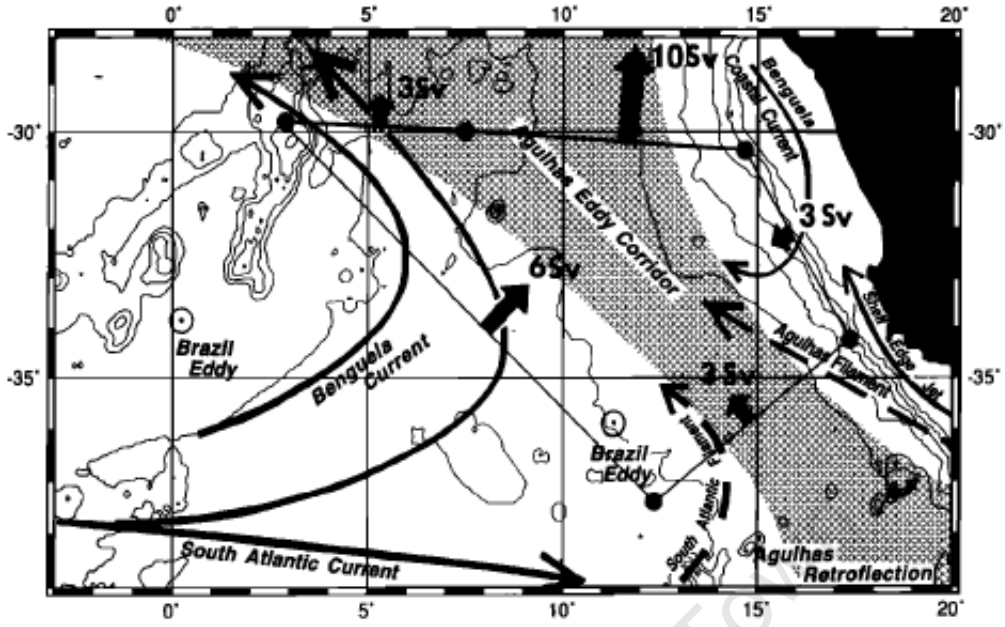

Figure 2.4: Schematic map of transport elements of the Benguela Current. The area shaded in grey represents the Agulhas eddy corridor through which Agulhas Rings and eddies migrate into the Atlantic Ocean (Garzoli and Gordon (1996)).

2.3.2 Water masses

Water masses of the Benguela System are derived from both the equatorial Atlantic in the north via the Angola Current and the South Atlantic and Indian oceans to the south via the Agulhas Current. The principle water masses in the Benguela region are tropical (TSW) and subtropical surface (SSW) waters, thermocline waters, which include South Atlantic Central Water (SACW), South Indian Central Water (SICW) and Tropical Atlantic Central Water (TACW), Antarctic Intermediate Water (AAIW), North Atlantic Deep Water (NADW) and Antarctic Bottom Water (AABW). Shillington et al. (2006) generalize the surface, central and intermediate waters of the Benguela system as being more saline and warmer if originating from the tropics or less saline and cooler if influenced by Antarctic or sub-Antarctic waters. For a T-S plot of the characteristic water masses of the Benguela system refer to Figure 2.5.

Thermocline water, also known as central water is characterized by potential temperature and salinity characteristics in the range: 6°C,34.5 psu to 16°C,35.5

psu. It is this water mass that upwells to the surface along the coast and thus constitutes, often highly modified, the Benguela shelf-waters (Shannon and Nelson (1996)). Because the central waters of the south Indian and south Atlantic have very similar potential temperature/ salinity structures, Gordon et al. (1992) used chlorofluoromethanes as tracers and resolved that as much as two-thirds of Benguela Current thermocline water is drawn from the Indian Ocean, though Kamstra (1985) speculate that this may be an overestimation. Poole and Tomczak (1999) investigated the thermocline water mass structure of the entire Atlantic Ocean and found that the waters of the south Atlantic thermocline can de defined as Eastern South Atlantic Central Water (ESACW) and Western South Atlantic Central Water (WSACW), the former is derived from Indian central water via the Agulhas Current and the latter from the Brazil/Malvinas Confluence. ESACW was observed by Mohrholz et al. (2001) to be prevalent in the Cape Basin, while SACW dominates the thermocline waters of the Angola Basin , south and north of ~16 ° S respectively.

AAIW is formed at the surface in the sub-polar and polar regions and is associated with a salinity minimum deep in the water column. Based on temperature and salinity and oxygen concentrations, Shannon and Hunter (1988) were able to infer the general circulation characteristics of AAIW around southern Africa, which they supposed, along with surface water dynamics, controlled the movement of thermocline water. They located the core of AAIW at ~750 m in the south-east Atlantic and noted a poleward movement along the west coast to ~32 °S and a southward freshening. They did not resolve any significant seasonal differences. AAIW of tropical Atlantic origin is saltier than AAIW derived from the South Atlantic and is characteristically low in oxygen (Shannon and Nelson (1996)).

NADW flows poleward and is located beneath AAIW, between 1000-3500 m depth. It is well oxygenated, relatively saline and warm with typical potential temperatures and salinities of ~ 3° C and $>$ 34.8 psu respectively (Shannon and Nelson (1996)).

Beneath NADW, AABW ($<$ 1.4°C, $<$ 34.82 psu) is situated at depths exceeding 3800 m and flows equatorward into the Cape Basin and turns back on itself creating a cyclonic loop that results in a deep poleward flow along the continental margin of

western Africa.

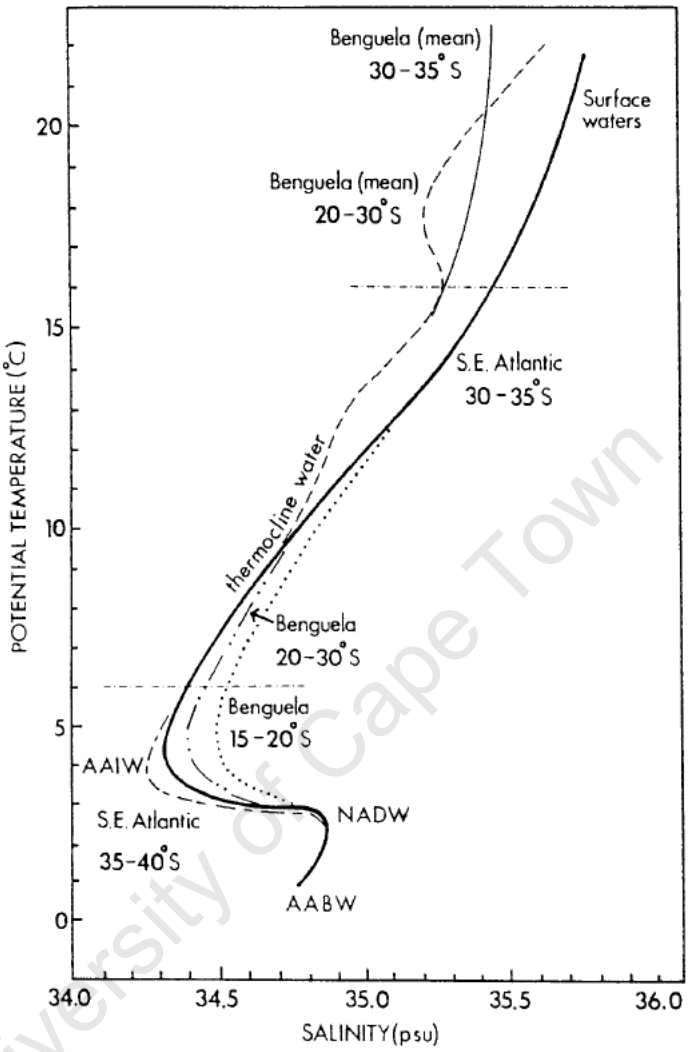

Figure 2.5: Water masses and their characteristic potential temperature-salinity properties in the Benguela system. Figure from Shannon and Nelson (1996).

2.4 The Benguela upwelling regime

The upwelling regime of the Benguela system spans the west coast of southern Africa from the Angola-Benguela Frontal Zone (ABFZ) at ~16°S southward to Cape Agulhas (at ~35°S), the southern tip of Africa. Upwelling intensity along the coast is far from contiguous, but instead is characterised by a number of cells of enhanced activity, which on the smaller scale is related to the orientation of the coastline. Demarcq

et al. (2003) used satellite-derived SST maps spanning 1982 - 1999 to create climatologies and to investigate variability of upwelling in the Benguela system. Their observations revealed that the Benguela system is fragmented into separate cells and in the annual mean they resolved three major upwelling areas: ~22.5-28°S, ~30°S and ~33-34°S. They also noted that in the vicinity of Lüderitz was the region of most intense upwelling in the Benguela system. Lutjeharms and Meeuwis (1987) used satellite SSTs to identify individual upwelling cells (see Figure 2.3) and identified 7 on the west coast in total: Peninsula (34°S), Columbine (33°S), Namaqua (30°S), Lüderitz (27°S), Walvis Bay (24°S), Namibia (21°S) and Cunene (17.5°S). The seasonal signal of upwelling is driven by the meridional movement of the SAA, which is furthest north in May and furthest south in February. When the SAA is furthest north, during austral autumn/winter months westerly winds, which do not produce upwelling, are frequent in the southern Benguela. Therefore, a strong seasonal signal dominates the southern Benguela upwelling cells (i.e. south of Lüderitz) with maximum upwelling rates during austral spring and summer (Andrews and Hutchings (1980)), when the SAA is furthest south and produces an intense equatorward alongshore wind. The Lüderitz cell is the principle perennial upwelling cell and the seasonal signal toward the north (in the central Namibia region) remains low, but at the northernmost upwelling cell (Cunene) intensifies in autumn and spring (Boyd et al. (1987)). The average offshore extent of the upwelling regime (i.e disregarding the large offshore extent of filaments) is ~150 km, but it can extend as far as ~250 km offshore at the Lüderitz cell (Lutjeharms and Meeuwis (1987)).

The nature of the northern, southern and oceanic boundaries of the Benguela upwelling regime will be discussed in the following sections. The Lüderitz Upwelling Cell-Orange River Cone (LUCORC) barrier, which has been described as effectively dividing the northern and southern Benguela regions, will also be discussed.

2.4.1 Northern boundary: the ABFZ

The northern boundary of the Benguela upwelling area is commensurate with the Angola-Benguela Frontal Zone (ABFZ) that has been defined as the confluence between the cool Benguela upwelling system and the warm Angola Current. It presents

a cross-frontal dichotomy in not only in water masses (Mohrholz et al. (2001)), but also of biological distribution and abundance (John et al. (2001)). The location and variabiltiy of the ABFZ has been extensively studied via: in situ measurements (Shannon et al. (1987); Mohrholz et al. (2001)), satellite observations (Meeuwis and Lutjeharms (1990); Kostianoy and Lutjeharms (1999); Veitch et al. (2006)) and model output (Colberg and Reason (2006)). All locate the relatively stable position of the front to be situated between ~15-17°S (see Figure 2.6) and to be oriented in a west to northwesterly direction from the coast. The front is characterised by sharp meridional surface temperature gradients, of the order of 1°C per 28-90 km (Veitch et al. (2006)) and is most intense within 250 km of the coast, though traces of it have been found as far west as the Greenwich meridian (Shannon and Nelson (1996)). It is most intense in the upper 50 m, but vestiges of it have been observed to a depth of 200 m (Shannon et al. (1987)). Using high resolution satellite sea surface temperature (SST) data, Veitch et al. (2006) observed that the surface expression of the front was widest (narrowest) with most (least) intense gradients in summer (winter) and that the northern and southern boundaries of the front fluctuated independantly of one another. The seasonal cycle of the intensity of the ABFZ has been related to fluctuations of upwelling-favourable wind-stress, while its N-S migration is related to changes in the poleward flow associated with its northern boundary that, in turn, is related to the curl of the wind stress (Colberg and Reason (2006)). A model study has shown that the intensity of the ABFZ is related to fluctuations in upwelling-favourable wind stress in the northern Benguela, while variations in the position of the ABFZ are connected to variations in the poleward flow that is associated with the northern boundary of the ABFZ, which in turn, is subject to variations of the curl of the wind stress (Colberg and Reason (2006)).

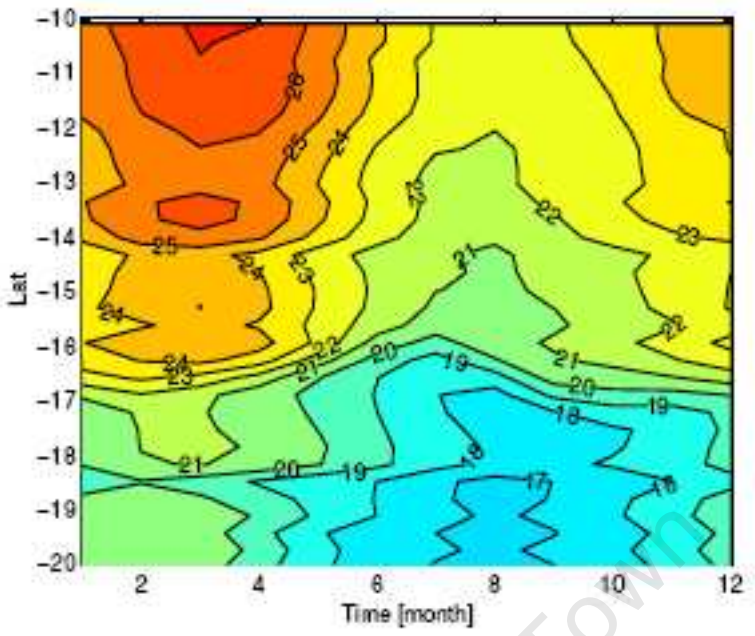

Figure 2.6: Hovmöller plot of the annual cycle of the temperature at a depth of 20 m, averaged between 10-14°E, based on ROMS model results. It represents the seasonal meridional movement of the ABFZ. (from Colberg (2006)).

The significance of the ABFZ on the Benguela upwelling regime lies principally in the fact that it presents a gateway into the ecologically sensitive upwelling system for water of equatorial/ tropical Atlantic origin. The relatively warm and saline Angola Current, originating from the South Equatorial Countercurrent (SECC), flows poleward along the coast until it reaches the ABFZ at which point it bends offshore due to Ekman transport (Mohrholz et al. (2001)). The water-mass analysis of Mohrholz et al. (2001) suggests the existence of a poleward undercurrent beneath the ABFZ, transporting warm and saline water into the cool and fresher upwelling regime. The poleward transport of tropical Atlantic thermocline water was observed by Gordon et al. (1995) to exist at the continental shelf floor as far south as 27°S and to feed the offshore Ekman transport there.

Low oxygen water (LOW) and hypoxic conditions commonly occur in the Benguela upwelling area and is detrimental to the health of pelagic and demersal fish as well as benthic biota. In the northern Benguela, LOW is controlled by the advection of remotely produced LOW and is strongly influenced by local upwelling that peaks

in austral winter (Monteiro et al. (2005)). The remote source of LOW has been identified by Lass et al. (2000) as the quasi-stationary, cyclonic Angola Dome that is situated in the Angola Basin. The poleward Angola Current and undercurrent are therefore of integral importance to the upwelling ecosystem of the northern Benguela as they transport LOW southward into the system.

Although the seasonal signal is dominant in the south-east Atlantic, the upwelling ecosystem is often devastated by the consequenses of periodic extreme-southward intrusions of tropical Atlantic water. Between about 1910-1995 these events recurred on an approximately decadal cycle (Taunton-Clark and Shannon (1988); Gammelsrod et al. (1998)), however in recent years they have tended to occur more frequently, but with less intensity (Veitch (2007)). These events are associated with anomalously southward penetration of warm, saline and low oxygen tropical Atlantic water and are known as Benguela Niños (Shannon et al. (1986)), based on their similarity to the Pacific counterpart: El Niño. Benguela Niños are remotely forced and have been connected to a relaxation of tradewinds in the western tropical Atlantic that forces a Kelvin wave eastward across the equator and eventually along the African coast (Shannon et al. (1986); Florenchie et al. (2003, 2004)).

2.4.2 Southern boundary: the Agulhas retroflection

As one of the four major eastern boundary current systems, the Benguela is unique in that its southern boundary is coincident with the termination of a western boundary current, namely the Agulhas Current. The retroflection area of the Agulhas Current lies south of the African continent in the westerly wind band and has been extensively described and investigated by Lutjeharms and van Ballegooyen (1988); Gordon (2003), among others. The importance of the retroflection lies in its role in the Indian-Atlantic ocean exchange of heat and salt and thus is also thought to have a key role in the maintenance of the global overturning of the ocean (Gordon et al. (1992); Lutjeharms (1996)). The primary mechanism of heat and salt exchange is via Agulhas rings, or eddies, that shed at the Agulhas retroflection, merge with the Benguela Current and travel into the Atlantic at a rate of about 6-9 per year (van Ballegooyen et al. (1994)). The shedding of eddies at the Agulhas retroflection

therefore has a significant control on the nature of the Benguela Current near its source. Boebel et al. (2003) coined the term 'Cape Cauldron' to describe the regime of turbulent mixing in the Cape Basin offshore of the southern Benguela upwelling system that is a consequence of the path and interaction of anticyclonic Agulhas eddies as well as smaller cyclonic eddies that are formed within the Cape Basin. As a result, dynamic variability in this region is comparable with the highly energetic western boundary currents (i.e. Kuroshio, Gulf Stream and the Brazil/ Falkland Current) Shannon and Nelson (1996), further highlighting the Benguela as unique among eastern boundary current systems.

Observations suggest significant seasonal and interannual variability of inter-ocean fluxes south of Africa and is supported by the model-based investigation of Reason et al. (2003). Their model results showed that the volume transport into the southeast Atlantic across 35°S was greatest in spring and summer (20.9 Sv and 18.2 Sv respectively) and least in winter and autumn (8.5 Sv and 14.7 Sv respectively). Occasionally unusually large intrusions of Agulhas water enter the southern Benguela. Such an event was documented by Shannon et al. (1990) to have occurred in late-1985/early-1986, resulting in anomalous warming of the south-east Atlantic during this time. Also using satellite imagery, Shannon and Nelson (1996) found evidence suggesting similar intrusions in austral summer 1992-93 and in austral winter 1994. These warm intrusions are linked to the highly varied westward position of the retroflection area, which Lutjeharms and van Ballegooyen (1988) found to be situated in the range 16-20 °E (see Figure 2.7).

The extent to which Agulhas rings directly interact with the upwelling regime is not yet very well understood. However, it is thought that the high steric heights introduced offshore in the southern Benguela by features associated with the Agulhas retroflection enhance the shelf-edge jet current (or Goodhope jet) (Lutjeharms (1996)). Also, it has been speculated by Duncombe-Rae et al. (1992b) that an Agulhas ring, situated 700 km west of the Orange River in April 1989, interacted significantly with the Benguela frontal system by enhancing the development of an upwelling filament that extended 450 km offshore at this time.

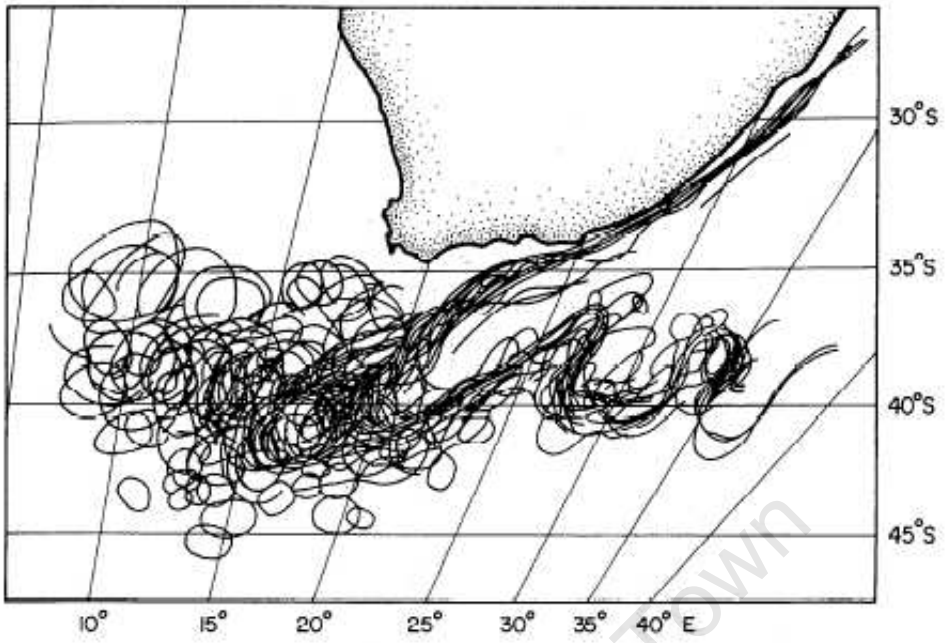

Figure 2.7: Thermal borders of features associated with the Agulhas retroflection and their manifestation of the southern boundaru of the Benguela Current system. Figure from Lutjeharms and van Ballegooyen (1988).

2.4.3 Offshore boundary: the upwelling front

The seaward extent of coastal upwelling is demarcated by a convoluted thermal front that has different characteristics in the northern and southern parts of the system (see Figure 2.8). South of Luderitz the upwelling front is well-defined and tends to follow the shelf-edge, while it is more diffuse in the north (Shannon and Nelson (1996)). Upwelling filaments in the the Benguela system extend offshore of the upwelling front and have a life-span of a few days to a several weeks. Their distict manifestation in SSTs has provided the means to observe them with relative ease via satellite data and thus they have been thoroughly documented (e.g. Lutjeharms and Stockton (1987); Shillington et al. (1990); Duncombe-Rae et al. (1992b); Shillington et al. (1992); Nelson et al. (1998)). On average, the filamentous band extends 100-500 km beyond the upwelling front (van Foreest et al. (1984)), but single filaments have been observed to extend considerable distances offshore (~1000 km) and tend to be confined to the vicinity of Luderitz (Lutjeharms et al. (1991)). The largest

filaments tend to develop meanders of the order of 250 km in wavelength and 100 km in amplitude. According to Lutjeharms et al. (1991) the meandering nature of the filaments imply the interaction between filaments at the front and the passage of Agulhas rings. Lutjeharms et al. (1991) also relate the formation of upwelling filaments with intense, seaward 'Berg' winds.

The significance of upwelling filaments is in their ability to advect upwelled water, rich in nutrients and biota, offshore. Large, persistent filaments can therefore have severe ramifications for the productivity of the upwelling ecosystem (Duncombe-Rae et al. (1992a)). A filament investigated by Duncombe-Rae et al. (1992b), extended some 450 km offshore and had become entrained in a passing Agulhas ring and could have resulted in an offshore volume flux of ~ $1.5 \times 10^6 m^3.s^{-1}$ (Lutjeharms et al. (1991); Duncombe-Rae et al. (1992a,b)).

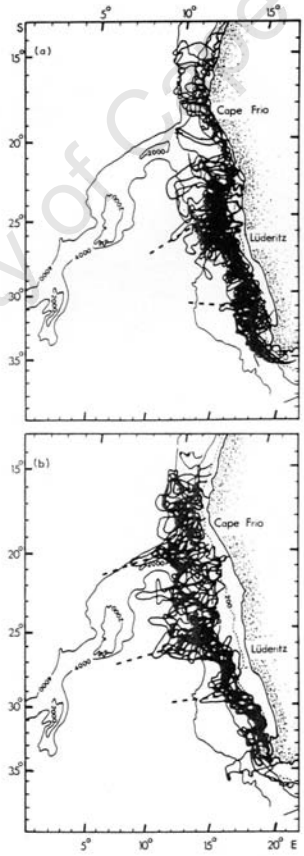

Figure 2.8: Montage of frontal boundaries, based on METEOSAT II SSTs, of the Benguela upwelling system for summer (a) and winter (b) months between December 1983 and August 1984. From Lutjeharms and Stockton (1987).

Lutjeharms and Stockton (1987) observed a large number of cyclonic eddies within the upwelling system and noted that they were preferentially situated downstream and offshore of the major upwelling cells and that they did not have a seasonal signal. Satellite images investigated by Strub et al. (1998) revealed the formation of cyclonic eddies within the regime of cool upwelled water and their subsequent offshore advection. The formation of cyclonic eddies is abundant off the Cape Peninsula. One such feature was studied by Lutjeharms and Mathyssen (1995), who found that they are not correlated with variations in the wind field. It has been suggested that filaments originating in the Agulhas retroflection initiate the development of cyclonic eddies off the Cape Peninsula (Lutjeharms and Stockton (1987)). Using satellite altimetry, offshore propagation of cyclonic eddies at the Cape Peninsula was observed by Strub et al. (1998).

A subsurface tongue of cool water was regarded as a semi-permanent feature off Cape Point during summer months by Andrews and Hutchings (1980) whose surface signal is masked during north-westerly winds (disappearing altogether during winter months). Using SSTs from aerial surveys Taunton-Clark (1985) also identified the Cape Point upwelling plume and suggested that its permanent subsurface nature facilitated the rapid response of its surface manifestation to local winds during summer months. Taunton-Clark (1985) concluded that the distinct cyclonic curvature of the wind at St. Helena Bay influenced the generation of the Cape Columbine upwelling plume and the Hondeklip Bay plume (~29.5°S) was found to be related to a region of maximum wind stress curl.

2.4.4 The LUCORC boundary

The LUCORC (Lüderitz Upwelling Cell-Orange River Cone) area, variously located between ~24-30°S (Hutchings (2004)), has been described as an environmental boundary effectively dividing the northern and southern Benguela regions. The Lüderitz upwelling cell has been identified as one of the worlds most active in terms of Ekman transport (Bakun (1996)). Its intensity and perennial nature is a consequence of its year-round maximum alongshore wind stress, together with the particular orientation of the coastline and bathymetry (Shannon and Nelson (1996)).

A defining characteristic of the LUCORC barrier includes the Orange River Cone, which is the broadest part of the continental shelf due to the input of sediment at the Orange River mouth at 30°S. The shelf narrows rapidly north of the Orange River Cone and less so toward the south. (Agenbag and Shannon (1988)).

Duncombe Rae (2004) investigated the hydrography of the LUCORC region and found that the source water for wind-induced upwelling to the north and south of it differed. North of the LUCORC barrier, the upwelling source waters originate from the more saline and oxygen depleted Angola Dome region and south of it the upwelling source waters originate from the central Cape Basin region, which is less saline and less oxygen deficient. The near-surface current structure provides a distinct impression that the LUCORC region presents a hiatus in the alongshore, equatorward flow regime on the west coast of southern Africa. A drifter study by Largier and Boyd (2001) showed rapid alongshore transport in the southern Benguela to the region of the LUCORC barrier, at which point the drifters turned sharply offshore (see Figure 2.9).

The intense offshore transport and turbulent nature of the LUCORC region is likely to have serious implications for planktonic communities with poor vertical migration capabilities and, indeed, the LUCORC region presents a distinct phytoplankton concentration minimum (Hutchings (2004)). A modelling study by Lett et al. (2007) shows that the LUCORC region is a barrier to the northward transport of certain ichthyoplankton of epipelagic species. The satellite SST-based work of Agenbag and Shannon (1988) suggests that longshore surface thermal gradients are too weak to explain a biological boundary. However, the model-based study of Lett et al. (2007) shows that a distinct subsurface thermal front, together with surface hydrodynamic patterns are the limiting factors in the northward transport of certain species of ichtyoplankton.

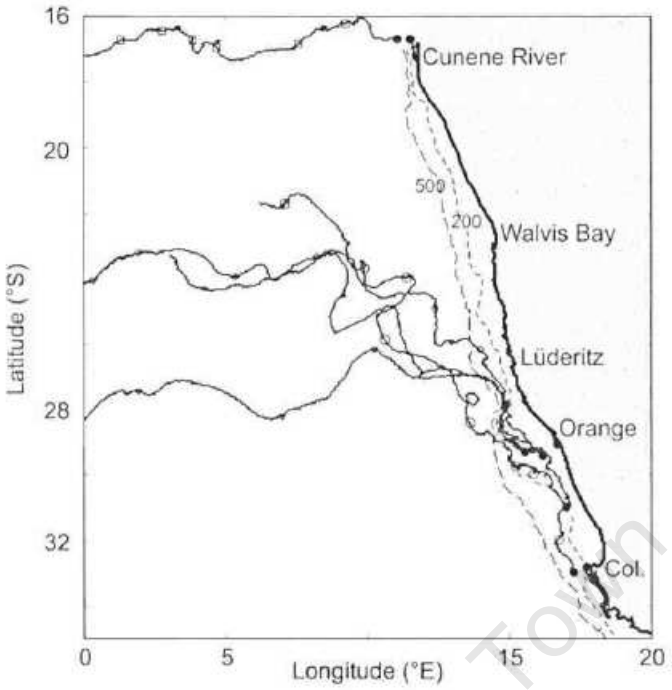

Figure 2.9: Drift tracks from 11 drifters released between mid-1999 to February 2000. The solid dots mark the locations of release. From Largier and Boyd (2001).

2.5 Shelf circulation

Currents over the shelf in the southern Benguela region, particularly in the regions of the Cape Peninsula and Cape Columbine, have been extensively studied over the years. The dominant feature of this area is the Goodhope Jet, which was anticipated (based on the intense horizontal density gradients) and then observed and described by Bang and Andrews (1974). The jet is located over the steep shelf in this region and has been observed to be permanently present, irrespective of wind conditions (Nelson and Hutchings (1983)). The jet has characteristic speeds of ~50 cm.s^{-1} and a width of between 20-30 km. From satellite altimetry Strub et al. (1998) noted a seasonal strengthening of the jet, which they associated with the injection of water with high steric heights, via Agulhas Current influx, on the offshore side of the jet and by upwelled water on the inshore side of the jet. It has been described by Shannon and Nelson (1996) as a convergent NW-oriented current system on the western Agulhas Bank that funnels into the west coast and bifurcates at Cape

Columbine into an offshore and alongshore component. The importance of the jet lies in the fact that it is the vehicle for the transport of fish larvae from their spawning ground on the Agulhas Bank to their nursery area in St. Helena Bay (Shelton and Hutchings (1982)). For a schematic of cirulation on the shelf in the south Benguela region see Figure 2.10.

Like other eastern boundary current systems, a poleward undercurrent is a dominant feature over the shelf in the Benguela system and is limited to an approximately 250 km coastal band (Shannon (1985)). Hart and Currie (1960) defined this current as a deep compensating current and, among others, observed it to extend as far south as Lüderitz. Its importance lies in the fact that it is the vehicle for the transport of low oxygen water, originating in the Angola Dome region, into the northern Benguela upwelling system. Indeed, oxygen has been used as a tracer of this poleward undercurrent and, based on a meridional oxygen profile, Mohrholz et al. (2007) demonstrated the southward deepening of the poleward undercurrent. While the poleward undercurrent have been frequently observed in the northern Benguela (perhaps due to its relative shallowness), Nelson (1989) has shown that the poleward undercurrent extends as far south as Cape Point and persists at the base of the shelf-edge and has speeds of 5-10 $cm.s^{-1}$.

Several investigations, based on in situ measurement's, have shown evidence of a net poleward flow over the inner shelf zone in both the northern (Nelson and Hutchings (1983)) and southern Benguela regions at depths of greater than ~40 m that is modulated by coastal trapped waves (Nelson (1989)) at periods of ~3-5 days. Based on in situ measurements at Yzterfontein (~33.25ºS) in the southern Benguela region, the speed of the poleward flow at a depth of 50-80m at the coast is of the order of about 5-6 $cm.s^{-1}$(Nelson (1989)). Viljoen (2006) used a numerical model to investigate the generation of the episodic nearshore poleward current in the southern Benguela and found that it was related to the relaxation of upwelling winds. The cause of the net poleward flow over the inner shelf however is yet to be fully understood.

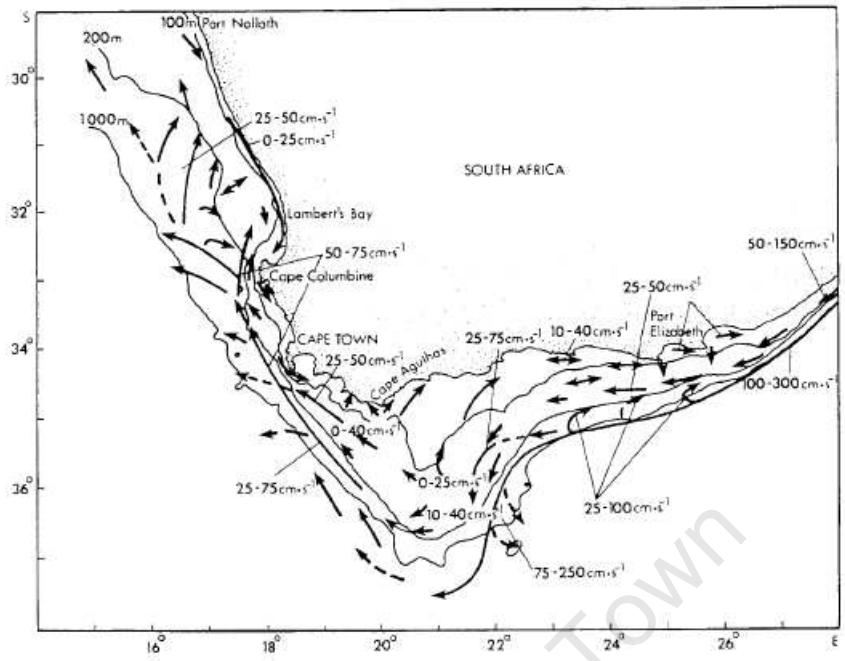

Figure 2.10: Schematic map of currents over the shelf, based on ADCP measurements obtained between November 1989 and January 1992. From Shillington (1998).

2.6 Modelling the Benguela system

While the upwelling regime of the Benguela system has been fairly extensively studied over the years due to its ecological and therefore economic importance, there has been a relative dearth of hydrodynamic modelling activity and progress in this regard has been slow. The first modelling attempt in the Benguela system was carried out by van Foreest and Brundrit (1985) who developed a two-mode numerical model for the southern Benguela, with the intention of investigating synoptic-scale current variability on time scales of a few days to a week. Their linear (i.e neglecting the non-linear advection terms) model extended northward from ~70 km south of the Cape Peninsula to ~70 km north of St. Helena Bay and to ~180 km offshore. Their model was forced with a constant, upwelling favourable wind for 3 days and reproduced certain features that have been observed in the area: most distinctly the Goodhope Jet. However, due to the linear nature of the model, there was no development of frontal zones that are defining dynamic features of this area. On

the inclusion of non-linear advection terms, they conducted some two-dimensional, flat-bottomed experiments that suggested the formation of frontal zones.

Penven et al. (2000) developed an idealized barotropic model in order to investigate the ecologically important retention processes in St. Helena Bay. Their configuration was based on the barotropic component of the SCRUM model (Song and Haidvogel (1994)), which solves the vertically integrated momentum equtions and, in this case, neglects density variations. A regular grid was developed with a horizontal resolution of 5 km, the alongshore lateral boundary conditions were periodic (i.e. the outflows at the southern boudary were inflows at the northern boundary, and vice versa) and the oceanic boundary condition was defined as a free-slip wall. A set of analytical functions described the topography and the wind forcing was a constant, upwelling-favourable wind stress. Their idealized model was able to reproduce the formation of a cyconic eddy in the lee of the Cape and showed that the evolution of this feature was related to a balance between advection and bottom friction. Retention is associated with this eddy and is positively related to the wind (for weak to moderate intensities), but for strong wind conditions retention reaches a maximum or slightly decreases.

A high resolution model of the St Helena Bay was developed by Viljoen (2006) in order to better understand small-scale features associated with upwelling relaxation periods. The Delft3D-FLOW model was used at a resolution of a few kilometers offshore to a few hundred meters in the nearshore regions and was forced by realtime winds calibrated by a coastal weather station. They resolved a nearshore poleward flow during upwelling relaxation events in a simulation with a straight coastline. The introduction of a more realistic coastline did not appear to make a significant difference in the generation of the poleward flow during relaxation events.

In order to investigate the transport processes of fish eggs and larvae from their spawning ground to the nursery area of St. Helena Bay, Penven et al. (2001) designed a 3-D regional configuration of ROMS over the southern Benguela region. A pie-shaped grid was developed, following the southwestern corner of the African continent from 28-40°S and from 10-24°E. The horizontal grid was variable (i.e. higher resolution near the coast) and both high and low-resolution simulations were run,

with a resolution of ~9 km and ~18 km at the coast respectively. The wind forcing was the COADS monthly mean climatology and the horizontal boundary conditions were from the AGAPE basin-scale model (Biastoch and Krauss (1999)). This configuration, for the first time, allowed for the successful resolution of nearshore circulation features that are important to the ecological functioning of the southern Benguela system. It was also able to resolve the mesoscale plumes, filaments and eddies characteristic of upwelling systems even though the forcing applied was large-scale in space and time (thus suggesting the the importance of intrinsic variability). This configuration (known as 'PLUME') has been used in several physical-biological coupled model studies using. One approach has been to couple this physical model to the two biogeochemical capabilties of ROMS, namely the NZPD and the $N_2Z_2P_2D_2$, in order to model primary and secondary productivity in the southern Benguela (Kone et al. (2005)). Another approach has been to couple the PLUME physical model to an individual based model in order to quantify the influence of flotability of eggs on their transport from the Agulhas Bank to St Helena Bay (Parada et al. (2003)).

The PLUME configuration was later used in Blanke et al. (2005) in order to diagnose the scales of wind stress relevant to warm and cold anomalous events in the southern Benguela as well as to build model-based dynamical indices aimed at characterizing the intensity and spatial extent of upwelling. In this study the PLUME configuration was forced by high resolution QuikSCAT winds spanning 1999-2003. Their results suggested that time resolution of the wind stress was a crucial factor in reproducing interannual SST anomalies.

The Finite Resolution Antarctic Model (FRAM) was used by Lutjeharms et al. (1995) to resolve large-scale processes associated with the south-east Atlantic upwelling area, from 24°S to the southernmost tip of Africa. The simulation was run at a resolution of $\frac{1}{2}^o$ longitude by $\frac{1}{4}^o$ latitude and forced with seasonal mean winds. Though at very low resolution, it was able to simulate upwelling cells, plumes and frontal eddies. While it resolved Agulhas rings, they tended to occur too regularly, thus inhibiting the use of this model at reproducing the interaction between these features and the upwelling front.

Skogen (1999) used a coupled biological/physical model (known as the Norwegian Ecological Model system: NORWECOM) in order to investigate the impact of upwelling and large-scale ocean climate parameters on primary production and trophic transfer processes in the Benguela ecosystem. The physical model used was the sigma-coordinate Princeton Ocean Model (POM) at a resolution of 20 km, spanning the African coast from 12-46°S and from 4-30°E. 6-hourly ECMWF (European Center of Meteorology and Weather Forecacst) winds were used to force the model and the lateral boundary conditions were prescribed by Levitus World Ocean Atlas. This model was successful in reproducing the Benguela upwelling system and the individual upwelling cells. The associated alongshore thermal upwelling front was represented, as was the distinct meridional temperature/salinity front characteristic of the ABFZ.

2.7 Eastern Boundary Current Systems

The four eastern boundary current systems (EBCS), namely; the California Current system, the Canary Current system, the Humboldt Current system and the Benguela Current system, share the role of being the most productive regions of the worlds oceans. It is therefore not surprising that the dynamics of these regions are driven by common large-scale ocean and atmospheric features. In the ocean, a sluggish equatorward flow that forms the eastern limb of the subtropical gyre characterizes the large-scale circulation regime. In the atmosphere, the combination of high pressures over the ocean basins and low pressures over land, together with the physical and thermal barrier at the coast, drives an alongshore, equatorward wind regime that is upwelling favourable. While the process of upwelling brings cool, deep water to the surface, essentially resulting in a shallower thermocline at eastern ocean boundaries, the basin-scale shoaling of the thermocline toward the east is consistent with Sverdrup theory and the propagation of Rossby waves toward the west. Using the regional- and basin-scale effects on the thermocline as an example, Capet et al. (2008) presented the idea that oceanographic features of EBCS's are a combination of the large-scale circulation regime and the process of coastal up-

welling. Indeed, the global significance of the equatorial upwelling tongue has been demonstrated by Boccaletti et al. (2003), who used an idealized, basin-scale model to investigate global heat budgets. The ocean surface is subject to greatest heat gain in the equatorial and eastern boundary upwelling regions where SSTs are especially low in comparison to the overlying air temperature. The heat gain in these regions is required in order to balance the huge heat losses in high latitudes and is controlled by the upwelling of cold water to the surface which, in turn, is controlled by the depth of the thermocline. A shallow thermocline will lead to very cold upwelled waters and large heat gain at the surface, while a deep thermocline will lead to warm upwelled waters and less heat gain. Boccaletti et al. (2003) showed that adjustments of the thermocline depth in the equatorial upwelling regime occur in response to variations in high latitude heat losses in order to maintain closed global heat budgets. On this premise, it can be concluded that eastern boundary upwelling regimes be suggested as locations for monitoring global change in terms of large-scale thermocline adjustments (i.e a deeper thermocline will inhibit the upwelling of cool, nutrient-rich water).

Of the four EBCSs, the California has been most extensively studied via observations (both in situ and satellite) and models. It extends from ~47°N where the eastward West Wind Drift meets the coast, separating the Alaska Current system from the California Current system, to ~21°N (near the tip of Baja California). The general system of currents in the California Current system are typical: a broad surface equatorward flow, a poleward undercurrent and an equatorward upwelling jet. The latter is known as the Davidson Current and reverses during boreal winter. Its reversal may be partly explained by the positive wind curl in a 200 km coastal band which, in accordance with the Sverdrup relation, drives a poleward flow that is overwhelmed by the strong upwelling favourable winds in spring and summer (that drive an equatorward current) (McCreary (1987)). Another mechanism put forward for the existence of the transient Davidson Current by McCreary (1987) is the generation of a pressure gradient force due to the relaxation of upwelling-favourable winds in winter. Carr and Kearns (2002) calculated seasonal offshore Ekman transports, based on satellite winds and found that strongest seasonal variability occurred north

of 34°N, with maximum upwelling in boreal summer and downwelling in boreal autumn and winter. South of 34°N, strongest wind forcing is during boreal spring and minimal seasonal variability occurs between 32-34°N. During the upwelling season, equatorward, mesoscale jets develop with peak speeds of 30-50 $cm.s^{-1}$(Barth et al. (2000)), with variability significantly modulated by topography (Song and Chao (2004)). Using satellite, drifter and moored current data, Kelly et al. (1998) observed a robust seasonal cycle of nearshore eddy kinetic energy (EKE), such that EKE increases as the equatorward current increases and moves offshore (to 127°W) during boreal summer and autumn. Haney et al. (2001) showed that the limited offshore propagation of surface EKE as observed by Kelly et al. (1998) is due to the vertical redistribution (or barotropization) of EKE to the deep ocean. The modelling study of Marchesiello et al. (2003) concluded that the dominant mesoscale variability in the California Current system is forced intrinsically via baroclinic instabilities of alongshore currents. The stratification and baroclinicity of the California Current system is enhanced due to its unique feature of increased salinity with depth.

The Humboldt Current system extends from northern Peru at 4°S to central Chile at 40°S and, unlike other EBCSs, it's equatorward boundary abuts the equatorial current system. As such, on interannual timescales it is directly affected by ENSO and has the most extensive depleted oxygen minimum layer (Freon et al. (2006)). Off Peru coastal upwelling is at a maximum in austral winter and is least during summer. Further south, in northern Chile (18-30°S), upwelling peaks in late austral spring and further south still, off central Chile (30-38°S), it peaks in late spring and summer. The progression of peak upwelling from north to south mirrors the southward movement of the subtropical high pressure system, which also dictates the more perennial upwelling in Peru as opposed to the strong seasonal signal in central Chile (where upwelling only occurs during spring and summer). Penven et al. (2005) investigated equilibrium conditions of the northern part of the Humboldt Current system (5-20°S), otherwise known as the Peru Current system. In this region the Andes forms a distinct physical barrier and channels the wind to flow northward, resulting in almost constant upwelling favourable winds and highest production rates of all the EBCSs. The dominant scale of variability is the interan-

nual effect of ENSO, which deepens the thermocline and strengthens the poleward currents, but does not have a significant impact on the local equatorward winds. In their model, Penven et al. (2005) demonstrate that the existence of a cyclonic wind stress curl throughout the Peru Current system drives a poleward flow beneath a shallow, equatorward surface layer. They also point out that the extreme shallowness of the thermocline in this region would create a significant sensitivity of upwelling source waters to the poleward propagation of Kelvin waves from the equator.

The Canary Current system is defined as the eastern boundary of the North Atlantic subtropical gyre and extends from northern Iberia at approximately 43°N to Guinea at approximately 10°N. The Canary Current is made up of contributions from the weak Portugal Current, which flows equatorward along the Iberian coast, as well as the eastward Azores Current. It flows southward to ~21°N where it veers offshore and feeds the North Equatorial Current. Between Cape Blanc (~21°N) and Cape Verde a permanent cyclonic recirculation cell exists, carrying water poleward along the coast and extending beyond Cape Blanc as an undercurrent. The seasonal signal of upwelling is related to the north-south migration of the Azores High pressure system, such that upwelling occurs during boreal summer off Iberia, perennial upwelling (with a maximum in summer) between 20-35°N and winter upwelling south of 21°N (Freon et al. (2006)). Large filaments have been observed to extend offshore, particularly where the Canary Current separates from the coast at 21°N. The Canary Current system is unique in that is the only EBCS that flows through an archipelago of islands that extends from within 200 km of the coast to the open ocean. The effect of the Canary Current flowing through the island chain is to create a significant downstream wake. This generation of mesoscale turbulence in the form of downstream eddies interacts with the west African upwelling regime by drawing out filaments several hundred kilometers offshore (Aristegui et al. (1994)). The broadest active area (i.e. offshore area of $>1 mg.m^{-3}$ of chlorophyll concentration) of all the EBCSs is found in the Canary Current system and, by comparing with the narrowest active area off California, Marchesiello and Estrade (2006) used a numerical model to identify topography (specifically, the width of the shelf, which

is large in the case of the Canary Current system) as a key factor.

Like the other systems, the Benguela Current system has features that are unique. The most outstanding feature of the Benguela system is the fact that its southern boundary is commensurate with the termination of the African continent as well as the retroflection of the western boundary current of the south Indian Ocean (i.e. the Agulhas Current). As a result, the large-scale equatorward flow of the Benguela Current is influenced by the high mesoscale variability introduced by features spawned at the Agulhas retroflection south of the African continent. A plot of satellite-derived EKEs for all four of the EBCSs is shown in Figure 2.11 (from Capet et al. (2008)) and highlights the unusually high levels of EKE in the offshore regions of the southern Benguela compared to other systems. Note that a log-scale is necessary in order to capture the very high offshore EKEs as well as the very low EKE in the nearshore regions of the Benguela system (the other systems do not require a log-scale). More than just its role in the global heat budget, the importance of the Benguela EBCS lies in the passage of Agulhas Rings, via the Benguela Current, into the North Atlantic, which forms a crucial part of the global thermohaline circulation.

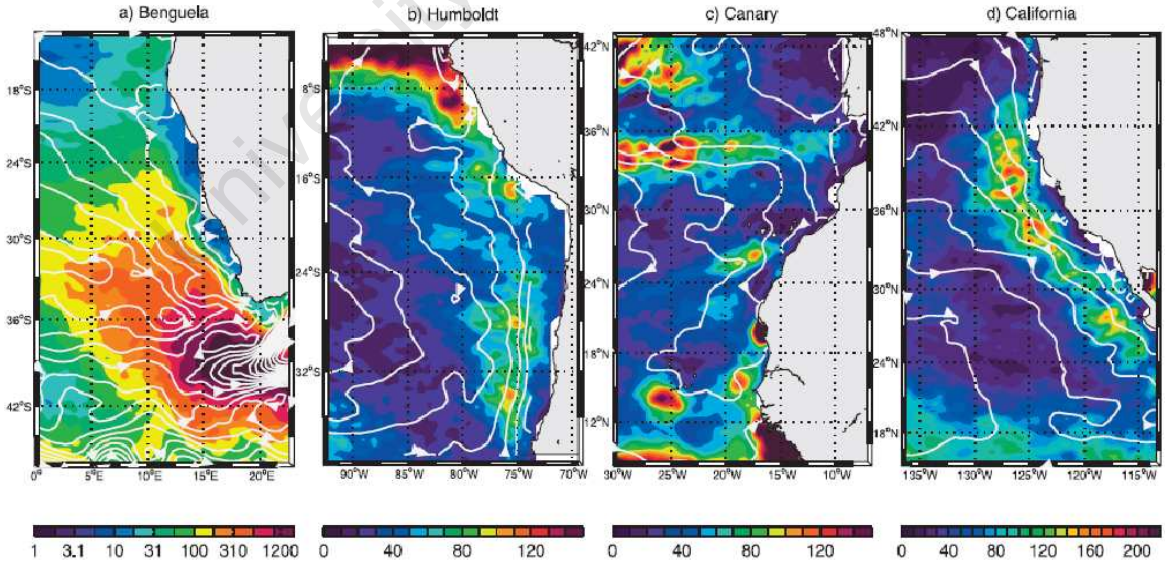

Figure 2.11: Measured EKE (in $cm^2.s^{-2}$) and sea-surface height (from Duacs SSH and Rio5 respectively) in white contours (6 cm interval). Note the log-scale of the EKE colourbar for the Benguela system that is necessary to capture the very large offshore EKEs as well as the low nearshore EKEs. (from Capet et al. (2008)).

2.8 Summary and motivation

This review section has served to collate current knowledge on the dynamics of the Benguela Current system and, in doing so, has provided a platform from which to identify gaps and shortfalls. The Benguela Current system is made up of the large-scale Benguela Current and the nearshore Benguela upwelling regime. The latter is made up of the eastern limb of the subtropical ocean gyre with significant contributions from Agulhas Rings. In the context of the global thermohaline circulation, much of the scientific research in the Benguela Current system has focussed on the salt and heat fluxes into the Atlantic Ocean via Agulhas Rings. On the other hand, while the upwelling regime of the Benguela Current system is of immense ecological and economical importance, relatively little research has been carried out on its salient dynamic features compared with other eastern boundary upwelling systems.

Certain physical features of the Benguela system have been identified as pivotal to the functioning of the upwelling ecosystem and research on them has tended to be somewhat constrained within a biological/biogeochemical framework. For instance, the Goodhope Jet is known to be crucial for the transport of fish eggs and larvae from the spawning ground on the Agulhas Bank to their nursery area in St. Helena Bay, but little work has been done on the dynamical forcing of it. Similary, while the poleward flow in the northern Benguela has been shown to have critical implications for the health of the upwelling ecosystem in the northern Benguela via its role in the transport of LOW, the full extent of its physical characteristics (e.g. forcing, geographical extent, seasonal signal) has not been rigorously investigated. Based on satellite and observational data, the northern and southern Benguela regimes have been considered disparate, with the LUCORC barrier identified as the transition region. Some work has been done on the biologcal significance of the latter, but its physics is not well understood. That the Benguela is unique among the worlds four eastern boundary upwelling systems, in terms of the proximity of its southern boundary to the Agulhas Current, is well documented. However, neither the direct nor indirect effects of Agulhas Current influx on the Benguela Current system is thoroughly understood. It is imperative that we improve our understanding of physical processes such as these if we hope to gain insight into the causes

and consequences of episodic extreme events that can have devastating ecosystem impacts.

The aim of this work is to use the spatially and temporally cohesive output from a model simulation in order to study the equilibrium dynamics and seasonal cycle of the Benguela system in a systematic way, inclusive of both the northern and southern regimes as well as the nearshore upwelling and large-scale offshore regimes. Our objective is to improve the general understanding of the dynamics of the Benguela system and, in doing so, to address some of the current gaps in knowledge:

- What characterizes the dynamical disparity between the northern and southern Benguela regimes?
  - How do the regimes differ from each other, in terms of nearshore as well as offshore dynamics?
  - Is the transition between them defined by a distinct physical barrier? If so, what forces it?
- What drives the large-scale flow regime in the Benguela system?
  - Why is the large-scale flow regime in the northern Benguela poleward, despite the prevailing southeasterly winds?
- How do transient features, associated with Agulhas influx, influence the mean state of the Benguela system?
  - How does Agulhas influx affect the large-scale flow regime of the Benguela system?
  - Does Agulhas influx drive the Goodhope Jet?
  - To what extent is the nature of the upwelling front and mesoscale features associated with it (e.g. filaments) related to Agulhas features?

Chapter 3

Data and Methods

3.1 The Regional Ocean Modelling System (ROMS)

3.1.1 General description

The Regional Ocean Modelling System (ROMS) is a split-explicit, free-surface, topographic-following coordinate model that is well suited to regional problems (see Shchepetkin and McWilliams (2005) and Shchepetkin and McWilliams (2008)). It makes the Boussinesq approximation, in which density variations are neglected except in their contribution to the buoyancy force in the vertical momentum equation, and the hydrostatic approximation, which assumes that the vertical pressure gradient balances the buoyancy force. ROMS solves the incompressible primitive equations based on these assumptions and is coupled with advection/diffusion schemes for potential temperature and salinity and a nonlinear equation of state. Its prognostic variables are the surface elevation, the barotropic and baroclinic horizontal velocity components and temperature and salinity. Shchepetkin and McWilliams (2003) and Shchepetkin and McWilliams (2005) provide a thorough description of the model formulation.

Equations of motion

With regard for the Boussinesq and hydrostatic approximation, the primitive equations, expressed in cartesian coordinates, include the horizontal momentum equa-

tions (equations C.1 and C.2), the advective/diffusive equations for potential temperature and salinity (equations 3.3 and 3.4), the hydrostatic balance (equation 3.5), the continuity equation for an incompressible fluid (equation D.4) and the equation of state (equation 3.7):

$$\frac{\partial u}{\partial t} + \vec{v}.\nabla u - fv = -\frac{\partial \phi}{\partial x} + \frac{\partial}{\partial z} A_v \frac{\partial u}{\partial z} + D_u \tag{3.1}$$

$$\frac{\partial v}{\partial t} + \vec{v}.\nabla v + fu = -\frac{\partial \phi}{\partial y} + \frac{\partial}{\partial z} A_v \frac{\partial v}{\partial z} + D_v \tag{3.2}$$

$$\frac{\partial T}{\partial t} + \vec{v}.\nabla T = F_T + D_T \tag{3.3}$$

$$\frac{\partial S}{\partial t} + \vec{v}.\nabla S = D_S \tag{3.4}$$

$$\frac{\partial \phi}{\partial z} = \frac{-\rho g}{\rho_0} \tag{3.5}$$

$$\frac{\partial u}{\partial x} + \frac{\partial v}{\partial y} = -\frac{\partial w}{\partial z} \tag{3.6}$$

$$\rho = \rho(T, S, P) \tag{3.7}$$

where:

- x, y are the horizontal and z is the vertical coordinate in a cartesian frame of reference (in m)
- u, v and w are velocity components in the x, y and z directions respectively (in $m.s^{-1}$)
- t is the time (in s)
- f is the coriolis parameter (in s^{-1})
- g is acceleration due to gravity (in $m.s^{-2}$)

- ϕ is the dynamic pressure ($= \frac{P}{\rho_0}$ in $m^2 s^{-2}$)
- P is pressure (in $N.m^{-2}$ or $kg.m^{-1}.s^{-2}$)
- ρ is density ($kg.m^{-3}$)
- ρ_0 is the reference density of sea water (taken to be 1024 $kg.m^{-3}$)
- T is potential temperature (in ^oC)
- S is salinity (in psu)
- A_v is the vertical mixing parameter
- F_T is the surface forcing term for shortwave solar radiation
- D_u, D_v are lateral momentum dissipation terms and in our simulation are formulated within the advection terms
- D_T, D_S describe the diffusion of temperature and salt

Vertical boundary conditions

External forcing terms are introduced into the model through vertical viscosity and and diffusivity via the surface and bottom boundary conditions.

At the surface, where z=ζ:

$$A_v \frac{\partial u}{\partial z} = \frac{\tau_S^x}{\rho_0} \tag{3.8}$$

$$A_v \frac{\partial v}{\partial z} = \frac{\tau_S^y}{\rho_0} \tag{3.9}$$

$$A_T \frac{\partial T}{\partial z} = \frac{Q_T}{\rho_0 c_p} \tag{3.10}$$

$$A_S \frac{\partial S}{\partial z} = (E - P)S \tag{3.11}$$

$$w = \frac{\partial \zeta}{\partial t} \tag{3.12}$$

and at the bottom, where z=-h:

$$A_v \frac{\partial u}{\partial z} = \frac{\tau_B^x}{\rho_0} \tag{3.13}$$

$$A_v \frac{\partial v}{\partial z} = \frac{\tau_B^y}{\rho_0} \tag{3.14}$$

$$A_T \frac{\partial T}{\partial z} = 0 \tag{3.15}$$

$$A_S \frac{\partial S}{\partial z} = 0 \tag{3.16}$$

$$-w + \vec{v}.\nabla h = 0 \tag{3.17}$$

where:

- ζ is the surface elevation (in m)
- $\tau_S^x$and τ_S^y are surface wind stresses in the x- and y-directions (in $N.m^{-2}$ or $kg.m^{-1}.s^{-2}$)
- $\tau_B^x$and τ_B^y are bottom stresses in the x- and y-directions (in $N.m^{-2}$ or $kg.m^{-1}.s^{-2}$)
- A_v,A_T and A_S are the vertical viscosity and diffusivity terms (in $m^2.s^{-1}$)
- Q_T is the surface heat flux (in $W.m^{-2}$)
- (E-P) is evaporation minus precipitation (in psu)
- $C_p$is the heat capacity of seawater (in $J.kg^{-1}.^oC^{-1}$)

Ocean-atmosphere feedback

The absence of an ocean-atmosphere feedback term can lead to model sea-surface temperature (SST) drift, but is addressed in ROMS by formulating the surface heat flux term as a relaxation of the model to climatological SST (Barnier et al. (1995)):

$$Q_T = Q + \frac{\partial Q}{\partial T_{clim}}(T_{model} - T_{clim}) \tag{3.18}$$

where Q is the total surface climatological heat flux obtained from COADS (see Figure 3.10), T_{model} is the model-derived SSTs and T_{clim} is the climatological SSTs, obtained from Levitus WOA. The term $\frac{\partial Q}{\partial T_{clim}}$ is the kinematic surface net heat flux sensitivity to the sea surface temperature and is made up of three contributions: infrared, sensible heat and latent heat, which are given by the following:

$$infrared = -4 \times \sigma \times T^3_{model} \tag{3.19}$$

$$sensible\ heat = -\rho_{atm} \times C_p \times C_h \times U \tag{3.20}$$

$$latent\ heat = -\rho_{atm} \times C_e \times L \times U \times 2353 \times log_{10}(q_s/T^2_{model}) \tag{3.21}$$

$$\frac{\partial Q}{\partial T_{clim}} = infrared + sensible\ heat + latent\ heat \tag{3.22}$$

where, σ is the Stefan-Boltzmann constant (5.6697x10^{-8}$W.m^{-2}.^oC^{-4}$), ρ_{atm} is atmospheric density, C_p is the specific heat of the atmosphere at sea surface (1004.8 $J.kg^{-1}.^oC^{-1}$), C_h is the sensible heat transfer co-efficient (0.66x10^{-3} $W.m^{-2}.^oC^{-1}$), C_e is the latent heat transfer coefficient (1.15x10^{-3}$W.m^{-2}.^oC^{-1}$), U is the wind speed at a height of 10 m, L is the latent heat of vaporization (2.5008x10^6-(2.3x10^{3}x surface atmospheric temperature) $J.kg^{-1}$) and q_s is the specific humidity at sea level.

Similarly, a drift in model-derived salinities can occur if no account is taken for ocean-atmosphere interaction in the model fresh water fluxes. The formulation in ROMS for the salt flux correction is as follows:

$$Salt\ flux = S_{clim}(E - P) + cst(S_{clim} - S_{model}) \tag{3.23}$$

where S_{clim} and S_{model} are the climatological (from COADS: see Figure 3.11) and model-deried sea-surface salinities respectively, $(E-P)$is the evaporation minus

precipitation based on COADS data. In the ROMS formulation the constant, *cst*, is equivalent to the $\frac{\partial Q}{\partial T_{clim}}$ term (3.22).

Lateral boundary conditions

Open-boundary conditions are a combination of outward oblique radiation and adaptive nudging toward prescribed external boundary conditions and are described by Marchesiello et al. (2001). The latter is necessary in order to maintain stability. Lateral viscosity is zero everywhere except in sponge layers at open boundaries, where it increases smoothly toward the edge of the domain in order to suppress model-data inconsistencies. The amount of damping depends on the quality of the data at the lateral boundaries. Lateral boundaries that are closed (i.e. land) are defined as masked regions. Computations occur over the whole domain and at the end of each time-step the values of variables within the masked regions are set to zero. At the mask boundaries however, the calculated velocity terms are corrected for free-slip or no-slip conditions. More information on the procedure can be found in Hedstrom (1997).

Vertical coordinate system

Three different vertical coordinate systems are commonly available for numerical ocean modelling: the geopotential, or z-coordinate, the isopycnic and the sigma-coordinate. The latter, terrain-following coordinate system is used by ROMS (refer to Figure 3.1 for an example) for its better representation of bathymetry-flow interactions (Marchesiello et al. (1998)). The use of sigma-coordinates requires the following transformation:

$$z = z(x, y, \sigma) \tag{3.24}$$

where, z is the cartesian height and σ is the distance from the free-surface, measured as a fraction of the water column at a particular location. That is, σ ranges between -1 and 0; at the free-surface ($z = \zeta$) it is equal to 0 and at the bottom ($z = -h(x, y)$) it is equal to -1 (Shchepetkin and McWilliams (2005)). The trans-

formation is performed following the method of Song and Haidvogel (1994) and can be stretched non-linearly according to surface- and bottom-stretching parameters (θ_s and θ_b respectively) so that, for example, resolution is enhanced at the surface. For this simulation, θ_s=6 and θ_b=0.

The approximation of the horizontal pressure gradient force in topographic-coordinate models has been a long-standing problem due to hydrostatic inconsistencies that develop in the transformation of the horizontal pressure gradient terms in sigma-coordinate, hydrostatic primitive equation models. The error occurs when the discretized pressure gradient force fails to vanish with horizontal isopycnals, thus resulting in spurious geostrophically-balanced currents (Shchepetkin and McWilliams (2003)). From comparisons with a laboratory experiment, Kliem and Pietrzak (1999) showed that this error was most significant in regions of steep topography and large density gradients. This issue was adressed by Shchepetkin and McWilliams (2003), who developed a new pressure-gradient algorithm, designed to reduce the pressure-gradient error, by achieving more accurate hydrostatic balance terms for the sigma-coordinate formulation. Their algorithm reconstructs the density field into z-coordinates as continuous functions of transformed coordinates and is then analytically integrated to compute the pressure-gradient force (Shchepetkin and McWilliams (2003)).

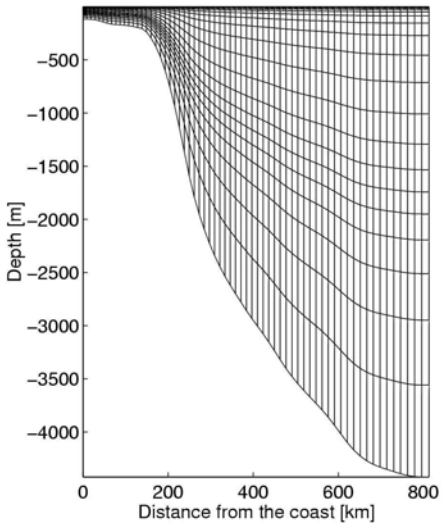

Figure 3.1: Example of a ROMS vertical grid as prescribed by the sigma-coordinate system (from Penven (2000))

Horizontal, vertical and temporal discretization

In the horizontal, the discretization of ROMS is based on the Arakawa-C grid (Arakawa and Lamb (1977)), has a characteristic variable-placement scheme shown in Figure 3.2, that is particularly suited to model resolutions that are finer than the first Rosssby radius of deformation. The staggered nature of the vertical discretization is shown in Figure 3.3.

For computational efficiency, a mode-splitting technique is used to separate (fast) barotropic and (slow) baroclinic modes. Time discretization follows the third-order leap-frog predictor and Adams-Moulton corrector scheme (Shchepetkin and McWilliams (2005)), which is robust and stable. It is designed such that a number of barotropic time-steps are run within one baroclinic time-step in order to develop the free-surface and depth-integrated momentum equations. The time-stepping kernel was developed by Shchepetkin and McWilliams (2005) and involves a consistent temporal averaging technique of the barotropic mode in order to provide conservation and constancy preservation properties required for the tracer fields. The weighted temporal averaging procedure of the barotropic mode allows for accurate representation of barotropic motions resolved by the baroclinic time-step (thereby avoiding aliasing). The stability of this scheme allows for greater time-steps and therefore, enhanced computing efficiency.

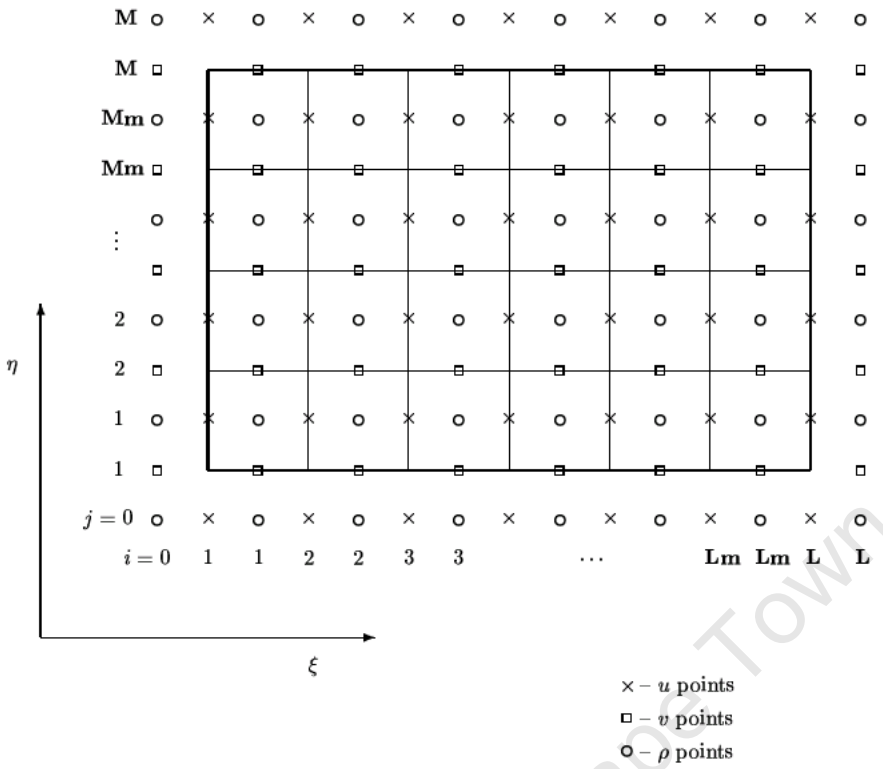

Figure 3.2: The Arakawa-C grid used in the horizontal discretization of ROMS. Temperature, salinity, vertical velocity, sea surface height, the coriolis force and depth are places at the ρ points in the center of each grid cell, while the v- and u-velocity components are places at the v- and u- points at the edges of each grid cell respectively.

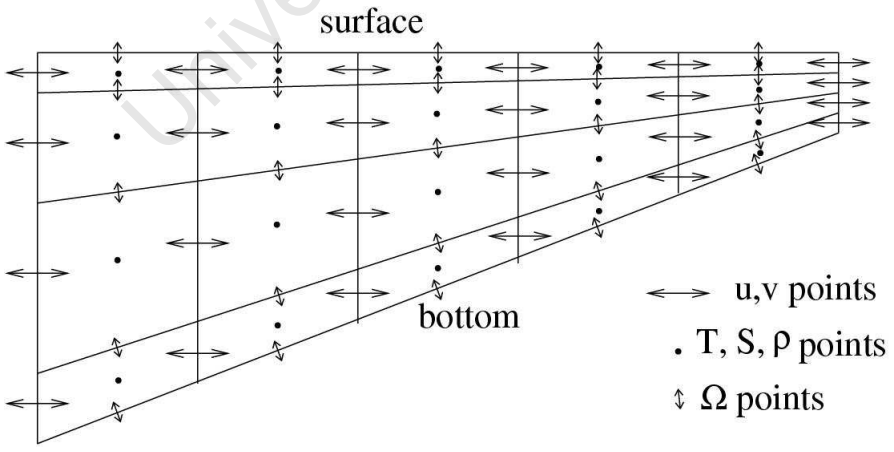

Figure 3.3: The vertical discretization scheme used in ROMS.

Advection scheme

The advection scheme is third-order upstream biased which reduces dispersion errors, based on excessive dispersion rates necessary to maintain smoothness. This essentially enhances the precision for a given grid resolution (Shchepetkin and McWilliams (1998)). The recent implementation of higher-order diffusive advection schemes has lead to spurious diapycnal mixing in sigma-coordinate models. A solution to this problem was addressed by Marchesiello et al. (2008a) and involves the split of advection and diffusion, the latter of which appears as a biharmonic operator. This solution, was implemented in our simulation in order to preserve the low dispersion and diffusivity capabilities of the original scheme while conserving water mass charactersitics.

Turbulent closure scheme

The parameterization of unresolved, subgrid-scale vertical mixing processes in done by the non-local K-profile Parameterization (KPP) scheme (Large et al. (1994)). The KPP scheme employs distinct methods to parameterize subgrid mixing processes in the ocean interior and in the boundary layer. Mixing in the interior is represented by taking into account shear instabilities (modelled as a function of the local gradient Richardson number), internal waves and double diffusion. The depth of the boundary layer at each grid point is determined by a critical value of turbulent processes that are parameterized by the bulk Richardson number and depends on surface forcing, buoyancy and the vertical velocity gradient. Diffusion within the boundary layer is formulated based on the similarity theory of turbulence and is matched to diffusion within the ocean interior.

The ROMS embedding approach

In order to maximize computing efficiency of a high resolution simulation of the Benguela system, the AGRIF nesting capability of ROMS is employed (Debreu and Mazauric (2006)). A nested approach is designed such that the boundary conditions of a high resolution 'child' domain are supplied by the lower resolution 'parent' domain within which it is embedded. This allows for more consistent boundary con-

ditions of the child domain than can be obtained from, often sparsely populated, in situ data. Penven et al. (2006c) evaluated the use of the 1-way nesting approach described above for the central California upwelling system and found that it improved the high resolution simulation, compared to the use of open boundaries at only a slightly higher computational cost. Our simulation makes use of the recently implemented version of the AGRIF package (see Debreu et al. (2008)) that allows for a 2-way nesting procedure, which also allows the child solution to feed into the parent domain.

3.1.2 The nested configuration

The parent grid: SAfE

The SAfE configuration is used as the parent domain and was designed by Penven et al. (2006a) to capture the salient oceanographic features of the southern Atlantic Ocean (see Figure 3.4). The domain is based on a Mercator grid and encompasses the region spanning 2.5^{o}W-54.75^{o}E and 46.75^{o}S-4.8^{o}S and has a horizontal resolution that ranges from 19 km in the south to 27.6 km in the north (i.e. a 230x194 grid), which allows for the resolution of Agulhas rings (which have a length scale of ~300 km (Penven et al. (2006b)). Time-stepping is 30 minutes and output is saved as 2-daily averages. 32-sigma levels define the vertical grid, which is stretched toward the surface. The boundary conditions are supplied by World Ocean Atlas (WOA) 2005 (Conkright et al. (2002)) temperature and salinity climatologies, from which the geostrophic velocities are calculated, together with the Quikscat climatological wind stresses for Ekman transports.

The child grid

The child domain has been designed to encompass the greater Benguela system (refer to Figure 3.5), inclusive of the coastal upwelling regime as well as features of the larger-scale Benguela Current system. Embedded within the parent domain, it spans 3.9^{o}E-19.8^{o}E and 35.6^{o}S-12.1^{o}S and has a horizontal resolution that increases from 9 km in the north to 7.5 km in the south (translating into a 314x194 grid).

The 32-sigma coordinates are stretched toward the surface such that the vertical resolution ranges from 0.31 m and 0.51 m at the surface and from 1.86 m to 784 m at the bottom for nearshore and oceanic regions respectively. The time-step of the child domain is 10 minutes and output is saved as 2-daily averages. The boundary conditions are supplied by the parent domain.

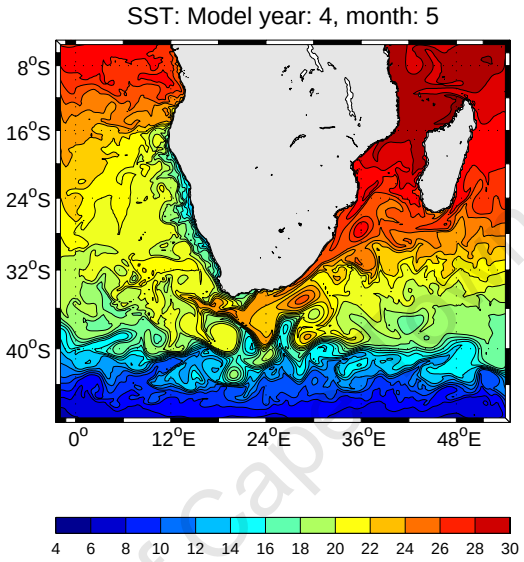

Figure 3.4: 2-daily averaged 'snapshot' of SSTs for the parent (SAfE) domain, showing salient oceanographic features around southern Africa such as the Agulhas retroflection and the Angola Benguela Frontal Zone, which can be though of the northern and southern boundaries of the Benguela Current system.

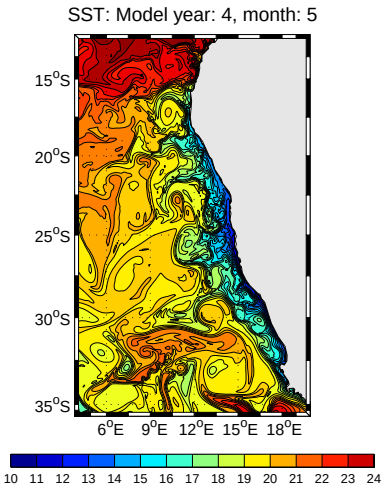

Figure 3.5: 2-daily averaged 'snapshot' of SSTs for the child domain, encompassing the greater Benguela Current system.

Topography

The topography of the nested configuration was produced with a bilinear interpolation of the 1' GEBCO (General Bathymetric Chart of the Oceans: www.gebco.net) product. In a further attempt at avoiding pressure gradient errors, the topography has been smoothed in order to maintain a 'slope parameter' ($r = \frac{\nabla h}{h}$) of less than 0.2 (Armstrong and Vazquez (2001)). Figure 3.6 compares the raw GEBCO topography (right) with the smoothed topography used in the simulation. While the smoothing process is immediately obvious, even sharp features such as the deep and narrow Cape Canyon (extending south-westward from the coast at ~33°S) are retained within the smoothed topography used by the model. The topographies of the child and parent domains are smoothly connected with a relation that uses an α parameter that is 0 within a few grid points (nband=15) of the child boundaries and reaches 1 as it approaches the lateral boundaries (Penven et al. (2006c)).

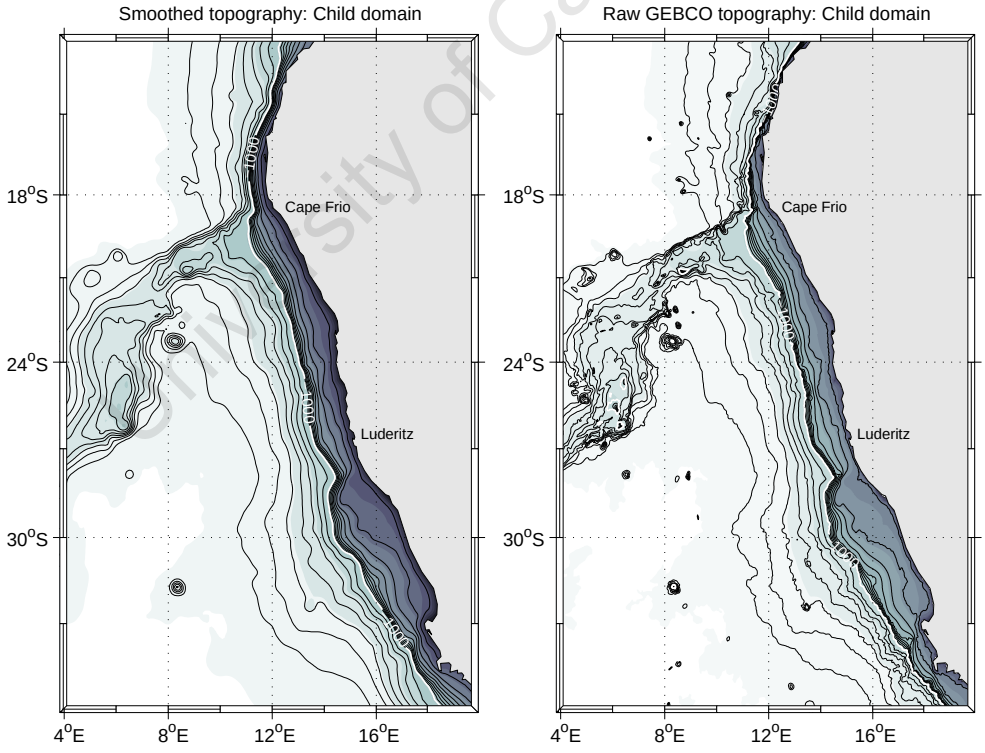

Figure 3.6: Smoothed topography used in the ROMS child simulation (left) and the raw GEBCO data (right). The contour interval in regions shallower than 1000 m (shown in white) is 100 m and in regions deeper than 1000 m the contour interval is 500 m.

Surface forcing

Due to the focus on equilibrium dynamics and seasonal variability, a 0.5^o QuikSCAT climatology of 2000-2007 wind data (Figure 3.7) was used to force the nested configuration, while surface heat (Figure 3.8) and salt fluxes (Figure 3.9) are provided by COADS-derived climatologies (Da Silva et al. (1994)). The model is initialized from a state of no flow and mean January temperatures from WOA. The absence of an ocean-atmosphere feedback term can lead to model SST drift, but is addressed in ROMS by formulating the surface heat flux term as a relaxation of the model to Pathfinder 9 km climatological SSTs (Barnier et al. (1995)). Due to the paucity of evaporation-precipitation forcing fields, a similar correction scheme is used for sea surface salinity (SSS).

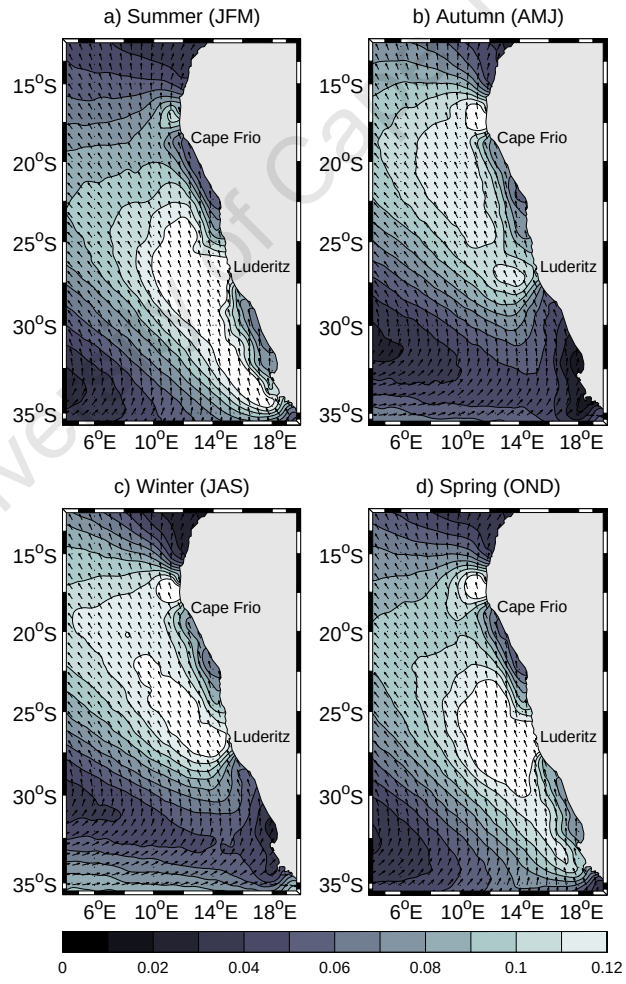

Figure 3.7: Seasonal mean QuikSCAT 0.5^o surface wind speed and direction. Units in $N.m^{-2}$.

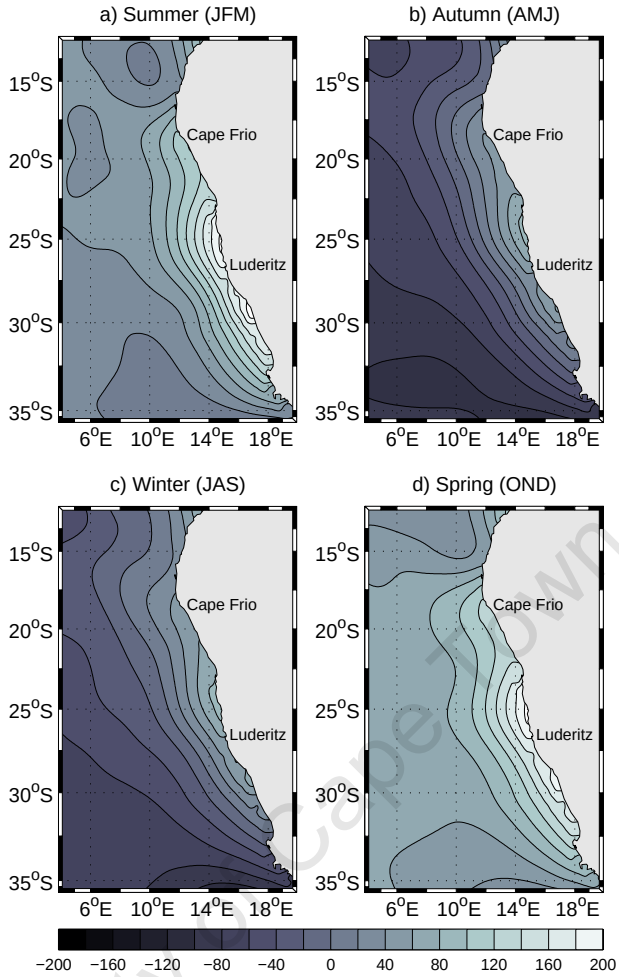

Figure 3.8: Seasonal mean COADS net surface heat fluxes (positive=net heat gain into the ocean). Units in $W.m^{-2}$.

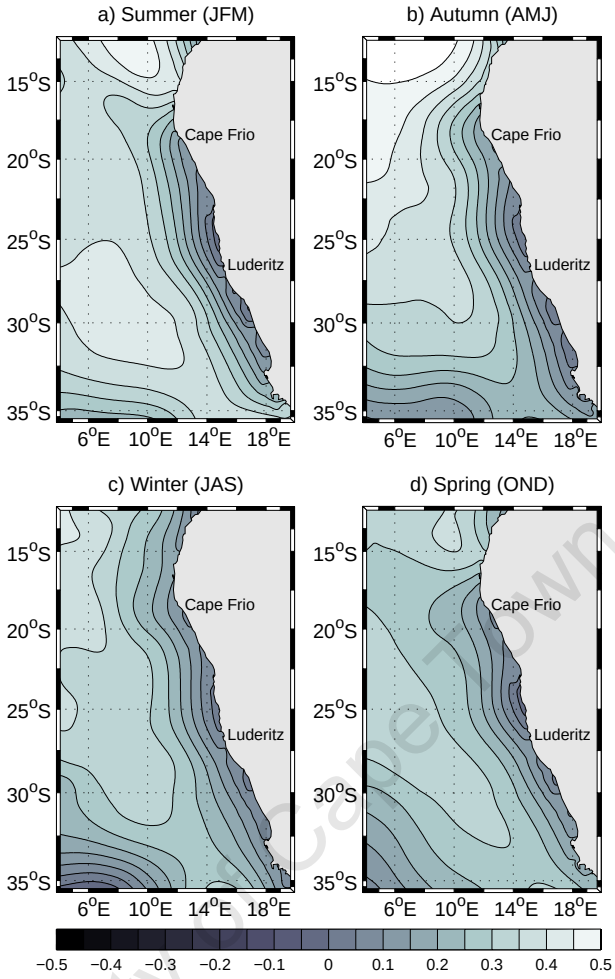

Figure 3.9: Seasonal mean COADS surface freshwater flux (evaporation-precipitation). Units in cm.d^{-1}.

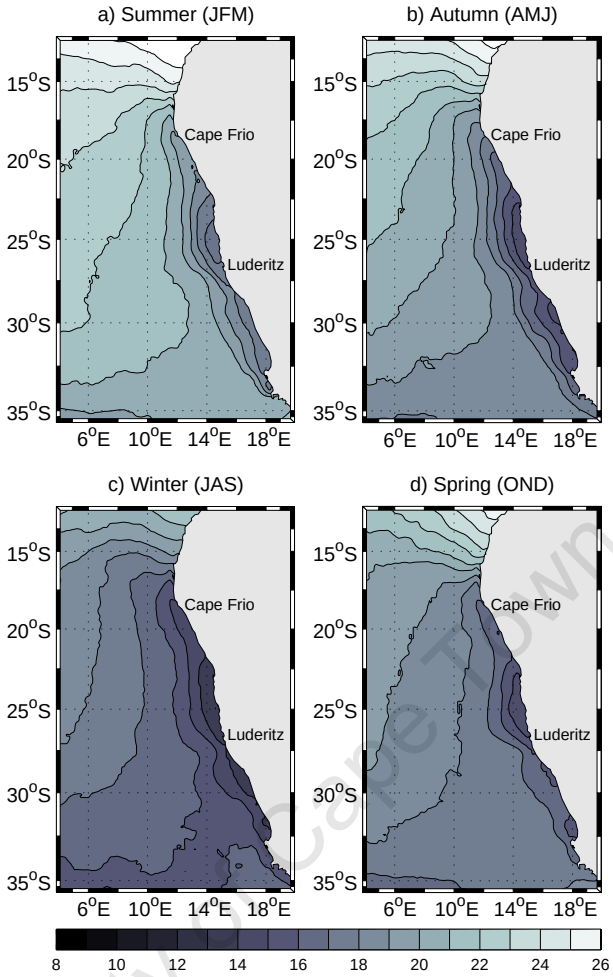

Figure 3.10: Seasonal mean 9km Pathfinder SSTs, used in the restoring term. Units in °C.

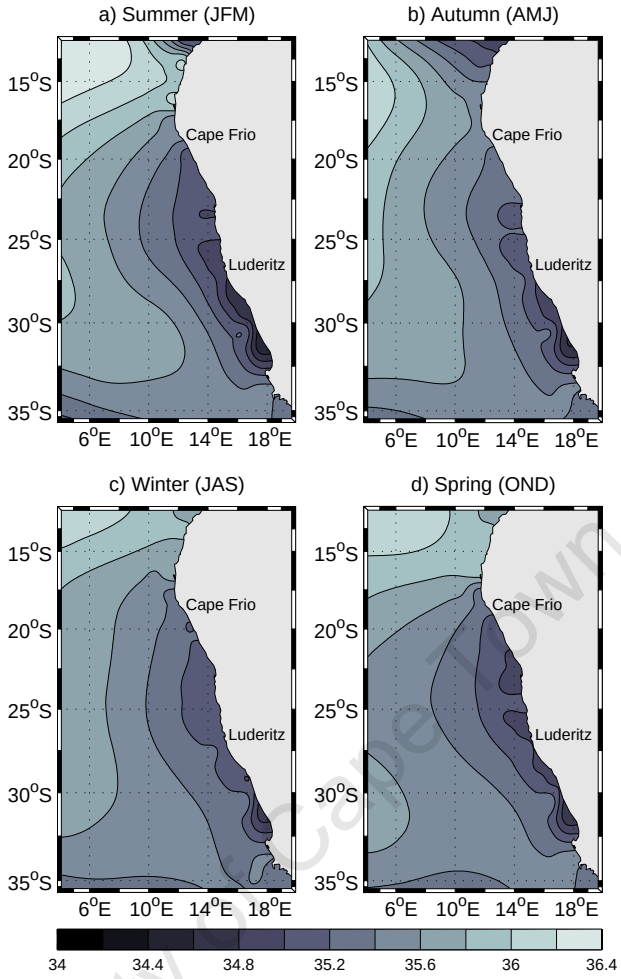

Figure 3.11: Seasonal mean COADS SSSs, used for initialization and the salinity restoring term. Units in psu.

Spin-up

The nested configuration requires approximately 6-8 months to reach statistical equilibrium. It is run for 10 years in total, during which time a robust seasonal signal approximately repeats itself from at least the first year. The spin-up time is estimated from surface and volume averaged kinetic energy (KE), which are shown for the child domain in Figure 3.12. After the rapid adjustment of the system (~8 months-1 year), statistical equilibrium is reached and the system does not exhibit any temporal drift. Analyses for this paper are based on seasonal and monthly climatologies, that are derived from model years 3 to 10. The volume averaged salinity suggests that there is some loss of water mass characteristics in the last year

or two of the simulation.

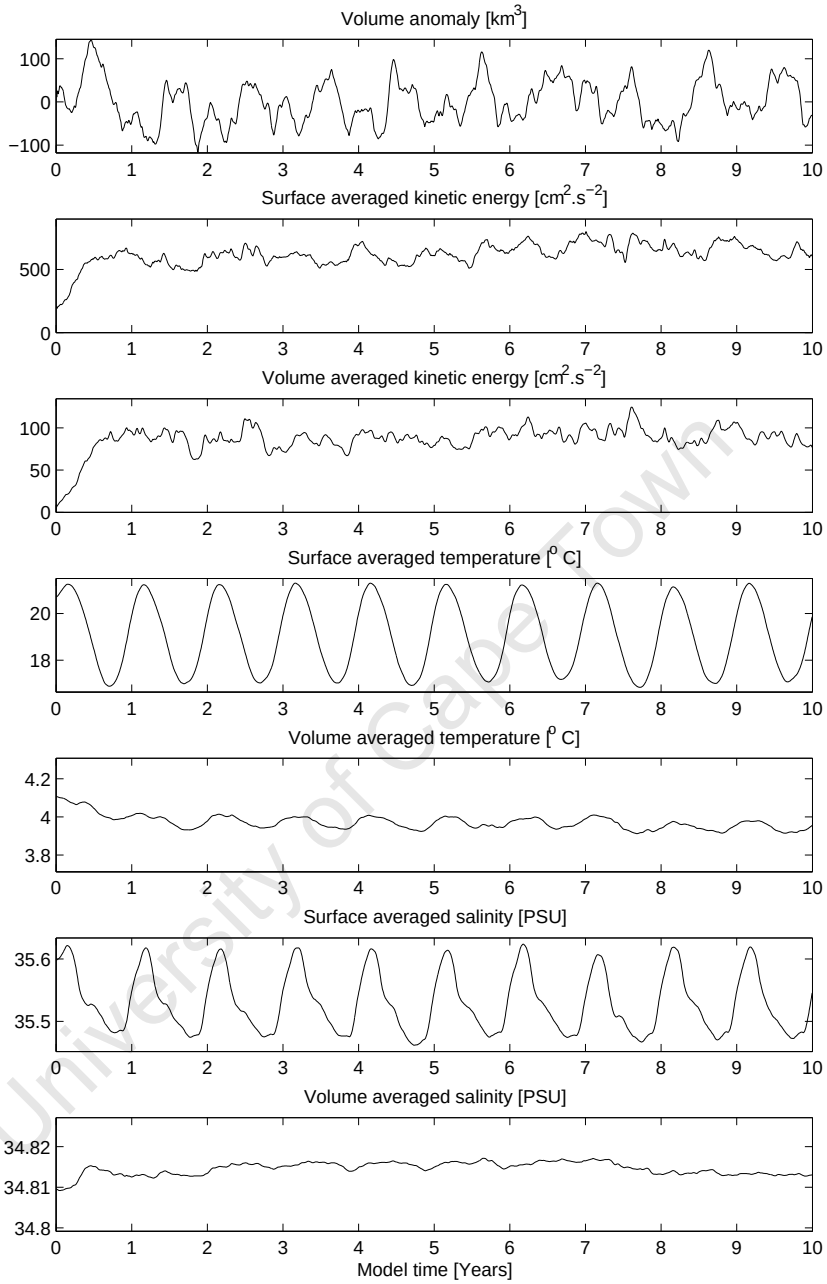

Figure 3.12: Monthly mean volume anomaly, surface averaged kinetic energy, volume averaged kinetic energy, surface averaged temperature, volume averaged temperature, surface averaged salinity, volume averaged salinity for the 10-year Benguela simulation.

3.2 Data Sources for Validation

3.2.1 World Ocean Atlas 2005 (WOA05)

The objectively analyzed temperature and salinity fields of WOA05 (Conkright et al. (2002)) were used in order to compare vertical sections of model-derived thermohaline properties as well as geostrophic flow with data. While the resolution of WOA05 is low (1^o), it provides consistent global climatologies of thermohaline as well as several nutrients that are useful for model validation.

3.2.2 AVISO Altimetry

The AVISO absolute dynamic product was used for model-data comparisons such as surface geostrophic flows and eddy kinetic energy (EKE). The $1/3^o$ gridded product, spanning October 1992-September 2008, was downloaded from www.aviso.oceanobs.com. The product is a sum of satellite-observed sea level anomalies and the mean dynamic topography. The latter is obtained from Rio5 (Rio and Hernanadez (2004)), which calculates the mean sea surface height above the geoid, corrected from geophysical effects and is based on both altimetry and in situ (i.e. hydrology and drifters) data sources. While the AVISO gridded data products provides a rich data source from which to compare model output, it is not reliable within a 50 km coastal band.

3.2.3 Envifish 4.5 km SST

A second satellite SST source used are the monthly mean climatologies of the 4.5 km envifish product, which was derived from data obtained from January 1982 to December 1999. The data were collated for the Cloud and Ocean Remote Sensing around Africa (CORSA) project of the Marine environment Unit of the Space Applications Institute of the Joint Research Centre of the European Commision. The higher resolution envifish data were degraded to be better approximate the ~9 km resolution of model-derived SSTs.

3.2.4 Pathfinder 4 km SST

Pathfinder Version 5.0 SST climatologies are used for comparison with model-derived SSTs. The SST climatologies are based on AVHRR SSTs collected from 1985-2001. The relatively high resolution of approximately 4 km has been acheived by the re-analysis effort of the AVHRR data stream by the University of Miami's Rosenstiel School of Marine and Atmospheric Science (RSMAS) and the National Oceanographic Data Center (NODC). For more information on this satellite product refer to the user guide which can be found at the following website:
http://www.nodc.noaa.gov/SatelliteData/pathfinder4km.

In order to make meaningful comparisons with model output to data sources of different resolutions, a simple spatial colocation technique is employed in order for higher (lower) resolution data to approximate the lower (higher) resolution of the model-derived data. A new, lower-resolution grid is defined for the higher resolution product by creating a new point at the centre of four points of the original higher-resolution grid. The variable at the new point is calculated by taking the average of the four surrounding points. This simple procedure halves the resolution of the higher resolution grid (e.g. a 4 km grid becomes an 8 km grid).

Chapter 4

Equilibrium Dynamics of the Benguela Current System: mean state and seasonal cycle

The objective of this chapter is to take advantage of the spatially, temporally and dynamically coherent data set obtained from a model simulation of the Benguela in order to improve the current understanding of the system, which has thus far been based on scarce in situ measurements, satellite-observed surface patterns and models that have either been of low resolution or have not been inclusive of the whole system. The inclusion of the whole system within one simulation allows us to gain a better understanding of the apparently disparate dynamics of the northern and southern regimes in a dynamically unified manner. This chapter focusses on the mean state and seasonal cycle in the hope that a more thorough understanding of equilibrium conditions, which can be thought of as the bench-mark from which extreme events are measured, will improve the interpretation of trends, cycles and episodic events within the system.

The reference simulation used for most of the analysis in this chapter is a 2-way nested ROMS (Regional Ocean Modelling System) simulation, forced with climatology products of QuikSCAT 0.5° winds and COADS fluxes (for more information on the model set-up see chapter 3). The climatological nature of the forcing helps to achieve a robust seasonal signal in the model output and ties in with the focus

on equilibrium state and seasonal cycle. Furthermore, it allows us to investigate intrinsic, unforced variability within the system, which will be the focus of Chapter 5.

In order to investigate topographical effects on the large- and meso-scale circulation structures as well as on the upwelling regime, the reference experiment is run with a smoothed coastline and bathymetry from Cape Point to the intersection of the Walvis Ridge with the coast. The limited extent of the coastline smoothing is done specifically in order to focus on the effect of alongshore shelf-edge fluctuations in the central Benguela and to maintain the influence of the Walvis Ridge. More information can be found on the smoothing procedure in Chapter 3.

This chapter is designed such that the temporal scales of variability are addressed in descending order; the dynamics of the mean state are presented first, followed by an investigation of the seasonal cycle. Model results are compared with satellite and in situ data sources where ever possible throughout the chapter. Topographical control is then investigated via the experimental approach in which the bathymetric smoothing has been applied. A synthesis of differences and similarities between the northern and southern regimes concludes this chapter along with a discussion of salient dynamic features of the system in general.

4.1 Mean State

4.1.1 Annual mean wind

The south-easterly winds that dominate the mean state of the Benguela system and produce the ecologically and economically important upwelling system are driven by the south Atlantic high pressure system and the continental heat low that exists over the African continent. Figure 4.1 (left) shows the annual mean magnitude of wind stress with direction arrows overlaid as derived from the 2000-2007 QuikSCAT satellite wind product that is used to force this simulation. A distinct maximum in wind stress occurs in the vicinity of Lüderitz, while the offshore maximum for the whole domain occurs at a distance of about 200-350 km, which is consistent with the *in situ* observational investigations of Kamstra (1985).

Figure 4.1 (right) shows the annual mean wind stress curl and reveals a cyclonic or negative wind stress curl (shown in darker shades of grey and demarcated as the region inshore of the bold line) is located in a 200-350 km coastal band (consistent with the position of the maximum wind stress), which is consistent with the results obtained from observations by Bakun and Nelson (1991). The cyclonic curl is thought to enhance the offshore extent of upwelling by the process of Ekman pumping (Bakun and Nelson (1991)). Based on the QuikSCAT winds used as forcing for this simulation, the magnitude of upwelling induced by Ekman pumping is very small (~0.2 m.d^{-1}based on equation 4.1) compared to upwelling induced by cross-shore Ekman transport (~4 m.d^{-1}, based on equation 4.12 and a horizontal length scale that is described in section 4.1.8) and so it is not likely a major player in the net upwelling rates in the Benguela system as resolved in this simulation. However, Pickett and Paduan (2003) estimated Ekman pumping in the California upwelling system using a high resolution (~9 km) atmospheric model reanalysis product (COAMPS) and their results showed that Ekman pumping was, in places, of the order of Ekman transport. They stressed the necessity of high resolution coastal winds in resolving the nearshore Ekman pumping velocities that are underestimated by coarser resolution products. Similarly, Enriquez and Friehe (1995) used high resolution wind measurements to force a two-layer model and found that higher coastal resolution wind products amplify the importance of the wind stress curl in contributing to the net upwelling flux, particularly in the vicinty of capes and points. We will see that the relative intensities of the several alongshore upwelling cells are fairly well represented in our simulation and the effect of Ekman pumping on upwelling is a key player in only much finer resolution investigations and near capes and headlands. Ekman pumping and Ekman transport are calculated as follows:

$$W_E = \frac{\bigtriangledown \times \tau}{\rho_0 f} + \frac{\beta \tau_x}{\rho_0 f^2} \tag{4.1}$$

$$T_E = \frac{\tau_{alongshore}}{\rho_0 f} \tag{4.2}$$

where W_E is the Ekman pumping velocity (in m.s^{-1}), T_E is the Ekman transport

(in $m^2.s^{-1}$), $\bigtriangledown \times \tau$ is the wind stress curl, ρ_0 is the reference density (taken to be 1024 $kg.m^{-3}$), f is the coriolis parameter, β is the change of coriolis with latitude (i.e $\frac{\partial f}{\partial y}$), τ_x is the zonal wind stress component, $\tau_{alongshore}$ is the alongshore wind component. The beta effect on Ekman pumping velocities (i.e. the second term in equation (4.1)) is small in this region.

The zero wind stress curl line shown in Figure 4.1 agrees well with the location of the shelf-edge and the distinct temperature front generated by the gradient of cool upwelled water near the coast and warmer oceanic water (see Figure 4.2). This alludes to the significance of ocean-atmospheric feedback mechanisms.

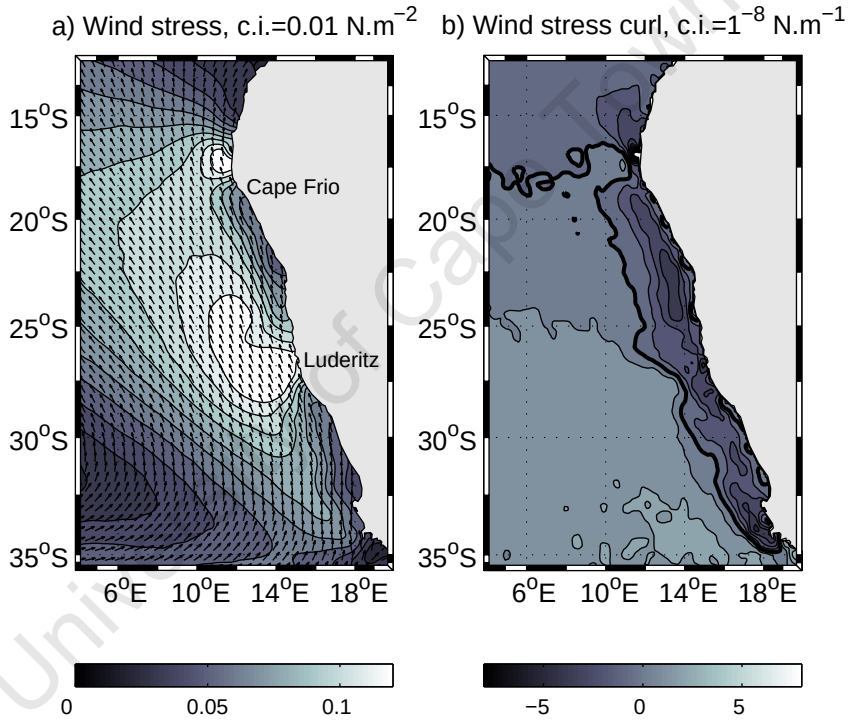

Figure 4.1: (a) Annual mean wind stress magnitudes (units: $N.m^{-2}$) and (b) wind stress curl (units: $10^{-8}N.m^{-1}$).

4.1.2 Surface patterns

Sea surface temperature (SST)

Providing a first impression of the large-scale features of the Benguela system, surface patterns of temperature also provide a useful and convenient means of comparing model output with readily available satellite data. Figure 4.2a shows the annual

mean SSTs as observed by the 4.5 km envifish satellite product, Figure 4.2b shows the equivalent as resolved by the model simulation and Figure 4.2c shows the difference (i.e. model-satellite SST). The higher resolution satellite product has been degraded in order to approximate the ~8 km resolution of the model output. The model resolves a realistic pattern of SSTs: it simulates a characteristically warm offshore and cool coastal regime that are separated by a distinct upwelling front. The model satisfactorily reproduces alongshore variations in the offshore extent of the upwelling front. Particularly, it simulates the significant inshore 'bend' of the upwelling front at the abrupt narrowing of the shelf at ~27.5° S and, to the north, a large offshore bulge between ~24-26.5°S. The position of the Angola-Benguela Frontal Zone (ABFZ) is also well resolved by the model and is located in the vicinity of $16^{o}S$ in both Figures 4.2a and 4.2b. Although the model is capable of reproducing the relative pattern of SSTs in the Benguela system with sufficient accuracy, warm and cool biases based on satellite SSTs are present and can be seen in Figure 4.2c. A distinct cool bias is present all along the coast, while a warm bias is present further offshore south of the region of Lüderitz at ~$27^{o}S$. The inshore boundary of this warm bias is somewhat constrained by the run of the shelf-edge which is shown as a dotted white line in Figure 4.2c. The underestimation of coastal SSTs and overestimation of offshore SSTs in the southern region are quantified in Figure 4.3. The solid line represents the cool coastal bias, averaged within a 50 km-band from the coast for the whole domain from ~34-$14^{o}S$. The coastal upwelling regime simulated by the model produces surface water that is, on average, ~1°C cooler than satellite observed SSTs. A similar cool bias in an investigation of the Peru upwelling system using the ROMS model was noted by Penven et al. (2005) and was addressed in the earlier work of Penven et al. (2001), who ascribed it to the poor resolution of the satellite wind product at the coast (in the case of QuikSCAT is only valid beyond 50 km of the coast), such that the drop-off of the wind is not properly resolved thereby generating too much equatorward wind-stress at the coast and therefore, too much upwelling.The dashed line Figure 4.3 shows the offshore model temperature bias, averaged between 150-250 km offshore and reveals a warm bias south of ~ 30°S that intensifies southward to a maximum of ~1.75°C. The implication of this is that the

model overestimates the amount of Agulhas water entering the Benguela system, which was similarly found by Speich et al. (2006) who connected it to the topographical smoothing that is done in ROMS as a way of reducing pressure gradient errors.

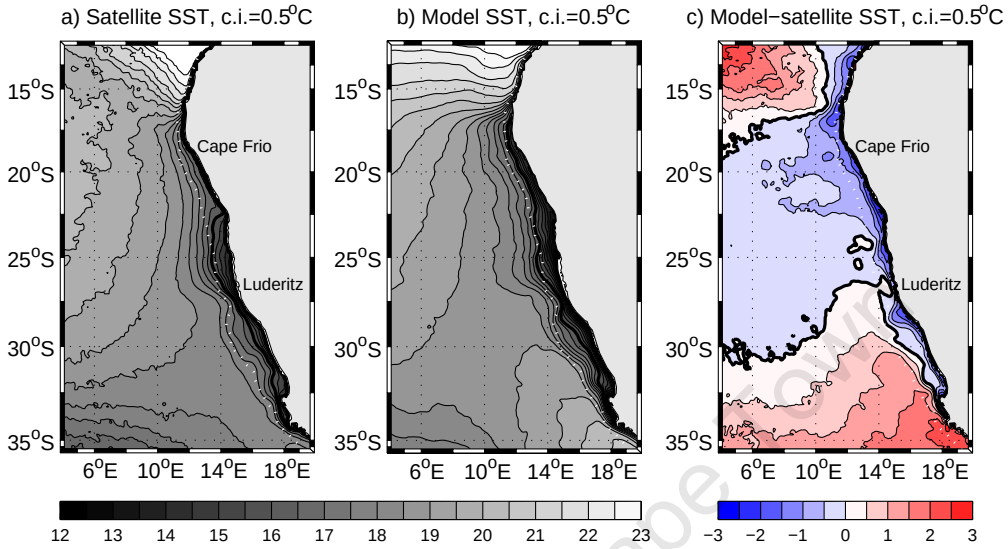

Figure 4.2: Annual mean satellite (a) and model (b) SSTs in the Benguela system. The dotted white line represents the approximate position of the shelf-edge. The difference between satellite and model SSTs (model - satellite) are shown in (c). Positive (negative) values indicate an over-estimation (under-estimation) of SSTs by the model.

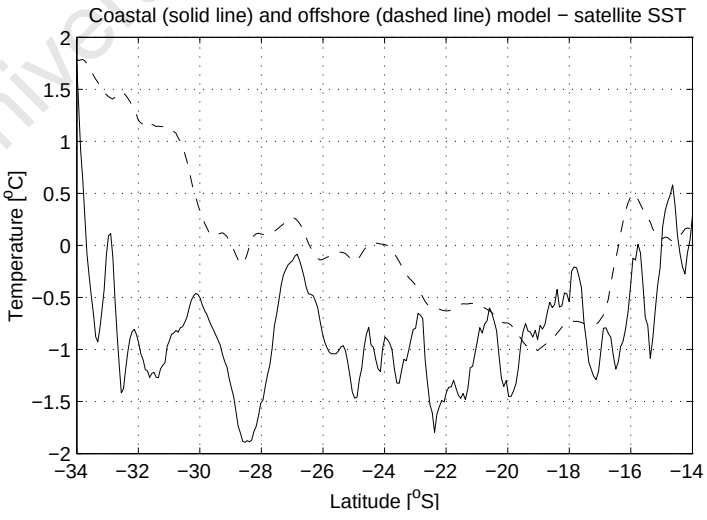

Figure 4.3: Annual mean model SST bias (i.e. model - satellite SST) averaged in a 50 km coastal strip (solid line) and offshore, between 150-250 km (dashed line). Positive (negative) values indicate an over-estimation (under-estimation) of SSTs by the model.

Sea surface salinities (SSS)

Annual mean SSSs are compared with the salinites stored in the objectively analysed climatological fields of the World Ocean Atlas (WOA) database (Figure 4.4). Although the resolution of the WOA dataset is at least ten-fold poorer than that of the ROMS simulation, we nevertheless see somewhat similar patterns of the salinity structure. Despite the fact that a restoring term exists in SSS and therefore influences the solution to some extent, the accurate large-scale pattern of SSS provides confidence in the success of the model solution. Most conspicuously and as we expect, is a regime of fresher water, which is commensurate with the upwelled water at the coast. Like the pattern of SSTs (Figure 4.2), 'bulges' of fresher water mimic the orientation of the shelf-edge and are centered on Port Nolloth and just north of Cape Columbine. This pattern is distinct in the model output and evidence of it also exists in the WOA data. The surface salinity signal of the ABFZ is well-defined in the model ouput, while the WOA data set only provides a hint of its existence. The higher salinity tongue offshore of the upwelling regime is characterised by lower salinities in the model compared to the lower resolution WOA data, particularly in the southwest corner of the domain where the ROMS simulated salinities are of the order of 0.02-0.04 psu lower than the WOA climatological mean. However, due to the poor resolution of the WOA data and subsequent interpolation, caution should be observed when making conclusions of the success of the model based on comparisons with this data set.

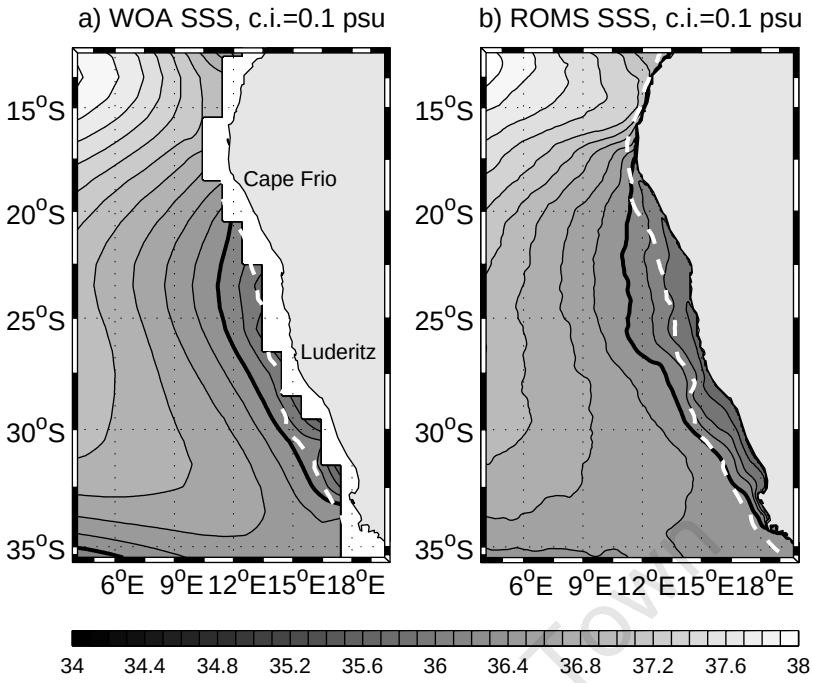

Figure 4.4: Annual mean WOA in situ (a) and model-derived (b) SSSs. The dashed white line represents the approximate position of the shelf-edge.

Sea surface height (SSH)

The AVISO absolute dynamic topography product is a sum of satellite-observed sea level anomalies and the mean dynamic topography, obtained from Rio5 (Rio and Hernanadez (2004)), which calculates the mean sea surface height above the geoid, corrected from geophysical effects and is based on both altimetry and in situ (i.e. hydrology and drifters) data sources. For the purposes of comparing the climatological mean SSHs, a sufficient approximation of the mean absolute dynamic topography of the model simulation was calculated as the deviation of the free-surface at each grid point from the spatial mean SSH of the whole domain. As a proxy for surface geostrophic flow, lines of constant SSH as derived by the model and obtained from the AVISO MADT product (Figure 4.5a and 4.5b respectively) suggest that the model captures the salient features of the large-scale surface flow regime. Arrows on the lines of constant SSH in Figure 4.5 are based on geostrophic flows derived from the SSHs:

$$u_g = -\frac{g}{f}\frac{\partial \eta}{\partial y} \tag{4.3}$$

$$v_g = \frac{g}{f}\frac{\partial \eta}{\partial x} \tag{4.4}$$

where u_g and v_g are the zonal and meridional geostrophic flow components, x and y are the zonal and meridional cartesian co-ordinates, g is acceleration due to gravity (9.8m.s^{-2}) and η is SSH.

The broad, northwestward Benguela Current and its offshore veering from about 30^oS is evident in both the model output and satellite-derived SSHs and is in agreement with the in situ observations of Reid (1989). South of its offshore veering, the model-derived and satellite-observed Benguela Current is characterized by two 'streams', separated by a conspicuous cyclonic meander. The offshore stream is situated on the western edge of the 'Agulhas eddy corridor' (as defined by Garzoli and Gordon (1996)) so that passing anticyclonic eddies enhance the mean northwestward flow in this region and inhibit it slightly offshore of the shelf-edge. The path of deep-reaching Auglhas rings is likely to be somewhat controlled by the broadening of the continental shelf at depth northward of ~33°S (see the 3500 m isobath in Figure 4.5). The meandering nature of the mean flow is therefore a manifestation of the preferential path of transient eddies in this region. Indeed, the modelling study of Matano and Beier (2003) showed that most of the energy of the Benguela Current is supplied by eddy fluxes. The inshore stream of the Benguela Current, south of its offshore veering, is subject to a strong topographical control and tends to follow alongshore variations in the shelf-edge. The topographical control is associated with the input of warmer Agulhas water and the juxtaposition of its high SSH signal with the low SSH signal of the upwelling regime on the broad shelf in the southern Benguela. This results in a significant offshore gradient of SSH and produces a geostrophically balanced current that approximately follows the alongshore run of the continental shelf. The narrowing of isolines around Cape Point is consistent with the existence of a strong equatorward jet that was anticipated, and subsequently located by Bang and Andrews (1974). The offshore veering of the Benguela Current coincides with the offshore veering of the higher SSH signal induced by path of Agulhas rings, causing an offshore-shift and weakening of the resulting geostrophically-balanced north-westward flow.

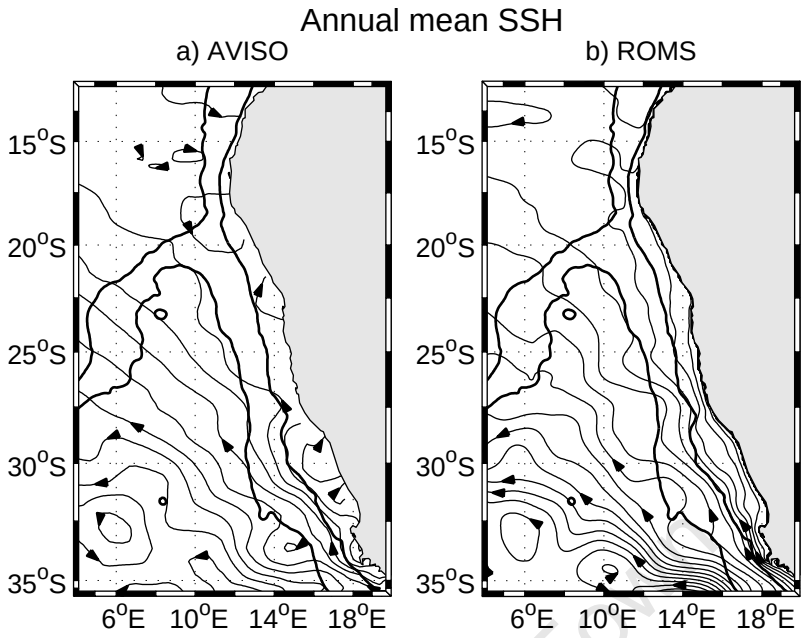

Figure 4.5: Satellite (a) and model (b) lines of constant annual mean SSHs as a proxy for surface geostrophic flow. The bold line represents the position of the ~500 m (i.e. the approximate position of the shelf-edge) and 3500 m isobaths.

Patterns of SST and SSS (Figures 4.2 and 4.4 respectively) suggest that a topographical control exists in the southern part of the system such that the upwelling front, manifest in both SST and SSS, follows the orientation of the shelf-edge. The surface geostrophic flow, as depicted in lines of constant SSH (Figure 4.5), also tends to follow the undulations of the shelf-edge in the southern region. The apparent topographical control of the upwelling front and large-scale circulation pattern is confined to south of ~$28^{o}S$, which is the position of a distinct inshore bend of the shelf-edge, so that to the south it is relatively broad, while it is much narrower to the north of ~$28^{o}S$. Based on these differences in the nature of the surface manifestation of the upwelling front relative to the shelf-edge, the Benguela system can be divided into distinct northern and southern regimes.

4.1.3 Vertical structure: temperature, salinity, density and alongshore geostrophic currents

In order to produce a representative cross-section of the mean vertical structure of the northern and southern regimes, in each region a 300 x 350 km (alongshore x cross-shore) box is placed parallel to the coast from which an alongshore average is calculated. Henceforth, all vertical sections representative of the northern and southern Benguela systems will be based on the alongshore averages of these pre-defined boxes, the positions of which are shown in Figure 4.6.

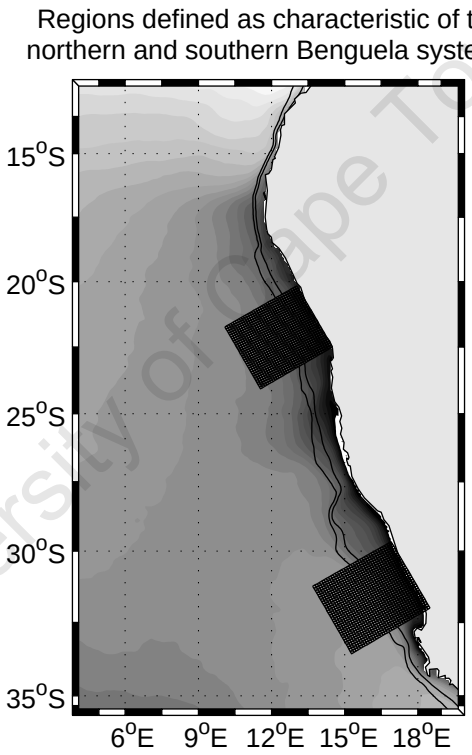

Figure 4.6: Position of boxes from which alongshore averages are computed as representative of the vertical structure of the northern and southern Benguela systems. Areas shaded in grey are $< 18^{o}$C, darker shades are cooler. The black lines represent the 300 m and 500 m isobaths.

Temperature and salinity sections

Annual mean temperature and salinity sections based on model-derived data are compared with the equivalent climatological mean WOA sections, and are shown in Figures 4.7 and 4.8 as representative of the northern and southern Benguela regimes respectively. The 16° C isotherm is highlighted in bold and has been taken to approximate the location of the thermocline, based on its central position in the region of closely-spaced isotherms, definitive of the thermocline. Large-scale oceanographic processes and their effect on the depth of the thermocline can significantly affect the productivity of an upwelling system by changing the temperature and nutrient content of the source region of upwelled water. The extent to which the model maintains a realistic salinity structure is suggestive of its ability to reproduce and conserve realistic water masses.

In the northern Benguela the model simulation captures the annual mean depth of the thermocline within 10 m of reality as depicted by the WOA (Figure 4.7a). The upward slope of the isotherms at the coast, indicative of upwelling processes, is present in the model output but not in the WOA dataset as it does not resolve an approximately 100 km coastal band. Downward sloping isotherms at the coast between ~150 to at least 1000 m in the model output provides evidence for a distinct poleward undercurrent in the northern Benguela. Though there is some indication of the downward slope of isotherms toward the coast in the WOA data, particularly shallower than 200 m, but also at greater depths, the coastal resolution is not sufficient to detect the full expanse and intensity of the poleward undercurrent. Distinctive of the vertical salinity structure in the northern Benguela (Figure 4.7c) is a high salinity core in the vicinity of the shelf-edge, for which there is evidence in both the WOA and model-derived data to a depth of 200 m. At depths of ~550-950 m for both WOA and model-derived data is a salinity minimum layer and is commensurate with the Antarctic Intermediate Water mass (AAIW), whos core was located at ~750 m depth by Shannon and Hunter (1988). The salinity minimum associated with the core of the AAIW mass is 34.45 psu for WOA data and <34.55 psu for the model-derived data, suggesting that the model is losing the water mass characteristics of the deep AAIW by causing it to become slightly more saline.

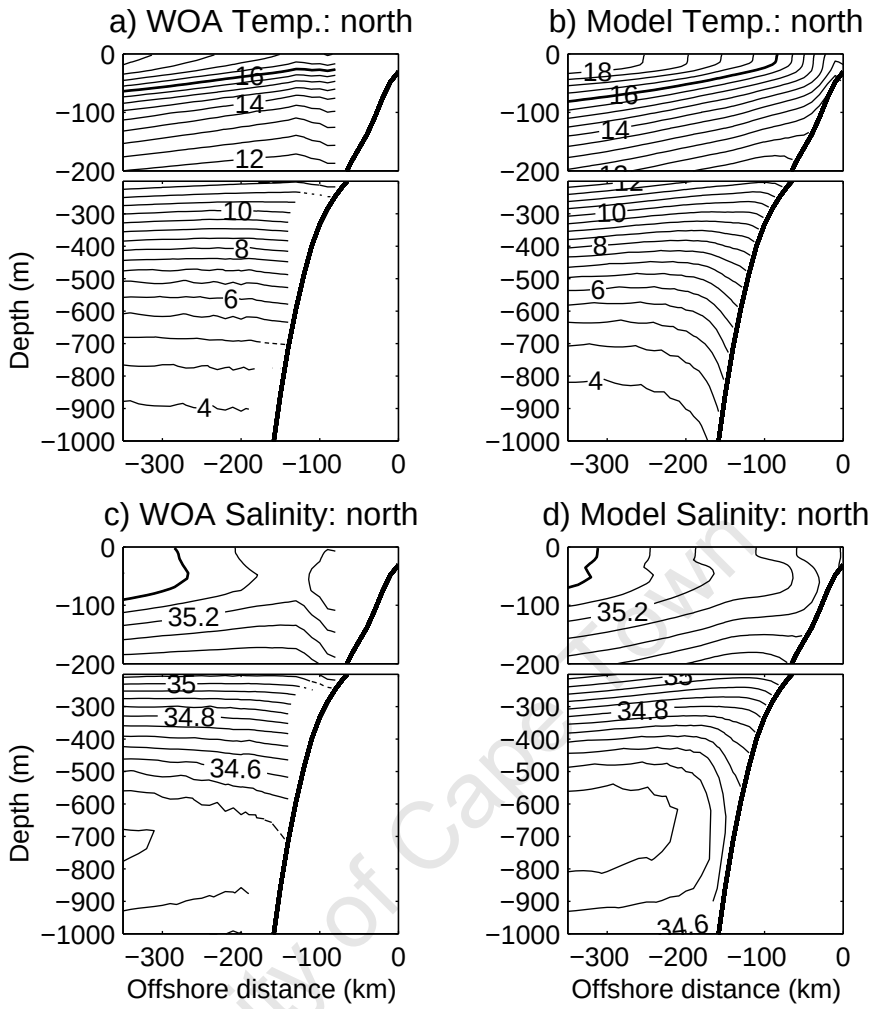

Figure 4.7: Alongshore average in the northern Benguela 'box' of annual mean temperatures (top) and salinity (bottom) based on WOA (left) and model-derived (right) data. Contour interval for (a) and (b) is 0.5°C, for (c) and (d) is 0.05 psu.

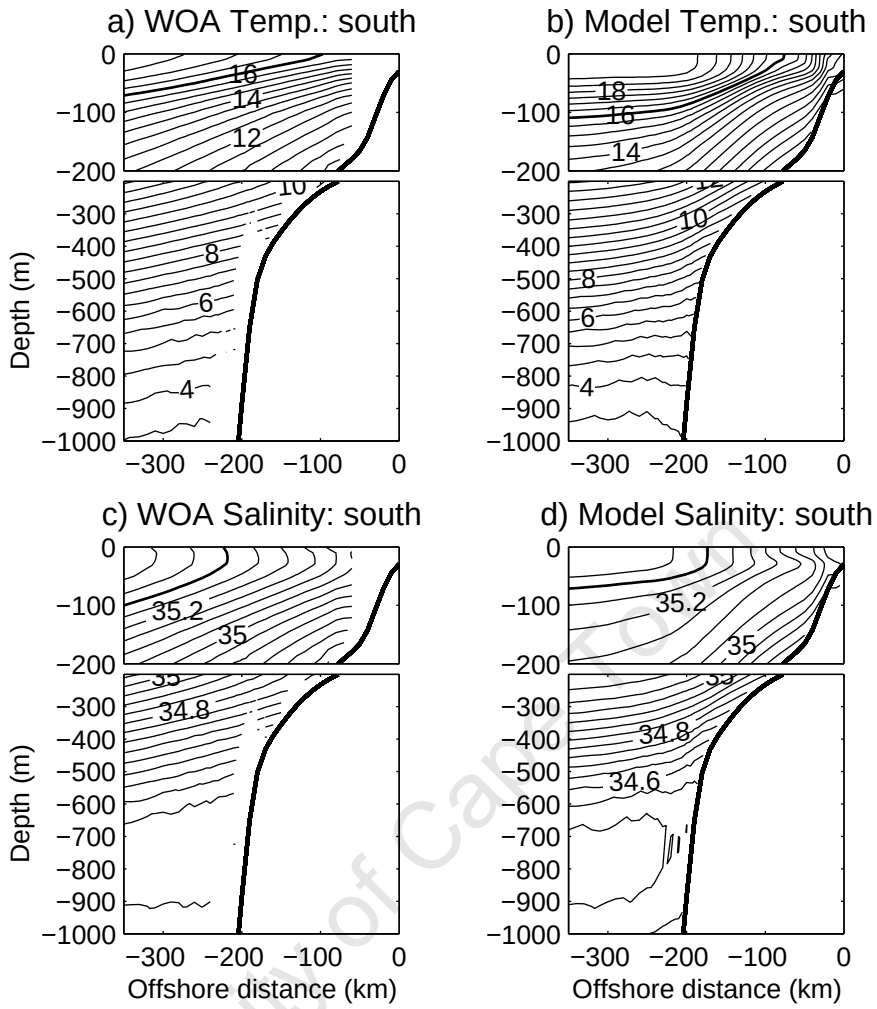

Figure 4.8: Alongshore average in the southern Benguela 'box' of annual mean temperatures (top) and salinity (bottom) based on WOA (left) and model-derived (right) data. Contour interval for (a) and (b) is 0.5°C, for (c) and (d) is 0.05 psu.

The vertical thermal structure of the southern Benguela (Figure 4.8 (top)) system differs to that of the northern Benguela in that the isotherms slope more acutely, particularly offshore of the shelf-edge, in the southern Benguela. This is related to the striking juxtaposition of warm offshore water, associated with Agulhas Current input and cool water inshore, associated with the upwelling regime. The implication of more steeply-sloping isotherms in the southern Benguela is increased available potential energy (APE). Weakly downward-tilting isotherms at the shelf-slope at depths of greater than ~800 m in the model output, suggests the existence of a weak poleward flow in this region. Due to its restriction to the very near-shelf region, this

evidence of a poleward undercurrent does not exist in the WOA data. The depth of the $16^{o}C$ isotherm, as resolved by the model, is ~30 m deeper in the offshore regions of the southern Benguela due to the fact that too much Agulhas water enters the Benguela in the model simulation. This warm bias is most pronounced in the upper 150 m, while at greater depths the model agrees more favourably. The salinity structure in the southern Benguela (Figure 4.8 (bottom)) also shows steeply-sloping isolines offshore of the shelf-edge and alludes to the increased storage capacity for APE in this region. The AAIW mass is again present and lies between ~650-900 m based on both WOA and model-derived data. However, the fact that the minimum salinity for this water mass is 0.1 psu less based on WOA data (34.4 psu) than for model-derived data (34.5 psu) suggests, once again, a slight loss of some deep water mass characteristics.

Density structure

Differences between model-derived and WOA-based temperature, salinity and density for the northern and southern Benguela are shown in Figures 4.9 and 4.10. The differences have been normalised with respect to the corresponding range of temperature, salinity and density so that they may be more objectively compared. In both the northern and southern Benguela systems, large postive temperature biases (i.e which tends to decrease the density) are, in places, coincident with positive salinity biases (i.e. which tends to increase density) and, via spiciness, results in a model density structure that agrees more favourably with reality, as reflected in fairly low resolution WOA data.

In the northern Benguela, while the temperature and salinity biases can be quite large (i.e. maximums of +5 % and -15 % of the range of actual temperatures and salinities, which equates to maximum anomalies of +0.97°C and -0.15 psu respectively), the maximum density bias is less than 3 % of the range of densities (-0.23 $kg.m^{-3}$). The central water mass, which extends from approximately the base of the mixed layer (~150 m) to the AAIW (~550 m) is associated with a negative temperature bias, which acts to increase the density, and a negative salinity bias (to a depth of ~600 m), that results in decreased densities. Density solutions based on

the non-linear equation of state and this combination of negative temperature and negative salinity biases therefore results in a density solution that is closer to reality. Beneath the central water mass is the AAIW mass, which is subject to a positive salinity bias and a negative temperature bias. The negative temperature and salinity bias at the coast, associated with the models overestimation of upwelling, results in a very slight density bias. The mean negative temperature, salinity and density biases for the northern Benguela are -0.26°C, -0.05 psu and -0.1 kg.m^{-3} respectively and the mean positive biases are 0.43°C, 0.04 psu and 0.03 kg.m^{-3}.

Though still significantly less than temperature and salinity biases, model density biases in the southern Benguela are somewhat larger (with a maximum of -10 %, linked with an actual bias of -0.69 kg.m^{-3}) than in the northern Benguela, particularly in the upper 200 m offshore of the shelf edge. The increased negative density bias in the mixed layer and upper central waters of southern Benguela is related to a large temperature bias (with a maximum of ~20 %, linked to an actual bias of 3.07°C) that is not sufficiently compensated for by a salinity bias that is positive nearshore and on the shelf, but negative offshore in the upper layers. The positive temperature bias offshore in the upper 700 m in the southern Benguela is linked to the models overestimation of Agulhas input. The positive salinity bias is not in the same location as the positive temperature bias; it is located over the shelf, within the central water mass and deeper. This suggests that it is not only linked to the warm offshore bias associated with the overestimation of input from the Agulhas Current, but also to the loss of deep water mass characteristics. The mean temperaure, salinity and density negative biases for the southern Benguela are -0.11°C, -0.02 psu and -0.33 kg.m^{-3} respectively and the mean positive biases are 1.49°C, 0.07 psu and 0.05 kg.m^{-3}.

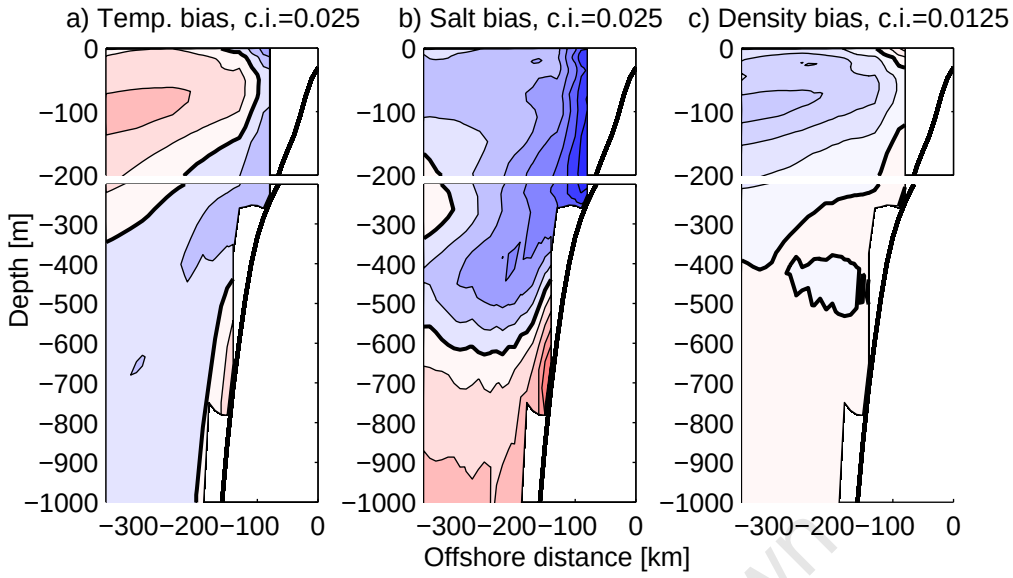

Figure 4.9: Normalised temperature (a), salinity (b) and density (c) bias for the northern Benguela alongshore-averaged 'box' section. Positive (negative) values correspond to regions where the model overestimates (underestimates) WOA data.

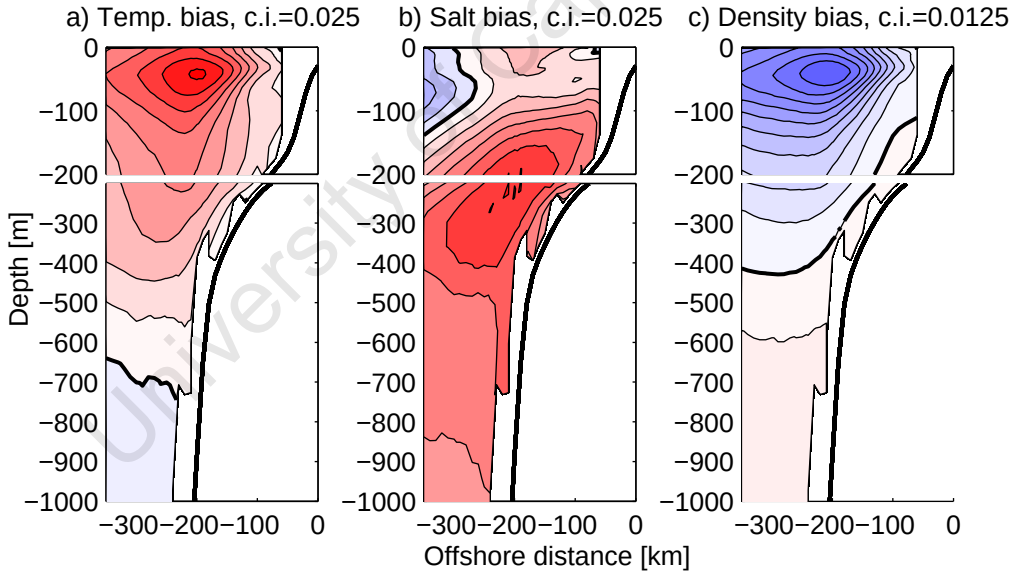

Figure 4.10: Normalised temperature (a), salinity (b) and density (c) bias for the southern Benguela alongshore-averaged 'box' section. Positive (negative) values correspond to regions where the model overestimates (underestimates) WOA data.

The annual mean vertical density structure at the shelf-edge is shown in Figure 4.11 for both WOA observations (Figure 4.11a) and for the model-derived data (Figure 4.11b) and adds alongshore variations to the surface density biases shown in Figures 4.9 and 4.10. It shows that surface density derived by the model is lower

than WOA surface densities throughout the domain, but most conspicuously in the southern Benguela (southward of ~28 ^{o}S) where the model simulates less dense water to depths increasing southward to ~50 m at ~33.5 ^{o}S due to the increased input of Agulhas water. However, the general pattern of model densities at the shelf-edge compare favourably with observations: a shallow sloping of the isopycnals toward the south, with a distinct upwelling of isopycnals that introduces a discontinuity in the upper 50 m at ~ 25^{o}S. This region is the Lüderitz Upwelling Cell-Orange River Cone (LUCORC) region, which is transboundary between the northern and southern Benguela regimes and is commensurate with the most vigorous and perennial upwelling cell. Duncombe Rae (2004) demonstrated that to the north of this region, the upwelling source waters were more saline in character than to the south and is reflected in Figure 4.11. It has also been shown to be a region where alongshore currents veer offshore, effectively forming a 'gate' of nearshore water properties to the oceanic domain. The 'doming' of the alongshore density structure in Figures 4.11a and 4.11b, in fact suggest an inshore (at ~24^{o}S) and offshore (at ~26^{o}S) flow in this region. South of this, the isopycnals reflect mesoscale variations that are related to the meadering nature of the Benguela Current and passing Agulhas eddies. There is some indication of a similar pattern in the WOA density plot, however the poor resolution filters much of the mesoscale variability.

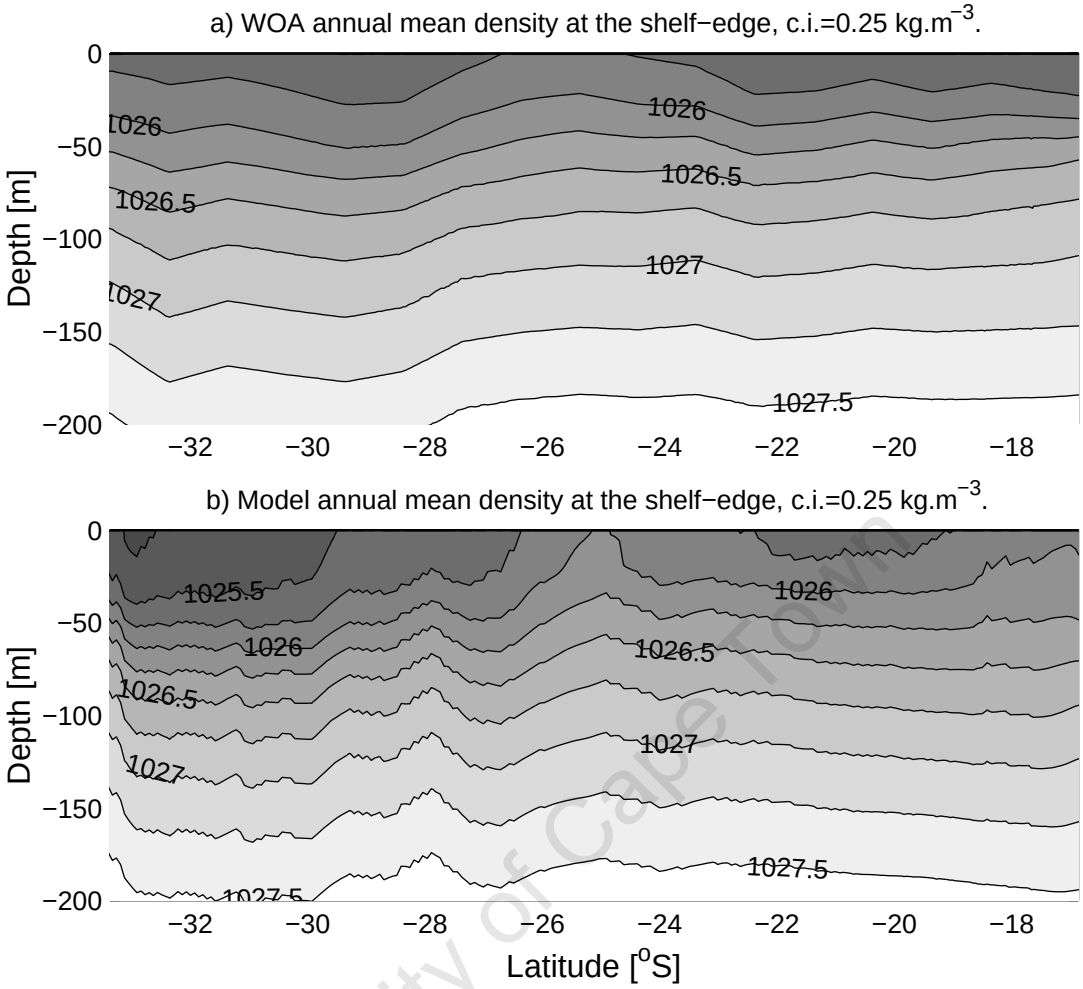

Figure 4.11: Alongshore sections of annual mean density at approximately the shelf-edge from 19-34 ^oS, based on WOA (a) and model-derived (b) data.

Stratification

To further elucidate the nature of the vertical structure of the near-shore Benguela system and alongshore variations, the Brunt-Väisälä frequency (N^2) is derived from model-ouput as well as in situ WOA data and is a measure of stratification of the water column (see equation 4.5).

$$N_2 = -\frac{g}{\rho_0}\frac{\partial \rho}{\partial z} \tag{4.5}$$

where N^2 is the Brunt-Vaisala frequency (in s^{-2}), ρ is the density (in $kg.m^{-3}$) and z is the depth.

Despite the fact that the model introduces too much warm Agulhas water in

to the Benguela system, the ability of the model to reproduce the vertical structure of density relatively successfully gives confidence in validity of the stratification calculation (equation 4.5). Figure 4.12 is a vertical section of annual mean Brunt-Väisälä frequency averaged across the shelf (i.e. from the coast to the approximate position of the shelf-edge) and is shown for the domain spanning 17-34°S and from the surface to ~200 m depth. It is shown as derived from both WOA observations (Figure 4.12a) and model-derived data (Figure 4.12b). Figure 4.12 shows that between 24-28°S and 10-100 m depth a distinct minimum of stratification exists for both the WOA observations and the model output. This discontinuity is related to the perennial and vigorous upwellling cell in this location and the vertical density structure at the shelf-edge (see Figure 4.11) extends the definition of the division between northern and southern Benguela regimes (refer to Figure 4.6) into the vertical dimension. The wider southern Benguela shelf is more stratified than the northern Benguela shelf and this is likely to be associated with less available potential energy (APE) on the shelf there and therefore, a region of relative quiesence. Figure 4.8 suggests that, while stratification appears relatively strong on the shelf in the southern Benguela (indicated by the horizontal and closely spaced isotherms), near the shelf edge and further offshore the slope of the isotherms becomes significant, the implication being that the storage of APE is greater (and, therefore, the potential for baroclinic instabilities) is large seaward of the shelf-edge in the southern Benguela. The model produces enhanced stratification in the southern Benguela compared to WOA and is due to the overestimation of Agulhas Current influence in the southern Benguela. On the other hand, the model is too diffuse the northern, tropical region, which can also be seen in Figure 4.11. The mixed layer in the model is very distinct compared to WOA, in which it is not to not be properly resolved (Marchesiello et al. (2003)).

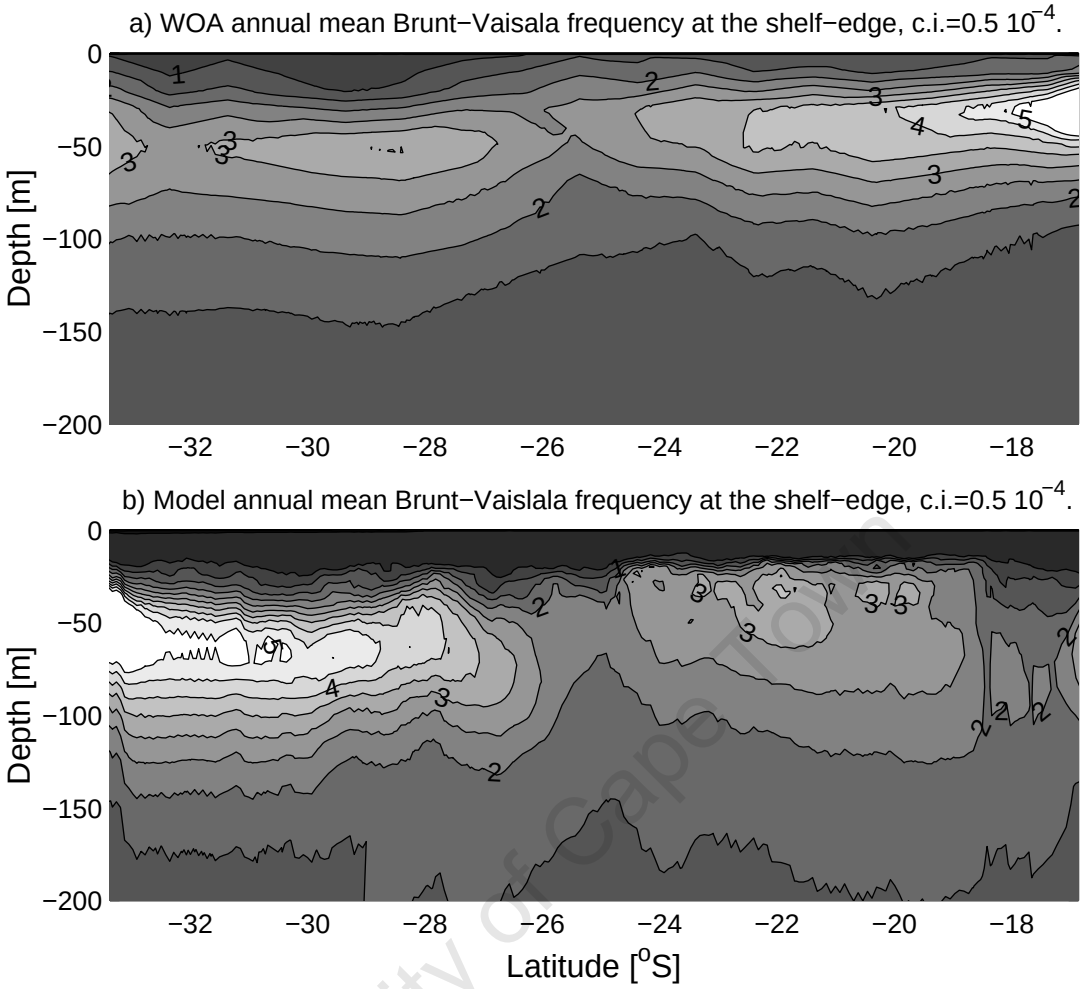

Figure 4.12: Alongshore sections of annual mean Brunt-Vaisala frequency (in s^{-2}) at approximately the shelf-edge from 19-34°S for WOA (a) and model-derived (b) data.

Geostrophic Flow

Vertical sections of alongshore averaged geostrophic velocities are shown in Figure 4.13 for the northern and southern Benguela regions. The geostrophic velocities are derived from the thermal wind relation (equation 4.6) for both the WOA and model-derived density field (which are derived from the temperature and salinity fields via the equation of state), using the surface geostrophic flow (calculated from satellite and model SSHs) as the reference level from which to perform the vertical integration.

$$f\frac{\partial v_g}{\partial z} = -\frac{g}{\rho_0}\frac{\partial \rho}{\partial x} \tag{4.6}$$

Both the WOA and model-derived alongshore geostrophic velocities in the northern Benguela (Figure 4.13a and 4.13b) suggest the dominance of a poleward flow in this region. The poleward flow derived with the model density field tends to be somewhat more confined to the shelf-edge, while the WOA-derived poleward flow is rather more diffuse and extends over a broader offshore domain. Nevertheless, the average velocities of the poleward flow as derived by the model are well within the range of those derived by the in situ data. Furthermore, the peak poleward flow, in both data sets, is situated at the shelf-edge at a depth of ~300 m. The distinct equatorward upwelling jet that is resolved by model-derived geostrophic velocities within 50-80 km of the coast is not resolved by the WOA data set.

Model-derived alongshore geostrophic velocities for the southern Benguela reveal an equatorward jet (Figure 4.13d) at the coast as well as at the shelf-edge, some 200 km offshore. Between these two jets is a region of relatively weak velocities. The bottom boundary layer over the shelf is characterized by a weak poleward flow that extends over the shelf-edge and, though weak, it dominates the deeper layers (i.e. $>$ ~400 m) in the offshore domain. The WOA density field satisfactorily resolves the equatorward shelf-edge jet, with velocities equivalent to those derived from the model density field (i.e. ~14 cm.s). As in the northern Benguela, nearshore features are not captured by the WOA dataset, nor is the weak poleward flow that characterizes the bottom boundary layer over the shelf (according to the model). However, the deep offshore portion of the poleward flow is captured by the WOA-derived geostrophic flow, but is slightly shallower, further offshore and more intense than is resolved by the model.

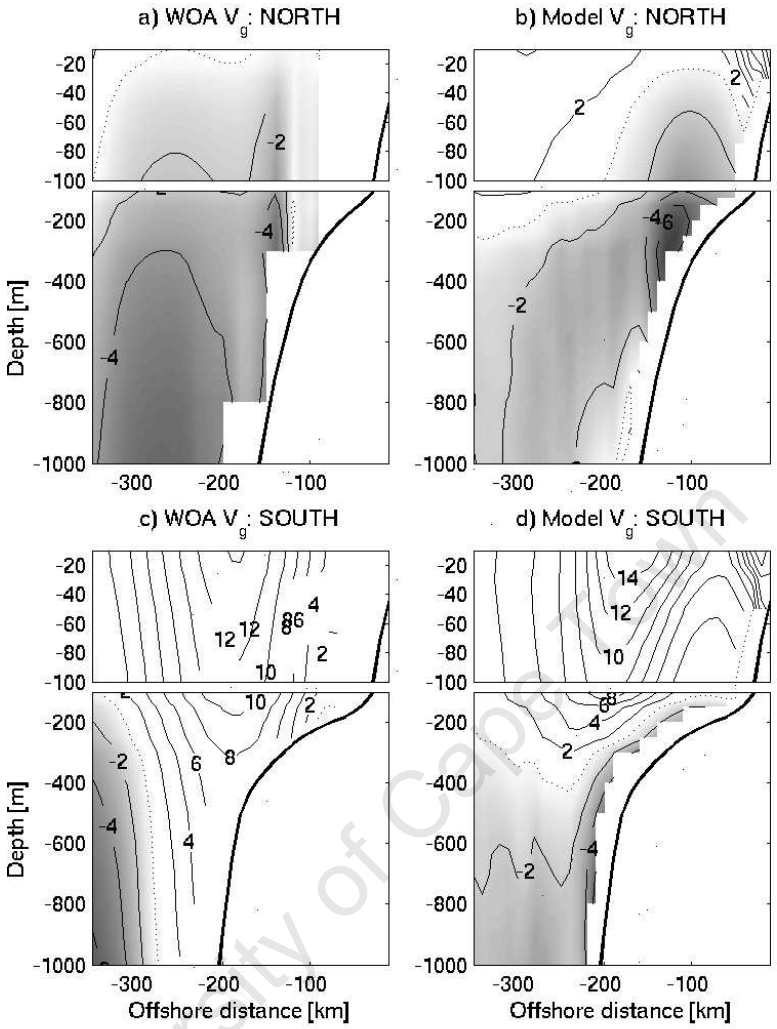

Figure 4.13: Annual mean, alongshore averaged, alongshore geostrophic velocity component for the northern and southern Benguela regions (top and bottom respectively), based on the WOA and model-derived density field (left and right respectively). Negative (grey) values represent poleward velocities.

4.1.4 Water mass analysis

Figure 4.14a and 4.14b are potential temperature-salinity curves (TS-curves) of a meridional section 200 km offshore for WOA and model-derived data respectively, with the meridional position colour-coded so that blue is furthest south and red is furthest north. It reveals that, for a given temperature and water mass (i.e. AAIW, which is represented by the salinity minimum of the curve, the central water mass which is represented by the linear part of the TS-curve and upwells at the coast or

surface water which is everything warmer than the central water mass) the salinity increases toward the north for both observational and model-based plots. This is a well-known feature of the water-mass characteristics of the Benguela system and is a function of the more saline source waters at the northern boundary of the Benguela system (i.e. those derived from the equatorial region via the Angola Current). From *in situ* data Duncombe Rae (2004) showed that water mass characteristics between the Orange River mouth (~28.4^oS) and Walvis Bay (~22.6^oS) are discontinuous in the region of Lüderitz (~26.4^oS), such that the salinities to the north are higher for a given potential temperature than to the south. A black solid line in both the TS-curves in Figure 4.14 represents 25^oS, to the north of this the central water mass is more saline than to the south of it for a given temperature. The black line on the model-based TS-curve also coincides with the position of a discontinuity in the surface water mass characteristics, such that it represents an alongshore salinity minimum for a temperature range spanning 15-17^oC. This signature is related to the enhanced coastal upwelling at approximately this latitude (see Figure 4.24) and the intense offshore motion (see Figure 4.15), together with the fact that salt is a conservative property while temperature is not: i.e. cool and fresh upwelled waters are advected offshore and while at the surface they get warmer but their salinties remain constant. This process is not well resolved in the WOA data.

Differences between observational and model-derived water mass characteristics include the overestimation of temperature and salinity in the surface waters in the south, shown as the blue 'tail' in the model TS plot in Figure 4.14a and previously seen in the vertical sections shown in Figures 4.9a and 4.10a. In TS-curves for this region, AAIW is identified as the salinity minimum at temperatures cooler than the central water mass (i.e. the linear part of the curve). The model resolves AAIW as a salinity minimum, but underestimates it slightly (by ~0.1 psu), suggesting that the model is not completely conserving the AAIW mass.

The erosion of the deep AAIW mass in the ROMS model was identified by **?** as a result of spurious diapycnal mixing common in sigma-coordinate models. They developed a method of reducing the error that involves splitting the advection and diffusion schemes, the latter is rotated for numerical stability and appears as

a biharmonic. Our simulation includes their split advection-diffusion scheme and, though the salinity minimum associated with the AAIW is somewhat eroded, it is an improvement of the original scheme (for a comparison see Chapter 3).

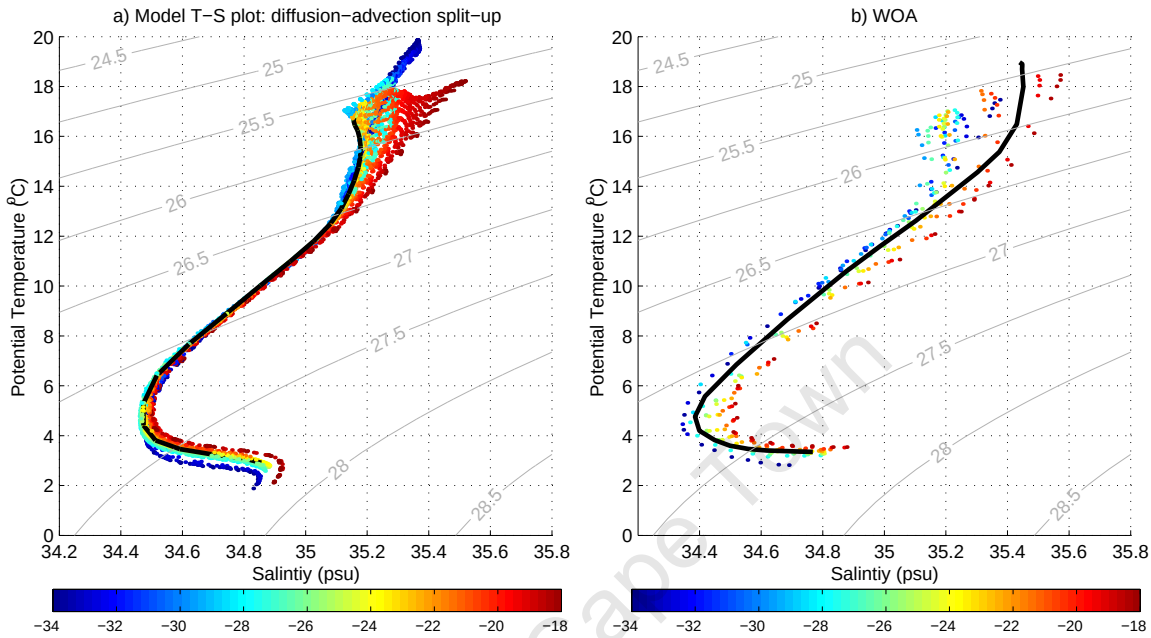

Figure 4.14: Potential temperature-salinity plot of a 200 km offshore section, based on model-derived data (a) and WOA in situ data (b). The colour bar represents the meridional position along the section, blue being furthest south and red being furthest north. The black line is 25°S.

4.1.5 Large-scale flow regime

Large-scale general circulation features of the Benguela system can best be visualized as streamlines (which require the assumption that scales of horizontal motion are far larger than scales of vertical motion), calculated as the streamfunction of the meridional and zonal-components of flow, integrated from the surface to 1000 m. Figure 4.15a shows streamlines of flow in the upper 1000 m and elucidates the division of the Benguela system into two distinct regimes. North of Lüderitz the general flow follows the orientation of the coast and is poleward, with a relatively low volume flux of between 1-2 Sv. The flow regime south of Lüderitz is dominated by the northwesterly meandering path of the Benguela Current and passing Agulhas rings, that also tends to follow the orientation of the coastline until ~30°S, where it begins to veer offshore. Although somewhat higher at the western edge of the do-

main, transports of the Benguela Current as resolved by the model are of the order of measurements taken during the 'Benguela Sources and Transports (BEST)' project during austral autumn and can be found in the work of Garzoli and Gordon (1996); Garzoli et al. (1997). Figure 4.35a shows the annual mean and seasonal integrated model-derived transport at 30°S from the coast to the edge of the model domain at 10°E and integrated over the upper 1000 m. Also shown (as circles) are the approximate transport values derived from Current-Temperature-Depth (CTD) data during BEST2 (07/05-02/07/1993) for the same location (refer to Figure 5 in Garzoli and Gordon (1996)), which were recorded during autumn. Comparing the autumn transport fluxes based on model-derived data with in situ data (Figure 4.35a), it is evident that while a couple of outliers are present, the model agrees favourably with transports calculated from data obtained from the BEST cruise. Both the observational and model-derived transports suggest two cores of the Benguela Current: one that is close to the coast (~14-14.5°E) and a second that is further offshore. The current diverges into a coastal and offshore stream offshore of the Cape Peninsula at ~ 34°S (see Figure 4.15a).

Between the poleward northern regime and equatorward southern regime, is an area where the flow crosses contours of $\frac{f}{H}$, with the most perpendicular orientation just north of Lüderitz. When planetary vorticity is large compared to relative vorticity, flow is expected to follow lines of constant $\frac{f}{H}$. The dimensionless Rossby number (see Appendix A for a scale analysis) in the region of interest is small suggesting that planetary effects are more influential that non-linear effects. The small Rossby number ($R_o = \frac{U}{fL}$) is based on a length scale (L) of 150 km, which is taken as the approximate width of the poleward flow, a velocity scale (U) of 1.5 cm.s^{-1}, which is the average velocity poleward flow and a coriolis parameter (f) of -6x10^{-5}s^{-1}for the region just north of the cross-$\frac{f}{H}$. flow. Because the Rossby number is small, the offshore (cross-$\frac{f}{H}$.) deflection of the poleward flow is therefore somewhat unexpected and remains to be explained.

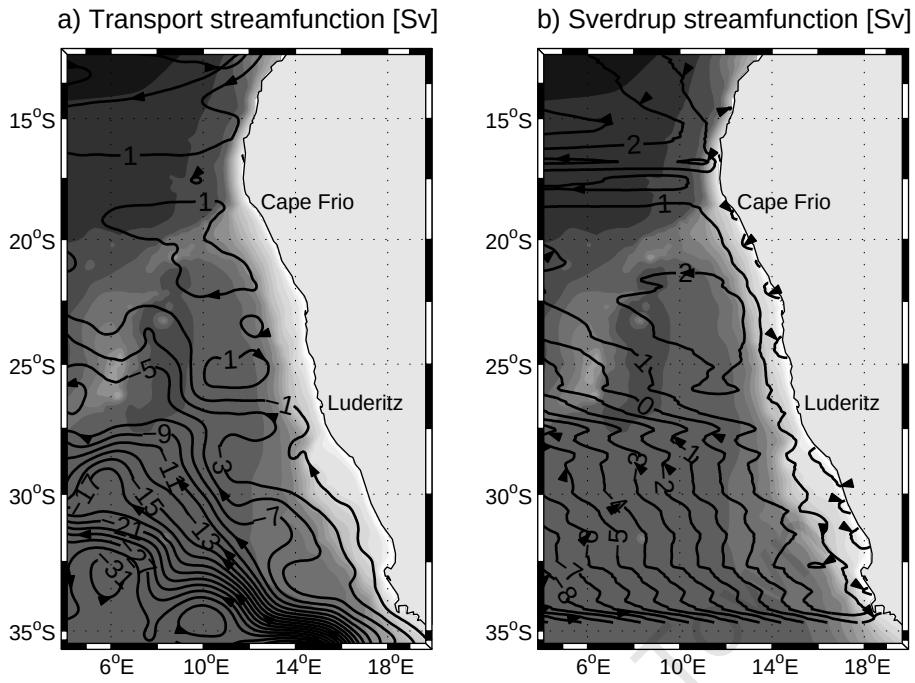

Figure 4.15: (a): Transport streamfunction calculated from model-derived integrated zonal- and meridional-components from the surface to 1000 m depth. and (b): Transport streamfunction based on Sverdrup relation. The contour interval is 2 Sv (i.e. 10^6m.^{3}.s^{-1}). The shades of grey represent lines of constant $\frac{f}{H}$.

It is somewhat counter-intuitive that the prevailing winds in the northern Benguela (refer to Figure 4.1) are in the opposite direction to the ambient poleward flow in this region. A possible explanation for this could be the Sverdrup relation, which relates meridional flow with the torque induced on the ocean by the curl of the wind field. Equation 4.7 is the steady-state solution of the Sverdrup relation and is derived from the vorticity equation. It is derived from the geostrophic vorticity equation and is therefore only valid for flow regimes in which planetary vorticity exceeds relative vorticity (refer to Appendix B).

$$-\beta\frac{\partial\psi}{\partial x} = \frac{\bigtriangledown \times \tau}{\rho_0} \tag{4.7}$$

where ψ is the transport function (in m^3.s^{-1}).

Figure 4.15b is a plot of the transport streamfunction as derived from the Sverdrup relation and reveals the background flow regime that would be induced by the curl of the wind stress alone. It gives a convincing impression that the poleward flow

in the northern Benguela and its offshore advection at ~27 ^{o}S are indeed a product of the Sverdrup relation, forcing an average southward flow in the upper 1000 m at the eastern boundary of the order of ~2 cm.s^{-1}. The Sverdrup relation does not hold for the southern Benguela region due to the inflow of the Agulhas Current and important eddy fluxes associated with it.

A cyclonic meander is coincident with the shelf-edge discontinuity at ~28°S such that offshore transport occurs as the equatorward transport approaches the region of distinct shelf-narrowing. While the Sverdrup relation appears to be the dominating force in the offshore advection in the vicinity of Lüderitz, the offshore transport related to this cyclonic meander does not appear to be linked to the Sverdrup relation.

The distinct alongshore discontinuity in stratification on the shelf shown in Figure 4.12 and its coincidence with the shelf-edge discontinuity inspired an analysis of the possible effects of JEBAR (the 'Joint Effect of BAroclinicity and Relief') on causing the mean flow to cross contours of $\frac{f}{H}$. The first diagnostic calculations of the effect of along-isobath density gradients were carried out by Sarkisyan and Ivanov (1971) (cited in Csanady (1985)) and has since been investigated analytically by several others (e.g. Shaw and Csanady (1983); Huthnance (1984); Csanady (1985); Sakamoto and Umetsu (2006)) and been applied to understand, for example; an unexpected veering of the Kuroshio (Guo et al. (2002)) and the coastal separation of the Gulf stream at ~35 $^o N$ (Myers et al. (1996)).

Shaw and Csanady (1983) and Csanady (1985) provide a succinct description of the dynamics of JEBAR. Horizontal density perturbations will result in a vertical shear in the flow due to the thermal wind relation. If the density perturbation occurs in the along-isobath sense over a sloping-bottom, the net transport in deeper regions will be more than in shallower regions resulting in a divergence. By the necessity of the conservation of mass, this divergence is compensated for by a barotopic transport field, which stretches the vortex lines, causing the water column to veer into deeper water. The steeper the slope and the more intense the along-isobath density gradient, the stronger this effect will be. We investigate this effect in the Benguela system at the density and topographic discontinuity at ~28 $^o S$ and its

possible relation to the cyclonic meander in this region.

The JEBAR term appears in the depth-integrated vorticity equation and its derivation can be found in Appendix C, in which the non-viscous, geostrophic and hydrostatic approximations are made. With these assumptions, the depth-integrated vorticity equation for stationary flow simplifies to:

$$\vec{M}.\nabla\frac{f}{H} = J\left(\phi, H^{-1}\right) \tag{4.8}$$

where:

- H is the water depth
- $\phi = \frac{g}{\rho_o}\int_{-H}^{0}\rho z dz$ is the baroclinic potential energy (in $m^3.s^{-2}$)
- $\vec{M}.\nabla\frac{f}{H} = M_y\frac{\partial}{\partial y}\left(\frac{f}{H}\right) + M_x\frac{\partial}{\partial x}\left(\frac{f}{H}\right)$ is the vortex stretching or advection of planetary vorticity (in s^{-2})
- J is the Jacobian and represents: $J(A,B) = \frac{\partial A}{\partial x}\frac{\partial B}{\partial y} - \frac{\partial A}{\partial y}\frac{\partial B}{\partial x}$
- $M_x = \int_{-H}^{0} u dz$ and $M_y = \int_{-H}^{0} v dz$ are the vertically integrated u- and v-transport components (in $m^2.s^{-1}$)

Equation 4.8 suggests that, if the JEBAR term (i.e. the right-hand side) is indeed a dominating factor in the offshore veering of the alongshore flow, it should balance the term that describes the advection of potential vorticity (APV: i.e. the veering of flow from lines of constant $\frac{f}{H}$). Figure 4.16 shows these two terms for the middle-Benguela region and reveals that they are most significant on the shelf-edge, with high negative values of APV where the mean flow (depicted by the streamlines) veers offshore at the narrowing of the shelf (represented as a dashed line) at 28.5°S. The negative APV is compensated for by high positive values of the JEBAR term. The implication of this is that the alongshelf discontinuity in stratification and topography indeed has a role to play in the formation of the cyclonic meander in this region.

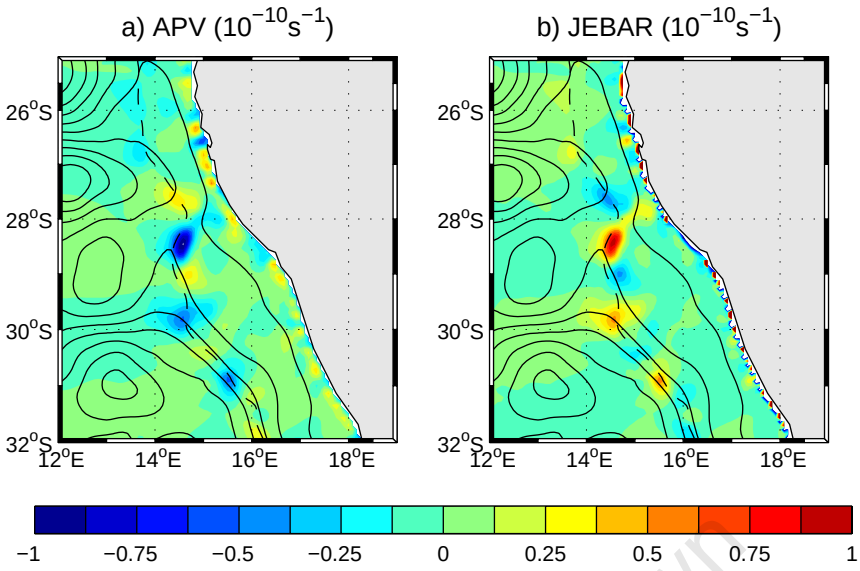

Figure 4.16: (a) Advection of potential vorticity (APV) and, (b) JEBAR terms derived from the depth-integrated vorticity equation. Overlaid are streamlines of flow and the position of the shelf-edge (dashed line). The units are 10^{-10} s^{-1}.

We now have compelling evidence that the wind is the dominating factor in the large-scale offshore veering in the central Benguela at ~27°S and that alongshore density and topographical variations have some influence further south at ~28.5°S.

4.1.6 Shelf-edge features

Figure 4.17 shows that vertical motion at a depth of 300 m in the northern and southern Benguela systems is strikingly dichotomous, such that it is persistently downward in the north and, though predominantly upward in the south, a wave-like alternating upward and downward pattern (seen as alternating red and blue regions just off the 500 m isobath in Figure 4.17) is distinct, particularly south of ~32°S. The downward motion at 300 m in the north is commensurate with the path of the poleward flow, for which evidence exists in the streamlines of transport (integrated from 0-300 m) shown on Figure 4.17). In the south, the offshore veering of the Benguela Current at about 30°S is coincident with a large area of upward motion and the path of the coastal Benguela Current as it follows the shelf-edge to ~30°S overlies the wavelike pattern of upward and downward motion. This pattern of downward

(upward) velocities in the north (south), associated with the poleward (equatorward) flow is consistent with Ekman veering. The transition from predominantly upward to predominantly downward motion occurs in the vicinity of Lüderitz, where the transport regime changes from alongshore (equatorward in the south and poleward in the north) to offshore, which can be seen in the streamlines in Figure 4.17. The northern limit of upward motion due to divergence induced by the offshore motion at the transition between the two systems is at ~$26^{o}S$ and exists just offshore of the downward motion at the shelf-edge.

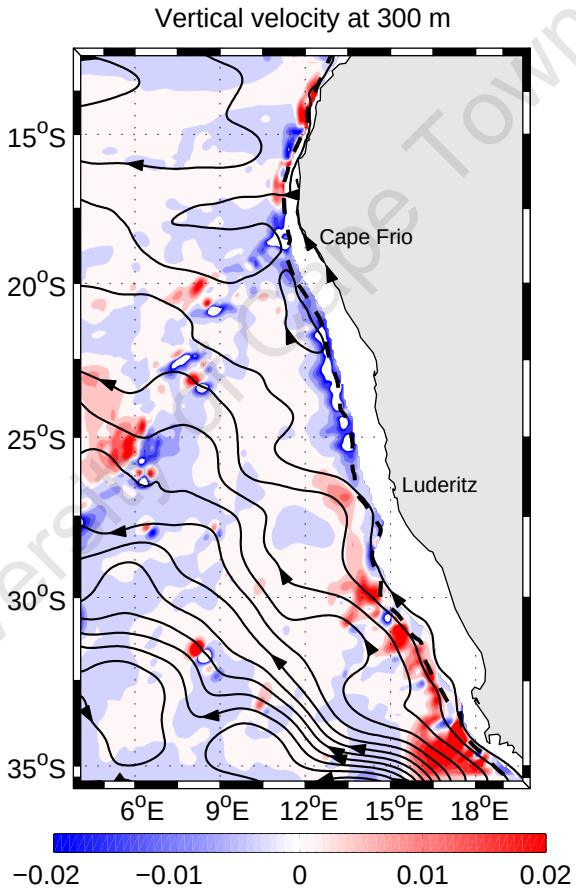

Figure 4.17: Annual mean vertical motion at a depth of 300 m with the 500 m isobath shown in a dashed line. The colourbar is in units of cm.s^{-1}. Overlaid are streamlines for depth-integrated transport from 0-300m.

The distinctly different vertical structure of shelf-edge dynamics of the northern and southern systems and the obvious transition between them is unequivocal in Figure 4.18, which shows the annual mean alongshore, cross-shore and vertical velocities at the shelf-edge (~500 m) from 34°S to 14°S. The alongshore, cross-shore and vertical transport vectors north of ~26°S are relatively uniform, such that the poleward flow is commensurate with predominantly downward and onshore motion. On the other hand, the meandering nature of the equatorward flow in the southern Benguela produces an alternating offshore-onshore pattern for the cross-shore component and a wave-like pattern of the alongshore velocity component associated with an alternating flow strength that results from the onshore-offshore meandering of the core of the equatorward flow.

The distinct shelf-edge poleward flow in the northern Benguela is shown in shades of grey in Figure 4.18a. It remains near-surface until ~26°S, but the core starts deepening toward the south from ~22°S and this can be seen in the vertical velocity structure, in which shades of grey represent downward motion. Much of the poleward flow veers offshore between ~25-26°S and from ~26°S southward, the poleward flow continues to deepen and no longer has a near-surface component, but rather is overlaid by the meandering, equatorward flow of the coastal Benguela Current.

The ABFZ region (i.e. 14-16°S) is defined as the convergence region of the poleward Angola Current and dynamics associated with the Benguela upwelling regime (Veitch et al. (2006)) and is well represented in Figure 4.18. In Figure 4.18, the Angola Current has an offshore component that is consistent with the finding of Gordon and Bosley (1991) that the southern boundary of the cyclonic Angola Gyre is commensurate with the ABFZ.

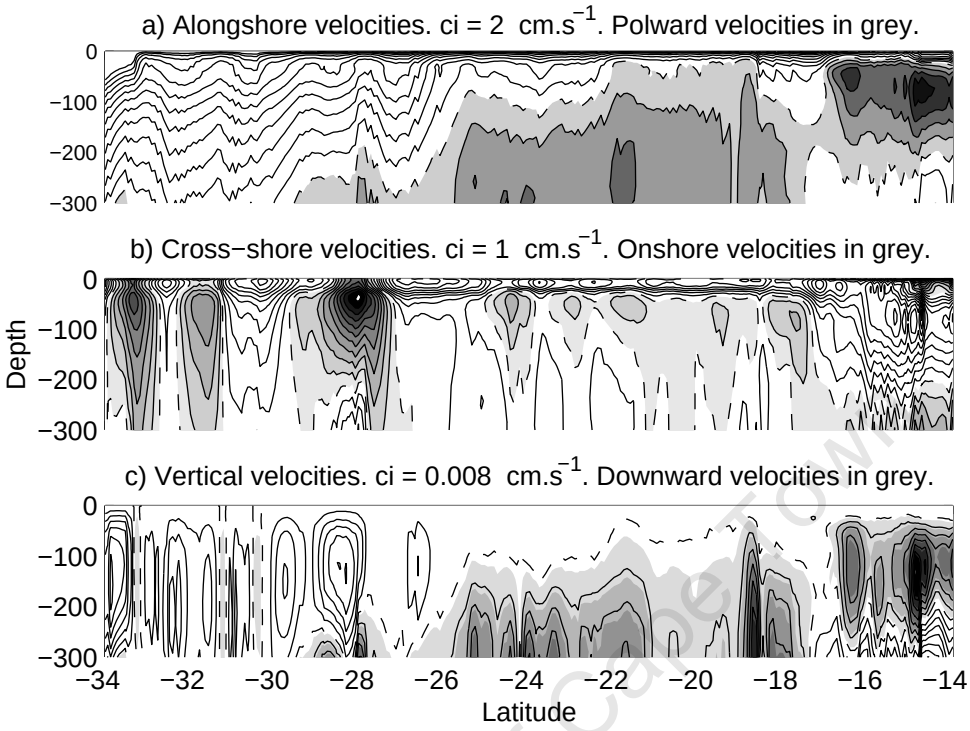

Figure 4.18: Annual mean alongshore (a), cross-shore (b) and vertical velocities (c) in the vicinity of the shelf-edge (~500m) from 34 to 14°S

A simple explanation for the deepening of the poleward flow in the northern Benguela lies perhaps in the conservation of potential vorticity (pv). The low Rossby number ($R_o = \frac{U}{fL}$; refer to appendix A for a derivation), based on a velocity scale (U) of 1.5 cm.s^{-1}, a length scale (L) of 150 km and a coriolis parameter (f) of -6x10^{-5}s^{-1}associated with the poleward flow in the northern Benguela implies that planetary effects far outweigh advective effects. Therefore, the relative vorticity term can be neglected and the potential vorticity is simplified to a relationship between planetary vorticity and depth of the homogenous layer:

$$PV = \frac{f}{H} \tag{4.9}$$

where H is the depth of the homogenous, poleward flowing layer.

A visual inspection reveals that the base of the poleward flow at $16^{o}S$ is situated at approximately 300 m, thus allowing us to calculate PV. Because PV is conserved, we again use equation (4.9) to calculate the changing depths (H) of the base of the poleward-flowing layer as it moves southward, based on the already calculated pv and the coriolis parameter. The circles for each cross-section in Figure 4.19 show the depth of the poleward undercurrent as it moves southward, calculated from the potential vorticity equation. They agree well with the deepening of the poleward undercurrent as resolved by the model. This suggests that the deepening of the poleward flow as it moves southward is indeed related to the conservation of potential vorticity. Penven et al. (2005) showed a similar deepening of the Peru coastal undercurrent in the Peru upwelling system.

A secondary maximum of the poleward current begins to appear at ~$20^{o}S$ in Figure 4.19 and is very distinct at ~$23^{o}S$ where a distinct maximum exists near the coast and the secondary maximum some 150 km offshore. The inshore and offshore maximums are probably the phased seasonal, upwelling-related meridional flows on the shelf and South Equatorial Undercurrent (SEUC) further offshore respectively as shown in Figure 1 of Monteiro et al. (2008). Off the Peru upwelling system, a similar double-maximum of the poleward current has been simulated by Penven et al. (2005) to occur 200-300 km off Chimote (~$9.4^{o}S$), Callao (~$12.1^{o}S$) and Pisco ($14^{o}S$), which they suggested is commensurate with the Peru Coastal Counter Current (PCCC) and is forced by the large-scale pattern of wind stress curl via the Sverdrup relation.

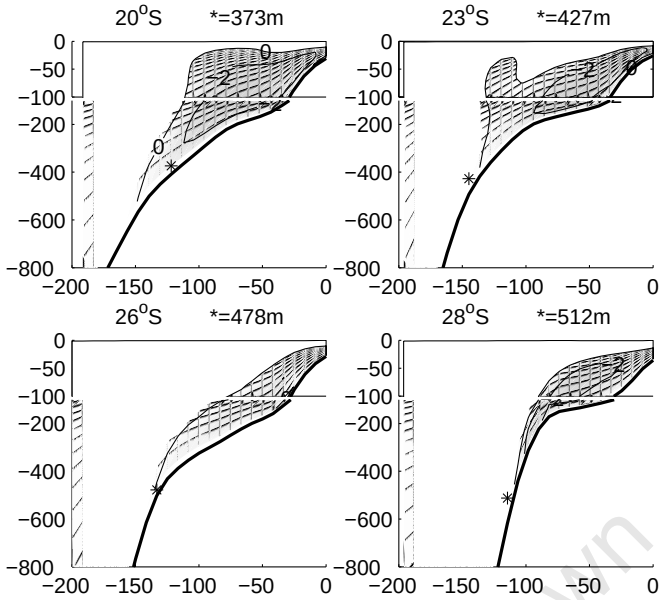

Figure 4.19: Southward deepening of the poleward flow in the northern Benguela shown in several sections. Overlaid are blue stars representing the deepening of the poleward flow based on the model of the conservation of potential vorticity in a low Rossby number regime.

Shelf-edge waves in the southern Benguela

The annual mean pattern of vertical motion on the shelf-edge in the southern Benguela, south of ~30°S (see Figure 4.17 and 4.18c) is suggestive of a standing wave feature (i.e. an alternating red (upward) and blue (downward) pattern just off the shelf-edge). Penven (2000) showed that standing shelf-edge waves can be produced in the lee of a cape, by a mean prograde equatorward flow (i.e. when the flow is oriented with the coast on its right). His investigation was based on a simple analytical model and substantiated by an idealized model configuration. The analytical approach of Penven (2000) is used here to elucidate the role of the wave-like pattern of vertical velocities on the shelf-edge in the southern Benguela.

Because interest lies in a standing-wave pattern in equilibrium conditions, the analytical approach of Penven (2000) was to rewrite the temporal derivatives in the frame of a cape that is moving and a 'mean flow' at rest, based on the assumption that the interaction of a mean flow (U_0) with a cape at rest is approximately equal to the interaction of a mean flow 'at rest' and a cape moving in the opposite direction

($i.e. -U_0$). The derivation of the analytical solution for the wavelength of standing waves produced in the lee of a cape by a mean flow is shown in Appendix D and is based on Buchwald and Adams (1968), Wilkin and Chapman (1987) and Penven (2000). Assumptions made in order to simplify the derivation are a rigid-lid, shallow-water and barotropic approximation (based on the fact that the horizontal length scale is very much larger than the depth scale). The latter implies a barotropic solution, especially on the shelf, which is not entirely unrealistic for our feature of interest, i.e. note the reasonably barotropic nature of the vertical velocity structure in the southern Benguela in Figure 4.18. It is assumed that the shelf slope does not change with respect to the alongshore direction and is given by a linear relationship that is defined as follows:

$$h = H_{max} e^{-2\lambda(Y_{max} - Y)} \tag{4.10}$$

where h and $H_{\max}$ is the maximum depth and depth respectively in the cross-shore direction, $Y_{\max}$ and Y are the maximum offshore distance and offshore distance respectively and λ is a constant that adjusts the steepness of the slope. $H_{\max}$, $Y_{\max}$, and λ are given values of 800 m, 80 km and 1.8x10^{-5}. Figure 4.20 shows the real slope in the vicinity of the Cape Penninsula ($\tilde{}34^{o}S$) as a solid line, while the linearized slope is shown as a dotted line.

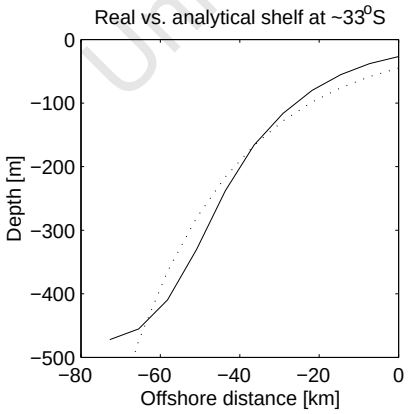

Figure 4.20: Real (solid line) and linearized (dotted line) slope in and representing (respectively) the region of the Cape Peninsula ($\tilde{}34^{o}S$).

The linearized slope topography approximates the Cape Penninsula well and

simplifies the derivation of the standing wave equation that is dependent on the magnitude of the mean flow and the characteristics of the cape and is shown in equation 4.11.

$$L_n = \frac{2\pi}{\sqrt{\frac{n^2\pi^2}{Y_{max}2} - \lambda^2 - \frac{2\lambda f}{U_0}}} \tag{4.11}$$

where L_n is the wavelength, n is the mode number, U_0 is the magnitude of the mean flow.

Based on a mode number (n) of 1, a Y_{max} of 80 km, a λ of 1.8x10^{-4}, an f of -8e-5s^{-1} (for the southern Benguela region) and a characteristic mean flow (U_0) of 0.2 m.s^{-1} (based on the model data: see Figure 4.23), a standing wave with a wavelength of ~50 km is analytically resolved to be generated in the lee of the cape described by the exponential function given in equation 4.10. Table 4.1 shows different characteristic wavelengths of standing waves produced by different mode numbers and different mean characteristic flows past the Cape Peninsula. For the first three wavenumbers [1,2,3], with characteristic mean flows in the range 0.1-0.3 m.s^{-1} standing waves with wavelengths in the range ~30-60 km are produced. A visual analysis of Figure 4.18 suggests that a wavelength of the order of ~30-60 km, given by the analytical solutions in Table 4.1, is of the order of the wavelike pattern of vertical velocities at the shelf-edge in the southern Benguela.

Table 4.1: Characteristic wavelengths (in km) of shelf-edge standing waves produced by different characteristic mean flows (U_0) and wavenumbers (n).

	n=1	n=2	n=3
$U_0 = 0.1\ m.s^{-1}$	36.26 km	33.76 km	30.53 km
$U_0 = 0.2\ m.s^{-1}$	50.28 km	44.16 km	37.58 km
$U_0 = 0.3\ m.s^{-1}$	60.41 km	50.56 km	41.29 km

For a more explicit verification that the wavelike pattern of vertical velocities at the shelf-edge in the southern Benguela is indeed a standing wave produced by the interaction of the mean equatorward flow past the Cape Peninsula, a wavelet analysis

is performed on the vertical velocities above the 500 m isobath at a depth of 300 m, for the southern Benguela region, spanning ~35.5^oS to ~25^oS. As a statistical tool, the wavelet analysis is useful in that it not only gives the relative power of separate wavelengths that contribute to the resulting signal, but it also gives their variation along the time-series (or rather, in this case, 'space-series'). More information on the wavelet analysis technique can be found in Torrence and Compo (1998) and the software was provided by C. Torrence and G. Compo and is available at URL: http://paos.colorado.edu/research/wavelets/.

Figure 4.21a shows the standardized vertical velocities above the 500 m isobath at a depth of 300 m for the full alongshore expanse of the domain and Figure 4.21b is the associated wavelet power spectrum, where the white cross-hatched lines represent the region where edge-effects become significant and statistical results are inconclusive and the bold black line encompasses signals of greater than 95% significance. Two bands of significance exist at ~60 km and at ~ 130 km at various locations between 35^oS and 25^oS. A couple of degrees northward of Cape Columbine (at ~33 ^oS), the dominant vertical velocity signal has a wavelength of the order of 60 km, which is of the order of the analytical solutions of a standing wave produced by a prograde current flowing past a cape at several different scales of mean flow (see Table 4.1). Between 35-34^oS and 31-28^oS, a wavelength of ~130 km is significant for the alongshore signal of vertical velocities. This is consistent with the length-scales of the alongshore variations of the shelf-edge (refer to Figure 4.5 for the alongshore run of the shelf-edge), which elucidates the topographical control in this region.

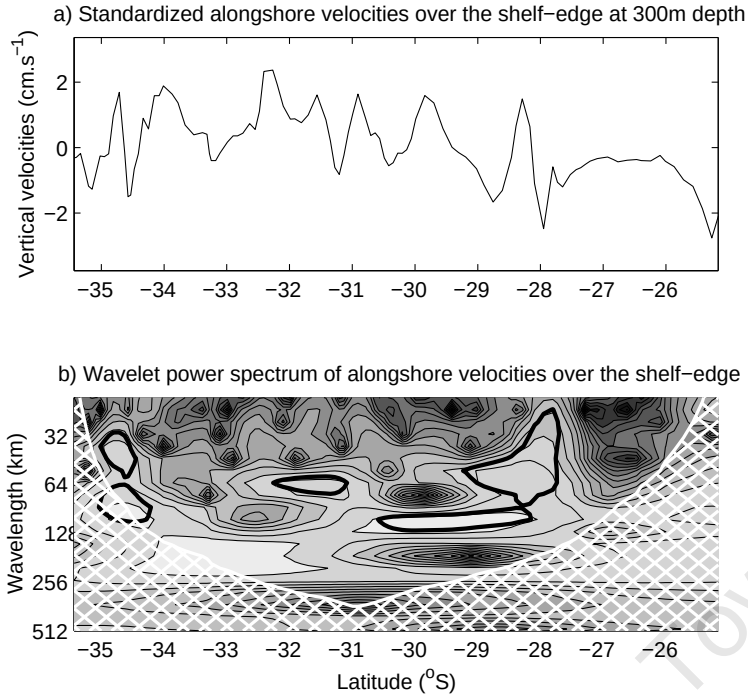

Figure 4.21: (a) Time-series of vertical velocities at the shelf-edge (at ~500 m isobath) at a depth of 300 m from 35^oS to 25^oS and (b) the associated wavelet power spectrum. The area hatched in white represents the 'cone of influence' where edge effects become significant and the bold black contours highlight regions of 95 % significance.

4.1.7 Cross-shore velocity structure: offshore-nearshore transition

The annual mean circulation features along much of the shelf in the Benguela system are characterised, in some way, by typical upwelling processes that have been extensively studied in both analyical and numerical (idealized and realistic) models (e.g. McCreary (1981); Philander and Yoon (1982); Suginohara (1982); Yoon and Philander (1982); McCreary and Chao (1985); Marchesiello et al. (2003); Penven et al. (2005)) as well as *in situ* and satellite observations (Nelson and Hutchings (1983); Lutjeharms and Meeuwis (1987); Lutjeharms and Stockton (1987); Hardman-Mountford and Villacastin (2003)). Salient features, typical of upwelling systems include an offshore Ekman transport in the surface layers forced by equatorward alongshore winds, which is compensated for by an onshore flow at depth and an equatorward baroclinic jet that develops in response to the shoreward-sloping

isotherms, brought about by upwelling of cool water at the coast. Poleward undercurrents are commonly observed features in eastern boundary upwelling systems and, due to their seemingly paradoxical nature, they have been extensively studied in idealized numerical experiments. In his idealized numerical model, Suginohara (1982) found that alongshore variations in equatorward wind forcing produced a poleward undercurrent below the thermocline over the shelf. This result has been repeated by others and Yoon and Philander (1982) showed that due to the formation of an alongshore pressure gradient (in the presence of alongshore variations), Kelvin waves are generated that travel poleward and, on reaching equilibrium, retard the acceleration of the equatorward jet and eventually result in a poleward undercurrent. Figures 4.22 and 4.23 show annual mean alongshore, cross-shore and vertical velocity components for the characteristic northern and southern regimes (defined in Figure 4.6) respectively and both reveal typical upwelling features within about one baroclinic Rossby radius of the coast (which in this region is of the order of ~30-40 km, Chelton et al. (1998)). The baroclinic Rossby radius of deformation in this region shows little latitudinal variation, unlike the Peru or North African upwelling regions and therefore baroclinic instabilities should be, to some extent, latitudinally homogeneous.

The transition from upwelling-dominated dynamics on the relatively narrow shelf to large-scale circulation features in the northern Benguela is characterized by the very distinct and shallow poleward flow situated alongside and above the shelf-edge that is not part of upwelling-induced dynamics, but is generated by the Sverdrup relation (see Figure 4.15b). Based a transport of 1 Sv, derived from the Sverdrup relation, across a distance of ~80 km at 24 ^oS (refer to Figure 4.15b), an average alongshore velocity of ~1.25 cm.s^{-1} in the upper 1000 m can be inferred, which is consistent with the depth-averaged speed of the poleward flow in Figure 4.22). This poleward flow is also reflected in the downward-sloping isotherms of satellite and model-derived alongshore averaged temperatures in Figure 4.7b. As seen in Figure 4.18, Figure 4.22 shows that the poleward flow in the northern Benguela is commensurate with a downward motion that, to some extent, serves to conserve potential vorticity (PV) of the poleward flowing layer as it enters lower coriolis-

parameter regions (refer to 4.9 and Figure 4.19). To get an idea of the downward velocities that are required in order to conserve PV, the depth of the base of the core of the poleward flow (defined as the flow exceeding 2 cm.s^{-1}) is read off Figure 4.19 at 23^{o}S and 24.5^{o}S as ~150 m and ~350 m respectively. The time it would take for a particle to travel the ~167 km between these locations at a speed of ~2 cm.s^{-1} is ~8x10^{6}s. In this time a particle would need to travel downward at a speed of ~0.0024 cm.s^{-1} to deepen from 150 m at 23^{o}S to 350 m at 24.5^{o}S . Therefore, the requirement to conserve PV produces only about 20% of the total downward velocity (~0.01 cm.s^{-1}, on average) associated with the path of the poleward flow, the rest could be accounted for by the convergence of the poleward flow at the shelf-edge or by Ekman veering. In order to get an estimate of the downward velocity that would result from the bottom Ekman layer we assume constant vertical mixing, and neglect the effect of the slope on the Ekman layer. Based on equation (41) in Kundu (1990), a bottom velocity of ~2.5 cm.s^{-1} and an Ekman depth of 30 m, we approximate a maximum downward Ekman velocity of ~0.006 cm.s^{-1}. While this method is vague, it does suggest that a dominant factor in the downward velocities at the shelf in the northern Benguela is bottom Ekman friction.

The broad shelf in the southern Benguela is characterized by upwelling-dynamics in the inner-shelf region and relative quiescence on the middle and outer regions of the shelf, which is also implied by the flatness of isotherms in Figure 4.8b. Large-scale circulation features in the southern Benguela significantly influence shelf-edge dynamics, but in the mean state do not significantly impinge on the wide shelf region. The southern box encompasses the important phenomenon of the splitting of the equatorward jet as it passes Cape Columbine, such that one branch approximately follows the shelf-edge and the other veers offshore as observed by Shannon (1985); Boyd and Oberholzer (1992); Stenevik et al. (2008) and is simulated by the model. The importance of this feature is in the transportation of fish eggs and larvae into the St Helena Bay nursery area (e.g.Penven (2000); Stenevik et al. (2008)). The flow divergence at the shelf-edge, suggested by the cross-shore flow pattern (i.e. onshore transport in the inner-shelf region and offshore transport over the shelf) and the corresponding shelf-edge upwelling could be related to divergence associated with

the splitting of the equatorward jet at Cape Columbine. A poleward undercurrent is present at depths greater than ~600 m and, at the shelf-break, is associated weak onshore velocity which results in convergence and downwelling.

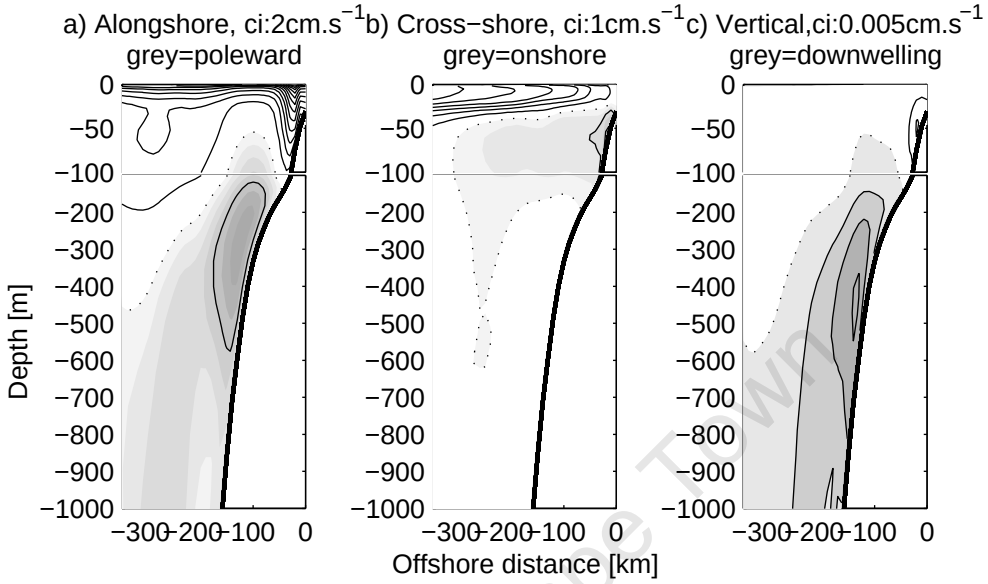

Figure 4.22: Alongshore averaged, alongshore (positive = equatorward) (a), cross-shore (positive = offshore) (b) and vertical currents (positive = upward) (c) in the northern Benguela box.

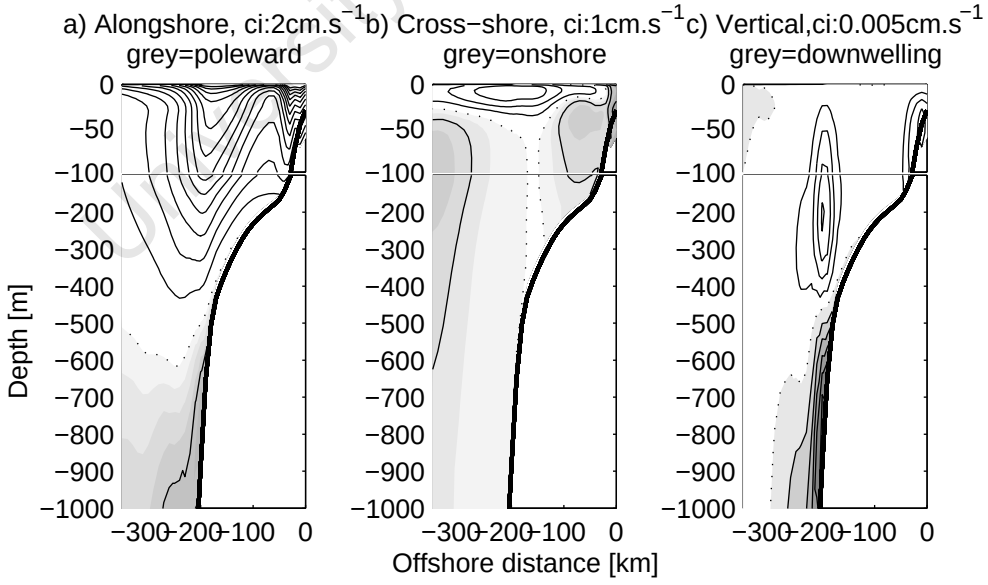

Figure 4.23: Alongshore averaged, alongshore (positive = equatorward) (a), cross-shore (positive = offshore) (b) and vertical currents (positive = upward) (c) in the southern Benguela box.

4.1.8 Upwelling

The ecological and economic importance of the Benguela upwelling system has facilitated consistent research since at least the 1960s. The investigation of upwelling rates in the Benguela has either been limited to direct calculations based on in situ measurements (for which Nelson and Hutchings (1983) provide a review), or has relied on indices based on satellite SST or wind products (e.g. Lutjeharms and Meeuwis (1987); Carr and Kearns (2002)). While the former provides accurate measurements of upwelling rates, it is spatially and temporally scarce, with a bias toward the central and southern Benguela regions. On the other-hand, satellite data allow us to investigate upwelling activity based on a proxy derived from SST products in a more cohesive manner for the whole system, but do not provide a direct estimate of upwelling rates. Upwelling rates can be more directly inferred from calculating Ekman transport fluxes from the alongshore wind component (e.g. Johnson and Nelson (1999); Carr and Kearns (2002)), under the assumptions that the effect of shelf-waves in suppressing upwelling is negligible, the effect of Ekman pumping is negligible and that the coriolis force balances friction in the Ekman layer (i.e. the alongshore wind stress component) (Johnson and Nelson (1999)). Spatially and temporally cohesive model output, inclusive of the whole Benguela upwelling system provides the means to clarify present estimations of upwelling locations, intensities and seasonal signals.

We compute seasonal and annual mean upwelling fluxes, based on Ekman transport velocities (derived from the alongshore wind stress and known as the Bakun upwelling index) as well as on model-derived vertical velocities. We base our calculation of alongshore wind-derived upwelling velocities on the Ekman coastal upwelling index as derived by Bakun (1973) that appears as follows:

$$E_k = \frac{\tau_{alongshore}}{L_u \rho_0 f} \tag{4.12}$$

where E_k is the upwelling velocity in m.s^{-1}, $\tau_{alongshore}$ is the alongshore wind stress component in N.m^{-2}. L_u is the width of active Ekman divergence and is frequently and mistakenly taken to be commensurate with the internal Rossy radius,

which describes the cross-shore scale of geostrophic adjustment scale of the pycnocline slope (Estrade et al. (2008)) and not the upwelling cell structure. For L_u we use the formulation of Estrade et al. (2008) who developed an analytical model of two-dimensional upwelling to show that the the cross-shore width of active upwelling can be better approximated as:

$$L_u = \frac{0.75D}{S} \tag{4.13}$$

where D is the depth of the Ekman layer and S is the slope of the shelf. We calculate the average slope over the shelf for each cross-shelf section and define the Ekman layer depth as 30 m based on Figure 4.22, which is consistent with in situ data for Cape Columbine (Johnson and Nelson (1999)). The Ekman transport velocities are then integrated in the alongshore and cross-shore directions (within the zone of Ekman divergence, calculated in equation 4.13) to obtain seasonal and annual mean upwelling fluxes that are shown in Figure 4.38b in units of $Sv.km^{-1}$. Our results are of the order of the estimates of Carr and Kearns (2002), who used the ERS2 wind product to calculate their fluxes (their units are shown in $m^2.s^{-1}$ or, $m^3.s^{-1}.m^{-1}$). However, their results are somewhat lower than ours and could be due to differences in the definition of L_u.

Results of the more direct method of calculating annual mean upwelling fluxes by extracting model-derived upwelling velocities at the base of the Ekman layer and integrating alongshore and cross-shore (within the width of L_u) is shown as a solid line in Figure 4.24a. Model-derived upwelling fluxes suggest that upwelling intensity along the coast is far from contiguous, but instead is characterized by a number of cells of enhanced activity, which on the smaller scale is related to the orientation of the coastline (Shannon and Nelson (1996)). A similar pattern is present in Ekman transport fluxes shown as a dashed line in Figure 4.24b, however the prominent peaks of, particularly, the Namaqua, Walvis Bay and Namibia cells are underestimated. Individual upwelling cells tend to be located in regions of enhanced wind stress curl (Shannon and Nelson (1996)), a quantity that has been ignored in the Ekman transport flux index, thus resulting some inconsistencies between the directly calculated upwelling fluxes versus the Ekman transport flux

index. However, while Ekman pumping fluxes contribute to enhancing individual upwelling cells, their magnitudes are much lower (see Figure 4.24c) than the Ekman transport fluxes, therefore the contribution of wind-stress curl to the underestimated alongshore wind-stress derived upwelling flux is relatively small. A distinct inconsistency in the model-derived upwelling fluxes and the Ekman transport fluxes is the fact that the latter is consistently higher in the northern Benguela region (north of ~23°S). This disparity can be explained by the process of geostrophic upwelling (Marchesiello and Estrade (2009)) and is covered in the next section.

Seasonal fluctuations have so far been ignored, therefore the alongshore upwelling variations in Figure 4.24 should be used merely as an approximation of long-term mean upwelling intensities. Demarcq et al. (2003) used satellite-derived SST maps spanning 1982 - 1999 to create climatologies to investigate variability of upwelling in the Benguela system. Their observations similarly revealed that the Benguela system is fragmented into separate cells and in the annual mean they resolved three major upwelling areas: ~22.5-28°S, ~30°S and ~33-34°S. Model-derived upwelling fluxes however resolve the seven distinct upwelling cells that were located by Lutjeharms and Meeuwis (1987) using satellite SST imagery. They located upwelling centers at 34°S, 32°S, 29°S, 25°S, 22°S,19°S and 17°S, which they named the Peninsula, Columbine, Namaqua, Lüderitz, Walvis Bay, Namibia and Cunene cells respectively. The mismatch in the locations of the centers of some of the cells is likely to be related to the fact that the satellite SST images used in the investigation by Lutjeharms and Meeuwis (1987) were processed into 1°x1° boxes. While the annual mean upwelling rates and volume fluxes inherently underestimate (overestimate) maximum (minimum) upwelling intensities, this is particularly true for the three upwelling cells to the south of Lüderitz that have the greatest seasonal standard deviations (see Figure 4.38e). However, the annual mean upwelling fluxes and rates in the Benguela upwelling region provide a guage from which to quantify and compare the equilibrium state of the separate cells. Average transport fluxes for each cell are 0.06 Sv (Cape Peninsula, which has a length of ~111 km), 0.23 Sv (Cape Columbine: 120 km), 1.04 Sv (Namaqua: 467 km), 1.55 Sv (Lüderitz: ~401 km), 0.74 Sv (Walvis Bay: ~278 km), 1.16 Sv (Namibia: ~543 km) and 0.56 Sv (Cunene: 197 km). The

respective annual mean upwelling rates from the Cape Peninsula cell northward are 2 m.day^{-1}, 7 m.day^{-1}, 8 m.day^{-1}, 13.44 m.day^{-1}, 9 m.day^{-1}, 7.12 m.day^{-1} and 9.12 m.day^{-1}. While upwelling rates are consistently higher in the Lüderitz cell, Demarcq et al. (2003) showed that the highly active Lüderitz upwelling region is somewhat paradoxical due to its very low concentrations of chlorophyll and therefore, productivity (Demarcq et al. (2007)). Somewhat counter-intuitive is that the less intense upwelling cells to the north and south of this are highly productive and support important demersal and pelagic fisheries (Hutchings (1992)).

Figure 4.24c is an upwelling index based on the method of Carr and Kearns (2002) and is the difference in coastal and offshore (~500 km in our case) SSTs. The index based on coastal-offshore SST difference resolves all seven of the upwelling cells labelled in Figure 4.24a, however the temperature difference in the southernmost cells is likely to be overestimated due to the warm offshore bias (refer to Figure 4.3).

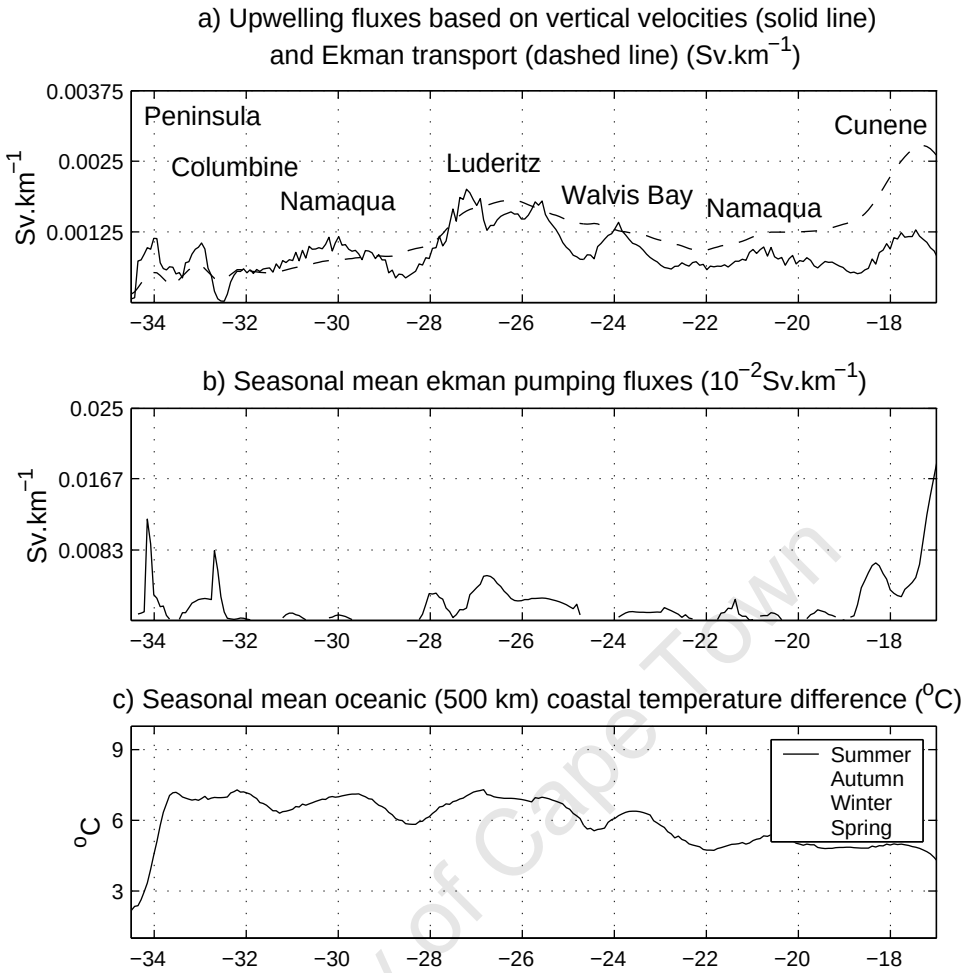

Figure 4.24: (a) Annual mean upwelling volume fluxes within 30 km of the coast at 30 m depth based on model-derived vertical velocities (solid line) and based on Ekman transport calculations (dashed line), units: Sv.km^{-1}, (b) Ekman pumping fluxes within 30 km of the coast (note the different scale to (a)) and (c) upwelling index based on coastal (20 km) -oceanic (500 km) temperature difference, units: ^{o}C.

Geostrophic convergence

The role of geostrophic convergence in inhibiting upwelling fluxes off the coast of New Caledonia was recently investigated by Marchesiello and Estrade (2009). They formulated a new index for coastal upwelling in which they introduced a geostrophic upwelling term into the traditional Bakun index (equation 4.12), so that their index for coastal upwelling (CUI) appears as follows:

$$CUI = \frac{\tau_{alongshore}}{L_u \rho_0 f} + GUI \tag{4.14}$$

where GUI is upwelling related to geostrophic currents alone and appears as follows:

$$GUI = -\int_{x=0}^{x=L_u}\int_{z_0}^{0}\left[\frac{\partial u_g}{\partial x}+\frac{\partial v_g}{\partial y}\right]\partial z\partial x \tag{4.15}$$

where z_0 is the depth of the Ekman layer and u_g and v_g are the cross-shore and alongshore geostrophic velocity components (calculated using the thermal wind relation, with the model-derived density field and then rotated to align parallel and perpendicular to the coast). A second formulation of GUI was derived by Marchesiello and Estrade (2009) for narrow shelf regions that approximated wall boundary conditions (where the onshore velocity component is directly converted into vertical velocities by the discreet continuity equation at the wall):

$$GUI = -\frac{1}{L_u}\int_{z_0}^{0} u_g \partial z \tag{4.16}$$

In Figure 4.25 we plot the annual mean Bakun upwelling index (dashed line), modelled upwelling fluxes (solid line) and the Bakun upwelling index corrected with GUI (dot-dash line) in order to take into account the inhibition or enhancement of coastal upwelling by geostrophic currents. In the broader regions of the shelf in the southern Benguela we use equation 4.15 to calculate the GUI and for the narrower shelf in the northern Benguela, we found equation 4.16 to be more appropriate. The correction of the Bakun upwelling index for geostrophic convergence reveals a much better agreement with the modelled upwelling fluxes as can be seen in Figure 4.25. The fact that modelled upwelling fluxes are less than those predicted by the Bakun upwelling index is a result of the inhibition of upwelling by geostrophic currents that converge at the coast and lead to downwelling. Marchesiello and Estrade (2009) similarly noted an overestimation of upwelling fluxes by the Bakun index in the northern Benguela and related it to eastward equatorial currents that feed into the cyclonic Angola Dome. Their work highlighted parallels with the tropical regions of the Canary and Peru upwelling systems by suggesting the role of the Guinea and Peru Domes in counteracting coastal upwelling by geostrophic convergence. In the far south, the Bakun upwelling index underestimates the upwelling rate, suggesting

that there is geostrophic divergence in this area resulting in enhanced upwelling rates. The correction of the Bakun index for geostrophic convergence (or, in this case, divergence) for the southern part of the system shown in the dot-dash line in Figure 4.25 shows that upwelling is indeed enhanced by geostrophic upwelling (i.e. the addition of the GUI to the BUI results in an upwelling index more comparable to modelled vertical velocities).

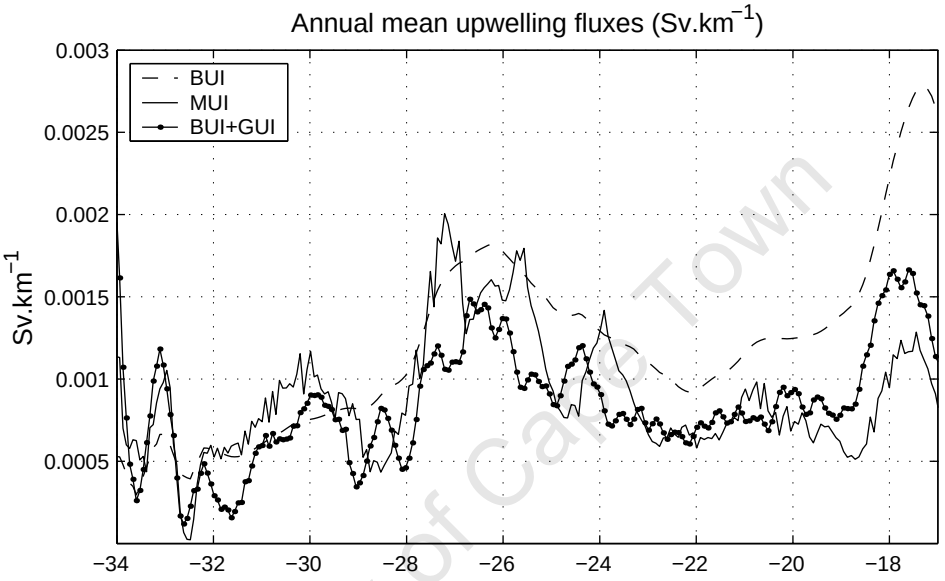

Figure 4.25: Annual mean upwelling fluxes, based on the Bakun upwelling index (BUI: dashed line), model-derived vertical velocities (solid line) and the Bakun upwelling index + geostrophic upwelling (BUI+GUI: dot-dash line).

4.2 Seasonal variability

4.2.1 Wind forcing

The mean wind stress magnitude and direction, as derived from the 0.5° QuikSCAT satellite wind product (using data spanning 2000-2007) are shown in Figure 4.26 for each season. The wind stress is always high off Lüderitz and also in the vicinity of Cape Frio at the northern boundary of the upwelling regime (but less so during summer for the latter location). The general tendency is for the wind to reach a maximum some 200-300 km offshore, which is consistent with the findings of Jury (1985) and Kamstra (1985), which were based on in situ measurements. Peak wind

stress occurs further south during spring and summer, shifting northward in autumn and winter. This is consistent with the meridional fluctuations of the large-scale atmospheric system that is fundamental to the dynamics of the Benguela upwelling regime.

The anticyclonic winds associated with the South Atlantic high pressure system (or, South Atlantic Anticyclone: SAA) and the continental low pressure field provide the means for upwelling processes in the Benguela system by aligning and intensifying the winds parallel to the coast (Shillington et al. (2006)). Seasonal differences in the intensity of upwelling-favourable winds are related to seasonal variations of the continental low and the fluctuating position of the SAA which shifts seasonally, moving northwestward in autumn and southeastward in spring (Preston-Whyte and Tyson (1993)).

Figure 4.27 shows spatial and temporal variations of monthly mean upwelling-favourable winds in the Benguela system and agrees well with Fig. 2 in Strub et al. (1998) which unfortunately spans only 35-23°S. While their alongshore wind stress is calculated from ECMWF surface wind fields and spans 1987-1988, their upwelling favourable wind stress is of the order of ours, which is based on the QuikSCAT 2000-20007 climatology used to force our model. For example, the maximum annual alongshore wind stress off Lüderitz in Strub et al. (1998) is 0.16 $N.m^{-2}$ and 0.2 $N.m^{-2}$ in the summers of 1987 and 1988 respectivey. Our climatology yields a maximum annual wind stress of 0.15 $N.m^{-2}$ (also in summer). This comparison suggests that, while our simulation does not capture extreme upwelling favourable wind scenarios, it indeed represents the climatological nature of the upwelling-favourable wind regime with a good degree of realism. While maximum upwelling favourable wind stress occurs year-round off Cape Frio and Lüderitz, particular seasonal fluctuations are present within each of these regions. Cape Frio is subject to upwelling-favourable winds in excess of 0.12 $N.m^{-2}$ year-round, except during summer months when it weakens somewhat. Alongshore wind stress is generally weaker at Lüderitz than at Cape Frio, but stronger than anywhere else in the system. Winds in excess of 0.12 $N.m^{-2}$occur only during spring and summer in the vicinity of Lüderitz. The strongest seasonal signal (see STD plot in Figure 4.27) is present south of ~28°S, with most

intense upwelling-favourable winds during spring and summer that do not exceed ~0.1 N.m^{-2} (south of 33°S). The most perennial region of upwelling-favourable winds is situated in the vicinity of the Lüderitz upwelling cell, where the alongshore wind stress averages ~0.07 N.m^{-2}.

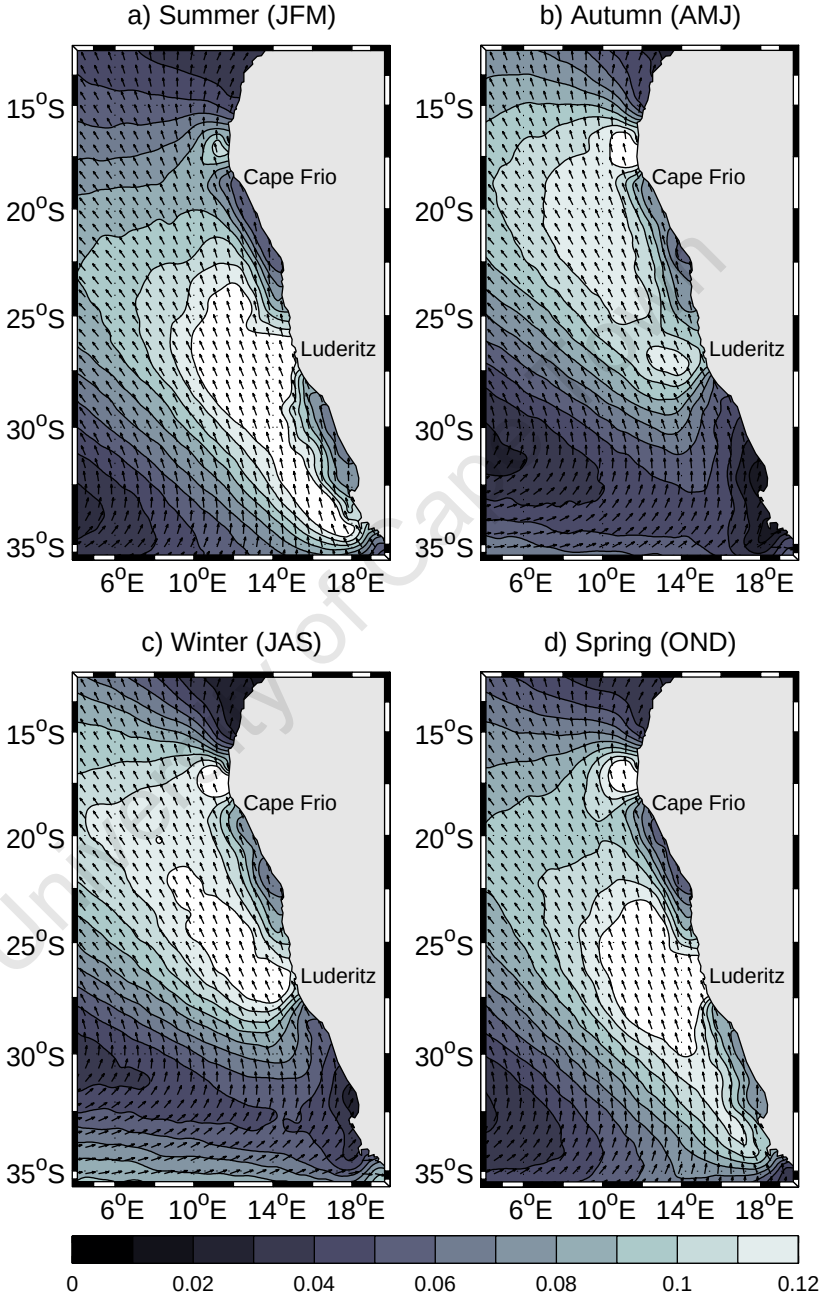

Figure 4.26: Seasonal mean mean wind stress (contour interval: 0.01 N.m^{-1}) magnitude and direction.

The importance of the wind stress curl in forcing a poleward undercurrent in the northern Benguela has been demonstrated in the mean state. Seasonal fluctuations of the wind stress curl are therefore likely to have significant implications on the large-scale dynamics of the northern part of the system. Figure 4.28 shows the seasonal mean wind stress curl patterns and, like the upwelling favourable winds (shown in Figure 4.27), the wind stress curl shows more seasonal variability in the southern Benguela than in the northern part of the system. Nevertheless, strongest negative wind stress curl occurs in the cyclonic band alongside the coast throughout the system during spring and summer months and is likely to have dynamical implications for the poleward flow in the northern Benguela.

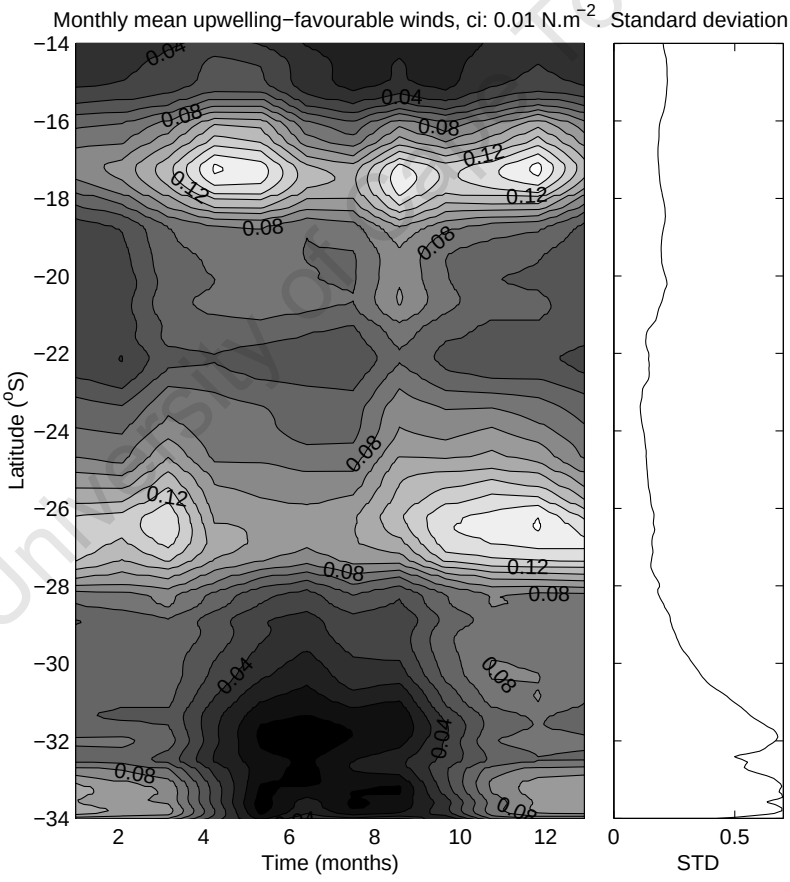

Figure 4.27: Monthly mean upwelling favourable wind stress (N.m^{-2}) at the coast from 34-14^{o}S (left) and its associated normalized (i.e. divided by mean wind stress at each alongshore location) standard deviation (right).

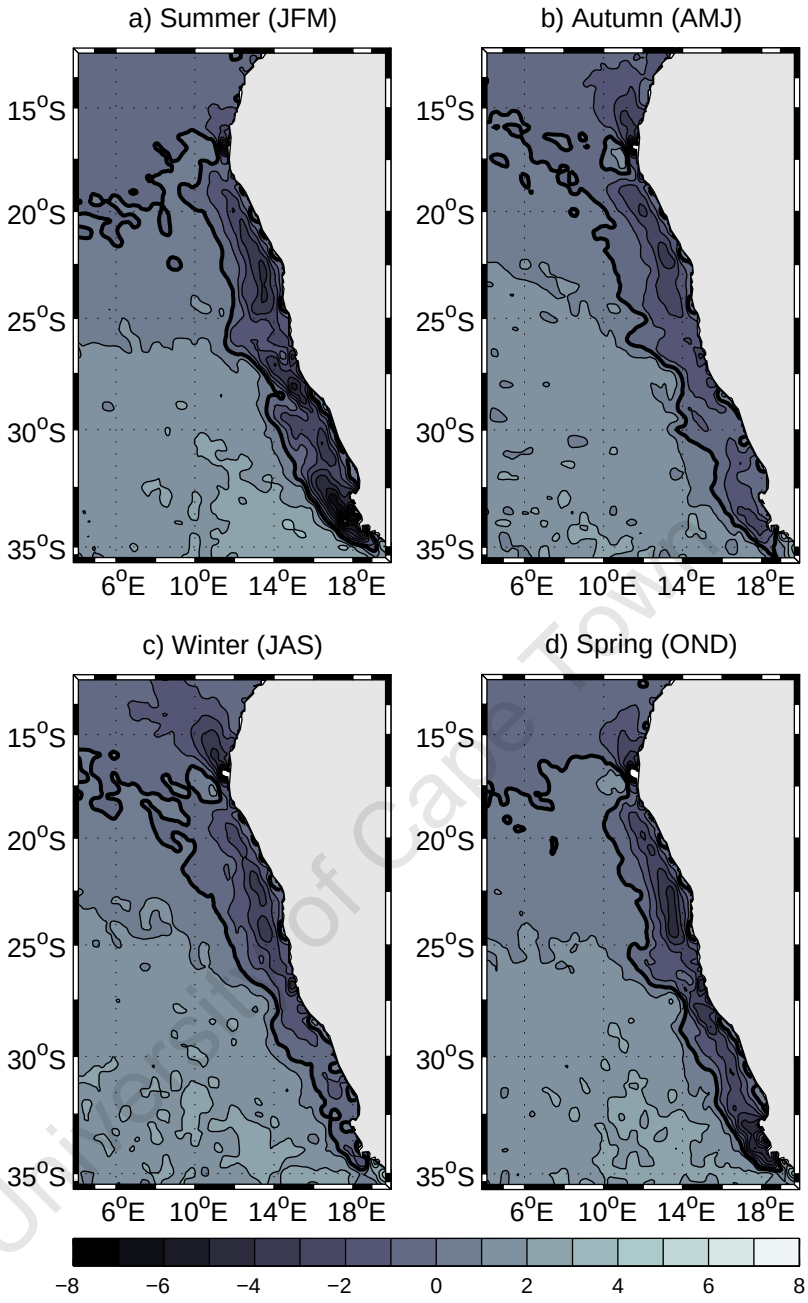

Figure 4.28: Seasonal mean wind stress curl. Contour interval: 0.1 10^{-8}N.m^{-1}. The bold black line represents the region of zero wind stress curl.

4.2.2 Surface pattern: SST

A distinct seasonal signal can be observed in model-derived and satellite summer and winter mean SSTs that are shown in Figure 4.29. The dominant signal of course, being in the offshore regions and is related to the seasonal cycle of solar heating.

The robust seasonal signal and alongshore variations of the upwelling favourable wind stress were discussed in the previous section and is, in a sense, reflected in the summer and winter mean coastal SSTs in Figure 4.29. For instance, enhanced upwelling in the southern Benguela region during summer is reflected by low coastal temperatures and a very strong offshore temperature gradient. The upwelling front of the southern Benguela system is strongly confined to the shelf-edge (which is represented as a white dotted line), which is likely to be related to the juxtaposition of the cool water upwelled at the coast during summer and the warm offshore water of Agulhas origin, that also tends to follow the alongshore run of the shelf-edge (e.g. see Figure 4.5). The cool 'bulge' at Lüderitz is present throughout the year, but is characterized by stronger offshore temperature gradients in summer than in winter. This is consistent with the fact that upwelling-favourable wind stress persists year-round in this region, but is stronger in summer than in winter.

Differences between summer and winter mean model-derived and satellite (i.e. model SST - satellite SST) observed are shown in Figure 4.30a and 4.30b respectively. A cool bias (associated with the poor resolution of the coastal wind drop-off: refer to Section 4.1.2) is present during both extremes of the upwelling cycle along the coast, but is most intense and extends much further offshore during summer months throughout the system. While we expect there to be less upwelling in the southern part of the system during winter (and therefore, less of a cool bias in the coastal region), we anticipate more upwelling during winter in the northern-most cells (and therefore, a greater cool bias). However the cool bias is strongly confined to the coast throughout the system, which is related to the lack of upwelling in the south and, in the north, to a significant offshore warm bias, which masks the coastal cool bias. The warm offshore bias in the north is, in part, related to the fact that the envifish satellite data set has not been processed with a cloud-masking algorithm. Therefore, during winter months, when SSTs are higher than usual in the northwest region of the domain, cloud formation might be enhanced, resulting in no data over the warmer waters and, essentially, cooler winter climatological SSTs than in reality. A significant difference in the summer and winter SST biases is the fact that the warm offshore bias in the south due to the influx of too much water of Agulhas

Current origin is far greater and extends further north during winter than summer, with maximum biases of 2.5°C and 1.5°C respectively.

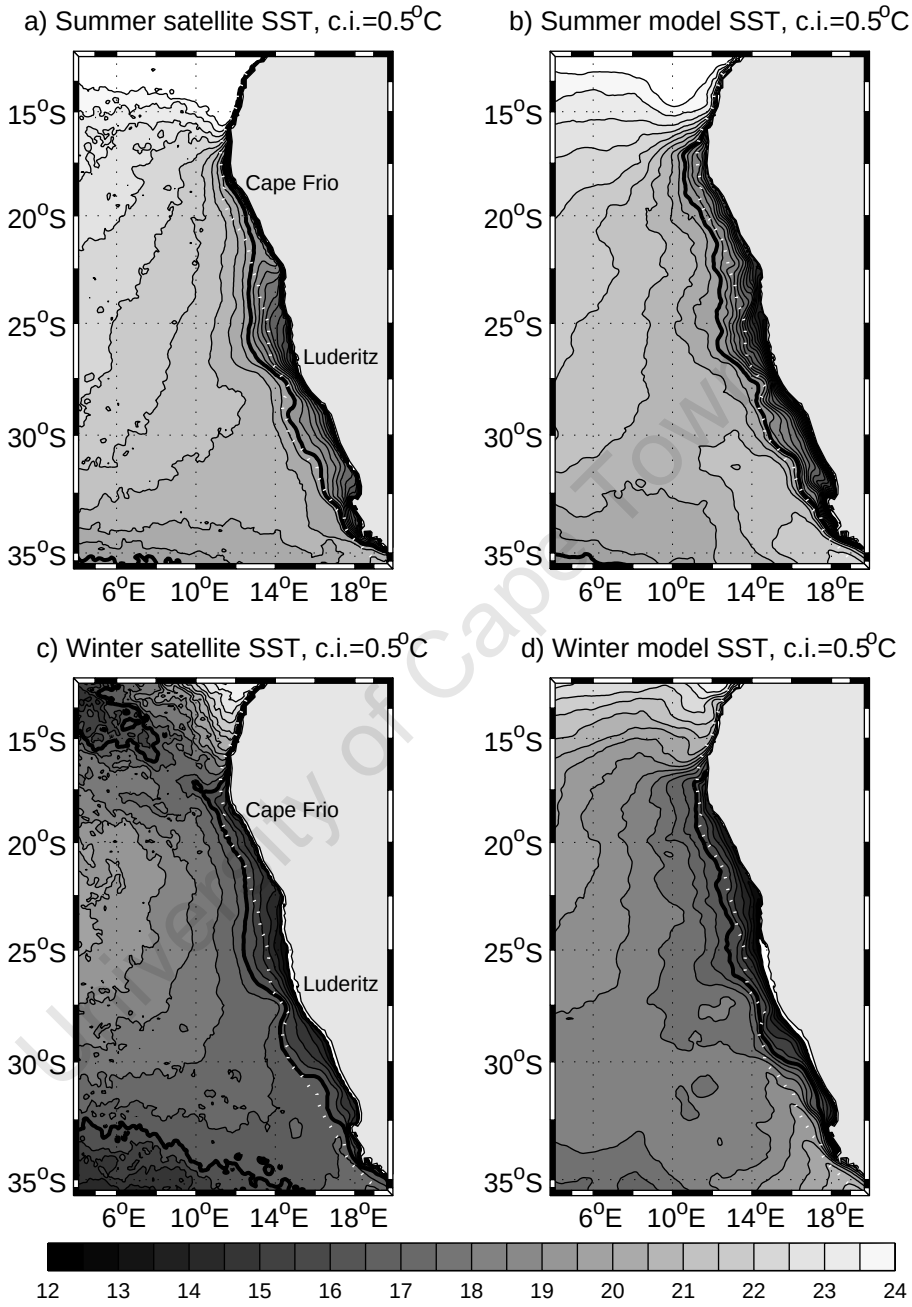

Figure 4.29: Summer and winter mean SSTs (top and bottom respectively), based on model output and envifish satellite data (right and left respectively). The bold black line represents the approximate position of the upwelling front (represented by the 15.5°C and 19.5°C isotherms for winter and summer respectively) and the dotted white line represents the approximate position of the shelf-edge.

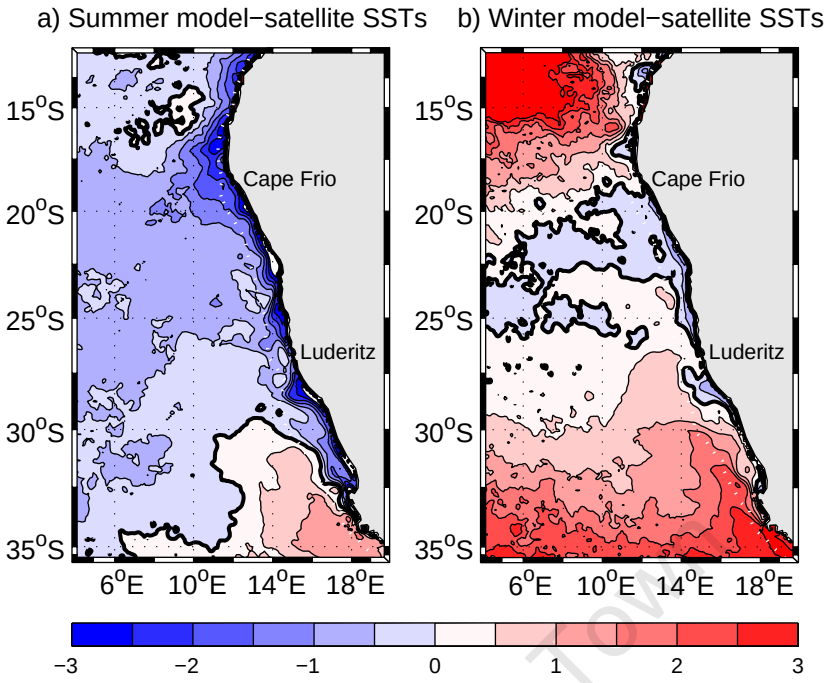

Figure 4.30: Model and satellite SST differences (i.e. model-satellite SST) for summer (a) and winter (b) SST biases. The bold black line represents zero difference and the contour interval is 0.5 °C.

Figure 4.31 shows the seasonal standard deviation (STD) of SSTs, based on seasonal climatologies of model output as well as satellite data and provides a more explicit indication of the extent to which the model captures variability of SSTs (and, by inference, upwelling rates) between seasons. The perennial nature of the upwelling cell in the vicinity of Lüderitz, associated with strongest upwelling favourable winds, is captured by the low seasonal STDs in both the model and satellite SSTs. Although the upwelling cells of Cape Point (34°S) and Cape Columbine (33°S) have a relatively strong seasonal signal, the combination of surface cooling (from upwelling) and heating (from solar radiation) result in low STDs in these regions. The narrow band of low STDs along the coast in the model output is erroneous and is associated with the interpolation technique of the wind data that underestimates the wind drop-off at the coast. Another discrepancy worth noting is that the satellite STDs show a high degree of seasonal variations on the shelf in the northern Benguela, while the model shows little seasonal variability of SSTs in this region. This discrepancy could be related to the fact that the model overestimates

upwelling throughout the year and therefore masks the seasonal warm signal at the coast that is related to the poleward movement of equatorial warm and saline water. In general, the relative patterns of seasonal SST variability are similar, but the satellite data reveals more seasonal variability than is resolved by the model.

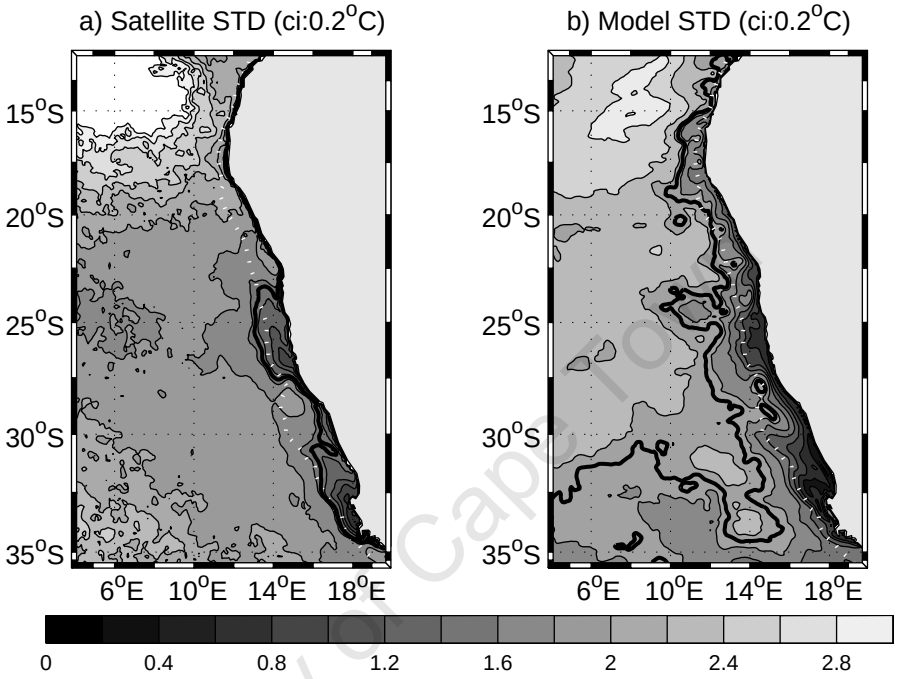

Figure 4.31: Standard deviation of seasonal SSTs, based on satellite data (a) and model output (b). The bold black line is 1.5°C and the contour interval is 0.2°C.

4.2.3 Vertical thermohaline structure

Seasonal standard deviations of temperature sections in the northern and southern Benguela systems are dominated by the cyclic effect of solar heating. This can be seen in Figure 4.32, which shows that highest seasonal temperature variations occur in the surface mixed layer for both regions. While the central water mass in the northern Benguela varies very little seasonally, shelf and slope temperatures vary slightly more due to the seasonal input of warmer water via the poleward current as well as the seasonally pulsing upwelling cycle. Central water in the southern Benguela experiences greater seasonal temperature fluctuations than in

the north due to the meandering nature of the Benguela Current and passing warm-cored Agulhas eddies. The broad shelf region of the southern Benguela is relatively quiescent and varies relatively little from season to season, while closer to the coast seasonal standard deviations are higher and are associated with the strong seasonal upwelling signal in this region.

The mixed layer depths (MLD) are calculated using the method derived by Lorbacher et al. (2006), which locates the depth of greatest curvature of the vertical temperature profile. The summer and winter mean MLDs are shown as a solid and dashed white lines respectively. The cross-shore profiles of the summer and winter MLDs in the northern Benguela are similar except that it is, approximately uniformly, ~20 m deeper during winter (at ~ 45m), which is what we expect as the shallower summer MLD is linked to increased surface stratification brought on by solar heating. During winter and summer (both seasons experience active upwelling in the northern Benguela), the MLD deepens in connection with the equatorward upwelling jet and its associated turbulence, enhancing vertical mixing. The winter MLD (at ~60 m depth) in the southern Benguela is ~40 m deeper than in summer in areas outside of the coastal upwelling regime. The generally deeper MLD in the southern Benguela as compared to the northern Benguela (for regions from the shelf-edge seaward) is due to enhanced surface mixing associated with the turbulent nature of passing Agulhas rings and eddies and their interactions with features generated at the southern Benguela upwelling front or it could be realted to the poleward increase in the MLD. The strong seasonal upwelling signal in the southern Benguela is reflected by the deepening of the MLD at the coast during summer and the peak upwelling season, causing strong vertical mixing due to the stronger winds and the denser water at the surface.

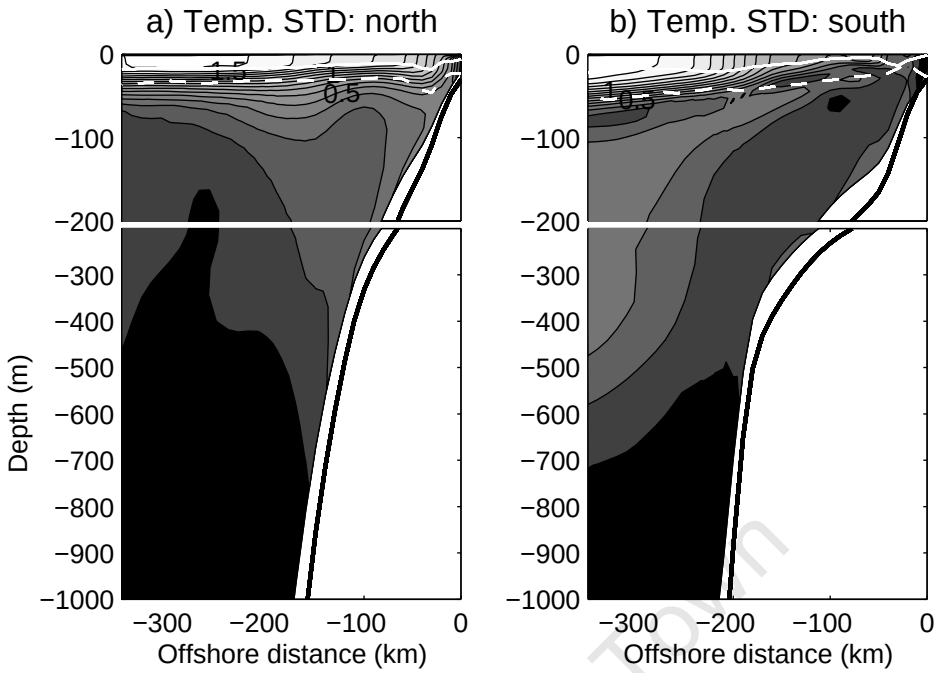

Figure 4.32: Seasonal standard deviation sections of temperature for the northern (a) and southern (b) Benguela boxes. Approximate mixed layer depths are shown for summer (solid white line) and winter (dashed white line). Contour interval is 0.1°C and darker shades represent lower values.

Seasonal variability of the vertical salinity structure in the northern and southern Benguela systems are shown in Figure 4.33. As a first order observation, seasonal salinity variations appear to reflect temperature variations, however with the strong effect of solar heating absent. High seasonal fluctuations of salinity in the surface layers and over the shelf and shelf-beak are present in the northern Benguela and are a function of the seasonal pulsing of the northern boundary of the cool and relatively fresh upwelling regime with the warmer and more saline subtropical waters. The high STD nearshore that is limited to a depth of approximately 40 m is a result of the seasonally pulsed coastal upwelling. Similarly, the lens of high salinity variability in the southern Benguela is a result of the seasonal cycle of upwelling. Once again, the central water mass in offshore regions of the southern Benguela has increased variabilty due to passing Agulhas rings and eddies.

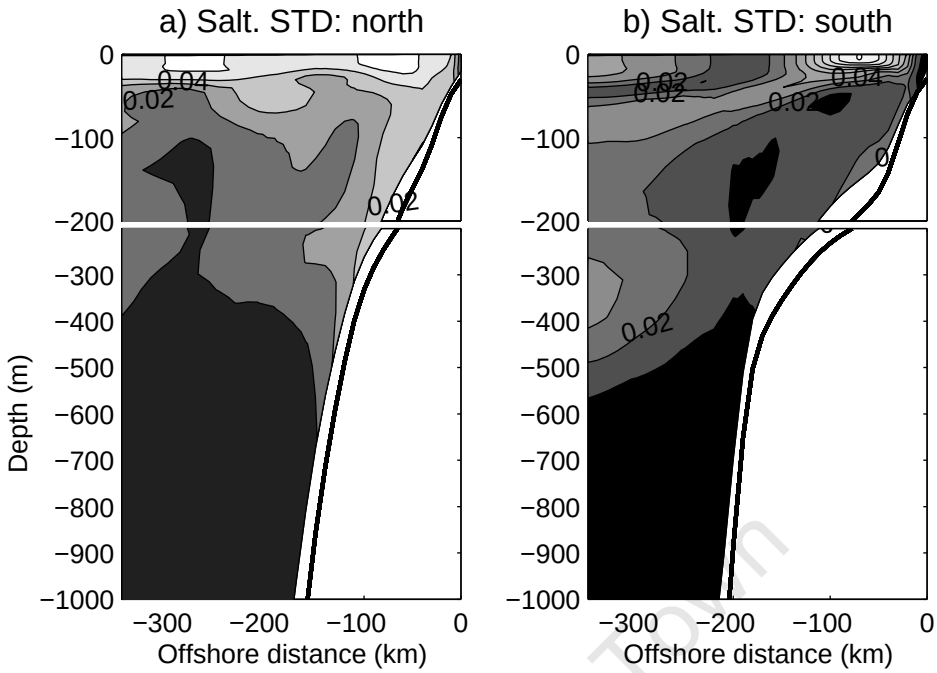

Figure 4.33: Seasonal standard deviations of salinity for the northern (a) and southern (b) Benguela regions. Contour interval is 0.01 psu and darker shades represent lower values.

The enhanced seasonal variability of thermohaline characteristics over the shelf and shelf-break in the northern Benguela is externally generated by the southward advection of water properties via the poleward current. This process is an important factor for the central and northern Benguela upwelling systems as, not only unusually warm and salty but also low oxygen water, originating from the Angola Dome region, north of the Angola-Benguela Frontal Zone (ABFZ), advects southward and can have serious implications for the health of the ecosystem. Table 4.2 lists the seasonal mean heat and salt fluxes over the shelf-edge (situated at approximately the 500 m isobath) across 18°S, which is well within the domain of the poleward current (see Figure 4.15). The fluxes are seperated into northward, southward and net fluxes. Greatest southward heat and salt fluxes occur during spring and summer, suggesting an increase in the transport of the poleward current during these seasons. Greatest northward fluxes are during autumn and winter, implying an enhanced equatorward upwelling jet, which is the dominant flow regime over the shelf (see Figure 4.22a). Only during summer does a net southward flux occur across 18°S, with a heat flux of -0.003 PW and a salt flux of -3.4 Sv.psu.

Table 4.2: Seasonal mean heat and salt fluxes across 18°S. Units are in PW (i.e. 10^{12} W) and SV psu (i.e. psu. $10^6 m^3.s^{-1}$) respectively.

Heat flux (PW)	**Summer**	**Autumn**	**Winter**	**Spring**
Southward flux	-0.014	-0.005	-0.007	-0.014
Northward flux	0.01	0.027	0.026	0.025
Net flux	-0.003	0.023	0.019	0.011
Salt flux (Sv.psu)	**Summer**	**Autumn**	**Winter**	**Spring**
Southward flux	-9.3	-4	-6.5	-11.3
Northward flux	5.5	16	15.7	15
Net flux	-3.4	12	9.2	3.7

4.2.4 Large-scale transports

Large-scale circulation features of the Benguela Current system clearly distinguish the northern and southern systems as separate entities as was seen in Figure 4.15. The northern Benguela is subject to a sluggish subsurface poleward flow that is forced by the curl of the wind stress and is described in the Sverdrup relation (equation (4.7)). Figure 4.34 shows the summer and winter mean transport streamfunction, based on 0-1000 m depth integrated model-derived velocities, as well as the corresponding streamfunction of the active layer, based on the Sverdrup relation. Both summer and winter months highlight the northern and southern regions as separate large-scale circulation regimes (Figure 4.34a and 4.34c): the meandering path of the Benguela Current dominates the southern region to about 30°S where it starts to veer offshore and the northern Benguela region is characterised by a weak poleward flowing regime in the vicinity of the shelf-edge that is, in places, manifested by a series of closed cyclonic loops. The summer and winter Sverdrup-derived streamfunction for the active layer similarly reveal the separation of the northern and summer regimes.

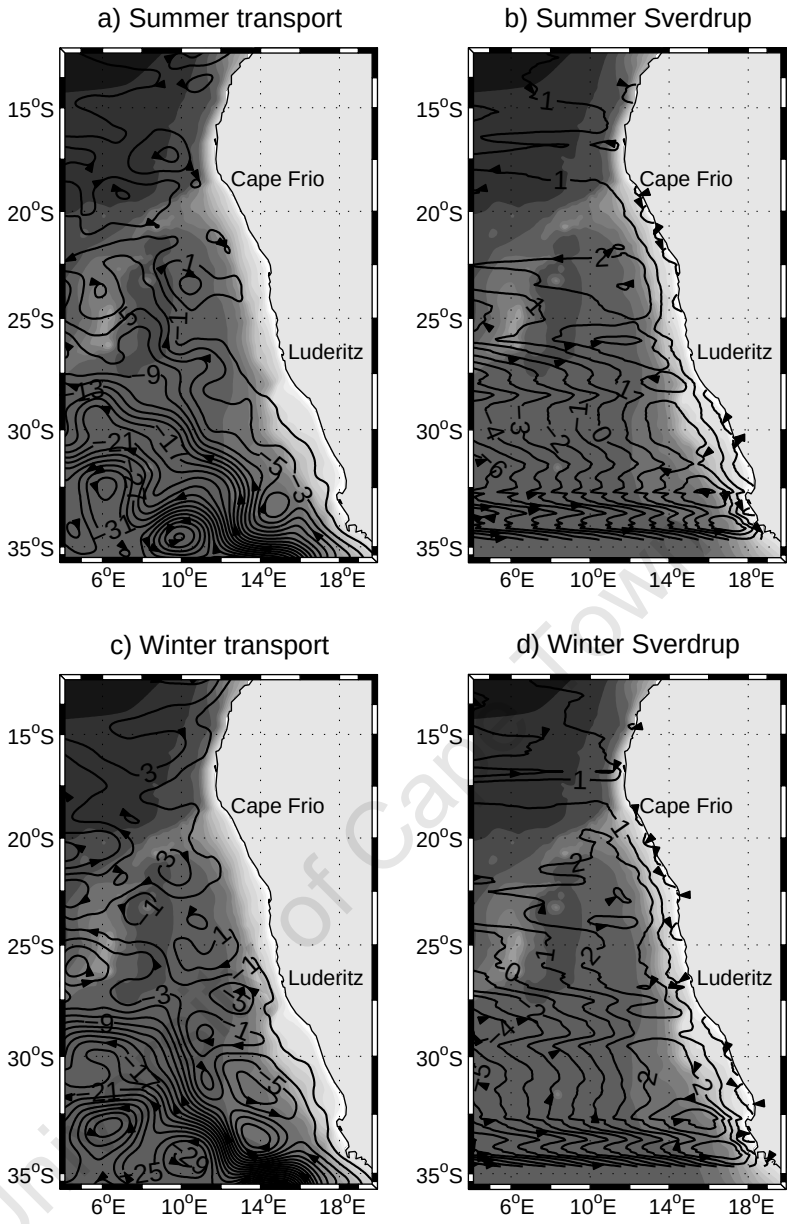

Figure 4.34: Summer (a) and winter (c) transport streamfunction, based on depth integrated (0-1000 m), model-derived velocities. Summer (b) and winter (d) Sverdrup streamfunction. Units: Sv.

Figure 4.35a and 4.35b show the seasonal mean depth-integrated (0-1000 m) volume transports across 30^oS and 23^oS respectively. Also shown (as circles) in Figure 4.35a are the approximate transport values derived from Current-Temperature-Depth (CTD) data during BEST2 (07/05-02/07/1993) for the same location (refer to Figure 5 in Garzoli and Gordon (1996)) from measurements taken during austral autumn. The observational and model-derived depth-integrated transports agree

well and both show that the two streams of the Benguela Current, as seen in the surface geostrophic flow regime (Figure 4.5), penetrate to depths of at least 1000 m. While the poleward transport across 23^oS is an order of magnitude lower than the northward transport across 30^oS, it's seasonal variability is significantly higher. Figure 4.35c and 4.35d are the seasonal standard deviations, as a fraction of the range of transport (i.e the normalized STDs) across 30^oS and 23^oS respectively. The small seasonal signal of transports of the Benguela Current was also suggested by Garzoli and Gordon (1996) from their study of 16 months of in situ data. The poleward transports are larger across 23^oS during spring and summer when the cyclonic wind stress curl in this region is most intense (refer to Figure 4.37), which is consistent with the previous finding that the poleward flow in the northern Benguela is driven by Sverdrup dynamics (see equation 4.7). This is also consistent with the greatest southward fluxes of heat and salt during spring and summer over the shelf-edge across 18°S (refer to Table 4.2). Although the seasonal signal of transport across 30^oS is relatively small, some interesting cross-shore seasonal fluctuations exist. For instance, over the shelf-edge (which spans the 500-2500 m isobath in this region and corresponds to 13.5-15^oE in Figure 4.35a), the northward transport is weakest during summer and spring due the more intense negative wind stress curl during these seasons, which leads to an enhanced poleward component. However, in offshore regions the equatorward transport is greatest during spring and summer, when the southeasterly wind stress component is strongest.

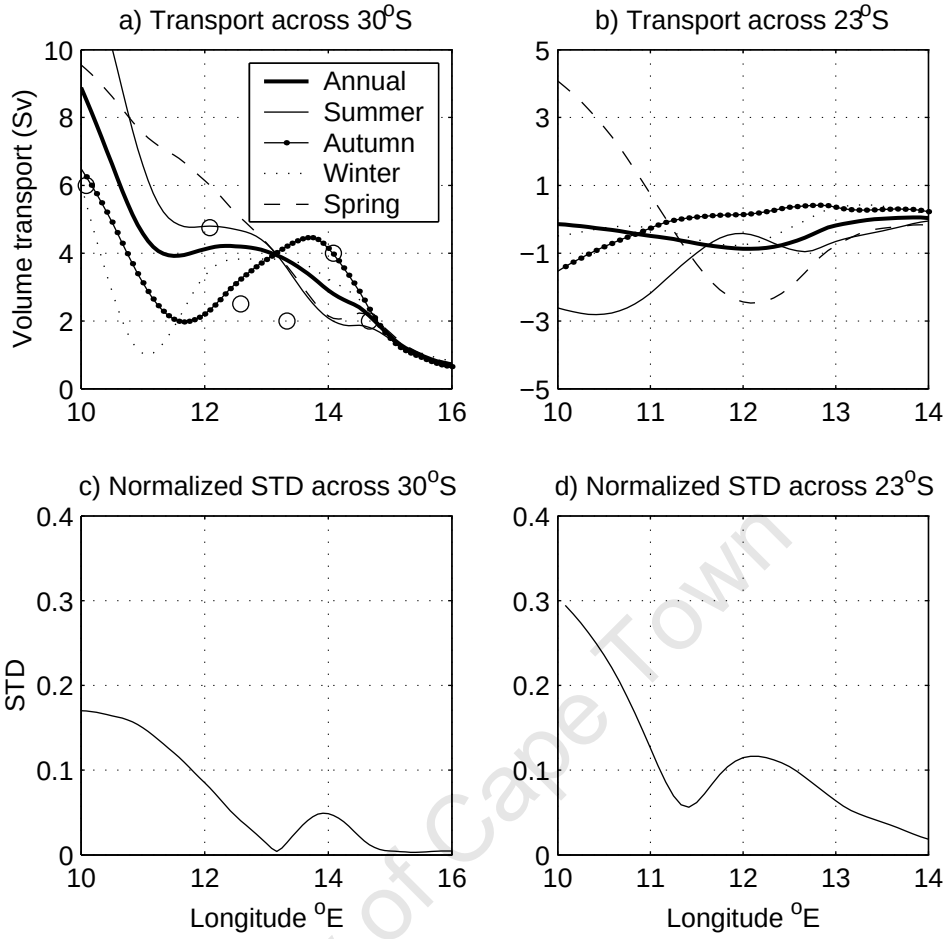

Figure 4.35: Seasonal transports, integrated from the surface to 1000 m across 30^oS (a) and 23^oS (b). Positive is northward. The circles in a) are the positions of 0-1000 m transports derived from in situ data measured during austral autumn on the BEST2 (07/05-02/07/1993) cruise. c) and d) are the normalized (i.e. STD/range) standard deviations of a) and b) respectively.

Seasonal mean transports across the shelf-edge are shown in Figure 4.36. The vertical lines represent the distinct inshore and offshore deflections of the shelf-edge at ~28.5^oS and ~27.75^oS respectively. The point where the shelf-edge narrows suddenly (~28.5^oS) corresponds, for all seasons, with the point where the offshore transport starts to become more onshore and vice versa for the point where the shelf starts to widen again (~27.75^oS), this sets up the anticyclonic-cyclonic meandering pattern in this region (see Figure 4.15a). This topographical control is dependant on the fact that the large-scale flow approximates geostrophy (i.e. it has a low Rossby number) and therefore tends to follow lines of constant $\frac{f}{H}$. The seasonal signal of

the prominent onshore transport at 27^oS, ranging from ~0.025 Sv in summer to ~0.075 Sv in autumn, is consistent with the seasonal fluctuations of the negative wind stress curl (4.37) and will have implications for source water properties of the vigorous Lüderitz upwelling cell.

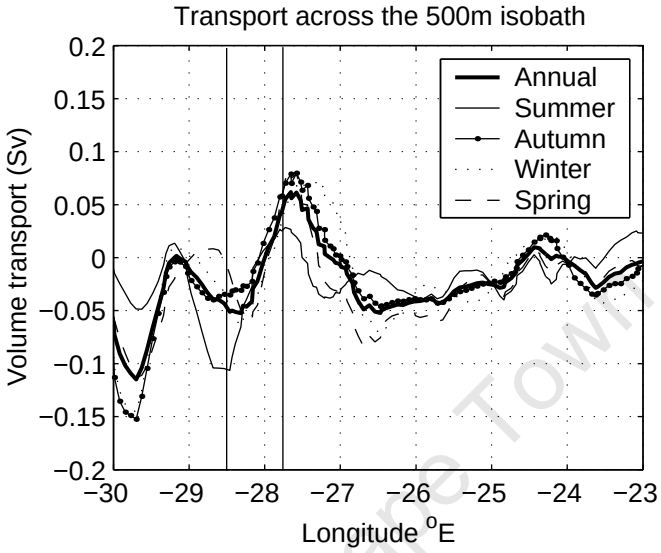

Figure 4.36: Seasonal mean cross-shelf (taken as the location of the 500 m isobath) transports. Negative values correspond to offshore transport. The vertical solid lines represent the distinct inshore and offshore deflections of the shelf-edge at ~28.5^oS and ~27.75^oS respectively.

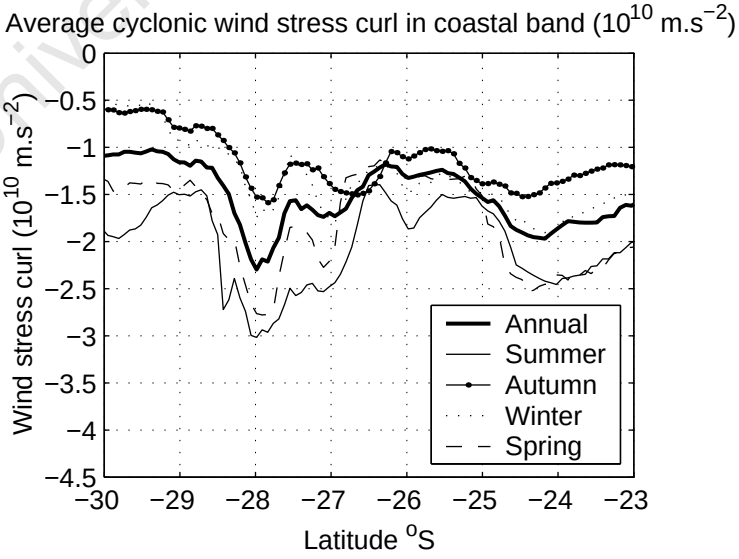

Figure 4.37: Seasonal average cyclonic wind stress curl, from the coast to the offshore location of zero wind stress curl.

4.2.5 Upwelling

Figure 4.38 shows the seasonal upwelling indices based on: a) model-derived vertical velocities, b) Ekman transport fluxes (refer to equation (4.12)) and d) the oceanic (at 500 km offshore)/ coastal temperature difference. Also shown are the seasonal mean upwelling fluxes based on the process of Ekman pumping (c) and the normalized seasonal standard deviation of the upwelling volume fluxes (i.e. STD/mean), based on model-derived vertical velocities (e). Note that the scales of the y-axes differ for each plot.

The plots in Figure 4.38 show that variation of upwelling intensity from season to season tends to be highest at the southernmost, least in the central region and increasing slightly toward the north. The Lüderitz cell has been described as 'effectively dividing the Benguela into northern and southern sections' by Shannon and Nelson (1996), due to its semi-permanent nature, which can be seen in Figure 4.38a,b and c. However, the Walvis Bay cell is subject to even lower seasonal variations. The fact that upwelling is greatest during spring and summer months in the southern Benguela has been well documented (e.g. Hart and Currie (1960); Lutjeharms and Meeuwis (1987)), the spring upwelling maximum at the Cunene upwelling cell at Cape Frio has been observed by O'Toole (1980) (cited in Nelson and Hutchings (1983)) and the winter maximum of the Namibia upwelling cell has been documented by Lutjeharms and Meeuwis (1987) in their analysis of satellite SSTs. These seasonal upwelling signals are well resolved by the model as can be seen in Figure 4.38a. The alongshore-varying seasonal cycle of upwelling fluxes, based on model-derived vertical velocities is in good agreement with the magnitude and seasonality of the Ekman transport fluxes (Figure 4.38b), emphasizing the dominance of the alongshore wind stress component in upwelling dynamics. However, upwelling fluxes inferred from Ekman transport fluxes are somewhat higher than fluxes derived from model-derived vertical velocities in the northern part of the system. These differences have been explained by the process of geostrophic upwelling (see section 4.1.8).

As an indication of upwelling intensity, Carr and Kearns (2002) derived an upwelling index for satellite data, based on coastal and offshore (~500 km) SST dif-

ferences. This index is shown in Figure 4.38d. Weeks et al. (2006) used the same upwelling index (but taking an offshore location of ~300 km) on a high-resolution satellite product and focused on the southern Benguela upwelling cells: St Helena Bay (~32.5 ^{o}S) and Cape Peninsula (~34 ^{o}S). Based on the upwelling index, they concluded that upwelling intensities in these southern Benguela regions were greatest in spring and summer months, which is consistent with our model results. Based on this upwelling index, the northern Benguela apparently experiences most upwelling during autumn. These results should be interpreted cautiously as the upwelling index does not take into account advection (for example, the southward advection of warmer water in the northern Benguela system). The fact that too much Agulhas water enters into the southern Benguela domain, results in a warm SST bias in the southern Benguela throughout the year.

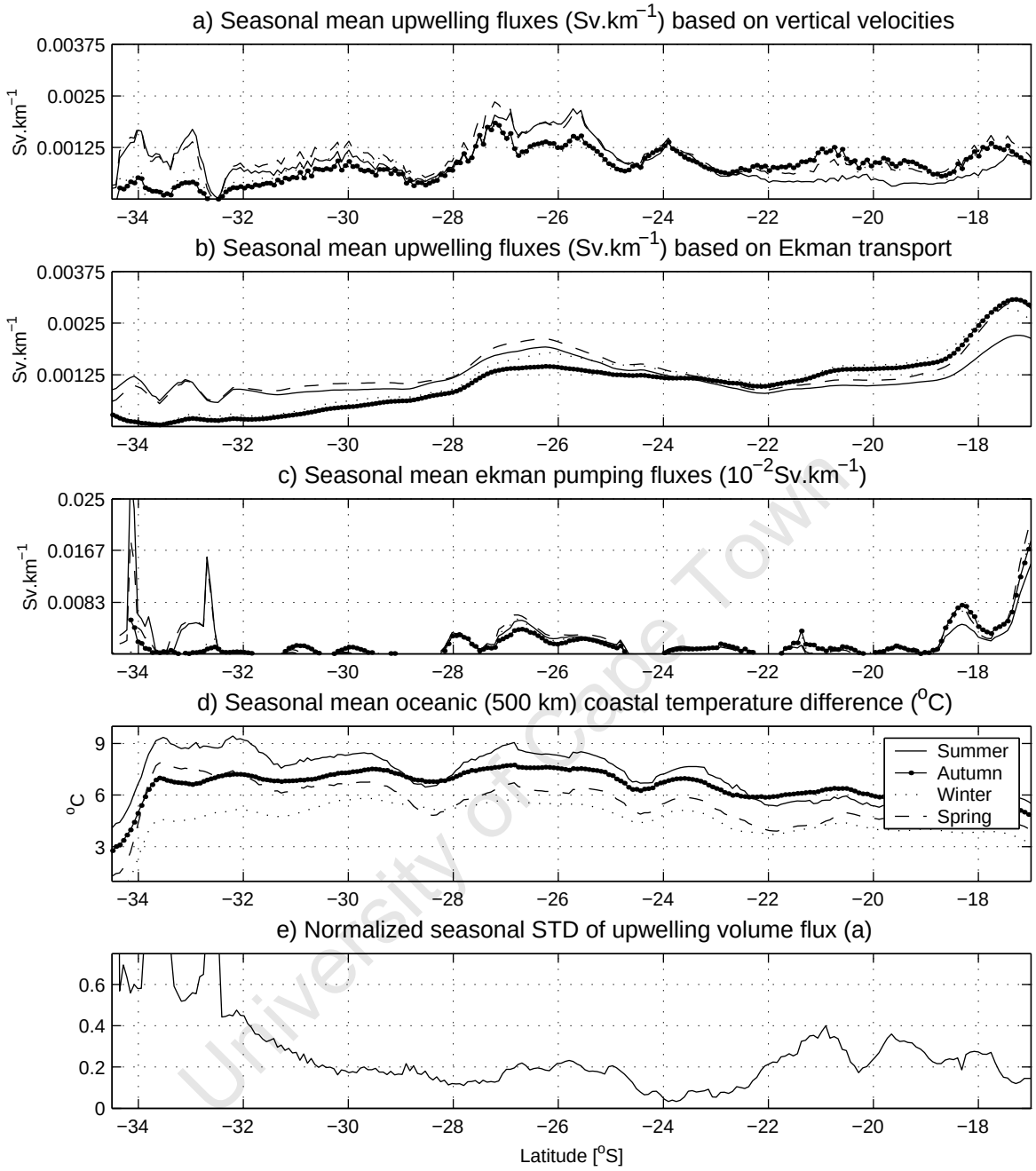

Figure 4.38: Seasonal mean upwelling fluxes (in Sv.km^{-1}) based on (a) model-derived vertical velocities and (b) alongshore wind stress via Ekman transport flux calculation and (c) wind-stress curl via Ekman pumping velocities. Note the different scales for each figure. d) upwelling index based on oceanic (500 km)/ coastal temperature difference. c) Normalized seasonal standard deviation (i.e. STD/mean), based on upwelling volume flux (a).

Table 4.3 quantifies upwelling fluxes and rates in each of the seven upwelling cells, based on model-derived vertical velocities and provides a convenient look-up

table of alongshore upwelling intensities and seasonal fluctuations. This reference is particularly useful as direct measurements of upwelling rates in the Benguela are scarce and certainly do not encompass all seasons and the whole system, inclusive of all upwelling cells.

Table 4.3: The seven upwelling cells present in the Benguela upwelling regime and their annual mean, maximum and minimum upwelling volume fluxes (in Sv) and average upwelling rates (in m.day^{-1}).

Cell	Mean flux (Sv) Mean rate (m.day^{-1})	Max flux (season) Max rate	Min flux (season) Min rate
Cunene	0.5	0.68 (spring)	0.24 (summer)
17-25^oS	7.29	9.92	3.5
Namibia	1.26	1.49 (winter)	0.75 (summer)
22.5-25^oS	6.68	7.9	3.98
Walvis Bay	0.78	0.84 (spring)	0.74 (summer)
25-22.5^oS	8.09	8.71	7.67
Luderitz	1.8	2.03 (spring)	1.67 (autumn)
28.5-25^oS	12.91	14.56	11.98
Namaqua	1.15	1.36 (spring)	0.92 (autumn)
32.5-28.5^oS	7.09	8.38	5.67
Columbine	0.26	0.36 (summer)	0.16 (autumn)
33.5-32.5^oS	6.21	8.6	3.82
Peninsula	0.06	0.12 (summer)	0.01 (winter)
34.5-33.5^oS	1.56	3.11	0.13

4.3 Topographical control

The extent to which topographical features influence the large-scale circulation and coastal upwelling regimes is investigated by re-running the Benguela reference simulation, but with a smoothed coastline and topography. The smoothing routine

focuses on straightening the coastline and shelf from ~32-21^oS, in order to simulate a Benguela system with an approximately uniform alongshore shelf profile (see Figure 4.39). The topography remains unchanged over and north of the Walvis Ridge in order to retain its influences on circulation features and not to complicate the effect of removing alongshore variations in the shelf and coastline.

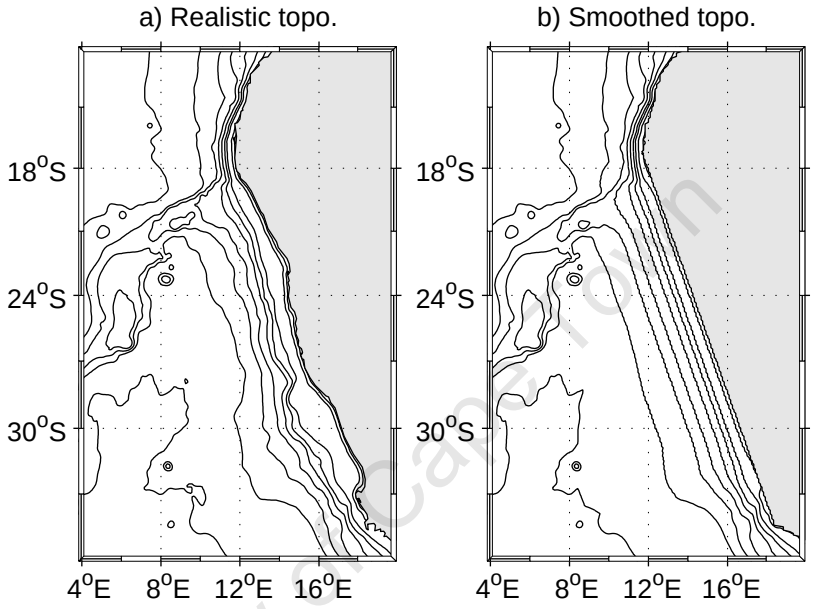

Figure 4.39: Topography of reference (a) and smoothed shelf and coastline (b) experiment

Figure 4.40a and 4.40b show the 0-1000 m integrated transport streamfunction and Sverdrup-derived (see equation (4.7)) transport streamfunction for the smoothed topography simulation respectively. Compared with the transport streamfunction for the reference experiment (Figure 4.15a), Figure 4.40a suggests that the distinct nature of the separation of the large-scale flow regimes of the northern and southern Benguela systems is, to some extent, topographically driven. The north-eastward flowing regime of the southern Benguela system (previously defined as south of ~28 ^oS) extends further north in the region ~300 km from the coast, but is qualitatively similar further offshore. While a poleward flow still features in the northern Benguela regime, it is confined to a narrower band (Figure 4.41b) due to differences in its interaction with the more intense equatorward flow (Figure 4.41a). Although

some evidence of meandering exists (due to the fact that some shelf structure still exists south of ~32 ^oS), the well-documented offshore-veering (e.g. Reid (1989); Garzoli and Gordon (1996); Richardson and Garzoli (2003)) of the inshore branch of the Benguela between ~29-31^oS, as simulated by the reference simulation (Figure 4.15a), is less distinct in the smoothed topography simulation. The Sverdrup-derived transport streamfunction for the smoothed topography experiment (Figure 4.40b), shows that the poleward flow would extend well into the southern Benguela region if forced by the wind-stress curl alone. The fact that the smooth coastline simulation prevents the distinct offshore veering of the Benguela Current between ~28-30^oS, allows it (and its associated nonlinear dynamics) to follow the shelf further northward, thus negating the presence of a poleward flow, as predicted by the Sverdrup relation.

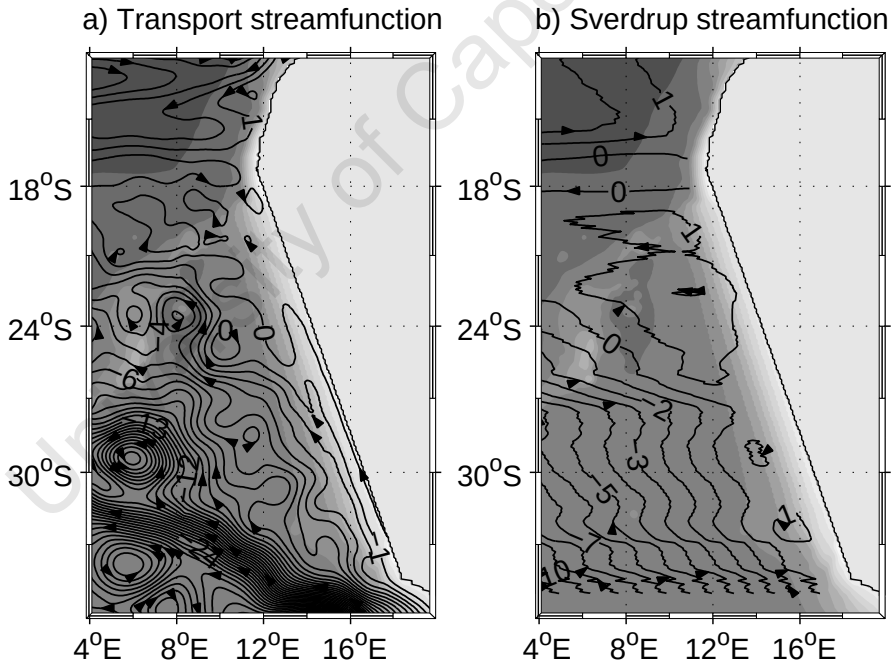

Figure 4.40: a) Transport streamfunction (0-1000 m) and b) Sverdrup-derived transport streamfunction for the smoothed topography simulation.

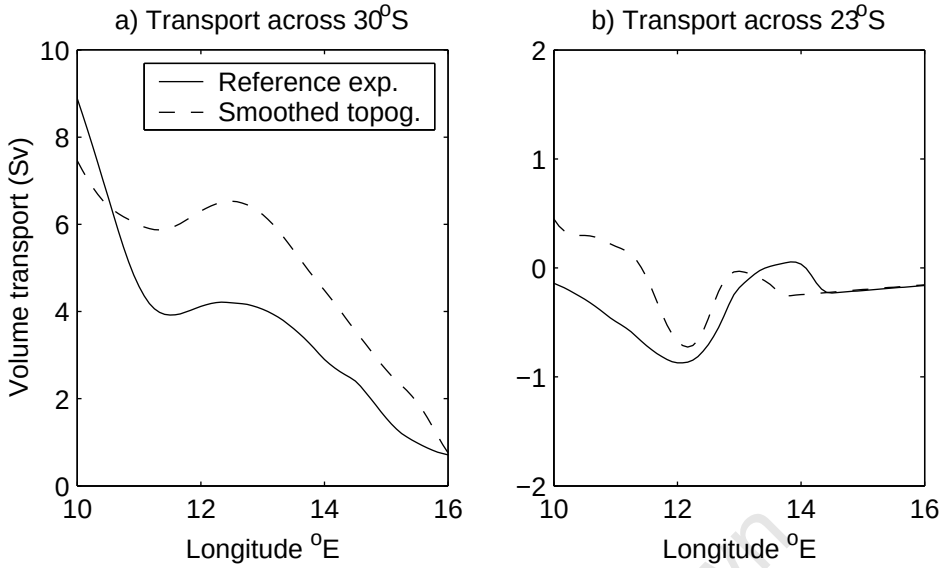

Figure 4.41: Alongshore transport across (a) 30^oS and (b) 23^oS for the reference (solid line) and smoothed topography (b) simulations.

Figure 4.15a suggests that the south-to-north transition in the Benguela system can be separated into three separate regions of cross-shelf exchange. While the southern Benguela is characterized by distinct meanders, a region of particularly intense offshore transport is situated between ~29-31^oS, which causes the Benguela Current to veer offshore. In the region between ~25-27^oS is another region of significant cross-shore transport that is responsible for the much of the offshore diversion of the poleward-flowing regime. These regions of offshore transport envelope a discontinuity of the shelf-edge as well as an anticyclonic standing meander. The solid line in Figure 4.42 shows the annual mean cross-shore volume fluxes for the reference experiment and quantifies the cross-shore transports of these three regions (negative represents offshore transport). The dashed line shows the cross-shelf fluxes for the smoothed topography experiment and reveals a similar meandering structure in the southern Benguela system, which is a product of the fact that the southern Benguela system (south of ~32^oS retains some of its alongshore shelf-structure. The peak in offshore transport at 30^oS is similar for both simulations, but the offshore transport for the reference experiment becomes evident from 31^oS, while cross-shore transport of the smoothed topography experiment is onshore between 31-30^oS. As a result, the net offshore cross-shelf transport estimates vary considerably between 31-29^oS

for the reference and smoothed topography experiments: 1.3 Sv and 0.12 Sv respectively. The anticyclonic meander at the transition region (~29-27^oS) is not present in the straight coastline simulation, in which offshore transport peaks at ~28.5^oS, with a secondary peak at ~26^oS. Cross-shore transports in the northern Benguela (north of ~25 ^oS) remain approximately the same for both simulations.

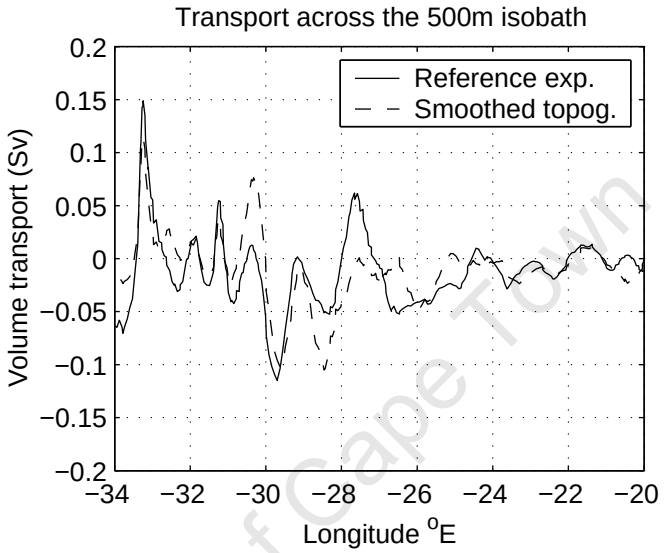

Figure 4.42: Cross-shelf transport across the 500 m isobath for a) the reference (solid line) and b) smoothed topography (dashed line) simulations between 34-20^oS.

Upwelling fluxes, based on model-derived vertical velocities for the smoothed topography simulation are shown in Figure 4.43a along with the fluxes derived in the reference experiment (dashed line and solid lines respectively). The smoothed topography and coastline experiment results in an upwelling zone that is more or less contiguous in the alongshore direction, with a slight peak in the vicinity of Lüderitz due to the stronger alongshore wind stress and wind stress curl, but in general the fluxes are lower than the peak fluxes resolved by the reference experiment. This suggests that alongshore topographical variations have an important role to play in enhancing upwelling fluxes. Indeed, numerical (Peffley and O'Brien (1976); Gan and Allen (2002a)) and laboratory (Narimousa and Maxworthy (1986)) studies have demonstrated the enhancement of upwelling downstream of topographical capes.

The semi-idealized numerical modelling study of Gan and Allen (2002a) demonstrates the ageostrophic decrease of pressure near capes due to enhanced alongshore velocities (causing an imbalance between the pressure gradient and coriolis terms and increased significance of the non-linear advection term). This results in increased negative pressure gradient downstream of capes and generates an onshore geostrophically-balanced flow on the shelf throughout the water-column, which helps to balance the offshore Ekman transport and is accompanied by positive vertical velocities over the inner-shelf. Figure 4.43b shows the orientation of the Benguela coastline in degrees (toward the west) from north of the Benguela system. The solid vertical arrows highlight the connection of peak upwelling regions with locations where the coastline veers toward the east (sudden changes in the orientation of the coastline represents the locations of prominent capes) and indeed implies an enhancement of upwelling intensity downstream (northern edge) of capes, implying that the mechanism suggested by Gan and Allen (2002a) is relevant in the Benguela upwelling system.

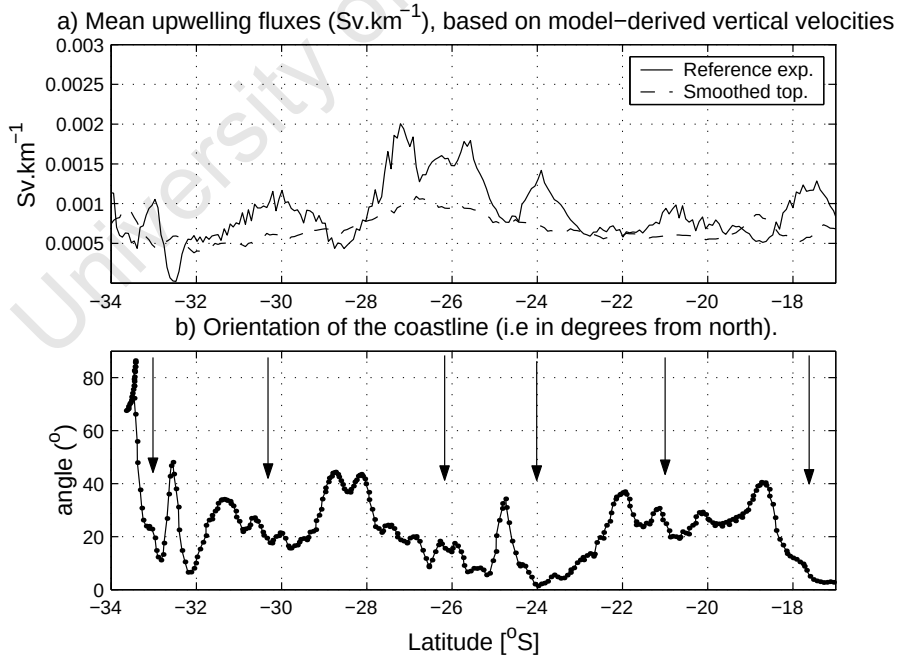

Figure 4.43: (a) Annual mean upwelling fluxes for the reference (solid line) and smoothed topography (dashed line) simulations. The grey line is the Ekman transport flux for the smoothed topography simulation. (b) Orientation of the coastline (degrees from north).

4.4 The northern and southern Benguela regimes

The different characteristics of the northern and southern Benguela regimes and the very distinct nature of their divide presents a natural laboratory and provides the opportunity for a systematic comparative study of different eastern boundary upwelling regimes within one system and within one simulation. Before separating the regimes on the basis of dynamic processes, they have distinct topographic characteristics that set the scene for oceanographic processes. The broad continental shelf of the southern Benguela narrows abruptly toward the north at ~28 ^{o}S, at which point the continental shelf remains relatively narrow and uniform (e.g. see Figure 4.2). Therefore, the southern Benguela (north of Cape Columbine) might be described as having a broad shelf, while the northern Benguela has a narrow and uniform shelf. The broader shelf in the southern Benguela harbours an area of relative queiscent, for which there is evidence in Figure 4.8 in the flat isotherms, which implies an area of low potential energy.

Depth-integrated, large-scale circulation patterns of the Benguela system give a convincing impression of separate regimes. The poleward flow of the northern regime meets the stronger, more meandering equatorward flow of the southern regime in the vicinity of Lüderitz. The weak poleward flow in the north has a distinct seasonal cycle that is controlled by the seasonal fluctuations of the cyclonic wind stress curl via the Sverdrup relation. The advection of tropical and low oxygen water characteristics by the poleward current into the northern and central Benguela can have serious implications for the health of the upwelling ecosytem. A good understanding of its dynamics is therefore essential. Transport of the Benguela Current is dominated by the non-linear advective processes asociated with the path of Agulhas rings and eddies and therefore does not adhere to the Sverdrup relation. The offshore stream of the Benguela Current tends to be more intense during spring and summer when the wind stress is stronger.

By virtue of its highest upwelling fluxes year-round (see Table 4.3), the Lüderitz upwelling cell has long been considered the division between the northern and southern Benguela upwelling regimes. However, our model results suggest that it is the different seasonal phasing of the northern and southern upwelling regions that de-

fine them as separate regimes. Greatest seasonal variability in upwelling intensities occur south of Lüderitz and particularly in the far south, with greatest fluxes during summer. While the Lüderitz and Walvis Bay upwelling cells are the most perennial, they also experience peak upwelling during summer months. North of Walvis Bay, the seasonal upwelling signal increases somewhat, mostly as a result of the much lower summer upwelling fluxes as upwelling rates are relatively constant during the rest of the year (with a slight peak in winter and spring for the Namibia and Cunene cells respectively). Another distinct difference between the northern and southern Benguela upwelling regimes is that the northern Benguela regime experiences the inhibition of coastal upwelling by the convergence of geostrophic currents at the coast.

During active upwelling, the upwelling front in the southern Benguela is topographically controlled, such that it follows the run of the shelf-edge. This feature is related to the topographical control of the inshore stream of the Benguela Current that advects warmer water of Agulhas origin into the southern Benguela system. Such a topographical control of the upwelling front in the northern Benguela does not exist.

While research of the Benguela upwelling system goes far back, the model simulation on which this work is based, provides the first opportunity to study salient features of the system in a spatially and temporally cohesive manner at a high enough resolution to capture nearshore dynamics. It has allowed us to characterise features definitive of the northern and southern regimes and to investigate the extent to which they can be regarded distinctly separate systems. The northern and southern regions of the Benguela provide an opportunity to compare two separate regimes within one system and within one simulation.

4.5 Synthesis and discussion

Equilibrium dynamics of the greater Benguela system has been addressed with the use of a ROMS climatologically-forced numerical model. The spatially and temporally cohesive output of a model simulation allows us to investigate, in a unified

manner, the system in its entirety; that is, the large-scale offshore circulation features as well as the full alongshore extent of the coastal upwelling regime. This is the first time that such an approach, at a sufficiently high resolution to capture upwelling-scale dynamics, has been applied to the Benguela Current system.

Research of the Benguela system, and eastern boundary upwelling systems in general, often tends to focus on the ecologically and economically important coastal upwelling regimes. However, the large-scale circulation regime plays a critical role via interactions with shelf dynamics and water property modifications of upwelled and shelf waters. The Benguela is unique among the worlds four main eastern boundary upwelling systems in that its northern and southern boundaries are characterized by highly dynamic warm water regimes of tropical ocean origin. Variability and fluxes across these boundaries can have significant ecological implications for the Benguela upwelling system. For example, Monteiro and van der Plas (2006)show that coastal hypoxia in the central Benguela is predominantly driven by advected oxygen fluxes from source waters in the Angola Dome region north of the ABFZ and intensifies during late austral summer when the shelf poleward flow strengthens. The ROMS simulation resolves this poleward flow, as well as its seasonal cycle, and provides insight into its fate as it travels southward. The wind stress curl (via the Sverdrup relation) has been shown to be the driving force of the poleward flow, which is strongest during spring and summer when the wind stress curl is most negative. As it flows southward it deepens and between ~25-27^oS much of it veers offshore due to the nature of the wind stress curl interacting with the northwestward path of the Benguela Current, which is influenced by alongshore topographical variations. Boundary conditions of the Benguela upwelling system, south of ~30^oS are commensurate with the path of Agulhas rings and eddies that, in the mean state, are represented by the meandering nature of the Benguela Current. Further inshore, the time-mean Benguela Current tends to be topographically controlled as it follows the run of the shelf-edge. Neither the inshore, topographically controlled, nor the meandering offshore streams of the Benguela Current exhibit a distinct seasonal signal (however, a slight seasonal signal of the offshore stream is associated with the strengthening of the wind stress curl in the southern Benguela region

during spring and summer). Agulhas rings and eddies advected into the southern Benguela system have been observed to interact with the upwelling front, causing nutrient-rich, upwelled water to advect far offshore (e.g. Lutjeharms and Stockton (1987); Duncombe-Rae et al. (1992a,b)). The effect of Agulhas Current input on the Benguela upwelling system will be addressed in the next Chapter.

The model distinctly resolves all seven of the major upwelling cells that have been observed in its domain namely, from the south: the Cape Peninsula, Cape Columbine, Namaqua, Lüderitz, Walvis Bay, Namibia and Cunene (or, Cape Frio). The three southernmost cells have the most seasonal variability, experiencing greatest upwelling during spring and summer months and least upwelling during autumn and winter, resulting in total upwelling fluxes of 4.8 Sv and 1 Sv respectively. Based on model-derived vertical velocities, average upwelling rates in the southern Benguela during periods of most active upwelling is of the order of $7m.day^{-1}$. By calculating the apparent uplift of isanosteres (lines of constant thermosteric anomaly) obtained from two cruises during active upwelling in the southern Benguela, Andrews and Hutchings (1980) estimated an average apparent uplift of $21m.day^{-1}$. Their estimate is significantly higher than the model-derived upwelling rates, but their method is subject to an inherent inaccuracy based on the fact that some of the uplift must be related to mixing processes. Furthermore, the model-derived peak upwelling season is subject to a climatological forcing, which underestimates highest and lowest alongshore wind stresses. Peak upwelling occurs throughout the year at the Lüderitz upwelling cell, where there is very little seasonal variability. The annual mean upwelling rate in this region is ~13 $m.day^{-1}$, which transpires into an average flux of 1.8 Sv. While the Walvis Bay cell is less active than Lüderitz cell (i.e ~8 $m.day^{-1}$, 0.8 Sv) it similarly experiences year-round upwelling. The two northernmost upwelling cells are subject to highest upwelling rates from autumn through spring (~$9m.day^{-1}$ and 2.2 Sv) and lowest in summer. The topographical effect on upwelling in the Benguela has been investigated by smoothing the shelf and coastline in the alongshore direction. This has allowed us to show that alongshore variations in the coastline and topography has the important effect of enhancing upwelling in the vicinity of capes. A significant finding is the fact that upwelling in the northern

Benguela (north of ~23°N) is inhibited by the convergence of geostrophic flow at the coast.

Based on its large, year-round upwelling rates as well as the fact that it is situated in the region of intense large-scale offshore transport, the Lüderitz upwelling cell effectively divides the Benguela upwelling system into northern and southern sections (Shannon and Nelson (1996)). The regions to the north and south of this may be thought of as different regimes in the sense that their seasonal signals differ: upwelling is most active during spring and summer in the south, while upwelling is least active during summer in the north. Boundary conditions at the alongshore extremities of the Benguela system influence upwelling regimes via the northern and southern large-scale flow regimes that are distinctly separable. While the poleward-flowing regime of the northern Benguela is tied to the strength of the wind stress curl and is strongly seasonal, the meandering equatorward path of the Benguela Current in the southern Benguela and is controlled by non-linear advection processes associated with the path of Agulhas rings and eddies. Veitch et al. (2009) take advantage of this numerical model simulation in order to identify key features separating the Benguela system into distinct northern and southern regimes.

This work has, for the first time, used a model simulation at a high enough resolution to capture the near-shore dynamics of the entire Benguela upwelling regime from the Cape of Goodhope to beyond the ABFZ. This has allowed a characterization of the salient dynamical features of the Benguela system and a distinct separation of features definitive of the northern and southern regimes. The poleward flow in the northern Benguela has been conclusively linked to the Sverdrup relation and a double-stream flow characteristic of the Benguela has been resolved in the southern Benguela. The importance of alongshore topographical variations in locally enhancing upwelling has been highlighted, suggesting that an upwelling index based on Ekman transport fluxes may underestimate actual upwelling rates. The discontinuity of the shelf-edge at ~28°S has been shown to enhance the offshore transport and therefore, the separation between the poleward and equatorward regimes in the north and south respectively.

The region of turbulent inter-ocean exchange offshore of the southern Benguela

upwelling regime has received a lot of attention (e.g Boebel et al. (2003)). Its importance lies in its role in the successful transport of Agulhas rings into the Atlantic Ocean that make an important contribution to the thermohaline circulation (Gordon (2003)). The interaction of the highly dynamic offshore environment and the upwelling regime has received less attention, other than occasional observations suggesting the interaction between Agulhas rings and characteristics of the upwelling front (e.g. Duncombe-Rae et al. (1992b)). In the next Chapter, the influence of mesoscale features originating from the Agulhas Current on the Benguela system, with a focus on cross-shelf fluxes and the impact on the upwelling regime will be systematically investigated. The role of eddies (both locally formed and those advected into the area) in transporting heat will be addressed and the formation of the former will be investigated in terms of baroclinic and barotropic instability processes.

Chapter 5

Mesoscale variability and the role of eddies in the Benguela system

As one of the worlds four major eastern boundary current systems (EBCS), the Benguela is unique in that it is influenced by tropical ocean waters at both its equatorward and poleward boundaries. While the Peru Current system is also strongly affected (if not more so) by equatorial dynamics (Penven et al. (2005)), the Benguela is the only system that is subject to the influence of tropical ocean waters at its poleward extreme. The so-called 'Cape Cauldron' (Boebel et al. (2003)) lies within the Cape Basin in the southern Benguela system and describes the region associated with the passage of Agulhas rings and eddies on their path from the Agulhas retroflection, situated south of the African continent and into the Atlantic Ocean. As a consequence of the advection of rings and eddies and the high eddy kinetic energy (EKE) signals associated with them, the Benguela has a mesoscale variability pattern unlike any of the other three major EBCSs. The review chapter by Capet et al. (2008) on eddies in EBCS provides an excellent impression of the present state of our understanding of the role of eddies in EBCSs and also points out the unusual nature of the Benguela Current system.

The importance of rings and eddies spawned at the Agulhas retroflection lies in their role in the Indian-Atlantic ocean exchange of heat and salt and thus is also thought to have a key role in the maintenance of the global overturning of the ocean (Gordon et al. (1992); Lutjeharms (1996)). Within this framework, much attention

has been given to the passage of Agulhas rings and eddies on their trajectory through (and beyond) the Benguela system (e.g. Byrne et al. (1995); Garzoli et al. (1996); de Ruijter et al. (1999); Schouten et al. (2000); Gordon (2003); Matano and Beier (2003); Treguier et al. (2003); Biastoch et al. (2008)). Much less work has been done on the effect of the turbulent offshore regime generated by the passage of Agulhas rings and eddies on the eastern boundary upwelling system itself. Research has been limited to observations of the interaction of individual Agulhas rings with the Benguela upwelling system, resulting in the formation of extreme frontal filaments (Lutjeharms et al. (1991); Duncombe-Rae et al. (1992b)) and the associated biomass losses (Duncombe-Rae et al. (1992a)), which can have detrimental consequences for the well-being of the highly-productive ecosystem. What is perhaps even more damaging to productivity in the Benguela ecosystem than the occasional interaction of an Agulhas ring with the upwelling front, is the region of high mesoscale variability that is generated by the Agulhas rings and eddies on their preferential path into the south Atlantic ocean. Gruber et al. (2007) have shown that, contrary to what has been found for open-ocean regions, mesoscale and submesoscale eddies in coastal upwelling regions tend to reduce biological productivity by bringing nutrient depleted waters closer to shore. Using FSLE (Finite Size Lyapunov Exponent) analysis Rossi et al. (2008) quantified the inverse relationship of lateral mixing and chlorophyll suggested by the work of Gruber et al. (2007).

In this chapter we investigate the mesoscale features of the greater Benguela system (i.e. both the large-scale current regime as well as the nearshore upwelling regime), with the influence of the Agulhas leakage on the Benguela system as our main objective. Despite the fact that we use climatological forcing and therefore only capture seasonal and intrinsically-forced variability within the system, we resolve most of the features that have been observed. Figure 5.1 is a 2-daily averaged snapshot of sea surface temperature (SST) and is an example of the success of the model at resolving finer-scale features, such as the extreme filaments in the vicinity of Lüderitz as well as Agulhas filaments entering from the south. The climatological nature of our model output allows us to get an impression of the mean effect of the intense offshore variability on the Benguela system, rather than to focus on

individual extreme events. A climatological simulation also gives us the opportunity to investigate how much of the variability in the system is intrinsically forced, rather than being dependant on time-varying winds.

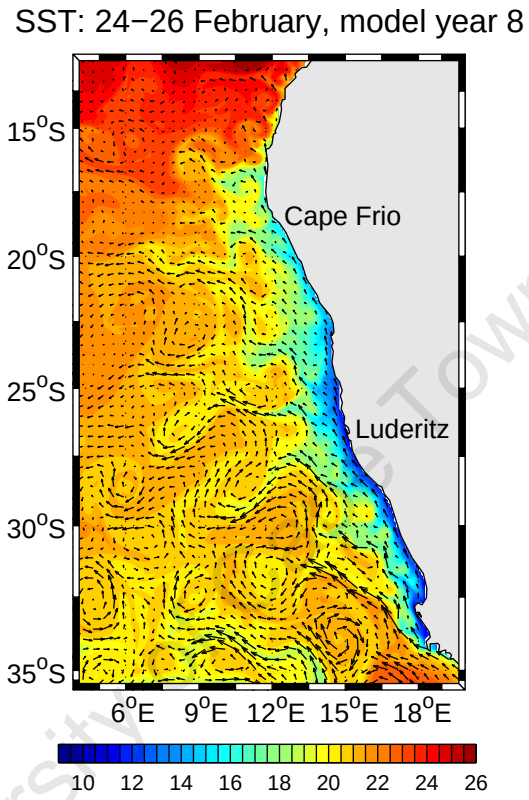

Figure 5.1: Snapshot of model sea surface temperatures for 24-26 February, model year 6. Arrows indicate surface currents.

5.1 Eddy kinetic energy (EKE)

Mesoscale variability can be inferred from measures of eddy kinetic energy (EKE), which can be obtained easily from satellite altimetry sources for surface geostrophic currents. Maps of global surface geostrophic EKE (Ducet et al. (2000)) reveal a distinct juxtaposition between the very high EKEs associated with western boundary currents and the very low EKEs linked to eastern boundary current systems (EBCS). The Benguela Current system is unique in that the pathway for Agulhas rings and eddies spawned at the Agulhas retroflection area south of the African continent is

situated within the southern part of the system, resulting in an unusually high-energy offshore environment for an EBCS. Eddy kinetic energy is calculated as follows:

$$EKE = \frac{u'^2 + v'^2}{2} \tag{5.1}$$

where the transient/eddy velocities (u' and v') are calculated as (in a generic formula, where ϕ represents any variable):

$$\phi' = \phi - \overline{\phi} \tag{5.2}$$

where $\overline{\phi}$ is the time-mean, which can be a long-term mean for calculating the total EKE or a monthly mean for calculating the non-seasonal EKE (i.e. removing the seasonal signal). The difference between the two is a reflection of the seasonal signal. The following section provides a characterization of the EKE structure of the Benguela Current system.

5.1.1 Surface patterns

Figure 5.2 compares time-mean satellite and model surface geostrophic EKE, which are identically calculated using equation (5.1), with surface geostrophic velocities as derived from sea surface heights (SSH) using equations (4.3) and (4.4) in Chapter 4. The satellite data is the weekly 0.33°AVISO mean absolute dynamic topography product, spanning 2000-2007 and the model data has been degraded (in space and time) in order to better approximate it. Figures 5.2a and 5.2b reveal a similar pattern of lowest EKEs at the coast and over the shelf and the extremely high EKEs offshore in the southern Benguela system that we expect due to the path of Agulhas rings and eddies. The log-scale required for capturing the contrasting regimes of very low energy on the shelf and extremely high energy offshore in Figures 5.2a and 5.2b is testament to the unusual mesoscale structure of the Benguela as compared to other EBCSs. For example, the California system typically has nearshore variability, measured in terms of EKE, of the order of 40 $cm^2.s^{-2}$, increasing to ~120 $cm^2.s^{-2}$ further offshore (e.g. Strub et al. (1998); Marchesiello et al. (2003)). Though distinct

differences do exist, the range of EKEs in the Canary and Peru systems are of the order of that in the California system (refer to Figure 2 in Capet et al. (2008)). In striking contrast, the inshore and offshore variability of the Benguela ranges from ~10 $cm^2.s^{-2}$ to in excess of 500 $cm^2.s^{-2}$ respectively. Enhanced EKEs (~40 $cm^2.s^{-2}$), associated with the Angola Benguela Frontal Zone (ABFZ) are present in both model and satellite EKEs, between ~14-16 ^oS within approximately 300 km of the coast. This is consistent with the offshore extent (~250 km) of the surface manifestation of the ABFZ as observed by Meeuwis and Lutjeharms (1990).

While the general pattern of model-derived surface geostrophic EKE agrees well with satellite observations, differences in magnitude exist; most generally, the model everywhere produces higher EKEs than observed by satellite. Figure 5.2c shows how much greater the model-derived surface EKEs are than satellite, represented as a percentage. Greatest differences occur within ~200 km of the shelf-edge throughout the system to about 20°S as well as in the central offshore region. These more significant biases are related to the fact that the model overestimates the amount of Agulhas leakage into the Benguela system and was discussed in section 4.1.2 of Chapter 4. It might seem counter-intuitive that the models overestimation of EKE is most extreme alongside the shelf-edge rather than in the turbulent region assocated with the path of Agulhas rings and eddies that has come to be known as the 'Cape Cauldron' (Boebel et al. (2003)). This could be related to the fact that the warm offshore bias causes an enhanced horizontal gradient between the density structure on the shelf and offshore, culminating in increased local instabilities in the vicinity of the shelf-edge. While the offshore region of the southern Benguela has highest EKEs (for both satellite and model), the model overestimation is less as there is less potential for locally produced EKEs, based on enhanced horizontal density gradients. The relatively high bias in the offshore central/northern region (i.e. between ~25-17.5°S) is, once again, likely to be related to the overestimation of Agulhas Current influence. Highest offshore gradients of EKE tend to coincide with the shelf-edge (shown as a bold contour): in the southern Benguela for satellite EKEs and from ~32°S northward for model EKEs. This suggests that the shelf forms a barrier to the high EKEs introduced by Agulhas influx (i.e. rings, eddies and Indian Ocean water mass charac-

teristics) into the offshore regions. However, the very steep gradient at the shelf-edge alludes to a potentially efficient means of the offshore flux of nearshore, nutrient-rich upwelled water. The model exhibits high EKEs on the shelf in the far south between ~32-34 °S where the satellite-observed data does not. This is perhaps related to instabilities associated with the Goodhope Jet (see Barth (1989)) which, according to Strub et al. (1998) is driven by inshore-offshore steric height differences. In the model simulation, the inshore-offshore steric height gradients are enhanced due to the overestimation of Agulhas leakage leading to greater potential to instabilities. However, the apparently enhanced model EKE in this area could also be ascribed to the fact that the satellite is not capable of capturing nearshore features (refer to http://www.aviso.oceanobs.com/no_cache/en/applications/coastal-applications).

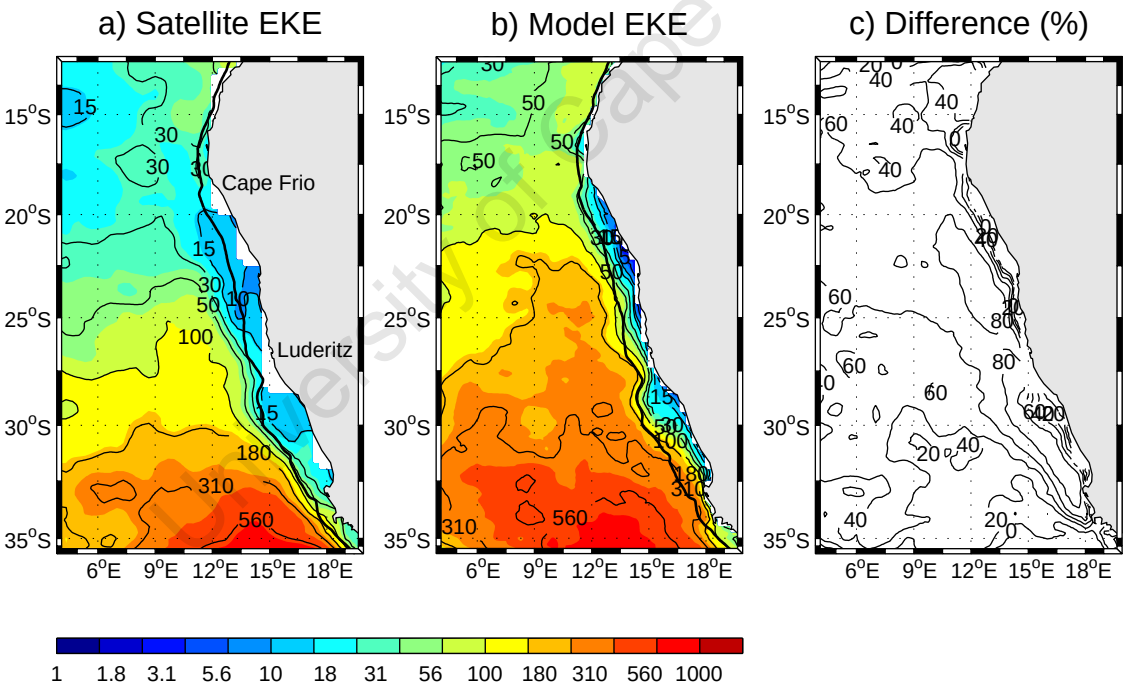

Figure 5.2: Satellite (a) and model-derived (b) surface geostrophic eke and (c) the percentage difference between the two. The bold black line represents the position of the shelf-edge (approximated as the location of the 500 m isobath).

Figure 5.3 separates the total geostrophic EKE into seasonal and non-seasonal components for both model and satellite-derived surface EKEs. Seasonal EKE corrects the total EKE signal for the seasonal cycle and therefore should be thought of as merely a reflection of the seasonal signal of currents. Both model and satellite

outputs reveal, unequivocally, that most of the total EKE is a result of non-seasonal variability, even though the model is forced with climatological winds and the satellite EKEs are a reflection of variability based on time-varying winds. This suggests that the majority of variability in the Benguela system is intrinsically forced and does not depend on time-varying wind. The seasonal forcing of the model does however produce higher seasonal EKEs (i.e. seasonal signal of currents) than observed, particularly in offshore regions subject to Agulhas Current influence and in the ABFZ region, which is likely a consequence of the fact that the model is forced by a climatology wind field and is therefore likely to produce a more distinctive seasonal signal of variability. Regions of peak total EKEs outside of the coastal upwelling domain (i.e. the Cape Cauldron and ABFZ regions) are also subject to peak seasonal EKEs. However, the seasonal EKEs in these areas are only of the order of 10% of the total EKE signal shown in Figure 5.2 (with the difference in satellite seasonal and total EKE being slightly lower). The percentage of total EKE at the coast contributed by the seasonal signal (figure not shown) is significant, exceeding 50 % with even greater values in regions of more perennial upwelling (i.e. the central and northern Benguela). The poor coastal resolution of satellite EKEs provides only some evidence of higher coastal seasonal EKEs in this active region (Figure 5.3a).

Model-derived SSHs and u- and v-velocity fields allow us to separate total EKE into geostrophic and ageostrophic parts. The total EKE is calculated from the surface u- and v-velocity components and the ageostrophic EKE is calculated from the difference between the total and geostrophic u- and v-velocity components. The separation of total EKE into its geostrophic and ageostrophic components is shown in Figure 5.4 and reveals that most surface EKE is a result of geostrophic motion. Satellite-derived geostrophic EKE therefore provides a good approximation of the total EKE in the Benguela system. Highest ageostrophic EKEs are located at the northern and southern boundaries of the Benguela system and while they could be associated with non-linearities introduced by the interaction of the highly dynamic regimes definitive of these boundaries, they could also be linked to spurious features at the parent-child boundaries.

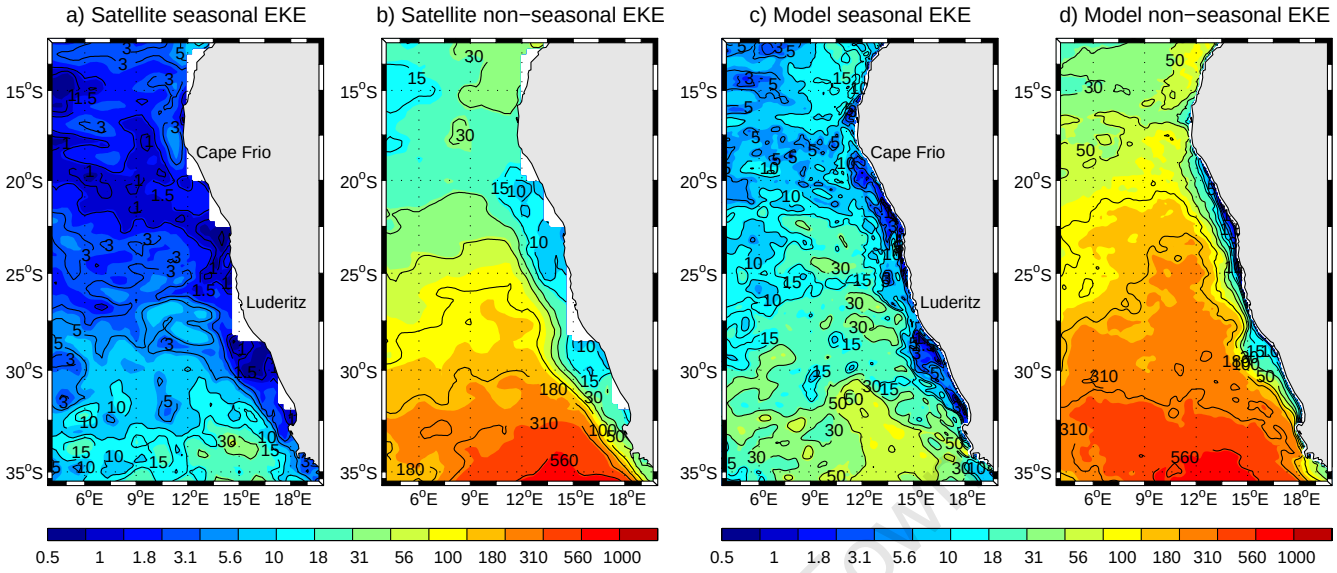

Figure 5.3: Seasonal (a,c) and non-seasonal (b,d) geostrophic surface eke (in $cm^2.s^{-2}$), based on satellite (a,b) and model (c,d) data.

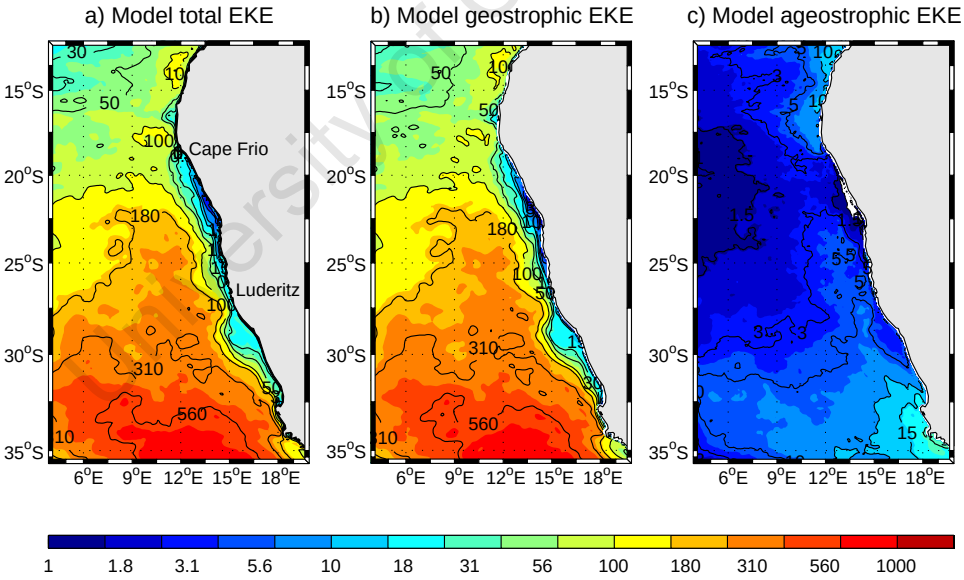

Figure 5.4: Combined seasonal and non-seasonal contributions of total (a), geostrophic (b) and ageostrophic (c: total - geostrophic) surface eddy kinetic energy (in $cm^2.s^{-2}$).

5.1.2 Propagation

Offshore

As a first approach at comparing the satellite observed and model-derived seasonal cycle of mesoscale activity and EKE generation, the Hovmöller plots in Figures 5.5 (left) and 5.5 (right) compare the monthly mean surface geostrophic EKEs at 32^{o}S as derived from satellite and model data. While the model-derived EKEs are higher than satellite observed EKEs, for reasons previously mentioned, both have a clear offshore propagating signal. However, this offshore propagating signal is only apparent seaward of the approximate position of the shelf-edge (indicated by a dashed white line) for this section which is representative of the southern Benguela. The fact that the offshore propagating speeds are approximately equivalent in both satellite and model-derived surface EKEs is evident in the similarity of the gradient of the phase lines shown in Figures 5.5 (left) and 5.5 (right). In order to quantify offshore propagation speeds, the lag time which coincides with the maximum significant correlation coefficient between sequential time-series' from the coast seaward was calculated. Model and satellite results compared favourably and revealed an offshore propagation speed of ~3.75 cm.s^{-1} seaward of ~16.3^{o}E. This is of the order of the offshore propagation speeds calculated by Kelly et al. (1998) from satellite data for the EKE field associated with the California upwelling system. Strub and James (2000) surmised that because the offshore propagating EKE speeds correspond to Rossby wave speeds, they were the prime reason for offshore propagation in the California Current system. The west-northwestward passage of anticyclonic Agulhas rings dominates the offshore dynamics of the southern Benguela region and accounts of the translation speed have been varied, ranging from 6 cm.s^{-1} to 17 cm.s^{-1}(Byrne et al. (1995); Doglioli et al. (2007)). In our propagation calculations, we take into account only a due west propagation direction. If we rotate our propagation speed so that it has a northwesterly direction, we obtain speeds of ~7 cm.s^{-1}, which is within the range of Agulhas Ring translation. At this latitude the Rossby wave propagation speed is ~3 cm.s^{-1} (Chelton and Schlax (1996)), which is too low to account for the propagation speeds revealed in Figure 5.5.

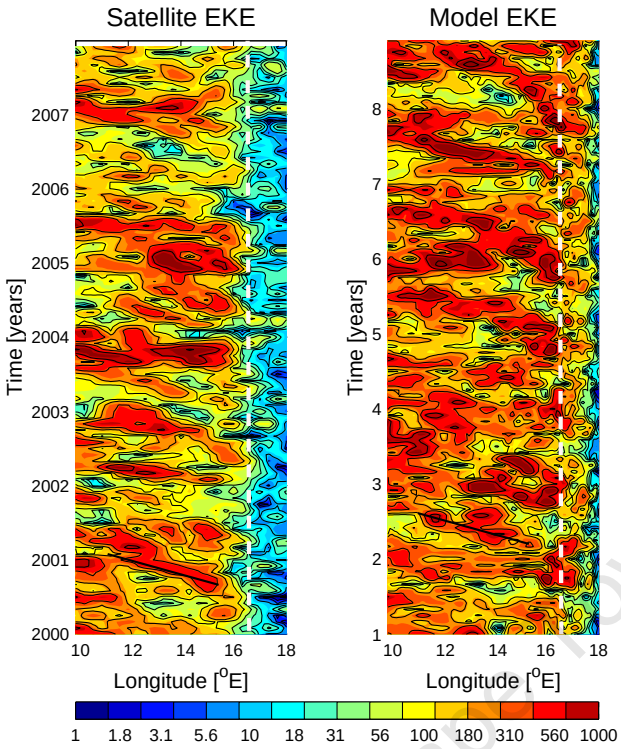

Figure 5.5: Time-longitude plot of monthly mean satellite (left) and model-derived (right) surface geostrophic, non-seasonal EKE at 32°S. Units in $cm^2.s^{-1}$.

The satellite observations of Kelly et al. (1998) and Strub and James (2000) link the generation of EKE with the equatorward upwelling jet, which was further investigated and revealed as baroclinic instability processes of the upwelling jet in the modelling study of Marchesiello et al. (2003). As a first order look into the connection of EKE and equatorward jets in the southern Benguela system, Figure 5.6 (left) and 5.6 (right) show the monthly mean geostrophic meridional velocities for satellite and model-derived data, plotted against longitude. Again, a westward propagating signal is obvious, but only from approximately the position of the shelf-edge and is calculated as ~3.75 $cm.s^{-1}$ (or, ~7 $cm.s^{-1}$in a northwesterly direction), based on both satellite and model-derived velocities. Both the coastal upwelling jet as well as the shelf-edge jet are resolved by the model and can be seen in Figure 5.6 (right) as being northward throughout the year, while the satellite only properly resolves the latter due to poor coastal resolution. The extent to which either of these jets are responsible for the generation of EKE will be investigated further by looking at the correlation between EKE and meridional velocity time-series' extracted from

the approximate position of the core of both the coastal and shelf-edge jets (from model data only for the former and from both data sources for the latter).

While the model-derived data in Figure 5.6 (right) suggests a clear seasonal signal of the coastal jet, only vestiges of this signal exists in satellite-derived geostrophic velocities in Figure 5.5c due to the poor resolution of satellite data in an approximately 50 km coastal band. To elucidate the signal of the coastal upwelling jet as resolved by the model, Figure 5.7 shows a time-series, extracted from the core region of the coastal upwelling jet (at ~17.8 °E), for both the geostrophic meridional velocity component as well as for non-seasonal EKE. The fact that equatorward velocities fluctuate in phase with EKEs at the coast is obvious from a mere visual analysis of this plot, with peaks tending to occur during the beginning and end of the year (i.e. during spring and summer when upwelling is most intense in the southern Benguela). The cross-correlation of the two time-series' gives a significant correlation coefficient of 0.43 (with the 95% confidence level at 0.21), which confirms the in-phase seasonality of the upwelling jet and the generation of EKE, thus providing evidence for a connection between the two.

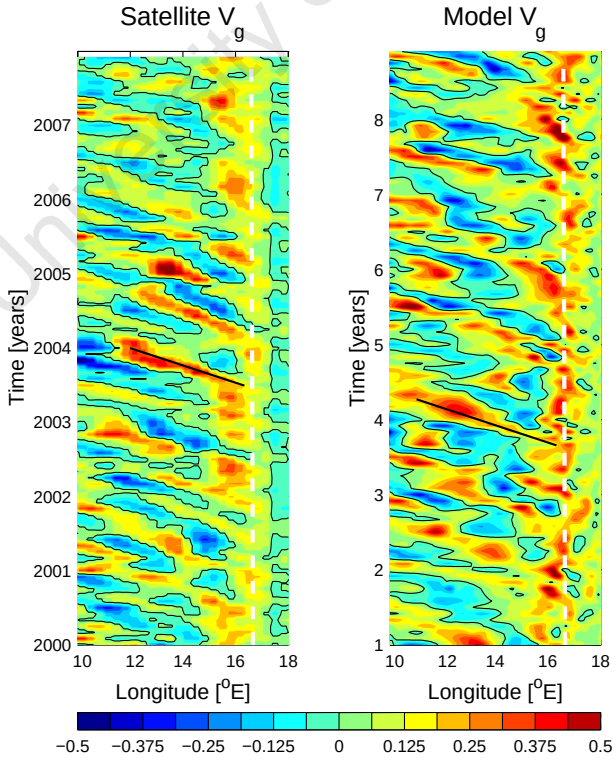

Figure 5.6: Time-longitude plot of monthly mean satellite (left) and model-derived (right) surface geostrophic meridional velocity (V_g) at 32°S.

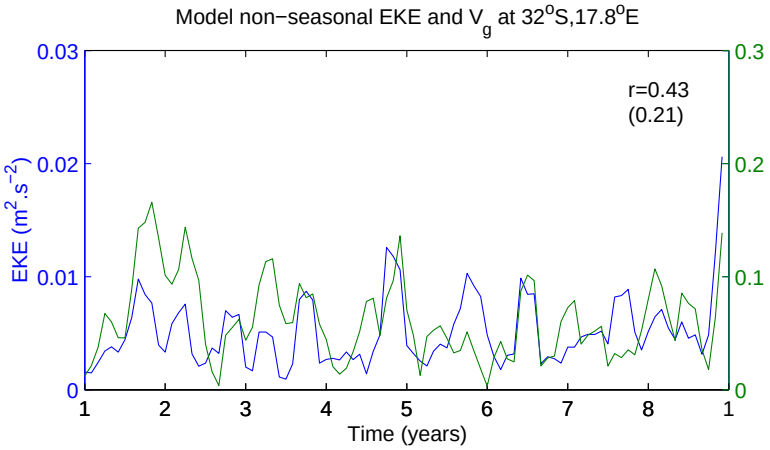

Figure 5.7: Time-series of monthly mean, non-seasonal EKE (blue) and meridional velocity (green) at 32°S, 17.8°E.

It is less simple to establish whether a distinct signal or pattern of the shelf-edge jet exists from Figures 5.5 and 5.6 alone. While the coastal jet is directly forced by isopycnal displacements of the seasonal upwelling cycle, the intensification of the shelf-edge jet forced by coastal and offshore steric height differences (Strub et al. (1998)), the former connected with the cycle of coastal upwelling and the latter with the more unpredictable passing of Agulhas rings and eddies (Lutjeharms (2006)). Figures 5.8a and 5.8b are time-series' of meridional geostrophic velocity and EKE extracted from the approximate location of the core of the shelf-edge jet, based on satellite and model data respectively and show that that they do not appear to fluctuate in-phase with one another. A cross-correlation analysis confirms that there is no correlation between variability of the shelf-edge jet and the generation of EKE. This suggests that EKE at the shelf-edge is not solely produced by instabilities of the shelf-edge jet and is likely to originate from a non-local source.

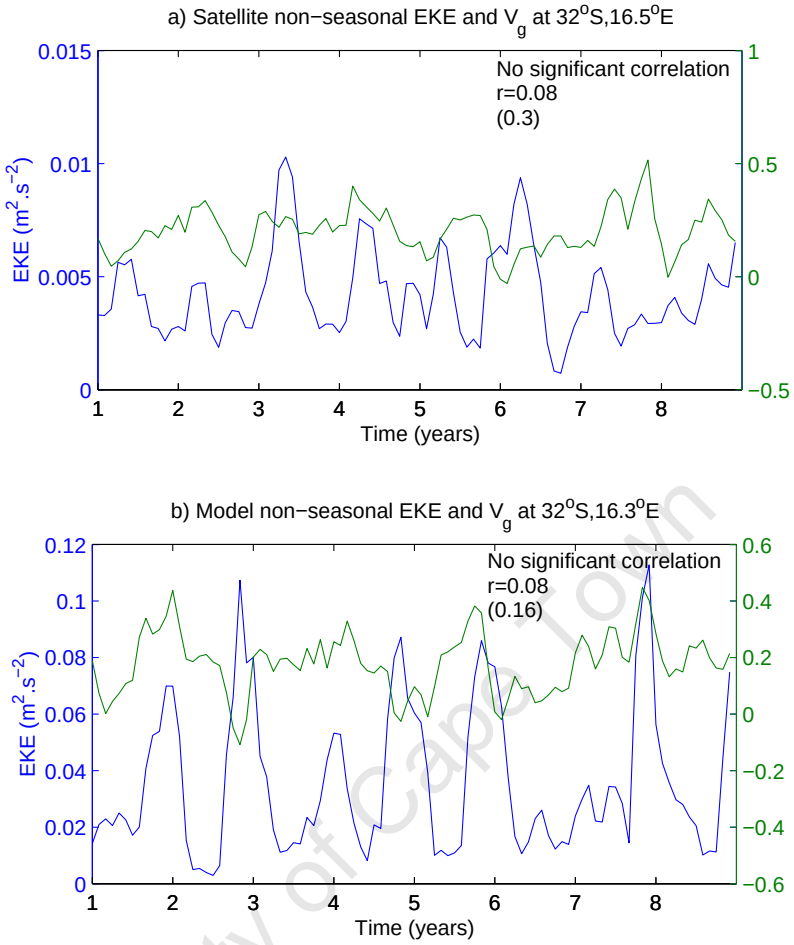

Figure 5.8: Time-series of monthly mean, non-seasonal EKE (blue) and meridional velocity (green) at 32°S, 16.3°E, based on satellite (a) and model (b) data.

The 32°S section was chosen to be representative of EKE patterns of the southern Benguela region, which is strongly controlled by the passage of Agulhas rings and eddies. There appears to be a distinct connection between the coastal upwelling jet and the generation of EKE, while the origin of EKE at the shelf-edge is probably influenced by the advection of non-local sources. Offshore propagation of the EKE signal only occurs from the position of the shelf-edge, suggesting either an alongshore propagation on the shelf or a dissipation process on the shelf. Figure 5.2 clearly shows the distinct differences in cross-shore EKE structure in the northern and southern regions of the Benguela system. In order to scrutinise the differences more closely, Hoffmöller plots of non-seasonal EKE and meridional geostrophic velocities are shown in Figure 5.9 and Figure 5.10 for a zonal section at 16.5°S, which is chosen

to be representative of the northern Benguela (note that the scale of colourbar for the meridional velocity component is different to Figure 5.6).

The most striking difference between satellite and model-derived EKEs, shown in Figures 5.9 (left) and 5.9 (right), is that the model produces more variability than is derived from satellite observations. The enhanced offshore EKEs in the model output originate from the ABFZ region, where the model resolves greater variability than is resolved by satellite observations. An animation of surface EKEs (see animation on supplementary CD) shows the southward and offshore (from ~16°S) advection of the high EKE signal originating from the ABFZ. EKE is also generated at the coast, which can be seen particularly well in Figure 5.9 (right) (the satellite data does not resolve near-shore features) where a distinct seasonal signal can be discerned. We surmise that this signal is associated with the upwelling-induced coastal jet, which can be seen in the Hoffmöller plot of geostrophic meridional velocities (Figure 5.10 (right)), based on model-derived data. To clarify the connection, Figure 5.11 shows a timeseries of both EKE and geostrophic meridional velocity (an indicator for the intensity of the upwelling jet), extracted from a nearshore location (we show only results from model output as the satellite does not resolve the nearshore region). The fact that they fluctuate in phase with one another is unequivocal and is substantiated by a correlation coefficient of 0.88 (with the 95% confidence level at 0.8). In order to test the effect of the poleward flow on EKE, we extract time-series' further offshore (~10°E) within the domain of the seasonally pulsing poleward flow (see Chapter 4) for both model- and satellite-based output (Figures 5.12a and 5.12b respectively). Both satellite and model results reveal a significant correlation and show that the EKE decreases (increases) when the poleward (equatorward) flow is most intense. The offshore propagation rates of the high EKE signals in the nearshore region are of the order of 3.5 $cm.s^{-1}$, which is consistent with offshore propagating Rossby wave speeds at this latitude (~3.5-3.75 $cm.s^{-1}$ according to Chelton and Schlax (1996)).

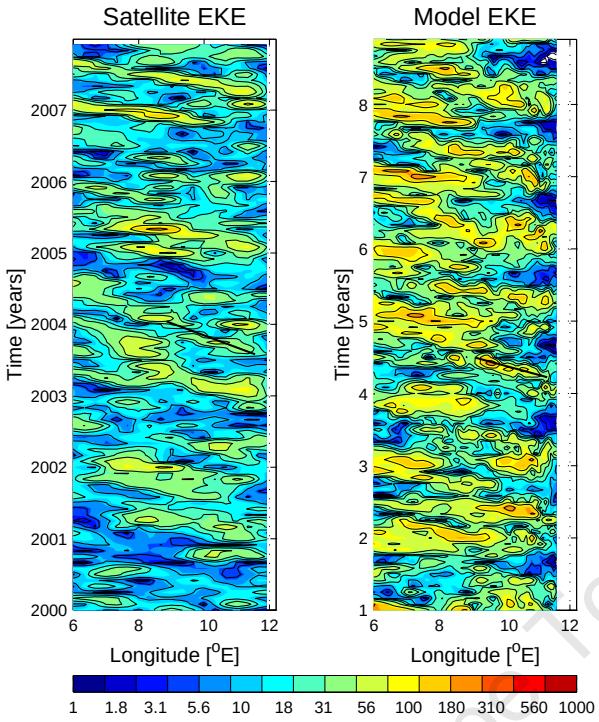

Figure 5.9: Time-longitude plot of monthly mean satellite (left) and model-derived (right) surface geostrophic non-seasonal EKE at 16.5°S. Units in $cm^2.s^{-1}$.

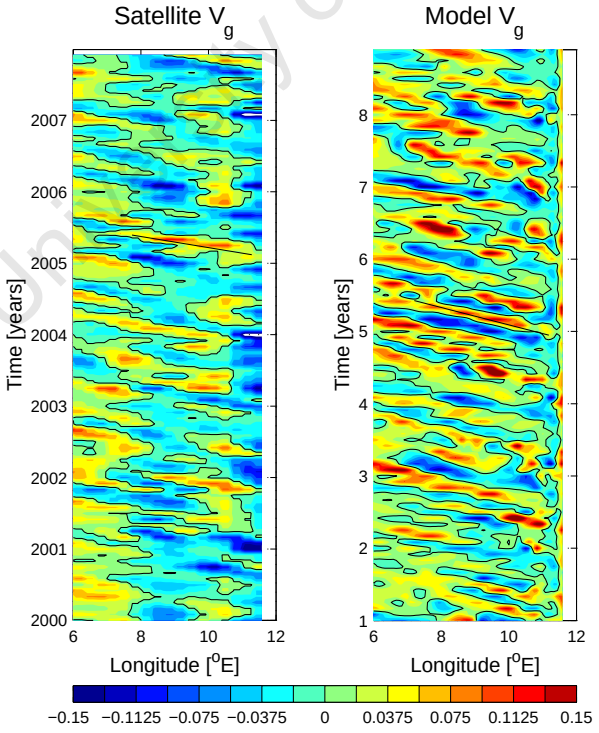

Figure 5.10: Time-longitude plot of monthly mean satellite (left) and model-derived (right) surface geostrophic meridional velocity at 16.5°S. Note: the scale differs from the similar plot shown for the southern Benguela in Figure 5.6.

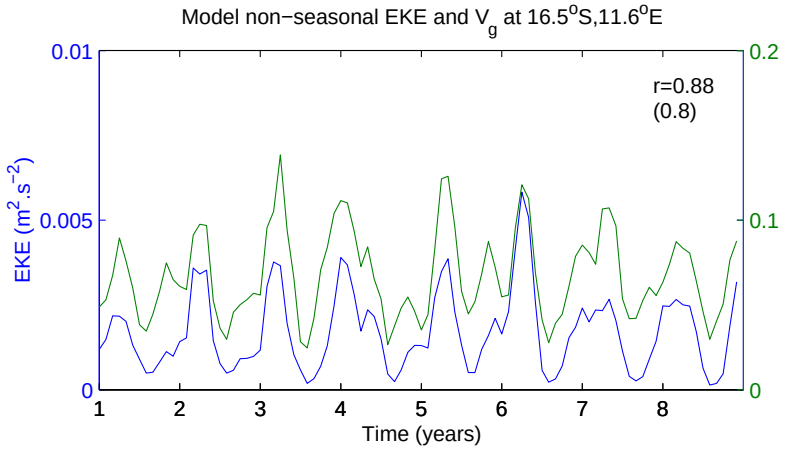

Figure 5.11: Time-series of monthly mean, non-seasonal EKE (blue) and meridional velocity (green) at 16°S, 11.6°E.

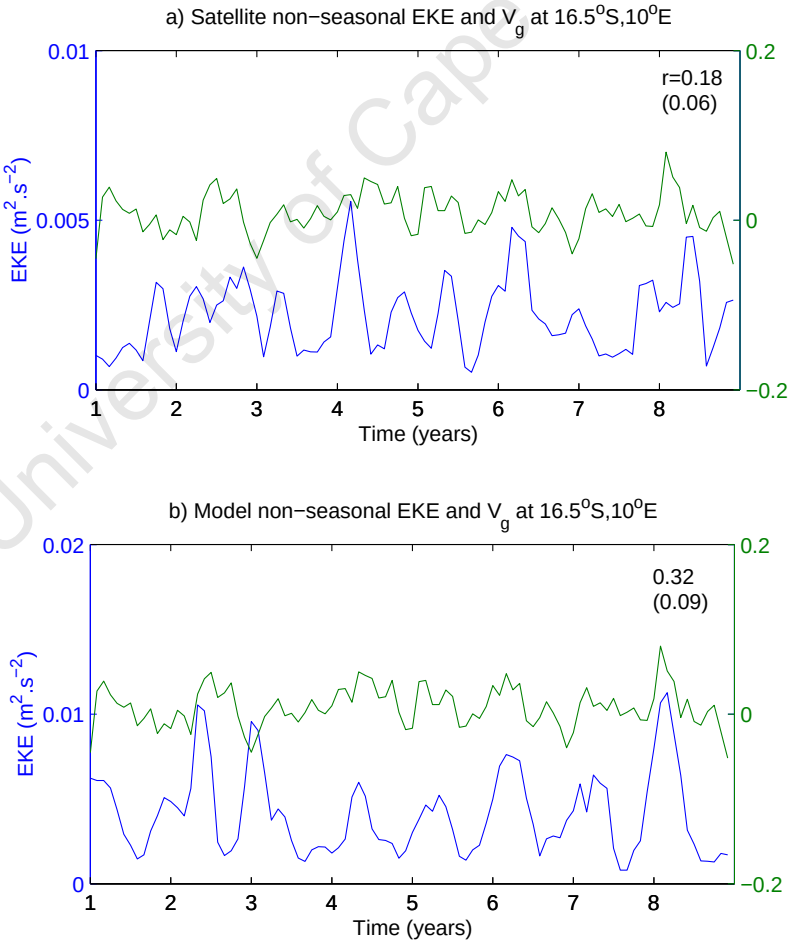

Figure 5.12: Time-series of monthly mean, non-seasonal EKE (blue) and meridional velocity (green) at 16.5°S, 10°E, based on satellite (a) and model (b) data.

Shelf-edge

The Hovmöller plots of monthly mean EKEs in Figure 5.5 suggest that there is little offshore propagation over the relatively broad shelf in the southern Benguela region, while similar plots representative of the northern Benguela region (Figure 5.9) imply that offshore propagation of the high EKE signal occurs from relatively nearshore locations. Figure 5.13 shows two-daily alongshelf (approximated by the 500 m isobath) non-seasonal EKEs plotted against latitude and reveals a pattern of equatorward propagation in the southern part of the system to approximately 26°S. There is evidence for poleward propagation in the north between ~14-16 °S as well as between ~18-24°S. While we have shown propagation only at the shelf-edge, similar figures (that are not shown) for the mid-shelf region (i.e. at the 200 m isobath) reveal an equivalent equatorward (poleward) propagation rates of EKE in the southern (northern) part of the system. This is more or less consistent with alongshelf fluctuations of the alongshore velocity component shown in Figure 4.18 of Chapter 4. Equatorward propagation rates in the southern part of the system are calculated as ~12 cm.s^{-1}and the average poleward propagation rate for the northern Benguela is ~2 cm.s^{-1}.

The source of the equatorward propagating EKEs at the shelf-edge in the southern Benguela may be linked to the equatorward upwelling jet (the significant correlation between the jet and EKEs is shown in Figure 5.7). However, the generation of cyclonic shelf-edge eddies, particularly in the lee of the Cape Peninsula and Cape Columbine, and their advection equatorward along the shelf-edge is likely to be an important contribution to this signal. Another important contribution to this signal is the meandering nature of the shelf-edge jet (see Figure 4.18).

Given that it's location is commensurate with the position of the ABFZ, the poleward propagating signal in the far north between ~14-16°S is no doubt related to fluctuations at the northern boundary of the upwelling regime. The poleward propagation of shelf-edge EKE (that originates at the coastal upwelling jet and is subsequently advected offshore) between ~18-24°S depends on the seasonal-pulsing of the wind-stress curl generated poleward flow.

Shelf-edge propagation of the depth-integrated EKE signal (figure not shown)

reveals equivalent equatorward propagation in the southern Benguela system, again to ~25°S. However, no poleward propagating signal is present in the northern part of the system. This result suggests that the EKE signal at the shelf-edge in the southern Benguela is barotropic in nature and is therefore significantly controlled by deep-reaching features, such as the meandering shelf-edge jet. Contrary to this, the EKE signal in the northern Benguela is predominantly a surface feature.

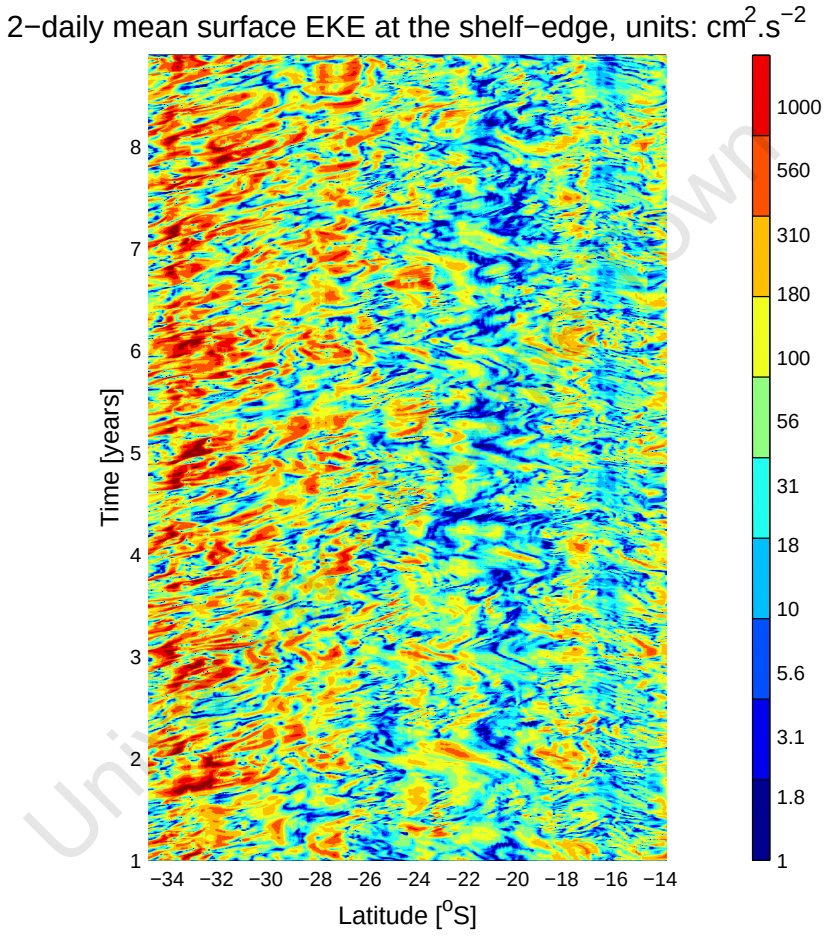

Figure 5.13: Time-latitude plot of total surface eke (in $cm^2.s^{-2}$) along the shelf-edge (~500 m isobath), using 2-daily model output.

5.1.3 Vertical structure

Depth-integrated vs. depth-averaged EKE

Thus far we have focussed primarily on surface mesoscale variability patterns of the Benguela system, which have revealed the striking juxtaposition of very low

EKEs on the shelf and very high EKEs further offshore in the southern region and a more typical pattern (compared to other EBCS's) in the northern region. Features spawned at the Agulhas retroflection and their advection into the Benguela Current system provide a huge source of energy to the greater Benguela Current system. While surface EKEs give an idea of the influence of Agulhas influx on the mesoscale variability in the Benguela system, it neglects subsurface effects which are likely to be significant considering (for example) the fact that Agulhas rings are deep-reaching features (they have been observed to reach as deep as 4500 m: van Aken et al. (2000)). As a first approach attempt at understanding the vertical extent of the EKE structure of the Benguela system, Figure 5.14a shows the total (geostrophic + ageostrophic and seasonal + non-seasonal) depth-integrated EKE for the whole domain with the position of the shelf-edge and the location of the Walvis Ridge represented by the 500 m and 3500 m isobaths respectively. It reveals that the Walvis Ridge appears to form a barrier to the northward propagation of the deep-reaching, high EKEs that are prevalent to the south of it. This suggests that the Walvis Rdige presents, at least a partial, 'topographic trapping' of the high EKEs associated with the interaction of features associated with Agulhas leakage and the Benguela Current system (particularly in the so-called 'Cape Cauldron' region). While several observational, as well as numerical, studies have been conducted on the interaction of eddies (both surface-intensified, anticyclonic and bottom-intensified, cyclonic) with the Walvis Ridge, no unanimous conclusion has been reached. van Ballegooyen et al. (1994) observed the slowing down of an Agulhas ring on approaching the Walvis Ridge, while the observations of Schouten et al. (2000) suggested that there was no systematic effect of the ridge on Agulhas rings. The idealized numerical study of Kamenkovich et al. (1996) indicated that the Walvis Ridge is likely to influence the amplitude and trajectory of eddies and is consistent with the realistic model investigation of Matano and Beier (2003) that showed the veering of surface-intensified anticyclones when in contact with either the Walvis Ridge or the Vema Seamount and bottom-intensified cyclones tended to be blocked by either of these topographic features. These contrasting effects, according to the authors, generates a concentration of barotropic energy to the east

of the Walvis Ridge, which is consistent with Figure 5.14a). A similar modeling study by Treguier et al. (2003) showed that while in the Cape Basin, Agulhas rings remain south of ~30°S. Although Figure 5.14a shows high EKEs throughout the Cape Basin, highest EKEs are situated in a very particular path south of ~30°S and is consistent with the offshore 'stream' of the Benguela Current (as manifested in an equilibrium state), which is shown as streamlines in Figure 5.14a.

While the depth integrated EKEs suggest a strong topographical control of the high EKE signal due to the presence of the Walvis Ridge, the depth integrated values are, of course, depth dependant so that deeper regions would more than likely have greater EKEs than shallower regions. In order to test the relative differences in EKEs from region to region (irrespective of depth), Figure 5.14b shows depth averaged EKEs. The region of highest EKEs remains unchanged as does the fact that the Walvis Ridge appears to form a barrier to the northward advection of the high offshore EKE signal. Depth-averaged EKEs allow us to identify areas of relatively high EKE production on shallower shelf regions, the most striking of which is associated with the shelf-edge jet (or the 'Goodhope Jet'), southward of ~30°S, but is most intense between the Cape Peninsula and 32°S. Northward of this feature, but south of the Walvis Ridge (i.e. south of ~20°S), highest depth-averaged EKEs tend to be confined to regions that are deeper than the shelf-edge. This implies that features giving rise to elevated EKEs in the offshore regions of the southern Benguela are somewhat barotropic in nature. North of the Walvis Ridge, the highest depth-averaged EKEs are situated on the narrow shelf and decrease offshore, which is what we might expect from instabilities associated with the upwelling jet.

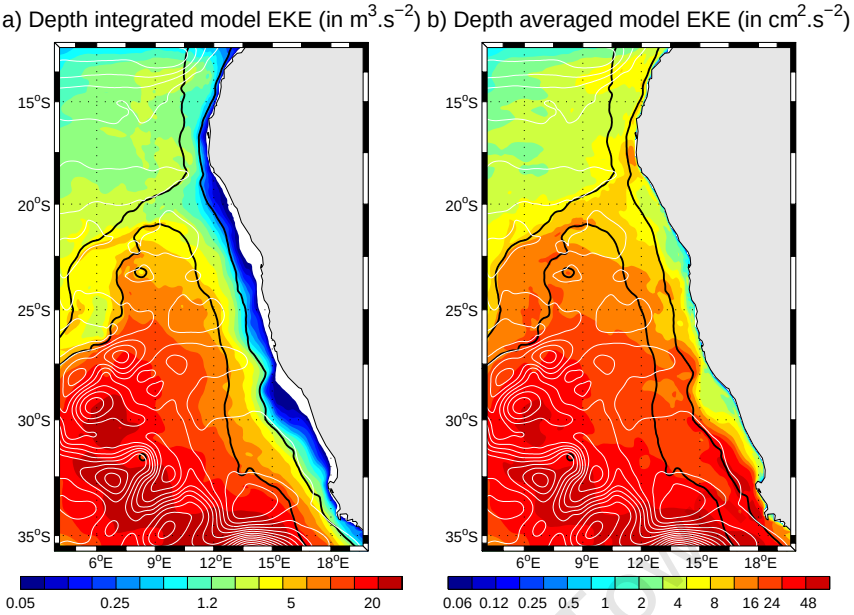

Figure 5.14: Depth-integrated, model-derived total (i.e. geostrophic + ageostrophic), total (i.e. seasonal + non-seasonal) eddy kinetic energy (EKE) in $m^3.s^{-2}$. The black contours show the 500 m and 3500 m isobaths, the former representing the position of the shelf-edge and the latter indicating the location of the Walvis Ridge. The white contours show the depth-integrated transport streamlines.

Vertical EKE sections

A more detailed view of the vertical EKE structure, representative of the southern and northern Benguela regions, is shown in Figures 5.15 and 5.16 respectively. Both figures show the total (i.e. geostrophic + ageostrophic) EKE, using the same log colour scale for the seasonal and non-seasonal components, as well as their sum (i.e. the total geostrophic + ageotrophic EKE). Shown in black contours are isopycnals, with a contour interval of 0.2 $kg.m^{-3}$and the 1026.4 $kg.m^{-3}$contour is shown in bold.

A zonal section at 32°S is used to represent the southern Benguela region and is shown in Figure 5.15, which reveals that most of the EKE is the result of non-seasonal fluctuations. The vertical sections elucidate the previous suggestion that high offshore EKEs do not tend to penetrate the relatively broad and shallow shelf of the southern Benguela. The relatively quiescent shelf region is associated with rather shallow-sloping isopycnals, and is flanked on both its shelf-edge and coastal boundaries by much more steeply sloping isopycnals that appear to be linked to

the local production of EKE. This can be most clearly seen in Figure 5.15b, which shows a strong seasonal signal (expressed as seasonal EKE) in regions of steeply-sloping isopycnals at the coast and at the shelf-edge (connected to the seasonal cycle associated with the coastal upwelling jet and the shelf-edge jet). The non-seasonal EKE signal is dominated by the path of the meandering offshore stream of the Benguela Current that is the vehicle for cyclonic and anticyclonic features originating from the Agulhas Retroflection and extends to depths of at least 1000 m. Plots not shown reveal that surface intensification of the EKE structure extends offshore of ~10°E, with values of the order of 50-100 $cm^2.s^{-2}$ from ~1000 m depth to the bottom and a surface intensification where values exceed 800 $cm^2.s^{-2}$. This region is coincident with highest depth-integrated and depth-averaged EKEs in Figure 5.14 and suggests the deep-reaching effect of the cyclonic and anticyclonic features on their northwestward path into the Atlantic Ocean.

The vertical EKE structure for the northern Benguela (represented by a zonal section at 16°S) is shown in Figure 5.16 and is very different to that of the southern Benguela, but much more similar to what one might expect from an upwelling system (for example, see Fig. 7 in Marchesiello et al. (2003)). The isopycnals shown on the plot give an indication of the alongshore current structure and reveal the presence of a coastal upwelling jet, a poleward undercurrent and there is evidence of a near-surface surface poleward counter-current offshore of the upwelling jet. The non-seasonal EKE signal shows peak values on the offshore edge of the equatorward upwelling jet and is coincident with a strong seasonal cycle (Figure 5.16b). A secondary peak seasonal cycle is present at the location of the poleward undercurrent, vestiges of which can be seen in the non-seasonal EKEs in Figure 5.16c. The secondary peak is not entirely locally produced as it is related to the southward propagation of EKE into the northern Benguela from the ABFZ. The downward and offshore fan of EKE from its source at the coastal upwelling jet suggests an inverse energy cascade, resulting in the barotropization of the vertical eddy scales. Scott and Wang (2005) showed that altimetry data has reached an accuracy and resolution capable of resolving the inverse energy cascade and was thus able to observe such geostrophic turbulence in the first barotropic mode in the South Pacific Ocean.

This structure has been similarly observed in the California Current system (Marchesiello et al. (2003)) and has been shown by Haney et al. (2001) to be connected with the transformation of upper ocean baroclinic EKE to deeper, barotropic EKE via nonlinear processes associated with baroclinically unstable waves.

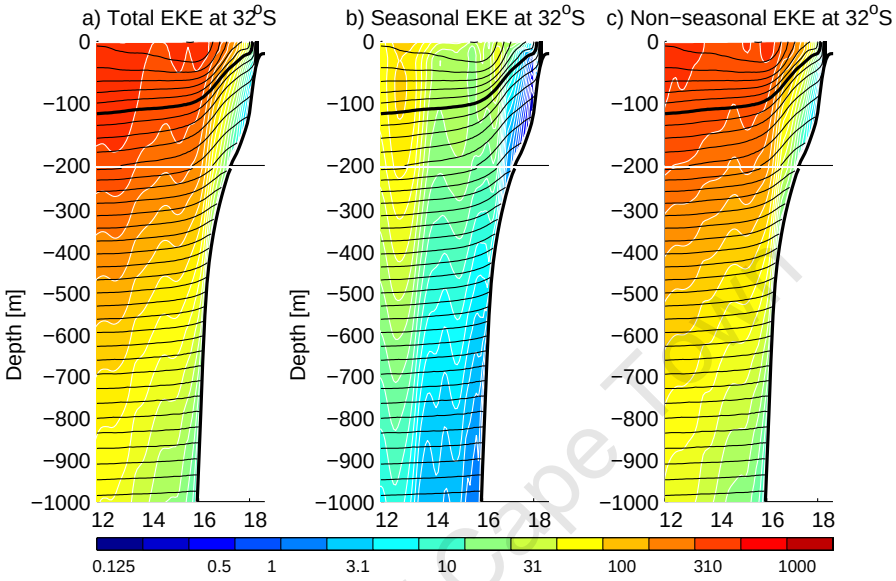

Figure 5.15: Seasonal (a) and non-seasonal (b) EKE at 32°S (in $cm^2.s^{-2}$) with isopycnals (bold contour represents 1026.4 $kg.m^{-3}$ and the contour interval is 0.2 $kg.m^{-3}$.

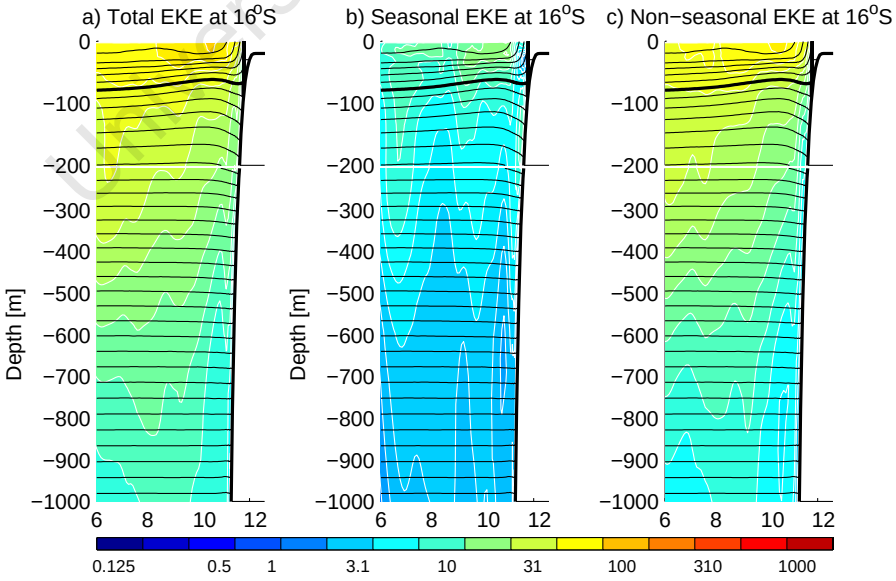

Figure 5.16: Seasonal (a) and non-seasonal (b) EKE at 16°S (in $cm^{-2}.s^{-2}$) with isopycnals (bold contour represents 1026.4 $kg.m^{-3}$ and the contour interval is 0.2 $kg.m^{-3}$.

5.2 Volume-integrated energy contributions

The previous section emphasizes the very significant offshore EKE gradient in the southern Benguela and alludes to the difficulty of separating locally produced EKE from EKE that is advected into the area. To the north of the Walvis Ridge, the EKE structure is more reminiscent of what we might expect of an eastern boundary upwelling system, taking the work of Marchesiello et al. (2003) as an example. We therefore expect differences in the contributions from mean and transient energy to the total energy in the northern and southern Benguela systems. In fact, the eddy-permitting modeling study of Matano and Beier (2003) showed that momentum fluxes in the Cape Basin are driven primarily by eddy fluxes with little input from the mean flow.

In order to quantify the relative contributions of mean and transient energy in the northern and southern Benguela and the cross-shore variations of each, we calculate the volume integrated mean and eddy kinetic energy for 0.5° zonal sections for the northern and southern Benguela regions. The northern Benguela is defined as the region north of the Walvis Ridge spanning 20-16°S and the southern Benguela is defined as the region spanning 34-30°S. Figure 5.17 shows the cross-shore variations in mean and eddy kinetic energy for the southern Benguela region. The average position of shelf-edge (for this alongshore averaged region) is approximately 16.3°E and forms a barrier between mean kinetic energy dominance on the shelf and eddy kinetic energy dominance off the shelf. The total, volume-integrated eddy kinetic energy offshore of the shelf edge in the southern Benguela (30-34°S) is 367×10^{15}J, which is more than double the total, volume-integrated mean kinetic energy of 145×10^{15}J. Conversely, the mean kinetic energy integrated on the shelf in the southern Benguela exceeds the total eddy kinetic energy by 1.5×10^{15}J (7×10^{15}J for the former and 5.5 J$\times 10^{15}$J for the latter). In short; while the momentum of the offshore domain of the southern Benguela is driven by transient energy, the shelf region is driven by mean energy.

While the northern Benguela is far less energetic than the southern Benguela (note the different scales of the y-axis on Figures 5.17 and 5.18), the total mean kinetic energy exceeds the eddy kinetic energy for the entire cross-shore expanse of the

northern Benguela system. The total, volume-integrated mean kinetic energy in the northern Benguela (16-20°S) amounts to 43.5x10^{15}J, while the total transient eddy kinetic energy is 35.8x10^{15}J. While the cross-shore kinetic energy profiles increase monotonically offshore in the southern Benguela, a peak (dip) occurs some distance offshore (~9°E) in the northern Benguela of the eddy (mean) kinetic energy profiles. This coincides with the location of the transition from equatorward to poleward flow that is suggested by the varying slope of the ispycnals in Figure 5.16 and reflects the role of the poleward flow in producing mesoscale fluctuations (via advection or local generation).

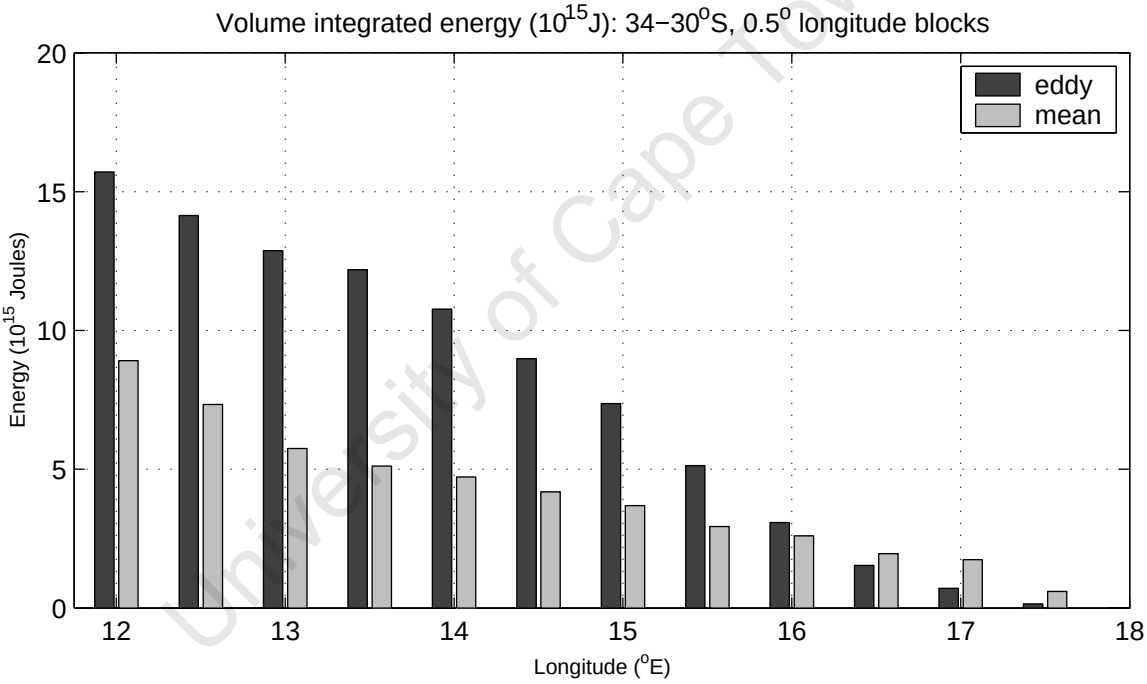

Figure 5.17: Volume integrated mean and eddy kinetic energy, between 34-30^oS in 0.5^o longitudinal blocks.

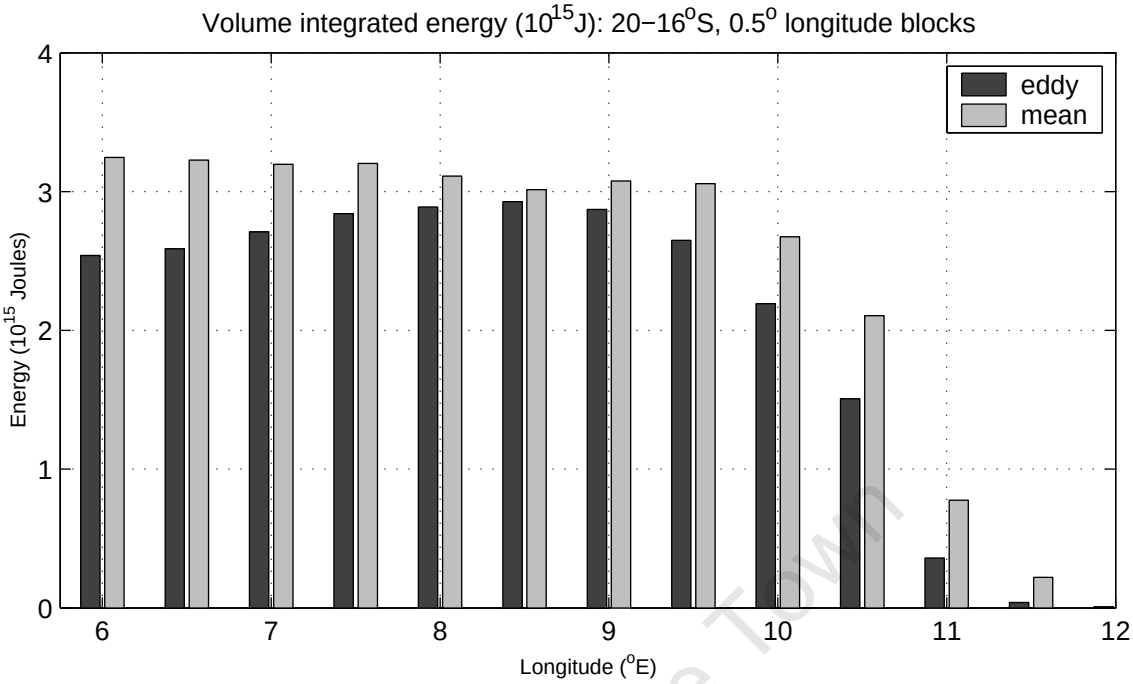

Figure 5.18: Volume integrated mean and eddy kinetic energy, between 30-16ˆoS in 0.5ˆo longitudinal blocks.

5.3 Coherent eddy structures

While the high EKE signal as resolved by the model is indicative of the turbulent nature of the Cape Basin, it does not give specific evidence of the passage of coherent eddy structures such as anticyclonic Agulhas rings and cyclonic eddies. In this section we identify anticyclonic and cyclonic features that are resolved by the model in order to more quantitatively define their location and preferential path. To do this we use the Okubo-Weiss parameter, which was more extensively used in the modeling study of Penven et al. (2005) to investigate eddy characteristics in the Peru upwelling system. The Okubo-Weiss parameter describes the relative dominance of deformation and vorticity and, as such, is useful in identifying eddy structures due to their transition from deformation at the edges to strong vorticity in their centres. It is written as follows:

$$\lambda = \left(\frac{\partial u}{\partial x} - \frac{\partial v}{\partial y}\right)^2 + \left(\frac{\partial u}{\partial x} + \frac{\partial v}{\partial y}\right)^2 - \left(\frac{\partial v}{\partial x} - \frac{\partial u}{\partial y}\right)^2 \tag{5.3}$$

The first two terms on the right-hand side (RHS) represent the deformation and the last term represents the relative vorticity. If deformation (relative vorticity) dominates, the Okubo-Weiss term (λ) will be positive (negative). Using this parameter, eddies (both cyclonic and anticyclonic) will therefore be represented by a large negative value at their centres, surrounded by positive values. This allows us to easily identify the location of eddies numerically by extracting all of the local minimums throughout the domain of interest because if a point is surrounded by values greater than it, it must represent the centre of an eddy. We identify seperately both cyclonic and anticylonic features by applying a mask based on selected sea surface height anomalies. Specifically, in order to extract the locations of anticyclonic (cyclonic) features, which have a positive (negative) SSHA signal, we only calculate the Okubo-Weiss parameter for regions where the SSHA is positive (negative). However, because the SSHA signals are so huge in the offshore domain, we the use fairly stringent thresholds also used by Matano and Beier (2003) for the positive and negative SSHAs used to identify possible anticyclonic and cyclonic eddy structures. Any positive value less than 25 cm is neglected in the identification of anticyclonic features and any negative value greater than -15 cm is neglected in the identification of cyclonic features, based on the Okubo-Weiss parameter. In order to locate cyclonic eddies on the shelf-edge, we use an SSHA threshold of 7.5 cm and neglect eddies offshore of the 2500 m isobath.

Figure 5.19 shows the location of all the selected anticyclonic eddies during all seasons located in the model domain during model years 5-7. Only output from three years are shown in order to avoid cluttering the figure. Note that the dots shown refer to the locations of eddies as they propagate through the domain, therefore the number of dots do not directly relate to the number of eddies. The red dots in Figure 5.19 relate to Agulhas rings propagating through the Cape Basin region and agrees well with trajectories observed by Treguier et al. (2003) in MODAS SSH fields (e.g. see their Fig. 3) as well as with the model results of Matano and Beier (2003) (see their Fig. 10). Agulhas rings do not tend to propagate northward of 30°S within the Cape Basin and, perhaps of more significance to the Benguela upwelling regime, do not propagate onto the shelf. The preferential path of the rings

tends to veer toward the west of the Vema Seamount and is, in general, coherent with the region of most intense depth-integrated EKEs as well as the area characterized by closely-spaced, meandering streamlines shown in Figure 5.14a. That the preferential path of the rings coincides with highest EKEs and the region of most intense mean meandering flow, as well as the fact that the offshore domain of the southern Benguela is dominated by eddy energy (see Figure 5.17) gives impetus to the statement that the mean flow of the Benguela Current is driven by the passage of Agulhas rings. Evidence of the fact that there is no dominant seasonality in the numbers of Agulhas rings identified per month is given in Figures 5.21a and 5.21b, which show the total number of eddies located per month for the whole 8 years of the model simulation and the associated spectral signal respectively.

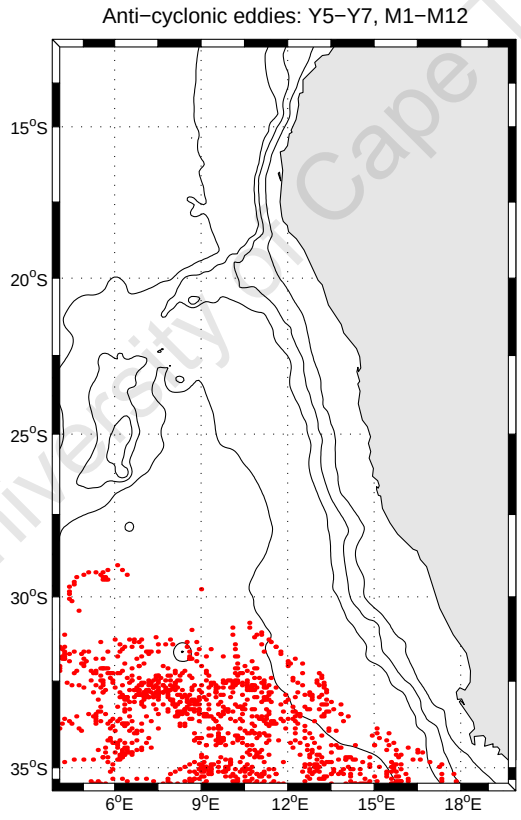

Figure 5.19: Locations of all anticyclonic eddies during all seasons identified using the Okubo-Weiss parameter from model year 5 to model year 7.

Figures 5.20a and 5.20b show cyclonic eddies identified during all summer and winter months respectively for model years 5 to 7. Blue dots indicate offshore cyclonic eddies (with an SSHA threshold of -15 cm) and the green dots represent

the locations and trajectories of cyclonic eddies over the shelf-edge (with an SSHA threshold of -7.5 cm). While there does not appear to be obvious seasonal variability of the trajectories or density of cyclonic eddies in the offshore domain, shelf-edge eddies are far more abundant during summer than in winter. During summer months we also see the formation of eddies in the region where the shelf-edge narrows at approximately 27°S. The dichotomy between the more distinct seasonality of the cyconic eddies over the shelf-edge than the offshore cyclonic eddies can be seen in time timeseries' and associated spectral signals in Figure 5.21. While the west-southwestward trajectories of the offshore cyclonic eddies are clearly demonstrated in Figure 5.20, eddies over the shelf-edge tend to be trapped to the shelf as they travel equatorward.

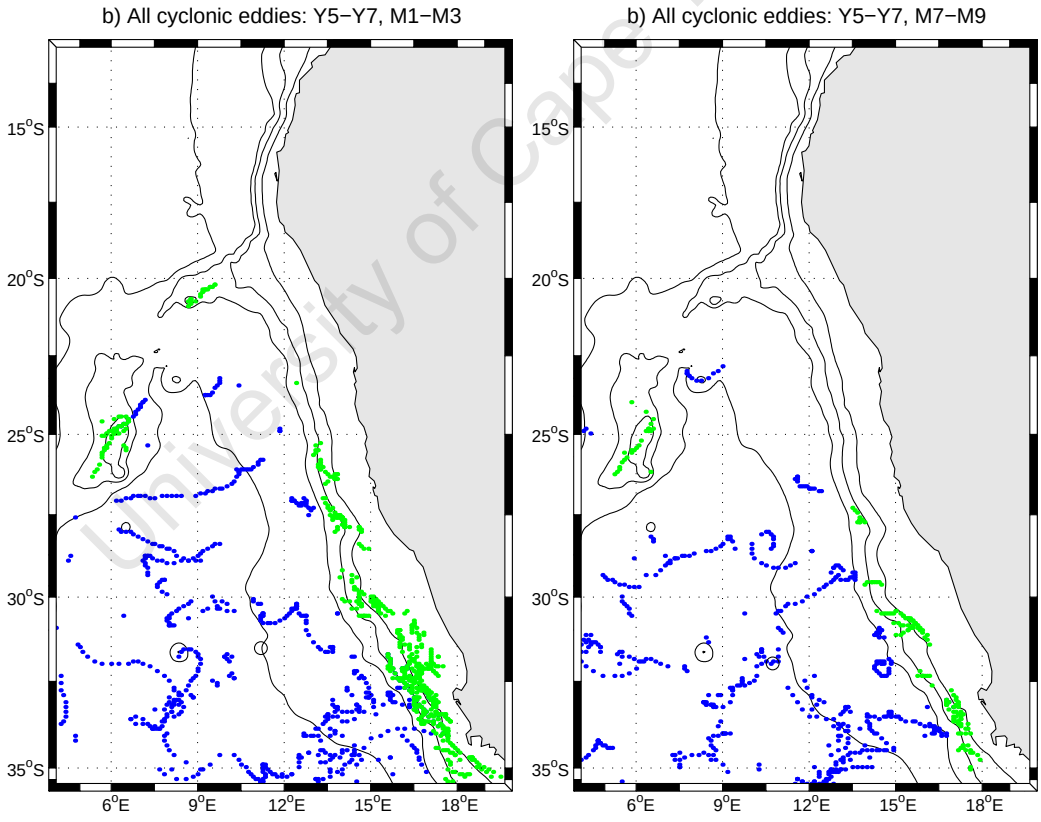

Figure 5.20: Locations of all cyclonic eddies identified during summer (a) and winter (b) months using the Okubo-Weiss parameter from model year 5 to model year 7.

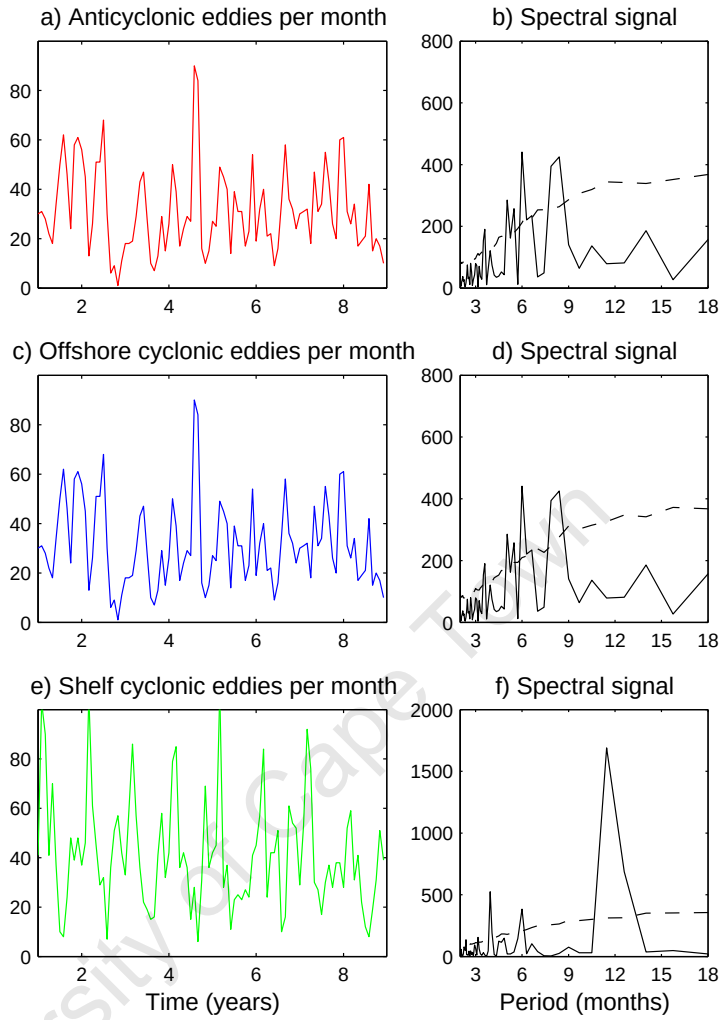

Figure 5.21: Total number of anticyclonic (a), offshore cyclonic (c) and cyclonic eddies on the shelf (e) per month identified for the full 8 years of model ouput. Alongside each are the respective signals (b,d and f respectively) with the 95% confidence level shown as a dashed line.

5.4 The role of eddies in the vorticity balance

The time-mean vorticity balance provides a concise and quantitatively instructive method of investigating the relative importance of terms driving the mean flow structure. Marchesiello et al. (2003) used the terms of the vorticity balance equation to show that, in fact, significant departures from the Sverdrup balance occur in the California Current system and are due to the non-linear terms. Based on the EKE analysis in the previous sections, we expect that the nonlinear terms are of impor-

tance to the dynamics of the southern Benguela system. We carry out a vorticity balance in order to better understand the eddy-mean flow interaction processes in the northern and southern Benguela systems.

The time-mean, depth integrated (from the free-surface to 1000 m) vorticity balance equation is derived in Appendix B and appears as follows:

$$\int_{-1000}^{\eta} \frac{\partial \xi}{\partial t} dz = \underbrace{\int_{-1000}^{\eta} f \frac{\partial w}{\partial z} dz - \beta \int_{-1000}^{\eta} v \, dz}_{\nabla\wedge\text{Coriolis}} \; \underbrace{- \int_{-1000}^{\eta} \overrightarrow{v} \nabla \xi dz}_{\nabla\wedge\text{Advection}} \; \underbrace{+ \nabla \wedge \frac{\vec{\tau}^{surf}}{\rho_0}}_{\nabla\wedge\text{Vertical mixing}} \tag{5.4}$$

where ξ is the relative vorticity and η is the free-surface. The Coriolis term has been separated into a vortex stretching term ($f\frac{\partial w}{\partial z}$, where f is the Coriolis parameter and w is the vertical velocity) and a beta term (βv, where β is equivalent to $\frac{\partial f}{\partial y}$ and v is the meridional velocity component). $\vec{\tau}^{surf}$ is the time mean surface wind stress vector (in N.m^{-2}) and ρ_0 is the reference density of sea-water (taken to be 1024 kg.m^{-3}). The surface forcing term is the dominant forcing term and far exceeds the bottom forcing term, which has therefore been neglected. Since vorticity advection is dominated by the horizontal advection, it can equivalently be written as follows: $curl_z[u\frac{\partial u}{\partial x} + v\frac{\partial u}{\partial y}, v\frac{\partial v}{\partial y} + u\frac{\partial v}{\partial x}]$, where u is the zonal velocity component. Using equation (5.2), we separate the mean and eddy vorticity advection terms, based on a time-mean current. The mean (MADV) and eddy (EADV) vorticity advection terms appear as follows (refer to Appendix B for a complete derivation):

$$MADV = \int_{-1000}^{\eta} curl_z \left[\frac{\partial \bar{u}^2}{\partial x} + \frac{\partial \bar{u}\bar{v}}{\partial y}, \frac{\partial \bar{v}^2}{\partial y} + \frac{\partial \bar{u}\bar{v}}{\partial x} \right] \tag{5.5}$$

$$EADV = \int_{-1000}^{\eta} curl_z \left[\frac{\partial u'^2}{\partial x} + \frac{\partial u'v'}{\partial y}, \frac{\partial v'^2}{\partial y} + \frac{\partial u'v'}{\partial x} \right] \tag{5.6}$$

where $[\bar{u}, \bar{v}]$ and $[u'v']$ are the time-mean and transient, zonal and meridional velocity components respectively. In a time-mean solution, the term on the left-hand side (LHS) of equation (5.4) tends to zero. Under the assumption of a low Rossby number regime and a rigid-lid, the vorticity advection (3rd term on the RHS of

equation (5.4)) and the vortex stretching (1st term on RHS) terms can be neglected. If these assumptions are valid and we can indeed neglect the corresponding terms we enter a regime that is controlled by Sverdrup dynamics, i.e. a balance between the beta term and the wind stress curl. However, in this section we are specifically interested in the role of eddies and therefore do not neglect the vorticity advection term, nor do we neglect the vortex stretching term as it may be significant in the presence of the large baroclinic or barotropic Agulhas Rings. In our time-mean solution, the tendency term on the LHS of equation (5.4) is null and we achieve a balance between the Coriolis, advection and surface forcing terms. Figure 5.22 shows the dominant terms of the depth-integrated vorticity balance as well as the separation of the Coriolis term (b) into its vortex stretching (c) and beta components (d) and the total vorticity advection (TADV) term (e) into its mean (MADV: f) and eddy (EADV: g) components.

The spatial pattern and strength of the dominant terms suggest that the Sverdrup relation is least applicable in the southern part of the Benguela system where the vortex stretching and advection terms make a significant contribution to the balance, particularly south of the Walvis Ridge (shown as white lines in Figure 5.22). More specifically, both terms are greatest in areas of most intense depth-integrated (0-1000 m) transport (which is shown in black contours). The separation of the TADV term into its MADV (Figure 5.22f) and EADV (Figure 5.22g) components reveals a more coherent pattern for the former that is tied to the standing meanders of the mean flow and a less structured pattern for the latter which nevertheless is greatest in regions of more intense flow. In a region of spatially homogeneous flow we expect the MADV term to be small. Therefore, we anticipate the significant MADV term related to the distinct standing meander pattern in mean flow of the southern Benguela, however the standing meander itself is a mean-state manifestation of the preferential path of the transient Agulhas Rings. All of the terms decrease northward, where they become increasingly of the order of the relatively small wind stress curl term.

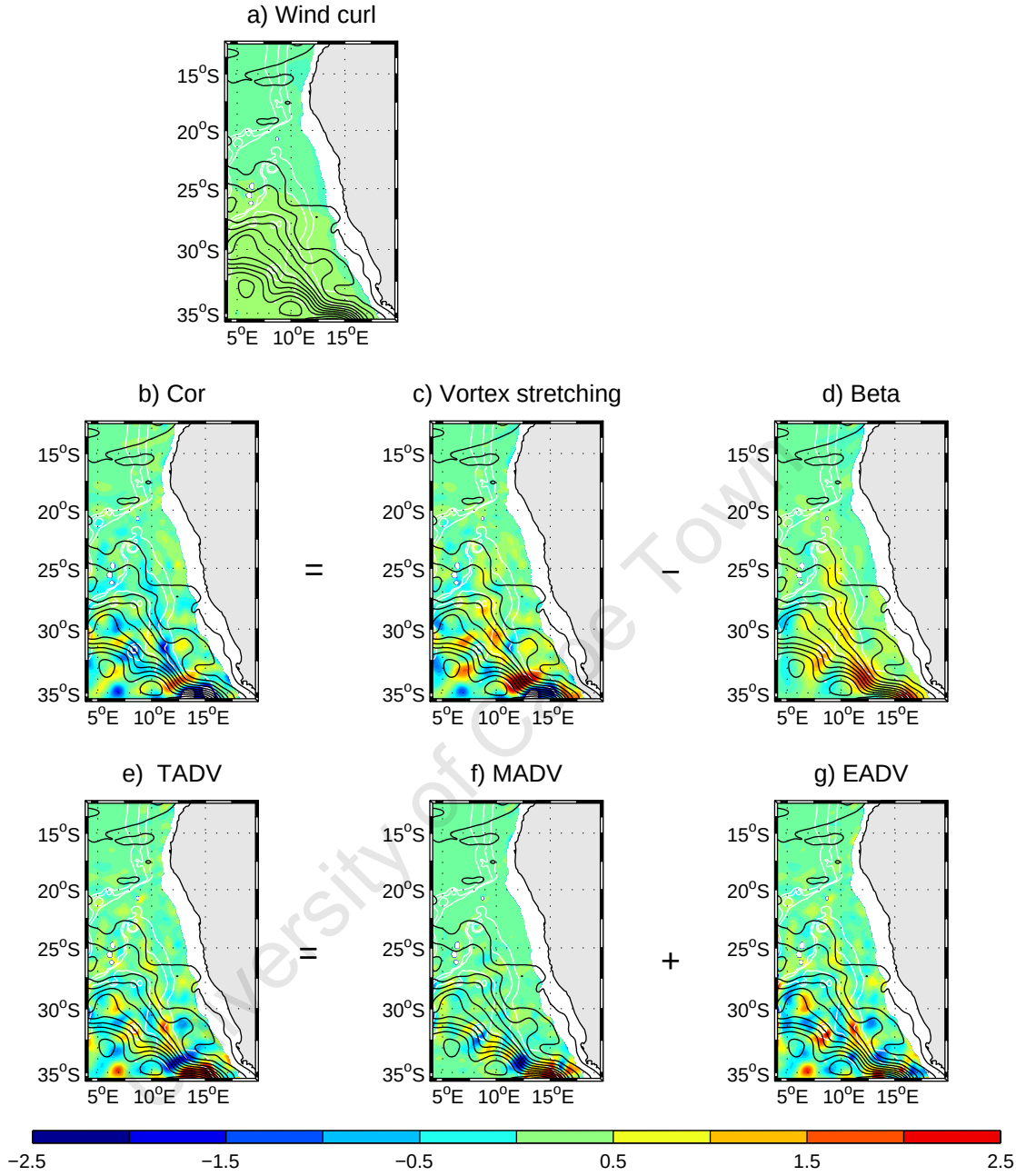

Figure 5.22: Maps of the dominant terms of the time-mean, depth integrated (surface to 1000 m) vorticity balance equation. Units are in 10^{-9}m.s^{-2}. The black contours represent 0-1000 m transport streamlines. The white contours show the 4100 m, 4500 m and 4900 m isobaths.

Figures 5.23 to 5.26 show the alongshore averaged dominant vorticity balance terms for four regions, representative of different regimes of the greater Benguela system: the tropical (13-18^{o}S), northern Benguela upwelling (20-24^{o}S), central Benguela upwelling (25-30^{o}S) and southern Benguela upwelling (32-34^{o}S) regions respectively. The balance of terms in the tropical region (Figure 5.23a) is primarily achieved by the beta and wind stress curl terms, which is consistent with Sverdrup dynamics and the results shown in Figure 4.15. It is also consistent with the results of Marchesiello et al. (2003). Deviations from a closed Sverdrup balance are accounted for by the vortex stretching term (vstretch), which is significant at ~75 km and ~175 km from the 1000 m isobath. While the TADV term is small it is greatest at approximately the same locations, which is commensurate with a region characterised by relatively high EKEs (see Figure 5.14) that may be related to instabilities associated with the ABFZ. The separation of the TADV term into its EADV and MADV components is shown in Figure 5.23b (note the different scale on the y-axis than in Figure 5.23a) and reveals that the positive TADV peak ~75 km from the 1000 m isobath is accounted for by transient vorticity advection (EADV). The negative peak further offshore (at ~175 km) is due to mean vorticity advection (MADV). Although these terms are very small, they may be associated with the generation of the larger vstretch terms that are required to close the balance.

The contribution of the TADV term in the vorticity balance of the northern Benguela upwelling regime (averaged between 20-24^{o}S) is significant throughout the domain as is the vstretch term (see Figure 5.24a: note the change of scale of the y-axis). Within 200 km of the 1000 m isobath the vstretch and TADV terms approximately balance each other out, their small difference accounting for the imbalance between the wind stress curl and beta terms. Further offshore their joint contribution to the vorticity balance becomes more significant. The relatively homogeneous nature of the flow in this region results in a small MADV component of the TADV term, with most of it being accounted for by the EADV component.

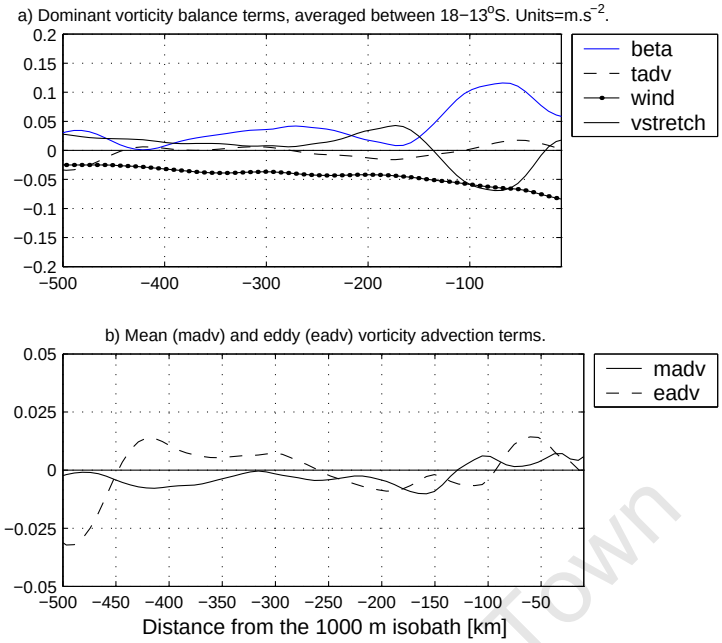

Figure 5.23: a) Dominant terms of the vorticity balance offshore of the 1000 m isobath for the tropical region, averaged between 13-18°S. b) The separation of the total vorticity advection term into its mean (madv) and eddy (eadv) components.

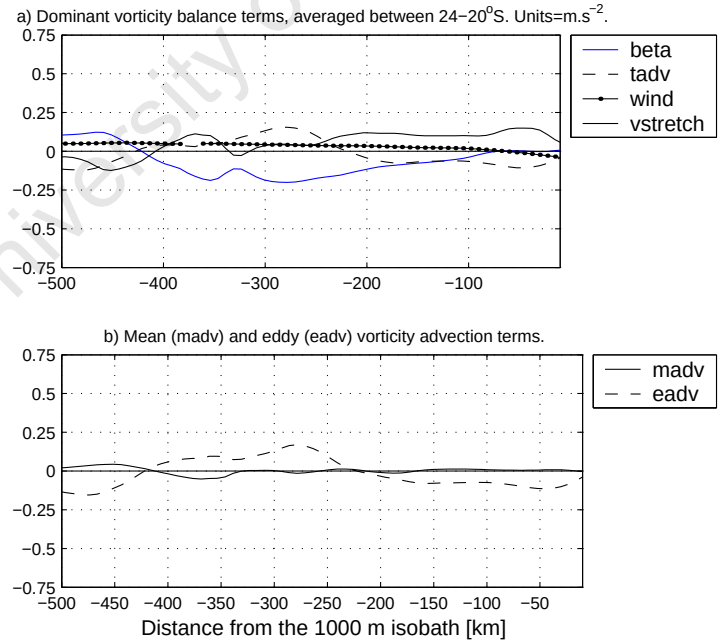

Figure 5.24: a) Dominant terms of the vorticity balance offshore of the 1000 m isobath for the northern Benguela region, averaged between 20-24°S. b) The separation of the total vorticity advection term into its mean (madv) and eddy (eadv) components.

The central Benguela region, situated between ~25-30^{o}S has been described in previous chapters as the transition between the disparate northern and southern Benguela regimes. It is characterized by a distinct offshore transport that has been associated with the Sverdrup relation (i.e. see Figure 4.15). However, the alongshore vorticity balance terms (Figure 5.25a) reveal that the Sverdrup balance only approximately holds in certain regions (e.g. within ~100 km, ~200 km and >450 km from the 1000 m isobath) and where is doesn't, the vorticity balance is closed by significant TADV and vstretch terms. Figure 5.25b reveals that the large TADV term is predominantly made up of the EADV component, despite the meandering nature of the mean flow regime in this region. The implication being that the meandering nature of the flow is the mean state manifestation of transient features.

The fact that non-linearities associated with the influence of Agulhas leakage in the southern Benguela negates the validity of the Sverdrup balance in that region has already been revealed in Figure 4.15. The vorticity balance terms for this region (spanning 32-34^{o}S) are shown in Figure 5.26 and quantifies the role of the non-linear advection terms in driving the mean flow in the southern Benguela regime. The primary balance lies between the beta term and the vstretch term with secondary contributions from the TADV term, which is greatest in regions of distinct standing meanders (i.e. ~375 km offshore: see Figure 4.15a). While the EADV contribution is once again dominant in the TADV term, the MADV component is significant (see Figure 5.26b). The large MADV term in the southern Benguela is likely a product of the fact that the very large scale of Agulhas Rings makes their signal impossible to completely remove with the rest of the transient signal (using equation (5.2)).

Figure 5.27 shows the percentage contributions of the dominant vorticity balance terms, averaged across-shore and alongshore in each of the domains described above. In all cases the positive and negative fluctuating TADV term shown in Figures 5.23a-5.26a results in a very small contribution to the box average of each domain. Particularly for the northern and southern Benguela upwelling regions (32-34^{o}S and 20-24^{o}S respectively), the box-averged vstretch term remains an important contribution to the balance and is probably related to vertical velocity mismatches at the surface and 1000 m as a result of the presence of Agulhas Rings, eddies and

associated features. The box-averaged vorticity terms suggest that the Sverdrup relation is most relevant for the tropical Benguela region (13-18^{o}S), with only slight deviations due to vortex stretching and non-linear processes. While the box-average vstretch term becomes more significant in the central Benguela region (25-30^{o}S), the dominant balance is between the beta and wind stress curl term, thus validating the Sverdrup relation in this region.

Our results are consistent with the global vorticity budget carried out by Lu and Stammer (2004). Their relatively coarse resolution (2^{o}x2^o) results showed a significant departure from Sverdrup balance in the upper ocean (surface to 985 m) in most areas except in regions unaffected by boundary currents. Their budget showed that the departure from Sverdrup balance was accounted for primarily by vortex stretching at higher latitudes and by the presence of advection in western boundary current regions. The fact that the southern Benguela system is significantly influenced by Agulhas leakage places it in the vorticity balance regime of western boundary regions where we would expect advection to be important.

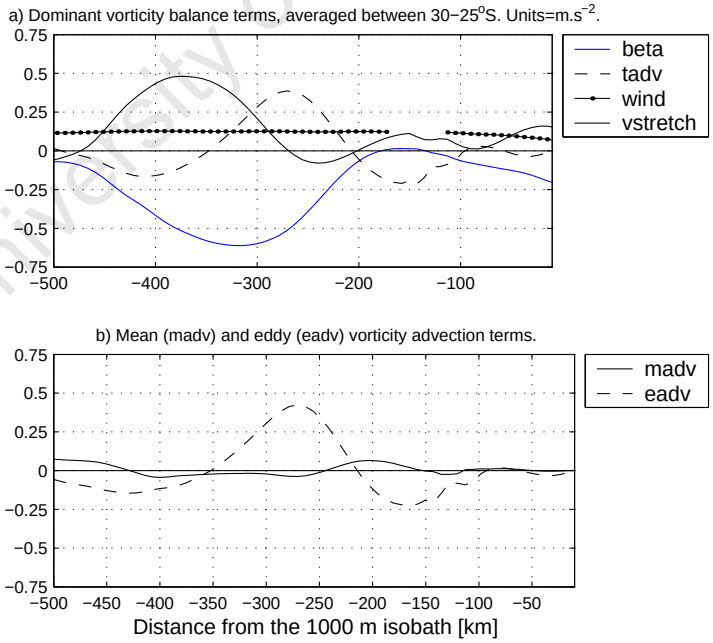

Figure 5.25: a) Dominant terms of the vorticity balance offshore of the 1000 m isobath for the central Benguela region, averaged between 25-30°S. b) The separation of the total vorticity advection term into its mean (madv) and eddy (eadv) components.

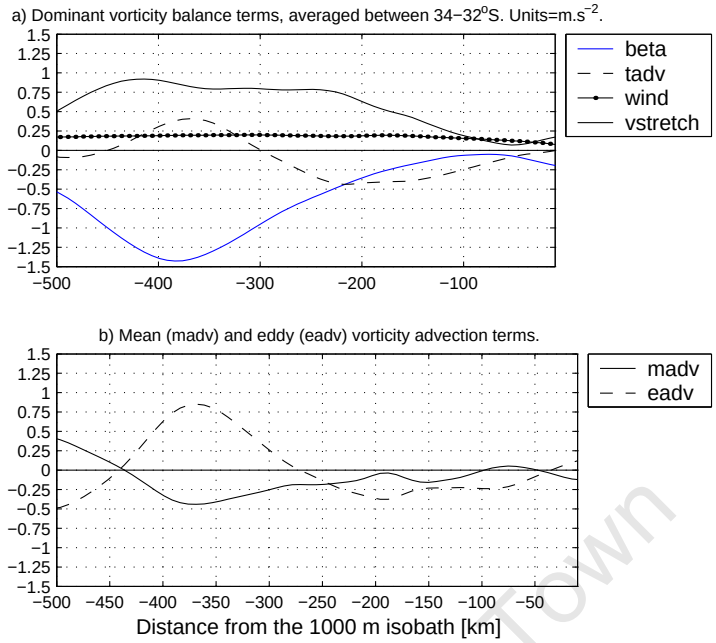

Figure 5.26: a) Dominant terms of the vorticity balance offshore of the 1000 m isobath for the southern Benguela region, averaged between 32-34°S. b) The separation of the total vorticity advection term into its mean (madv) and eddy (eadv) components.

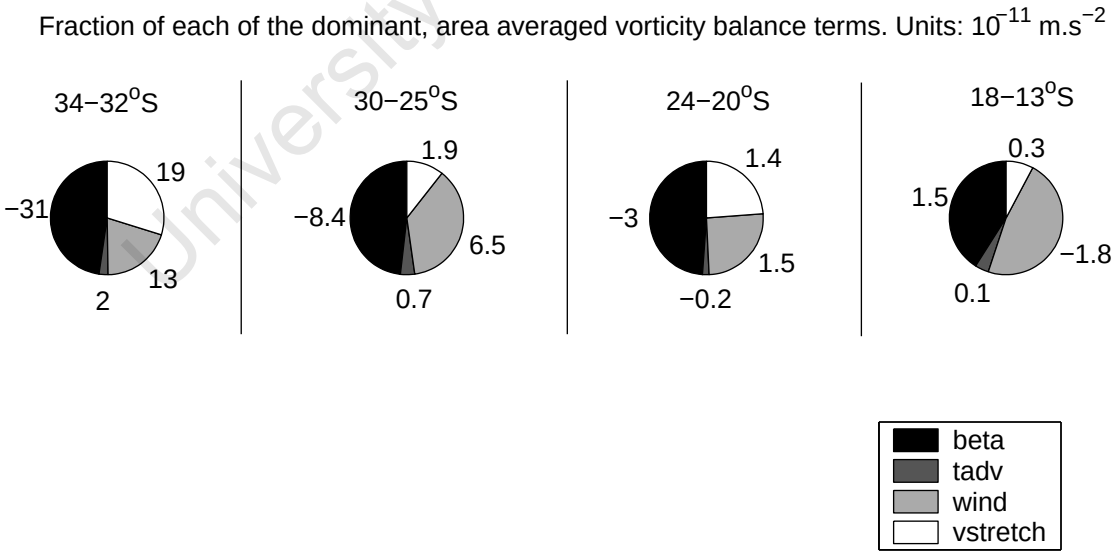

Figure 5.27: Area averages of the dominant vorticity balance terms, as a fraction of a pie, for each of the domains shown in Figures 5.23 to 5.26.

5.5 Energy conversion analysis

Examining terms of the mean and turbulent kinetic energy balance equations provides information about the source of instabilities and interaction processes between the mean and eddy regimes via energy pathways. In terms of energy and mesoscale fluctuations, the Benguela is unique among the worlds eastern boundary upwelling systems: the premise being that the exceptionally high offshore EKEs are a result of the throughflow of Agulhas rings and eddies. However, EKEs on the shelf are relatively low. While transport processes are likely to dominate the offshore EKE balance, we investigate the importance of baroclinic and barotropic processes in the generation of instabilities. The baroclinic (PeKe) and barotropic (KmKe) instability terms can be found in the final form of the eddy kinetic energy equation (for a derivation refer to Appendix E) and represent the conversion from eddy potential energy to eddy kinetic energy and from mean kinetic energy to eddy kinetic energy respectively. We also look at the energy input by the mean and eddy wind fields (FmKm and FeKe respectively) as well as the mean baroclinic conversion (PmKm) term, which describes the conversion from mean potential to mean kinetic energy. The full kinetic energy equation also contains two tranport terms that are due to pressure and Reynolds stresses and dissipation is intrinsically solved by the numerics of the high order advection scheme in ROMS. The depth-integrated terms that we will be focussing on appear as follows:

$$FmKm = \bar{U}\frac{\bar{\tau_x}}{\rho_0} + \bar{V}\frac{\bar{\tau_y}}{\rho_0} \tag{5.7}$$

$$FeKe = \overline{U'\frac{\tau_x'}{\rho_0} + V'\frac{\tau_y}{\rho_0}} \tag{5.8}$$

$$KmKe = \int_z^\eta \left[-\overline{\vec{v'}u'}.\nabla\bar{u} - \overline{\vec{v'}v'}.\nabla\bar{v}\right]\partial z \tag{5.9}$$

$$PmKm = \int_z^\eta \left[-\frac{g}{\rho_0}(\bar{w}\bar{\rho})\right]\partial z \tag{5.10}$$

$$PeKe = \int_z^\eta \left[-\frac{g}{\rho_0}(\overline{w'\rho'}) \right] \partial z \tag{5.11}$$

where $\vec{v'}$ is the turbulent velocity vector: $[u', v', w']$ in the x-,y- and z- directions, while $[\bar{u}, \bar{v}, \bar{w}]$ are the mean velocity components. The turbulent component is extracted from the total by subtracting the mean (e.g. $v' = v_{total} - \bar{v}$). $[\bar{\tau}_x, \bar{\tau}_y]$ and $\left[\tau'_x, \tau'_y\right]$ are the mean and turbulent zonal and meridional wind stress components respectively. $U = \int_z^\eta u dz$, $V = \int_z^\eta v dz$, $A_v \frac{\partial u}{\partial z} = \frac{\tau_x^s}{\rho_o}$ and $A_v \frac{\partial u}{\partial z} = \frac{\tau_y^s}{\rho_o}$ (we focus on the wind work an therefore neglect bottom stress). ρ is the density, ρ_0 is the reference density, taken to be 1024 kg.m^{-3} and g is acceleration due to gravity (9.81 m.s^{-2}). The density and velocity fields are interpolated from the terrain-following z-coordinate to a geopotential grid with dz=40 m prior to the calculation of the energy terms.

Baroclinic instabilities produce kinetic energy via buoyancy forcing and, as such, require a horizontal density gradient. Kinetic energy is extracted from the potential energy that is stored in sloping isopycnals as fluid parcels move along them. In this process, which can be described as the production of kinetic energy by buoyancy forcing (and symbolically written as $Pe \rightarrow Ke$ or $Pm \rightarrow Km$ for eddy or mean energy conversions respectively), baroclinic instabilities decrease the potential energy of the system by flattening out the isopycnals. Eady and Charney developed the theory of baroclinic instabilites in the atmosphere and summaries of their mathematical descriptions can be found in Vallis (2006). Barotropic instabilites are shear flow instabilities and arise from vertical or horizontal shear in the flow field. This type of instability can therefore occur in fluids of constant density. An example of barotropic instability is the Kelvin-Helmholz instability, which is seen often in the atmosphere and oceans, and in the case of the latter has been shown to produce cyclonic roll-up patterns in the California upwelling system by Marchesiello et al. (2003) (see their Fig. 2). Vallis (2006) discusses the scenario in which edge waves interact to produce barotropic instabilites. This may be an important mechanism in the vicinity of the shelf in the southern Benguela. Barotropic instabilities are produced in the conversion from mean kinetic to eddy kinetic energy and can be symbolically written as $Km \rightarrow Ke$.

Since we are specifically interested in the role of locally generated baroclinic and barotropic instabilities in producing the characteristic pattern of EKEs in the Benguela system (e.g. refer to Figures 5.2 and **??**), as a first order approach, we begin with Figure 5.28 which shows the annual mean, depth integrated terms for the whole domain. While we are primarily interested in the shelf and shelf-edge regions, Figure 5.28 provides a useful first impression of large-scale variations within the system. The conversion from eddy potential energy (Pe) to eddy kinetic energy (Ke) is shown in Figure 5.28a and represents baroclinic instability processes where the term is positive (i.e. $Pe \rightarrow Ke$). The grey contours are the streamlines of flow and show that the offshore stream of the Benguela Current is associated with highest offshore baroclinic instabilities. Large positive and negative $Pe \rightarrow Ke$ terms characterise the eastern and western flanks of the Vema Seamount respectively, suggesting that a region of relative stability exisits in the lee of the seamount. From observations, Schouten et al. (2000) showed that the splitting of Agulhas rings during their northwestward translation occurs preferentially at the Vema Seamount and Richardson (2007) conjectured that this process could result in the formation of cyclonic eddies. Our model results suggest (refer to Figure 5.20) that instabilities occur on the eastern flank of the Vema Seamount. Intense baroclinic instabilities are associated with the very active upwelling cells of Lüderitz and Cape Frio. Because the upwelling signal is more perennial in the north than in the south, baroclinic instabilities associated with the upwelling jet in the southern Benguela are filtered out in the annual mean $Pe \rightarrow Ke$ signal shown in Figure 5.28. A negative $Pe \rightarrow Ke$ on the shelf in the region of the ABFZ and to the north of it suggests that mesoscale fluctuations in this region produce potential energy, by modifying the density field.

The $Km \rightarrow Ke$ conversion term is shown in Figure 5.28b; positive values represent the generation of eddy kinetic energy by the kinetic energy of the mean flow via shear instabilities and negative terms show where eddies supply energy to the mean flow. The largest $Km \rightarrow Ke$ signal is positive and occurs at the shelf-edge in the region of the intense Goodhope jet and specifically off Cape Columbine and Cape Peninsula (~33^{o}S and ~34^{o}S respectively) and reveals that the cyclonic eddies generated in these regions are a product of barotropic instability processes. A fairly

significant negative $Km \rightarrow Ke$ term situated in the path of Agulhas Rings and where the mean flow is quite intense at ~12.5 ^{o}E reflects the fact that eddy fluxes largely drive the mean flow in this region.

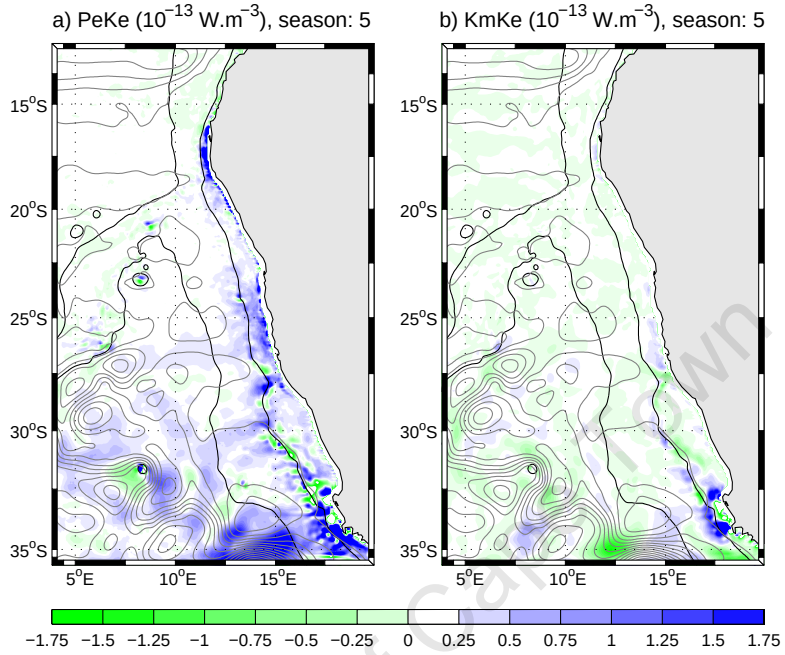

Figure 5.28: a) Baroclinic (PeKe) and, b) barotropic (KmKe) conversion term. Units are in W.m^{-3} and the isobaths shown are 500 m and 4000 m and represent the approximate position of the shelf-edge and the location of the Walvis Ridge (as well as the Vema Seamount) respectively. The grey contours are the depth-integrated streamlines of flow.

5.5.1 Barotropic and baroclinic instabilities

Now that we have a general impression of the relative importance of baroclinic and barotropic instabilities for the whole domain, we will now look at seasonal variations of the cross-shore structure of the depth-integrated, area-averaged (alongshore, and in 50 km cross-shore domains) $Pe \rightarrow Ke$ and $Km \rightarrow Ke$ terms for peak and mimimum upwelling seasons for the northern and southern Benguela regimes (Figure 5.29 and 5.30 respectively). In each plot, the approximate position of the shelf-edge is represented by the vertical dashed grey line. In the northern Benguela, baroclinic instabilities are always more significant than barotropic instabilities. While the seasonal variation in upwelling is much lower than in the southern Benguela, upwelling is less intense during summer (season 1) months and, in conjunction with a relatively

strong southward transport by the poleward flow, causes a rather distinct variation in the $Pe \rightarrow Ke$ conversion term on the shelf between the low and high upwelling seasons. When upwelling rates are low, the density field over the narrow shelf of the northern Benguela is relatively stable and is associated with more horizontally aligned isopycnals. The poleward flow causes a displacement of the isopycnals (in the opposite sense to an upwelling scenario, i.e. downward toward the shelf and coast) so that they are less stable and contain more potential energy. The negative $Pe \rightarrow Ke$ at the shelf-edge in Figure 5.29a is the result of this process. The term becomes positive at ~150 km offshore and stays approximately constant, other than dropping to close to zero at 400 km offshore. This location coincides with the centre of a sluggish cyclonic, gyre-like feature; evidence of which can be seen in the annual mean streamlines shown on Figure 5.28 and is forced by the mean summer wind-stress curl. This feature is most robust during summer months and is not present as a distinct, closed loop during other seasons (from figures not shown). During times of active upwelling, such as during autumn (season 2), baroclinic instabilities (i.e. when $Pe \rightarrow Ke$ is positive) dominate over the shelf in the northern Benguela and decrease in a linear fashion with distance offshore. Instabilities of the intense upwelling jet are enhanced via interaction with the poleward flow, thus producing a very large positive $Pe \rightarrow Ke$ conversion term. The downward sloping (toward the coast) isopycnals that are produced by the poleward flow helps to flatten out the steep, conversely inclined isopycnals that characterize active upwelling, thus lowering Pe by releasing Ke.

Both the northern and southern Benguela vorticity balances depend significantly on the advection and vortex stretching terms. The latter especially so, due to the passage of Agulhas rings and eddies and the general enhancement of mesoscale variability associated with Agulhas influence.

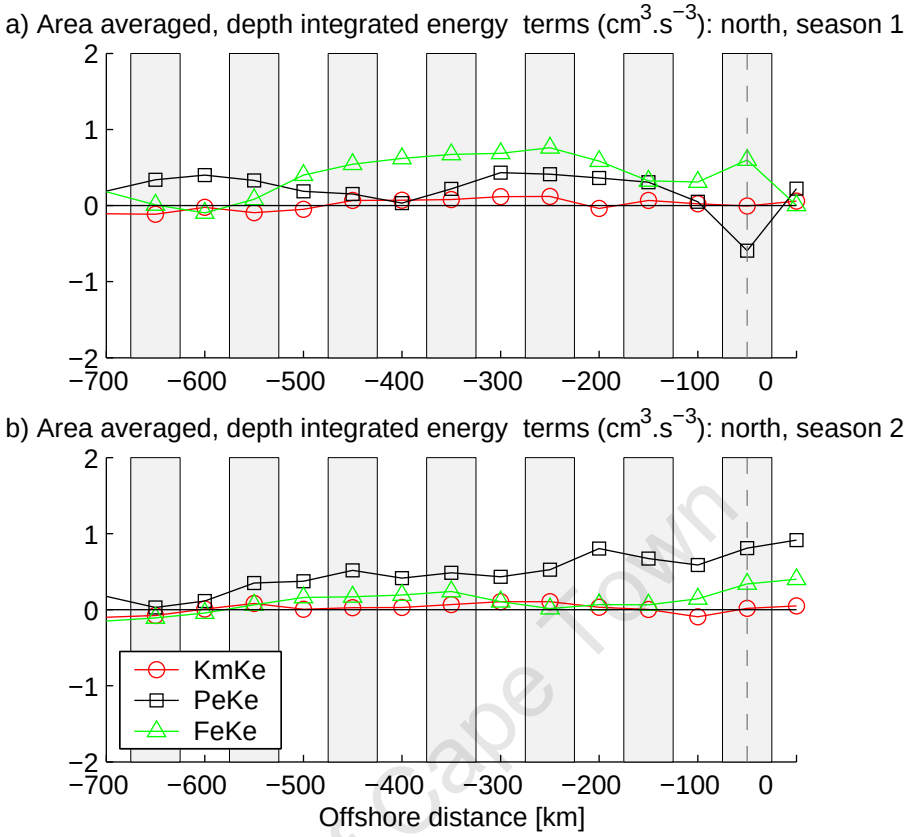

Figure 5.29: Area averaged (alongshore and in 50 km cross-shore subdomains), depth integrated baroclinic (PeKe) and barotropic (KmKe) conversion terms and eddy wind forcing term (FeKe) for the northern Benguela region (16-20°S) during, a) summer and b) autumn. The grey vertical dashed line represents the approximate location of the shelf-edge.

Cross-shore profiles of baroclinic and barotropic contributions to instabilities in the southern Benguela regime are shown for seasons representative of minimum and maximum upwelling (i.e. autumn and spring: season 2 and season 4 respectively) in Figure 5.30. Note that the scale of the y-axis is 5 times larger than for the equivalent plot of the northern Benguela (Figure 5.29). While the larger scale is necessary to capture the large conversion terms offshore, instabilities on the southern shelf are of the order of those on the northern shelf. Thus, once again, the contrasting nearshore and offshore regimes in the southern Benguela is illustrated and suggests that the high EKEs in the offshore regions of the southern Benguela, driven by Agulhas influx, has little direct influence on the inner-shelf regions (the vertical dashed grey line represents the approximate position of te shelf-edge). Barotropic or

shear instabilities are significant in the southern Benguela for a positive $Km \rightarrow Ke$ term and where $Km \rightarrow Ke$ is negative, the contribution of eddy energy fluxes to the mean flow is important.

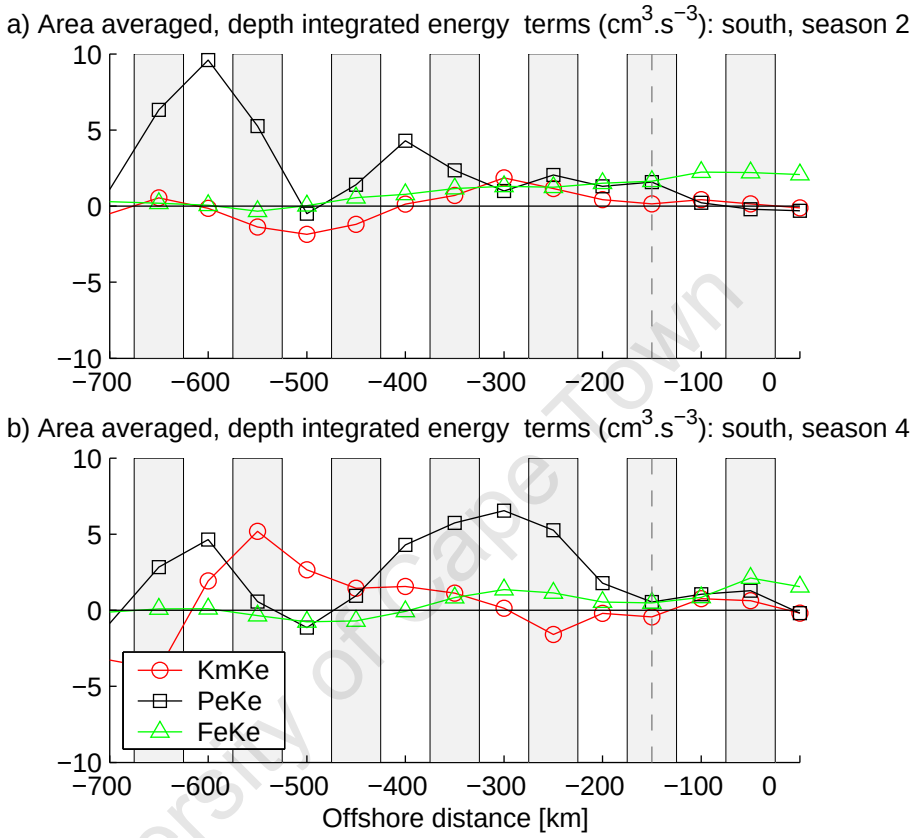

Figure 5.30: Area averaged (alongshore and in 50 km cross-shore subdomains), depth integrated baroclinic (PeKe) and barotropic (KmKe) conversion terms and eddy wind forcing term (FeKe) for the southern Benguela region (30-34°S) during, a) autumn and b) spring. The grey vertical dashed line represents the approximate location of the shelf-edge.

Alongshelf variations

To focus now on instabilities locally generated in association with upwelling dynamics, we look at the annual mean depth-integrated energy conversion terms averaged across the inner-shelf (from the coast to the 300 m isobath) and in 100 km alongshelf subdomains. Figure 5.31 shows the large $Pm \rightarrow Km$ (mean potential to mean kinetic energy conversion term) and $Fm \rightarrow Km$ (mean forcing to mean kinetic energy term) terms and reveals that approximate parity exists between them, particularly

in the northern part of the system. When interpretting this figure however, it is important to recall that it is more representative of the nearshore dynamics of the northern Benguela than the southern Benguela due to the fact that the seasonal signal of the former is far less than that of the latter. The $Fm \rightarrow Km$ term represents the annual mean wind work imposed on the system and extracts clear signals for the dominant upwelling cells (particularly the ones with less variability bewteen seasons). Most conspicuously the black line in Figure 5.31 shows the energy gained by the wind at the Cape Columbine (~33°S), Lüderitz (~27°S) and Cape Frio (~18°S) upwelling cells. Northward of the Lüderitz upwelling cell the large positive $Fm \rightarrow Km$ term is in very close balance with a large negative $Pm \rightarrow Km$ term, which is consistent with the energy pathway followed by Ekman transport: the wind directly forces a current and thereby produces mean kinetic energy, which then sets up a horizontal density gradient and, in doing so, produces mean potential energy ($Fm \rightarrow Km \rightarrow Pm$). Such a close balance does not hold on the shelf in the southern Benguela, with particularly distinct (negative) outliers at ~34°S and ~32°S. The negative outliers suggest that there exists a consistent source, other than the mean wind forcing, for the formation of mean potential energy in these regions. In other places, the $Pm \rightarrow Km$ term falls short of balancing the wind work term, such as between 29-31°S and 25-27°S which coincides with regions of strong offshore transport: the former being the region where the Benguela Current veers offshore and the latter the region of large-filament formation which is linked to the intense offshore transport associated with the Lüderitz upwelling cell. At these locations some of the mean kinetic energy produced by the mean wind field is lost to the large offshore fluxes and does therefore not contribute to the formation of potential energy.

The annual mean $Km \rightarrow Ke$, $Pe \rightarrow Ke$ and $Fe \rightarrow Ke$ conversion terms (depth-integrated, averaged across the inner-shelf and in 100 km alongshore subdomains) are shown in Figure 5.32. The dominant signal from the reigon of Lüderitz and northward are two peaks of positive $Pe \rightarrow Ke$ at 24-26°S and at 17°S, which points to baroclinic instabilities associated with the equatorward jets driven by the active upwelling cells at Lüderitz (which extends over a large area, spanning roughly 25-

28°S) and Cape Frio. Barotropic instabilities ($Km \rightarrow Ke$) are slight in the northern Benguela, with some enhancement in the far north, between 16-18°S due to the interaction of the poleward flow at the shelf-edge and the equatorward jet at the coast. In the southern Benguela there is a large contribution to the kinetic energy by the eddy wind forcing. This in fact is only a reflection of the high seasonal signal in the southern Benguela as the wind forcing is climatological and, therefore, the transient wind forcing describes the monthly deviations from the annual mean wind field. The steep shelf south of ~32.5°S appears to be most affected by offshore dynamics in that it produces a large positive and negative $Km \rightarrow Ke$ conversion term and a large negative $Pe \rightarrow Ke$ conversion term. The shear instability represented by the large positive $Km \rightarrow Ke$ conversion term at about 32.5°S is set up as the intense Goodhope Jet extends northward past Cape Columbine and sets up a significant horizontal shear with the weak currents in the lee of the Cape. The large negative $Km \rightarrow Ke$ conversion term at ~33.5°S indicates a situation in which eddy energy fluxes drive the mean flow. At this location, the eddies could be those that form at the Cape Peninsula (~34°S) and advect along the run of the shelf-edge or they could be related to mesoscale features spawned at the Agulhas retroflection and advected preferentially along the shelf-edge. In the same region is an approximately equivalent negative $Pe \rightarrow Ke$ term, which reflects the conversion of eddy kinetic energy to eddy potential energy. Because the inner-shelf of the Benguela broadens between 32.5-29°S, there is less interaction of offshore features with the nearshore upwelling regime.

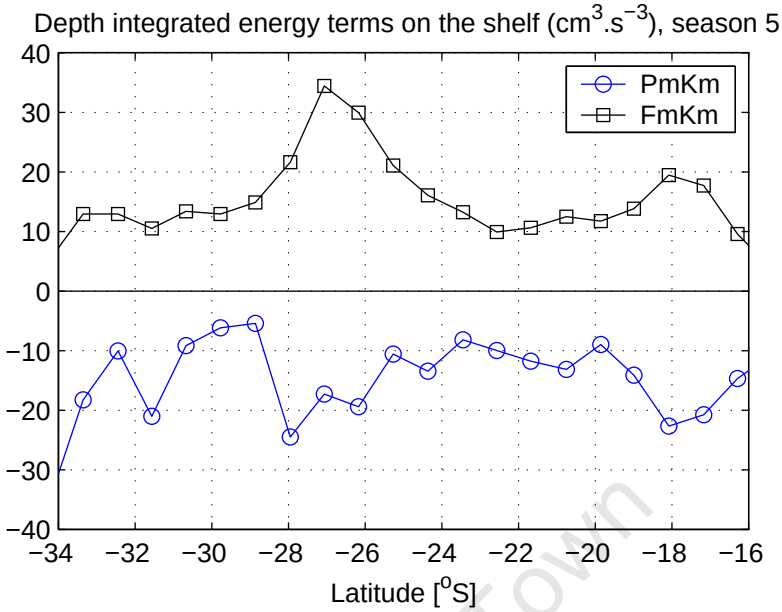

Figure 5.31: Area-averaged (in 100 km alongshore subdomains and across-shelf), depth integrated mean wind forcing (FmKm) term and mean baroclinic conversion term (PmKm) from 34°S to 15°S.

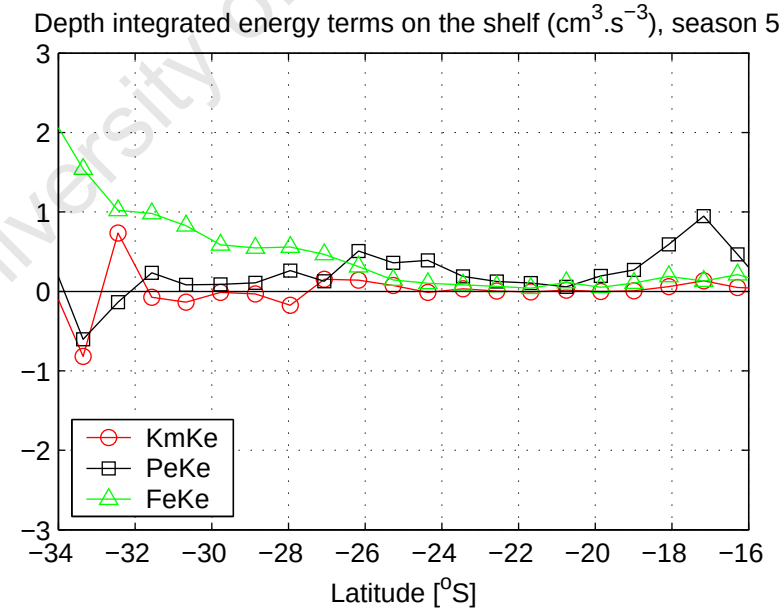

Figure 5.32: Seasonal, area-averaged (in 100 km alongshore subdomains and across-shelf), depth integrated baroclinic conversion (PeKe), barotropic conversion (KmKe) and eddy wind forcing (FeKe) terms from 34°S to 15°S.

5.6 Synthesis and discussion

The aim of this chapter has been to characterize the nature of mesoscale variability and to identify its role in the Benguela system; inclusive of the large-scale offshore regime as well as the nearshore upwelling regime. When comparing satellite and model-derived surface EKEs similar patterns of very high offshore EKEs juxtaposed against very low nearshore EKEs emerge. It is this pattern that exemplifies the uniqueness of the Benguela as one of the worlds four eastern boundary upwelling systems (EBUSs): it is the only system for which it is necessary to plot EKEs on a log-scale in order to resolve both the extremely high offshore values as well as the very low nearshore values (see Plate 1 in Capet et al. (2008)). A steep offshore gradient of EKE coincident with the shelf-edge in the southern Benguela (in both model and satellite data), suggests that the shelf-edge forms a barrier to the nearshore advection of high offshore EKEs. While model and satellite surface EKEs reveal an approximately equivalent pattern, the model produces more EKE than is observed by satellite and is related to the fact that the model overestimates Agulhas influx into the Benguela system (refer to Chapter 4). The decomposition of model and satellite surface geostrophic EKEs into seasonal and non-seasonal components shows that most of the EKE is generated by non-seasonal fluctuations. This, and the fact that the model and satellite produce equivalent levels of EKE (other than areas of overestimation by the model) implies that most of the variability within the system is intrinsically forced and does not rely on high frequency fluctuations in the wind forcing.

We have already highlighted the fact that, in terms of EKE, the Benguela system differs quite strikingly from other EBSs. It can also be said that the northern and southern regions of the Benguela system differ markedly from one another. The fact that the offshore EKE gradient in the southern Benguela far exceeds that of the northern Benguela is likely to have differing implications for cross-shore exchanges of water properties in these regions. Hoffmöller plots of monthly mean EKE at zonal sections representative of the northern and southern Benguela systems (16°S and 32°S respectively) show that a nearshore source of EKE generation exists for both the northern and southern Benguela systems. Similar plots of the meridional

velocity component (as an indicator of the equatorward upwelling jet), together with a correlated timeseries of EKE and meridional velocity at a nearshore location confirm that the EKE source is associated with the upwelling jet. The difference between the northern and southern systems in this regard, lies in the fact that a clear offshore propagating signal of ~3.5 cm.s^{-1}has been calculated for the nearshore source of EKE in the northern Benguela, but an offshore propagating signal only occurs from the location of the shelf-edge in the southern Benguela (no offshore propagating signal is present on the shelf area) and is a reflection of the northwestward translation of Agulhas rings. The EKE signal on the shelf in the southern Benguela propagates equatorward to ~30°S at a rate of ~12 cm.s^{-1} where it turns offshore. This pattern is consistent with the large-scale flow regime investigated in the previous chapter.

Demarcq et al. (2007) investigated the variability of chlorophyll-a within the Benguela system using satellite data. Their Hoffmöller plot of the offshore location of the 1 mg.m^{-3} chlorophyll a isopleth (their Figure 3d) provides evidence of the differences of the northern and southern Benguela systems. The offshore location of the chlorophyll-a isopleth gives an indication of the offshore extent of phytoplankton biomass (and, therefore, productivity) and Demarcq et al. (2007) found that it extended as far as 600 km offshore during times of active upwelling in the northern Benguela, while it only extended some 250 km offshore during times of active upwelling in the southern Benguela. The explanation for this could be related to the alongshelf propagating signal prevalent in the southern Benguela as opposed to the offshore propagating signal in the northern Benguela, which would essentially trap nutrients/chlorophyll on the shelf in the case of the former, but transport them offshore in the case of the latter. However, in instances where water mass properties do manage to extend beyond the shelf-edge, the high levels of horizontal mixing associated with the high offshore EKEs in the southern Benguela would decrease the chlorophyll concentration according to Gruber et al. (2007) and Rossi et al. (2008).

Depth-integrated and depth averaged plots of EKE show that the shelf-edge as well as the Walvis Ridge indeed form barriers to high levels of mesoscale variabilty associated with the path of Agulhas rings and eddies. Highest EKEs are situated in the path of the rather intense meandering path of the offshore 'stream' of the

Benguela Current (the divsion of the Benguela Current into inshore and offshore streams was defined in the previous chapter). A zonal section of EKE at 32°S clarifies the fact that the broad southern Benguela shelf acts as a barrier to the onshore advection of the high offshore EKE signal. While a slight peak of EKE exists at the coast, in association with the upwelling jet, the southern Benguela shelf is quiescent throughout and is dominated by mean kinetic energy (MKE), while the offshore regime in the southern Benguela is dominated by EKE. The vertical EKE section representative of the northern Benguela is more reminiscent of the California upwelling system (shown by Marchesiello et al. (2003)), in which the EKE signal spreads outward and downward from its source at the upwelling jet (resembling an inverse energy cascade in which vertical eddy scales increase with offshore distance). Using the Okubo-Weiss parameter to locate anticylonic eddies, we identify their preferential path as coinciding with the offshore meandering stream of the mean Benguela Current. This, together with the result that EKE far exceeds MKE in the offshore regions of the southern Benguela leads us to conclude that the offshore path of the mean Benguela Current is driven by the eddy energy fluxes provided by Agulhas rings (this is in agreement with Treguier et al. (2003) and Matano and Beier (2003)).

A vorticity balance analysis reveals that the rigid-lid and level of no motion assumptions should be used with caution as the vortex stretching term is not insignificant in the Benguela system and it is therefore not in perfect Sverdrup balance. The global modelling study of Lu and Stammer (2004) similarly showed deviations from a Sverdrup balance and a non-negligable vortex stretching term in the upper ocean (0-985 m). While the vortex stretching term is not entirely negligable in the tropical Benguela region (i.e. 13-18^{o}S), it is relatively small and the dominant balance is achieved by the terms of the Sverdrup relation: i.e. the beta and wind stress curl terms. Although the area-averaged, depth-integrated vorticity balance terms for the central Benguela region (25-30^{o}S), which is characterized by a distinct offshore flow, is also largely controlled by the beta and wind stress curl terms, the eddy advection and vortex stretching terms make locally important contributions. Both the northern and southern Benguela vorticity balances depend significantly on the

advection and vortex stretching terms. The latter especially so, due to the passage of Agulhas rings and eddies and the general enhancement of mesoscale variability associated with Agulhas influence.

An energy conversion analysis confirms that the nearshore generation of EKE at the coast in the northern Benguela is a result of baroclinic instabilities associated with the equatorward upwelling jet and is modulated by the poleward flow, the intensity of which is out of phase with the upwelling cycle. In the southern Benguela, the large baroclinic and barotropic conversion terms in the offshore regions dominate the cross-shore signal. However, baroclinic instabilities are greater on the shelf during active upwelling seasons. While barotropic instabilities are significant over the southern Benguela shelf (particularly south of ~32.5°S) due to the strong horizontal current shears, they tend to be insignificant in the northern Benguela.

This chapter has not only emphasized the dominance of the high offshore EKE signal in the Benguela system, it has also provided further insight into the disparity between the northern and southern parts of the system in terms of the role of eddies. It can also be said that this chapter has illustrated the difficulty of separating eddy activity advected into the area from locally generated instabilities, thus impeding attempts at understanding the effect of the former on the nearshore upwelling regime. In order to fully appreciate the effect of Agulhas leakage on the dynamics of the Benguela system Chapter 6 compares the reference simulation to a simulation in which Agulhas influence in the Benguela has been removed.

Chapter 6

The influence of the Agulhas Current on the Benguela system

Rings, eddies and filaments that spawn at the Agulhas retroflection have a significant influence on the mean state and mesoscale variability of the Benguela Current system. In fact, it is the proximity to a western boundary current that singles out the Benguela as unique among the worlds four eastern boundary current systems. The Benguela Current can be thought of as the vehicle for passage of Agulhas rings and eddies into the Atlantic Ocean. Varied accounts of the percentage of Indian Ocean water within the Benguela have been made and range from 3-20 Sv (Gordon et al. (1992)). Large differences may be attributed to the large variations in Agulhas input Gordon (2003), however the difficulty of separating the contributions from Indian Ocean Central Water (IOCW) and South Atlantic Central Water (SACW) due to their similar water mass characteristics may also be a factor. While there is no consensus on the quantification of the volume of water of Indian Ocean origin within the Benguela Current, the fact that it introduces an enormous pool of energy is unequivocal. For example, Matano and Beier (2003) found that the eddy fluxes of the Agulhas eddies supply most of the energy of the Benguela Current and the southeastern portion of the Cape Basin has been dubbed the 'Cape Cauldron' by Boebel et al. (2003) due to its highly energetic nature as a result of the interaction of Agulhas Rings, eddies and filaments.

The importance of this region of inter-ocean exchange lies in its, possibly critical,

role in the global thermohaline circulation via the transport of heat and salt into the north Atlantic (Gordon (2003)). As such, this region has received much scientific attention over the past few years, with a special edition of 'Deep-Sea Research' (Inter-Ocean exchange around Southern Africa: 2003, Volume 50, No. 1) dedicated to it. However, most research has focussed on the global impact of Agulhas influx into the Atlantic Ocean rather than its local effect on the eastern boundary, Benguela Current system.

Some observations have suggested that Agulhas Rings can have a direct impact on the Benguela system, for example: Duncombe-Rae et al. (1992a) connected the poor year-class of anchovy in 1989 with the unusually nearshore location of an Agulhas Ring and Duncombe-Rae et al. (1992b) speculated that Agulhas Rings can lead to the formation of extremely large upwelling filaments. Aside from these direct effects, ways in which the Agulhas influence the mean state of the Benguela system can have global ramifications. For example: an important aspect of the Benguela system as one of the worlds four eastern boundary upwelling regimes lies in its role in the maintenance of the global heat balance. The heat gain (from the overlying atmosphere) of the cold surface waters of upwelling regimes balances the surface heat loss at high latitudes. Boccaletti et al. (2003) showed that the structure of the thermocline is closely tied to the global balance of heat, of which these two regions are key. For example, less surface heat loss in the high latitudes needs to be compensated for by less surface heat gain in upwelling regions. To achieve this the water that upwells needs to be warmer and, in order for this to happen at a constant wind forcing, the thermocline has to deepen. The effect of the Agulhas on the nature of the Benguela upwelling regime can therefore also have significant global climate implications and should consequently not be neglected in research efforts.

The previous chapter illustrated the difficulty of separating features of Agulhas origin from those related to the upwelling regime due to the very large signal introduced by the former. While Agulhas leakage is characterized by rings and eddies, their relatively large size and symmetry are such that the removal of the transient (or eddy) signal does not entirely remove their effect from the mean state (Treguier

et al. (2003)). Consequently, conclusive results on the impact of Agulhas leakage on the Benguela system itself are difficult to achieve. In an attempt for more definitive answers on the role of the Agulhas Current, this chapter analyzes a model experiment in which the flow of the Agulhas Current has been diverted eastward at ~30°S on the east coast of South Africa (see Chang (2009)).

6.1 Removing the Agulhas Current

The model experiment in which the Agulhas Current is diverted eastward before reaching the tip of Africa (from now on referred to as the no Agulhas, or NOA, experiment) is based on the same ROMS model configuration that was used for the analysis of the mean state and mesoscale variability in Chapters 4 and 5 respectvely (we will refer to it as the reference, or REF, experiment from now on). The reference configuration is fully described in Chapter 3. In summary, it employs the 2-way nesting capability such that an approximately 27 km parent domain (the SAfE domain, designed by Penven et al. (2006a) and shown in Figure 3.4) supplies the boundary conditions for an approximately 9 km child domain that spans the entire Benguela upwelling system (refer to Figure 3.5). The 2-way nesting approach also allows the output of the child domain to feed into the parent domain, thereby reducing blockages at the boundaries. The wind forcing is based on a monthly climatology derived from the QuikSCAT 0.5° product spanning 2000-2007, the intial conditions and surface fluxes are from the WOA 2005 climatology. The only difference between the REF simulation and the NOA experiment is that the land mask has been adapted such that a curved dam has been created on the east coast of South Africa at 30°S, extending eastward to about 36°E (refer to Figure 6.1a).

As an indication of the effect on the mean flow by the diversion of the Agulhas Current in the NOA experiment, Figure 6.1 shows the annual mean depth-integrated transport streamlines and SSTs for both the NOA and REF simulations. The effect of the dam on the flow of the Agulhas Current is to deflect it eastward before it reaches the termination of the African continent, thus preventing rings and eddies shed at its retroflection from entering the Benguela system. The change in the mean

state manifestation of the Benguela Current is significant: the intense, meandering flow punctuated by anticyclonic features becomes a weaker, more steady northwestward flow. A further consequence of creating an early retroflection of the Agulhas Current is that part of the South Atlantic Current flows eastward onto the Agulhas Bank until about 30°S at which point it retroflects in an anticyclonic sense and flows westward along the coast and into the Benguela system. The streamlines in Figure 6.1a suggest that at the tip of the dam there is some leakage of Agulhas water westward and toward the south of the continent.

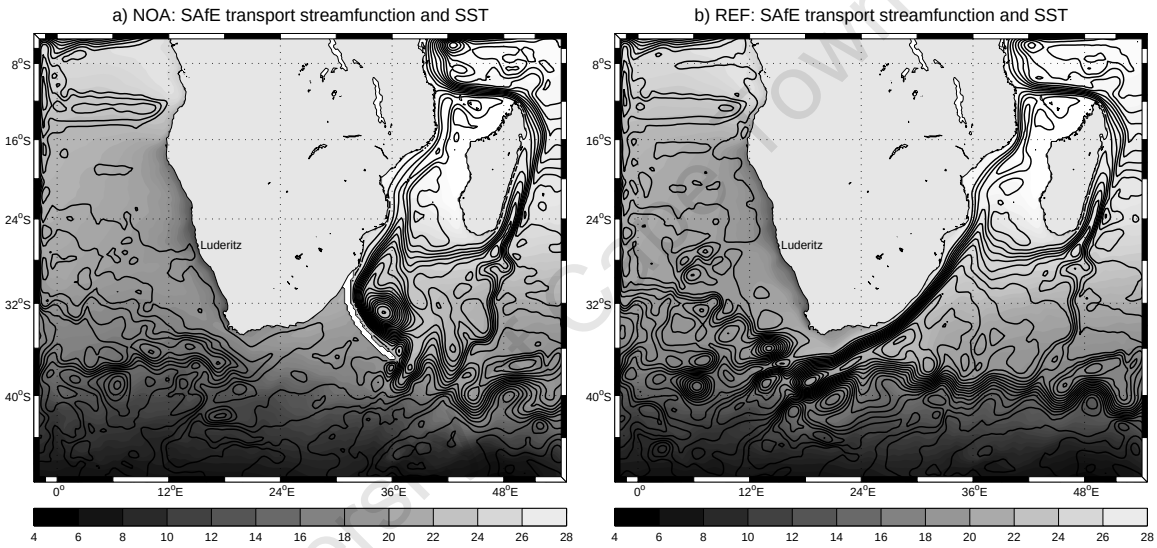

Figure 6.1: Annual mean, depth-integrated transport streamlines and SSTs for the (a) NOA and (b) REF simulations.

Figure 6.2 shows the annual mean surface EKE, based on 2-daily model output for the NOA and REF simulations. The huge surface EKE signal of the offshore regions of the southern Benguela system is essentially removed by the NOA experiment. Some Agulhas-induced variability extends southward and westward around the tip of the dam, but it does not extend enough westward to significantly influence the Benguela system. The boundaries of the parent domain are forced with WOA climatology data, which retains the signal from the Agulhas. However, since we are only interested in the local effects of removing the large offshore EKE signal within the child domain, the retention of an Agulhas signal at the parent boundaries does not influence our results.

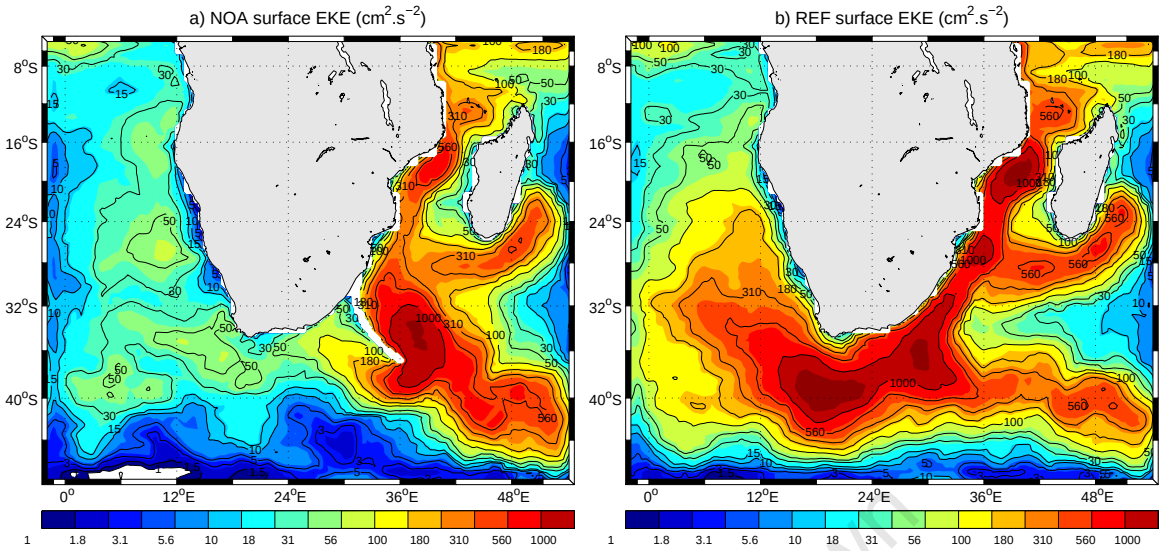

Figure 6.2: Annual mean surface EKE (cm^2s^{-2}) for the (a) NOA and (b) REF simulations.

Water mass properties of flow into the child domain are examined for both the REF and NOA simulations in order to test whether Agulhas leakage into the Benguela has indeed been 'switched off'. Figure 6.3a shows the annual mean flow at a depth of 60 m as well as the salinity for the REF simulation and Figure 6.3b shows a T-S plot for all grid points along the southern and eastern oceanic boundaries of the child domain (the colourbar represents the depth). Based on the currents in Figure 6.3a, two potential source regions are identified (shown by the white boxes) for water types entering the Benguela system at the southern boundary of the child domain. The source regions represent water of Agulhas/Indian and South Atlantic origin and their characteristic T-S profiles (averaged in their boxes) are shown on Figure 6.3b as a solid and dashed line respectively. For the REF simulation, the T-S profiles of water masses passing the southern boundary closely mimic the characteristic profile of the Agulhas/Indian source region. This is especially true for the lower central water mass (represented by the straight line part of the profile, spanning ~6-14°S and ~34.55-35.2 psu). The Antarctic Intermediate mass (AAIW), which is represented by the salinity minimum, is also dominated by the high salinity signal introduced by Agulhas/Indian Ocean water, but has lower salinity departures which indicate a greater influence of South Atlantic water. The surface waters (i.e.

100-150 m: represented in darkest shades of red) along the southern boundary of the child domain (i.e. 4-20°E) span a wide range of tempertures and salinities, suggesting water mass contributions (and their subsequent modification) from several sources and demonstrates the turbulent nature of the so-called 'Cape Cauldron'.

The T-S plot shown in Figure 6.4b is the equivalent of Figure 6.3b, but for the NOA experiment. In this case however, three potential source water regions are selected based on the adjusted flow patterns: Agulhas/Indian, south Atlantic and tropical Atlantic (refer to the white boxed regions in Figure 6.4a for their locations). The central and intermediate water masses are too fresh to be primarily made up of waters of Indian Ocean origin, but instead appear to be a mixture of tropical and south Atlantic origin (the dash-dot and dashed lines respectively that envelope the T-S properties of water crossing the southern boundary of the child domain). Water masses deeper than AAIW converge with T-S properties associated with south Atlantic water mass characteristics and are less influenced by tropical Atlantic waters. Once again, the surface waters are quite varied in their T-S properties. In fact, the range of surface salinities exceeds that of the REF simulation, with the dominant portion being fresher, but with distinct more saline (than evident in Figure 6.3b) excursions due to the input of highly saline tropical Atlantic surface water. Evidence that some leakage from the Agulhas does occur lies in the high temperature 'tail' on the NOA T-S plot. While the high salinities might suggest the tropical Atlantic as the source, the higher temperatures imply that the source is a warm and saline water mass that is near enough not to be modified too much by surface heat exchanges.

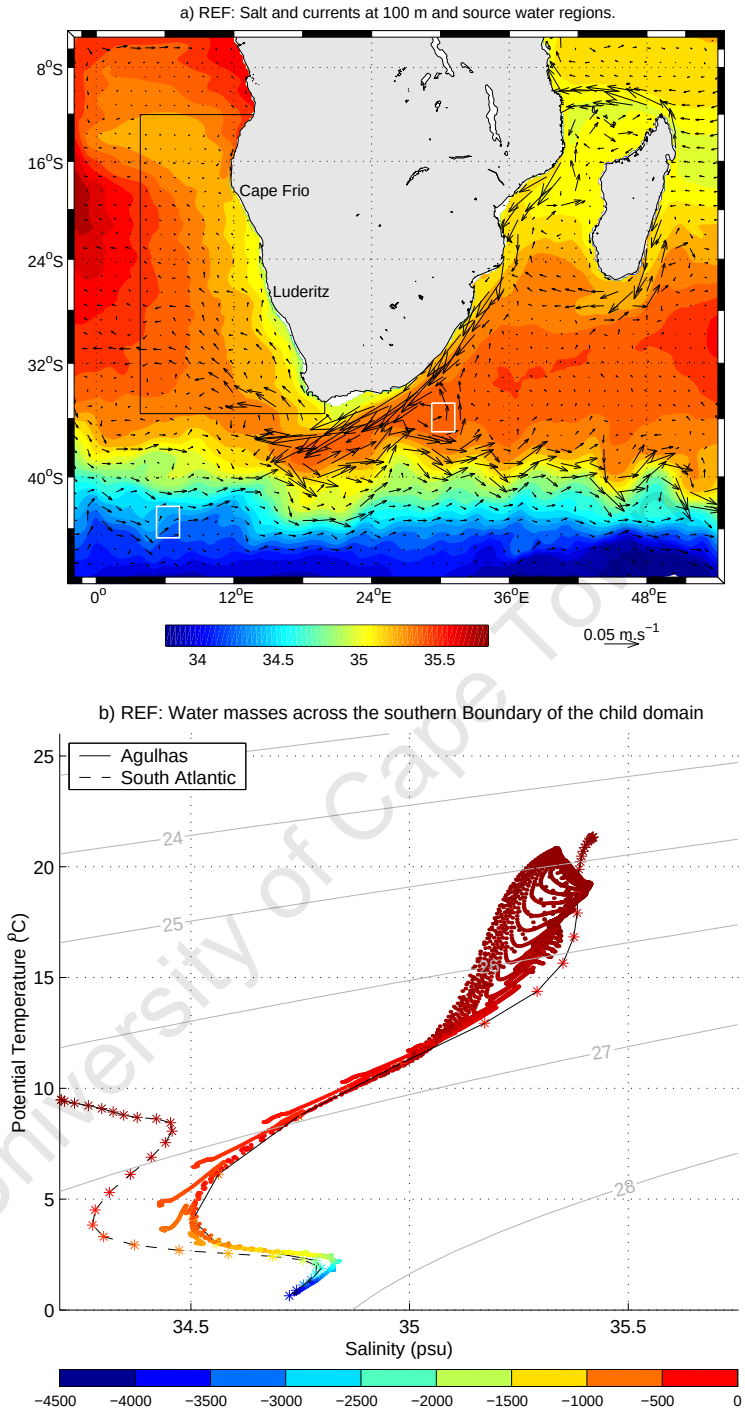

Figure 6.3: a) Salinity and currents at 100 m depth for the REF simulation. The white boxed areas represent source regions (and the associated water mass properties) of water entering the child domain from the south. The black box deliminates the child domain. b) T-S plot of all grid points along the southern and eastern oceanic boundaries of the child domain, with the colourbar representing the depth. The solid and dashed lines represent the characteristic water mass properties (Agulhas/Indian and South Atlantic respectively) of probable source waters (represented by the white boxes in a).

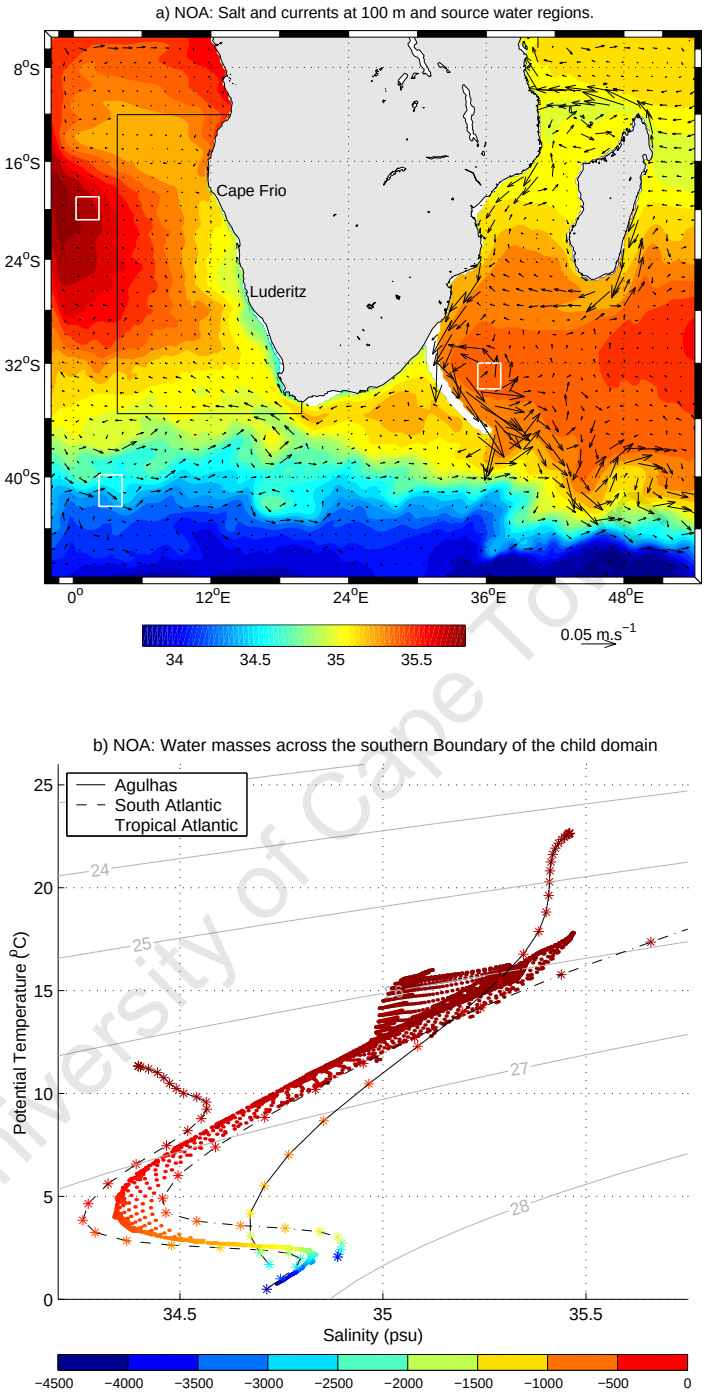

Figure 6.4: a) Salinity and currents at 100 m depth for the NOA simulation. The white boxed areas represent source regions (and the associated water mass properties) of water entering the child domain from the south. The black box deliminates the child domain. b) T-S plot of all grid points along the southern and eastern oceanic boundaries of the child domain, with the colourbar representing the depth. The solid, dashed and dash-dot lines represent the characteristic water mass properties (Agulhas/Indian, South and Tropical Atlantic respectively) of probable source waters (represented by the white boxes in a).

The annual mean currents and salinity at a depth of 60m shown in Figure 6.4a and the T-S plot in Figure 6.4b suggest that while there does appear to be some leakage of the Agulhas into the Benguela system for the NOA experiment, the effect seems to be relatively small, limited to the surface layers and the eastern edge of the child domain. Figures 6.1a and 6.1b show that a distinct manifestation of the influx of the Agulhas into the Benguela exists in SSTs and figures not shown suggest that the temperature signal of Agulhas influx extends to a depth of at least 1000 m. We calculate the mean heat flux across the southern boundary of the child domain at 35^{o}S (using data from the parent domain) for the REF and NOA simulations, taking advantage of the distinct temperature signal of Agulhas influx to make inferences on the success of the dam at removing it. The heat fluxes across the southern boundary of the Benguela system are extracted from the parent domain as its resolution is more comparable to the model used by Reason et al. (2003) to make the same calculations. The net mean heat flux across the southern boundary for the REF simulation is 1.2 PW, which is higher than the estimates of Reason et al. (2003) for the same section (6-20^{o}E at 35^{o}S) by about 0.17 PW (16 %). The fact that our estimate is higher is likely to be partly related to the fact that our simulation results in too much Agulhas leakage (this was discussed in Chapter 4). However, the resolution of the model results used by Reason et al. (2003) was ~36 km, as opposed to the ~27 km of our parent simulation. It is possible therefore that their heat fluxes are slightly underestimated due to the inability of their lower resolution simulation to capture higher resolution fluctuations resulting in enhanced heat exchange into the Benguela system.

Table 6.1 shows the seasonal mean heat fluxes for both the REF and NOA simulations and allows us to quatify the amount of heat that has been prevented from entering the Benguela system due to the eastward diversion of the Agulhas Current. Though there are seasonal differences, on average the net heat exchange into the Atlantic across 35^{o}S has been curtailed by ~50 %. In the REF experiment (the bars in black in Figure 6.5), the heat flux exchange pattern displays a distinct northward-southward alternating pattern between ~4-12^{o}E, which is related to the 'standing eddy' features that can be seen in Figure 6.1b and can be thought of as the

mean manifestation of the preferential path of Agulhas Rings. The direction of the NOA heat flux (the bars in grey in Figure 6.5) is always northward across 35°S and decreases toward the west, but not as significantly as in the REF simulation. At the far eastern edge of the southern boundary of the child domain, the northward heat flux of the NOA experiment exceeds that of the REF simulation. Based on Figures 6.1, 6.3a and 6.4a we hypothesize that the 'overshooting' of the Agulhas Current at the southern tip of the continent inhibits the advection of very warm surface water into the eastern-most reaches of the southern boundary of the child domain. On the other hand, the weaker westward 'retroflection' of the South Atlantic Current on the Agulhas Bank for the NOA experiment allows for the advection of the warmer waters of the Agulhas Bank into the near-shore regions of the southern boundary of the Benguela system.

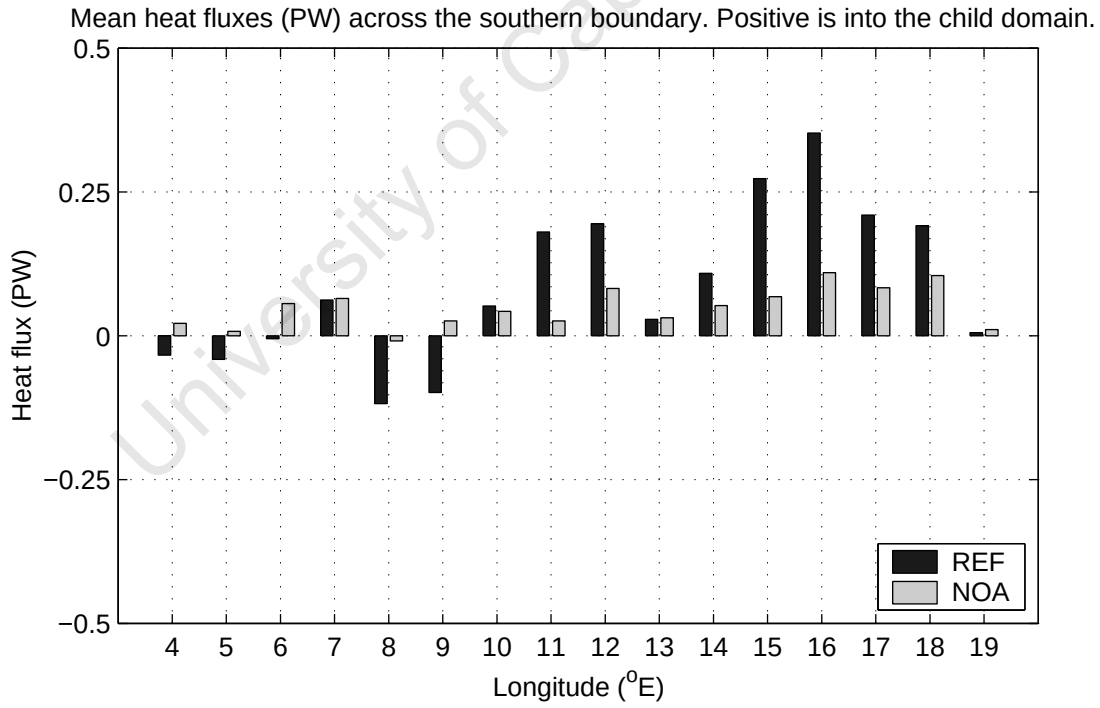

Figure 6.5: Annual mean depth integrated heat fluxes in 1° sections across the southern boundary of the child domain for the REF (black) and NOA (grey) experiments. 1 PW = 10^{15}W.

Table 6.1: Seasonal mean heat fluxes across 35°S, from 5-20°E and their standard deviation from Reason et al. (2003), as well as for the REF and NOA parent domains (in PW). The difference of the latter two are shown as a percentage.

	Summer	Autumn	Winter	Spring	Annual	Seasonal STD
Reason et al. (2003)	0.92	1.10	0.97	1.11	**1.03**	*0.1*
REF	1.1	1.2	1.1	1.5	**1.2**	*0.2*
NOA	0.66	0.73	0.62	0.6	**0.65**	*0.06*
Percentage Diff.	40 %	39 %	44 %	60 %	**46%**	*70 %*

The T-S plots and the heat flux calculations at the southern boundary of the Benguela system for the REF and NOA simulations give us confidence that, while some Agulhas leakage appears in the surface layers at the eastern edge of the southern boundary, on the larger scale its influence has been significantly reduced. In diverting the Agulhas Current eastward at 30°S, the flow pattern on the Agulhas Bank has been altered such that the northern edge of the South Atlantic Current flows onto the Agulhas Bank to approximately 30°E at which point it retroflects in an anticyclonic sense to flow westward along the coast and into the Benguela system around the Cape of Good Hope. Based on just the hydrographic variables (i.e. temperature and salinity) derived by the model, it is not possible to quantify the exact volume of purely Agulhas/Indian Ocean water entering the Benguela for the REF and NOA simulations. We are therefore unable to explicitly say by what percentage of the Agulhas influx has decreased in the NOA experiment.

6.2 Effect on mean state

6.2.1 Thermohaline characteristics

As a first approach at investigating the effect of essentially inhibiting the Agulhas leakage in the Benguela system, Figures 6.6 and 6.7 show the mean SSTs and SSSs, their seasonal standard deviation (STD) for the REF and NOA simulations along with their differences. The SST for the NOA experiment is cooler than for the REF simulation south of ~25 °S, which is commensurate with the region most strongly impacted by Agulhas leakage (evidence of this lies in the depth integrated and depth averaged EKE plots in Figure 5.14 in Chapter 5). Within this area, three regions that display greatest decreases in SST are associated with the Cape Columbine upwelling plume region (from ~33°S northward along the shelf), the southern boundary of the system and just to the south of the Lüderitz upwelling cell (~27.5 °S). All are related to the changing flow patterns. For example: for the REF simulation, a cyclonic meander is present in both the surface flow (see Figure 4.5) as well as the depth-integrated transport streamfunction (Figure 4.15), bringing warmer oceanic water closer inshore and thereby inhibiting the cool surface signal of SST in the vicinity of Lüderitz. This distinct meander is not present in the NOA experiment, therefore resulting in the much cooler SSTs we see in this region. The former two regions of much cooler SSTs (i.e. in the region of the upwelling plume off Cape Columbine and at the southern boundary) in the NOA experiment are related to the absence of the two distinct streams of the Benguela Current (see Figure 4.5) that advect warmer water into these regions for the REF simulation. The higher seasonal SST STD (refer to Figure 6.6f) for the NOA experiment is also limited to the region that, in the REF simulation, is dominated by Agulhas influx. In the REF simulation this region is constantly warmed by Agulhas leakage that has no clear seasonal cycle, however, without Agulhas input this region experiences distinct seasonal SST variability due to surface heating via solar radiation. Therefore, the seasonal SST STD is greater in this region for the NOA experiment than for the REF simulation. The greater sesonal signal in the NOA experiment could also be related with seasonal changes in the position of the Subtropical Front.

The mean surface salinity plots for the REF and NOA simulations (Figures 6.7a and 6.7b) and their difference (Figure 6.7c) show that, as we might expect, the water that upwells at the coast is fresher for the NOA than for the REF simulation. The lower SSS signal in the at the southern boundary of the NOA experiment (in blue) is evidence for the greater proportion of water of south Atlantic origin entering the Benguela system. Between these regions of lower SSS is a fan of higher SSSs in the NOA experiment (shown in red in Figure 6.7c). Higher seasonal variations in SSSs occur in the NOA experiment at the outer edges of the upwelling regime (i.e along the shelf in the southern Benguela and further offshore in the northern Benguela) as well as southward of about 30°S. The former is related to the strong surface salinity signal of the upwelling regime and, particularly, that its oceanic limits are no longer influenced by the perennial influx of Agulhas leakage in the NOA experiment. The high seasonal signal of SSS at the southern boundary in the NOA experiment is a result of seasonal fluctuations of the location of the Subtropical Front.

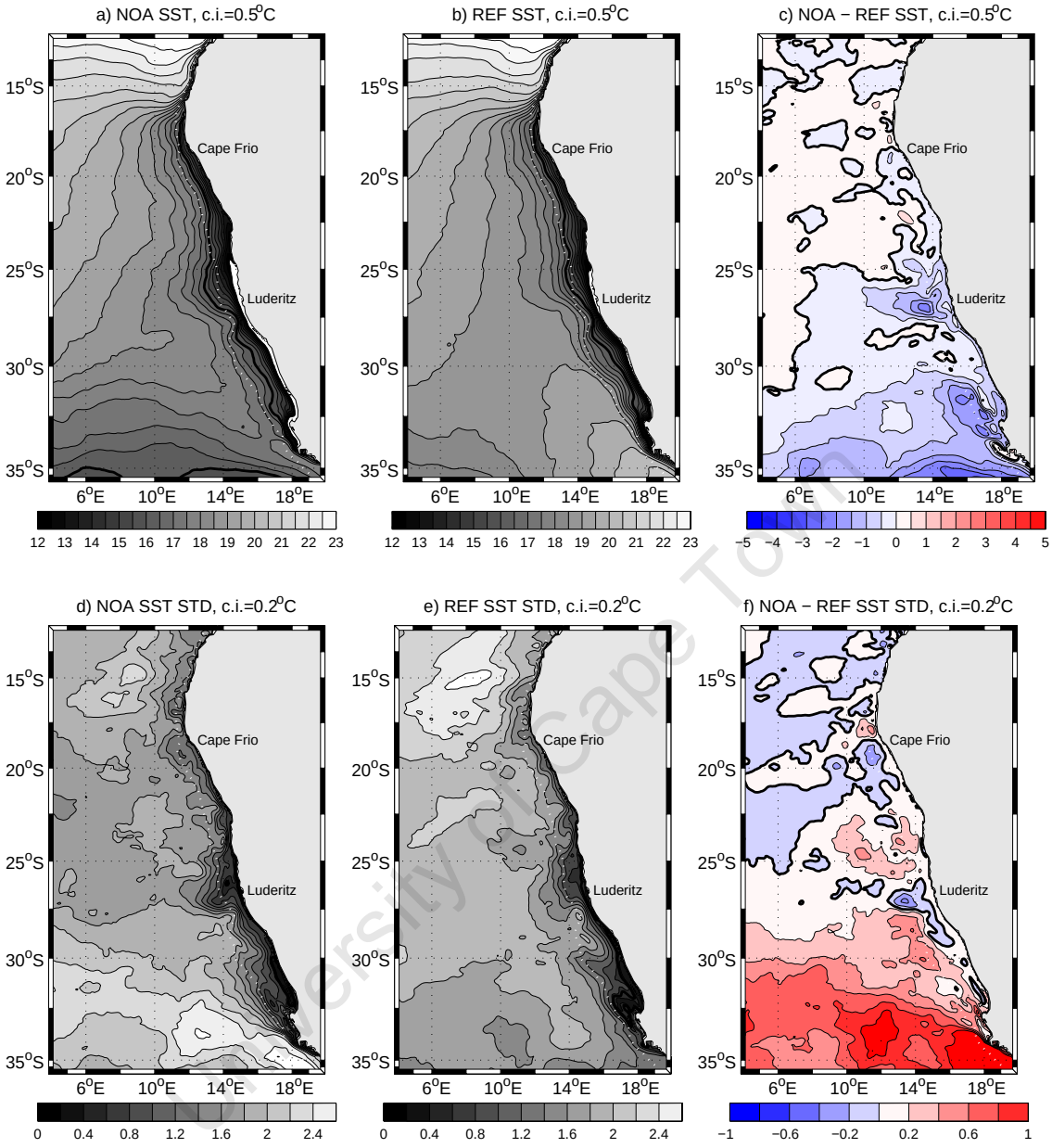

Figure 6.6: Annual mean SST based on the NOA (a) and REF (b) simulations as well as their difference (c: i.e., NOA-REF). The bold lack line in figures a and b represent the 16°C isotherm and in figure c in represents the 0°C isotherm. The dotted white line represents the approximate position of the shelf-edge.

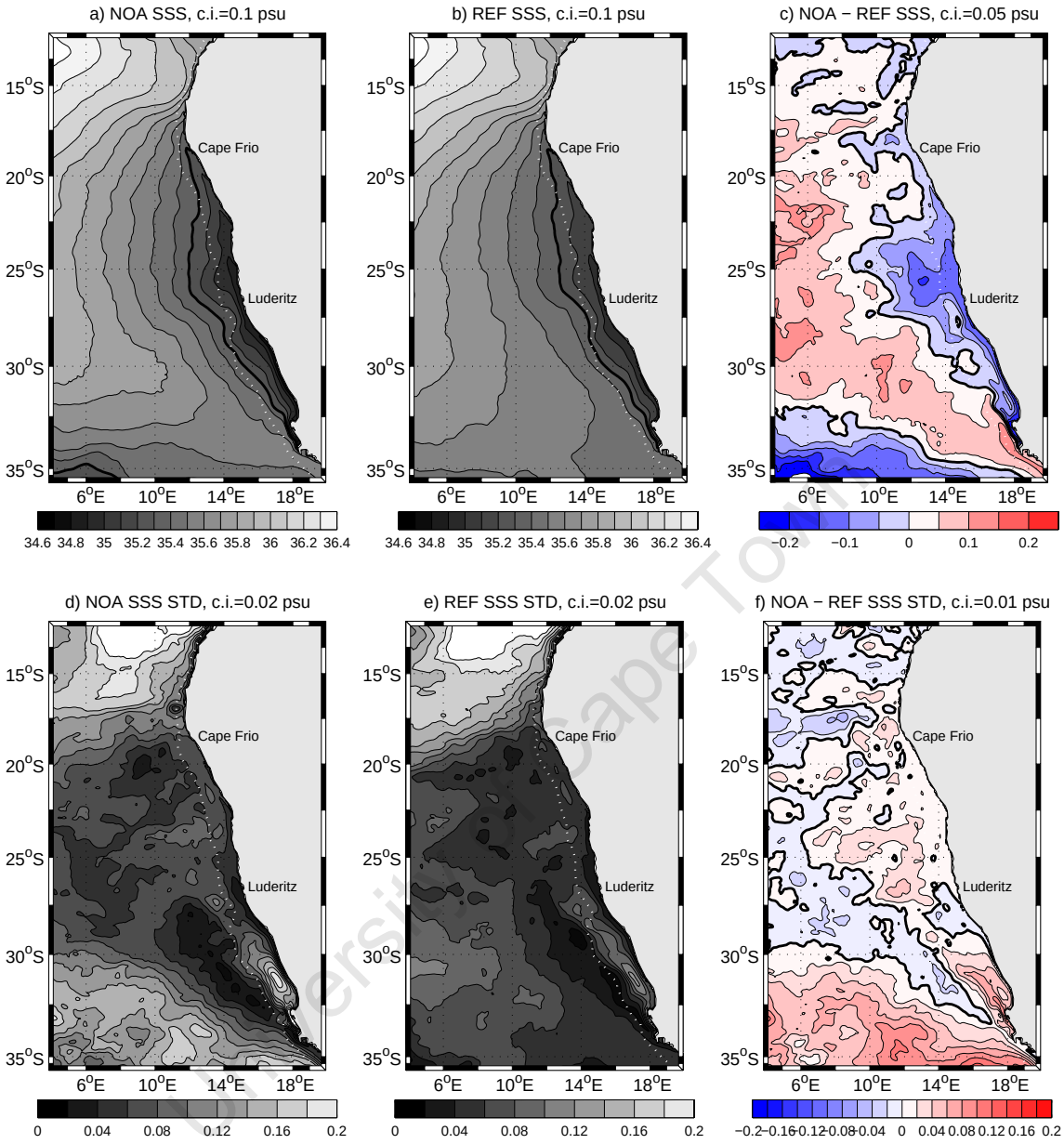

Figure 6.7: Annual mean SSS based on the NOA (a) and REF (b) simulations as well as their difference (c: i.e., NOA-REF). The bold lack line in figures a and b represent the 35.2 psu isoline and in figure c in represents the 0 psu isoline. The dotted white line represents the approximate position of the shelf-edge.

The impact of altered thermohaline influxes of the Benguela system on the vertical structure and associated stratification adjustments can have important consequences for the mean flow field as well as locally generated instabilities. Figures 6.8 and 6.9 show annual mean, alongshore averaged temperature and salinity sections for the NOA and REF simulations as well as the difference between the two for the southern Benguela box (as defined in Figure 4.6). Positive (negative) values are in red (blue) and show where the NOA experiment is warmer (cooler) and saltier (fresher) than the REF simulation. The temperature sections in Figures 6.8a and 6.8b reveal a shallower mixed layer and less steeply sloping isotherms at the shelf-edge for the NOA experiment than for the REF simulation. This suggests that there is less potential for locally generated instabilities at the shelf edge for the NOA experiment. For both simulations the horizontal nature of the isotherms over the shelf imply a relatively quiescent area. Indeed, the plot of the difference between NOA and REF temperatures in Figure 6.8 shows that removing the effect of the Agulhas decreases temperatures most significantly seaward of the shelf-edge and that the impact is much less on the shelf. The smaller decrease of temperatures on the shelf could be a result of the upwelling of cooler waters that originate beyond the shelf-edge and that are therefore more impacted by the removal of the Agulhas.

The alongshore averaged, annual mean salinity sections for the NOA and REF simulations in Figure 6.9 suggest that waters that upwell to the surface (i.e. the central water mass) are fresher and that the AAIW mass (which is characterized by the salinity minimum) is shallower for the NOA experiment. A more unexpected result is the higher surface salinities (in the upper 50-100 m) which, as discussed in the previous section, is associated with the greater influence of tropical Atlantic waters (that have a higher surface salinity signal than waters of Indian Ocean origin) in the NOA experiment.

Figure 6.10 is a T-S plot based on the alongshore averaged temperature and salinities shown in Figures 6.8 and 6.9 and extracted from a point 250 km offshore. It compares the T-S properties of the NOA and REF simulations and provides a succinct summary of thermohaline changes resulting from the early diversion of the Agulhas Current. The surface waters of the NOA experiment are more saline, have

lower temperatures and do not extend as deep as the REF simulation. Below the surface water is the central water mass from which water is upwelled and has been observed to upwell in the southern Benguela from depths of 100-300m within this water mass (Shannon (1985)). The NOA experiment produces a central water mass than is colder and fresher than at an equivalent depth in the REF simulation. The distinct salinity minimum represents the core of the AAIW and it is shallower and fresher in the NOA experiment. These temperature and salinity characteristics and the depth ranges of each water mass for the NOA and REF simulations are listed in Table 6.2.

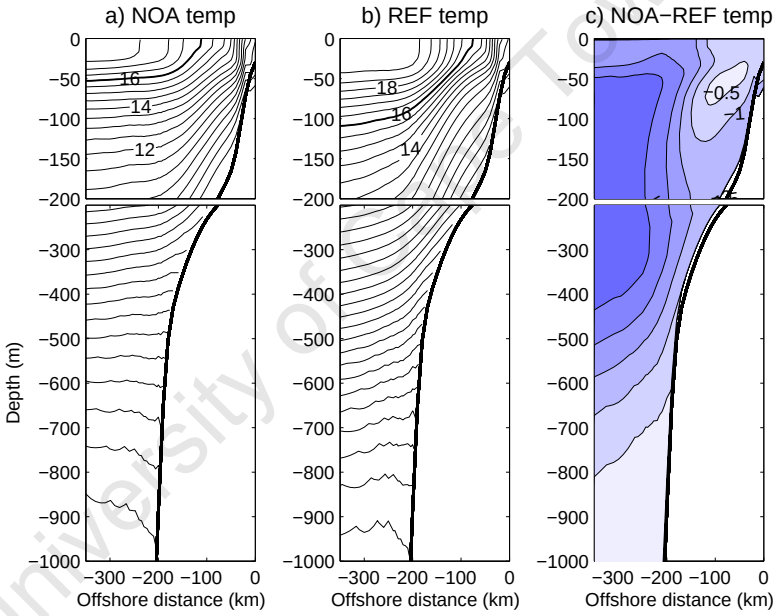

Figure 6.8: Alongshore averaged, annual mean temperature in the southern Benguela box (see 4.6) based on the NOA (a) and REF (b) simulations as well as their difference (c: i.e., NOA-REF). The bold lack line in figures a and b represent the 16°C isotherm and in figure c in represents the 0°C isotherm.

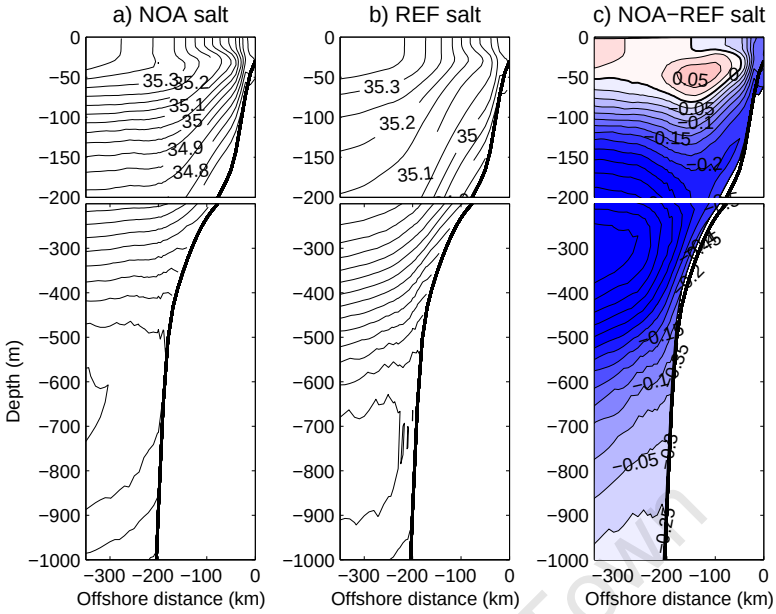

Figure 6.9: Alongshore averaged, annual mean salinity in the southern Benguela box (see 4.6) based on the NOA (a) and REF (b) simulations as well as their difference (c: i.e., NOA-REF).

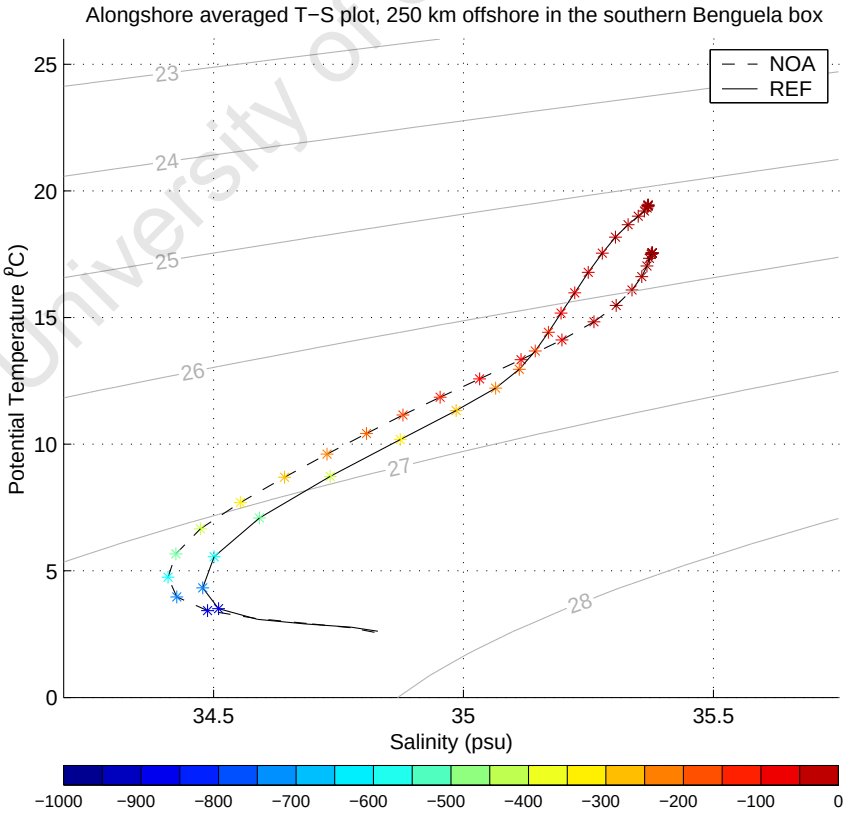

Figure 6.10: T-S plot for the average vertical profile for the offshore domain: 30-32°S, 10-12°E, based on the NOA (black) and REF (blue) simulations.

Table 6.2: Temperature-salinity characteristics and depths of the three water masses 250 km offshore in the southern Benguela.

	REF	NOA
Surface Water	14-18°C 35.15-35.75 psu 0-200 m	16-17.5°C 35.25-35.75 psu 0-100 m
Central Water	6-14°C 34.5-35.15 psu 200-700 m	6-16°C 34.45-35.25 psu 100-600 m
AAIW (core)	4.5°C $<$ 34.5 psu 700 m	5°C $<$ 34.45 600 m

6.2.2 Currents

Large-scale flow regime

Despite the removal of the Agulhas Current, the large-scale flow regime for the NOA experiment once again presents a clear impression of the contrasting northern and southern Benguela regimes. Figure 6.11 shows the depth integrated (0-1000 m) transport streamlines for both the NOA and REF simulations. They similarly reveal the separation of a sluggish poleward flowing regime in the north from a more intense equatorward regime in the south by a distinct offshore transport in the vicinity of Lüderitz. Without input from the Agulhas Current, the equatorward flow in the southern Benguela is weaker, takes on a more direct north-westward path and is unencumbered by the passage of Agulhas Rings that are manifest as large meanders in the mean flow of the Benguela Current. Furthermore, the distinct nearshore and offshore streams of the Benguela Current, separated by a cyclonic meander, that is present in the REF simulation does not apper in the NOA experiment. Though still present, the cyclonic meander southward of the distinct offshore transport at

Lüderitz is less intense, transporting less oceanic water shoreward into the upwelling regime. Evidence of this can be seen in the difference between NOA and REF annual mean SSTs (Figure 6.6c), which shows that the NOA experiment SSTs are significantly cooler at the Lüderitz upwelling cell due to the decreased influence of warmer oceanic water. While the cyclonic feature appears to be partially driven by the sudden narrowing of the continental shelf at this location (i.e. at ~27.5 °S), the presence of Agulhas leakage intensifies it and, in doing so, impacts on the Lüderitz upwelling cell (e.g. note the location of the 16°C isotherm at ~27.5°S in Figures 6.6a and 6.6b).

Figure 6.11c is the transport streamfunction based on the Sverdrup relation (see equation (4.7)) and presents a better comparison with the depth-integrated transport streamfunction for the NOA experiment than for the REF simulation.

In contrast to the seasonal fluctuations in the equatorward transport of the REF simulation, offshore of about 11°E at 30°S a persistent seasonal exists in the NOA experiment (refer to Figure 6.12) such that it is greatest during summer and least during winter.

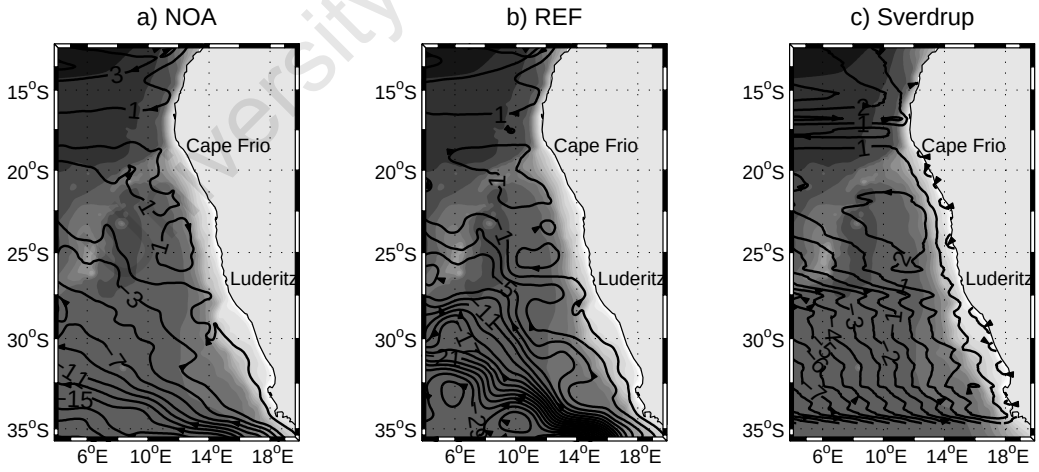

Figure 6.11: Annual mean transport streamfunction, based on the vertically integrated (0-1000 m) horizontal velocity components from the NOA (a) and REF (b) simulations. c) the transport streamfunction based on the Sverdrup relation. The bathymetry is shown in grey.

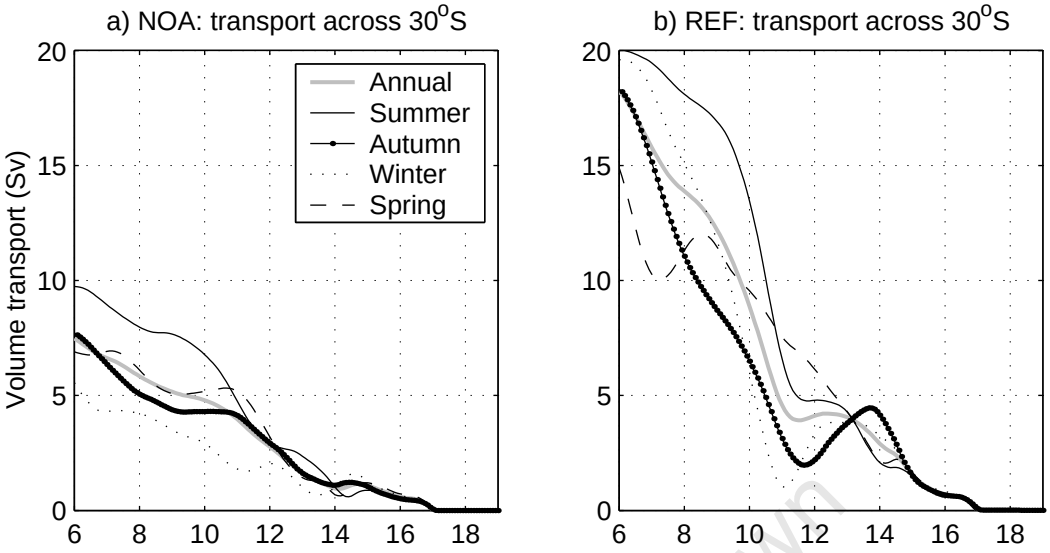

Figure 6.12: Annual and seasonal mean transports across 30°S, based on the NOA (a) and REF (b) simulations.

Currents on the shelf and within the upwelling regime

Annual mean alongshore, cross-shore and vertical velocities at the shelf-edge for the NOA experiment are shown in Figure 6.13. The shelf-edge flow pattern is important because it links the large-scale flow regime with the nearshore current structure and provides a window to boundary exchange processes that may have crucial implications for the upwelling system. The most striking difference between Figure 6.13 and the equivalent for the REF simulation (Figure 4.18 in Chapter 4) lies in the alongshore flow south of approximately 22°S. In the REF simulation the meandering, rather intense equatorward flow in the southern Benguela extends as far as ~22°S, but it shallows rapidly at ~27°S from ~300 m to ~100 m. While an equatorward current is still dominant at the southern Benguela shelf it is punctuated by regions of poleward flow (at 32°S and 33°S) and is much weaker. It extends only as deep as about 200-300 m southward of ~27°S where it abruptly gives way to a poleward current overlaid by a shallow equatorward flow. This transition of the alongshore currents is commensurate with a strong offshore current, with peak velocities of ~12 $cm.s^{-1}$ that results in the offshore diversion of the equatorward and a portion of the poleward flow. The poleward flow is associated with downward velocities and hence

deepens as it moves southward, as in the REF simulation. However, in the NOA experiment it extends southward beyond 27°S beneath the shallower equatorward flow (~200 m) and there is evidence that it enters the southern Benguela at even shallower depths (at 32°S and 33°S). This suggests that Agulhas leakage has a considerable role to play in preventing water of northern Benguela and perhaps even the low oxygen water of tropical Atlantic origin from entering the southern Benguela system.

As it is the circulation of the southern Benguela that is most affected by the removal of the Agulhas, cross-shelf sections (to 350 km offshore) of the three, alongshore averaged velocity components for the southern Benguela box (see Figure 4.6), based on the NOA experiment, are shown in Figure 6.14. Notably, the deep (>500 m) and intense (>20 $cm.s^{-1}$) shelf-edge equatorward jet (alternatively referred to as the inshore stream of the Benguela Current) that approximates reality and is shown in Figure 4.23 becomes shallower (~300 m), weaker (>10 $cm.s^{-1}$) and shifts shoreward and onto the broad shelf. The adjustment of the alongshore and cross-shore currents is accompanied by the disappearance of the shelf-edge upwelling cell that features prominently in the REF simulation (see Figure 4.23 c). The implication of this is that the meandering nature of the intense inshore stream of the Benguela Current causes shelf-edge upwelling via the divergence of flow at the shelf-edge.

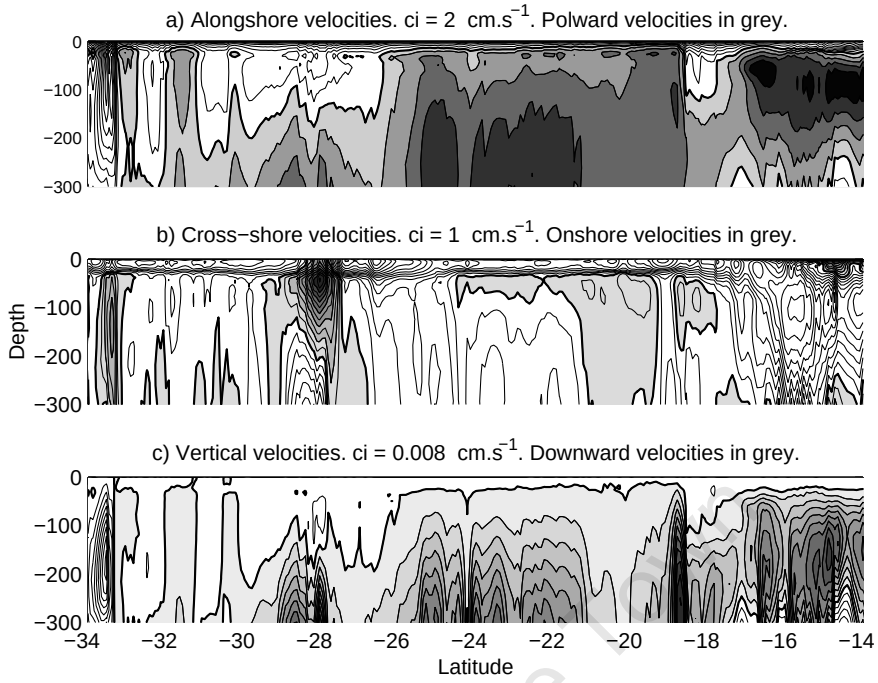

Figure 6.13: Annual mean alongshore (a), cross-shore (b) and vertical (c) velocities at the shelf-edge (taken as the 500 m isobath). Shades of grey represent poleward, onshore and downward velocities respectively.

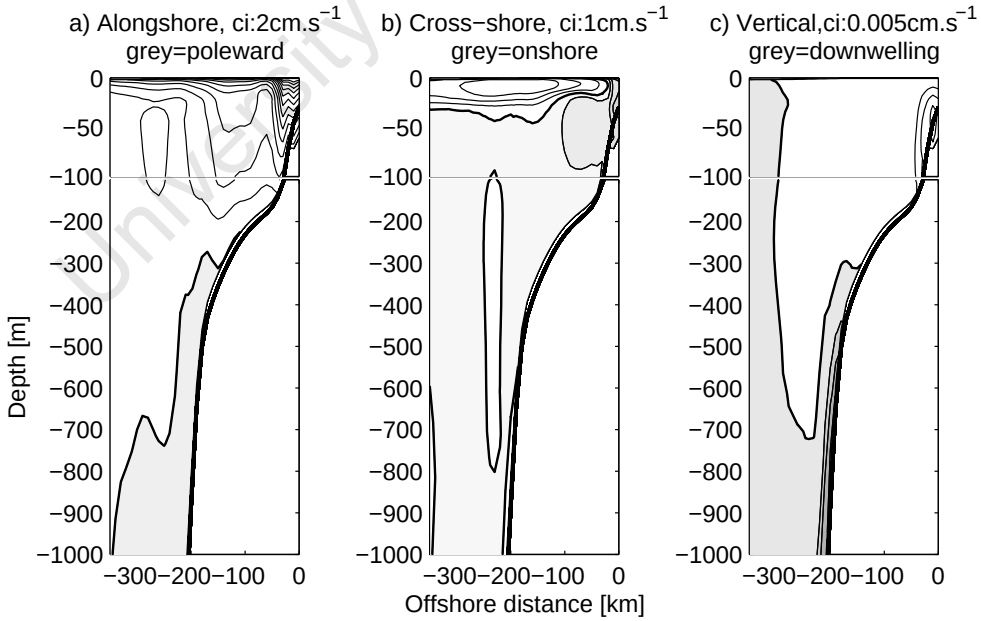

Figure 6.14: Annual mean, alongshore averaged, a) alongshore, b) cross-shore and c) vertical velocities in the boxed region chosen to be representative of the southern Benguela (see Figure 4.6). Grey shaded regions represent poleward, onshore and downward velocities.

Goodhope Jet

The role of the Goodhope Jet in transporting fish eggs and larvae from their spawning ground on the Agulhas Bank to their nursery area in St Helena Bay is a key factor in the high productivity of the southern Benguela region (Shelton and Hutchings (1982)). The intense horizontal gradients observed by Bang and Andrews (1974) was the first evidence for its existence and Strub et al. (1998) used satellite altimetry to investigate the seasonal signal of its surface manifestation. They noted a seasonal intensification that they associated with the interplay of the injection of high steric heights via Agulhas influx and the low steric heights associated with the coastal upwelling regime. The results of the NOA experiment allow us to reinforce current theories in a more conclusive manner.

Figure 6.15 presents the summer and winter mean current field at the surface for both the NOA and REF simulations and shows that an intense equatorward jet is present off the Cape Peninsula during both seasons for each. The mean summer currents over the shelf (shown as the blue dashed line) for the REF simulation reveal a jet that is extensive and is evident from Cape Agulhas to at least Cape Columbine. A distinct bifurcation of the jet appears not only at Cape Columbine (which has been well-documented) but also at Cape Point. The jet is reduced in winter to small areas off Cape Point and Cape Columbine of intense equatorward flow. The seasonal cycle of upwelling in this region can account for these seasonal variations in the nature of the jet (i.e. enhanced upwelling during summer results in a lowering of the coastal SSH and an increased offshore steric height gradient and, in turn, increased equatorward flow). While there appears to be a clear seasonal cycle in the flow pattern on the shelf, there is little change in the offshore flow pattern between seasons for the REF simulation. Seasonal variations in the nature of surface characteristics of the Goodhope Jet are similar for the NOA experiment, except that the jet is more intense and narrowly confined to the coast.

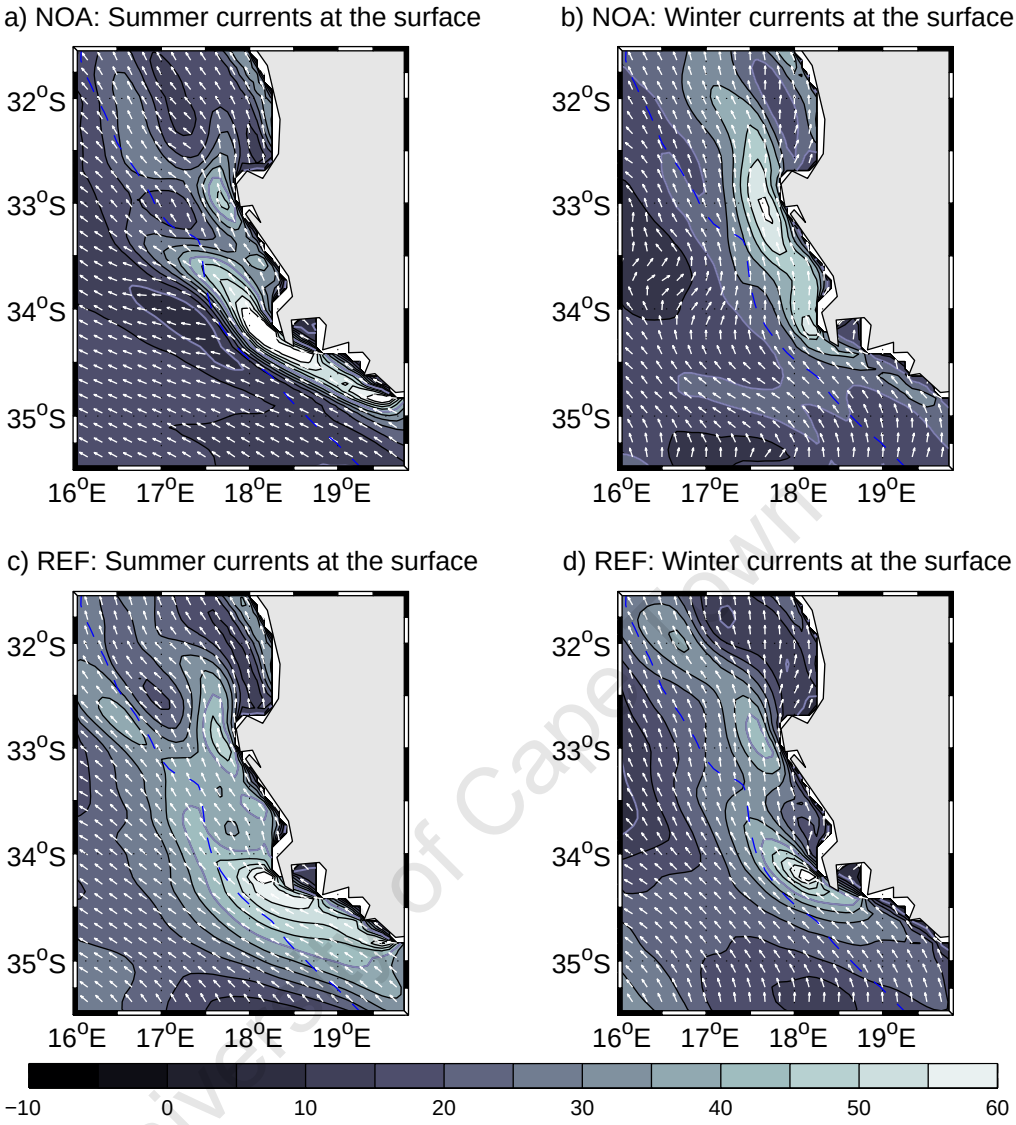

Figure 6.15: Summer and winter (left and right respectively) current speed (in $cm.s^{-1}$) and direction at the surface in the vicinity of the Goodhope Jet for the NOA (top) and REF (bot) simulations. The blue line represents the location of the shelf-edge.

A clearer impression of the seasonal variability of the Goodhope Jet for the REF and NOA simulations is provided in Figure 6.16 which shows the seasonal mean alongshore velocities across a section spanning the Goodhope Jet from the Cape Peninsula to 34.4°S, 17.3°E offshore. The NOA experiment produces a robust seasonal cycle of the nature of the Goodhope Jet, such that it is narrowest and more intense during periods of active upwelling (i.e. summer and spring) and broad but weak during autumn and winter months. In contrast to this clear pattern,

no obvious seasonal cycle is present in the Goodhope Jet across this section for the REF simulation (refer to the bottom plots of Figure 6.16). Figure 6.17 shows 2-daily mean velocities, averaged across (and with depth in) the Goodhope section (shown in Figure 6.16) alongside the spectral signal for both the NOA and REF simulations and it explicitly reveals the difference in seasonality for the two simulations. The NOA experiment has a distinct annual signal with greatest equatorward velocities during spring/summer as well as minor significant signals at ~6 and 8 months. Other than a few minor spectral peaks between 3 and 8 months, no significant annual signal exists for REF simulation. The suggestion of these contrasting results is that the perennial nature of Agulhas influx reflects on the seasonal signal of the average equatorward velocity of the Goodhope Jet.

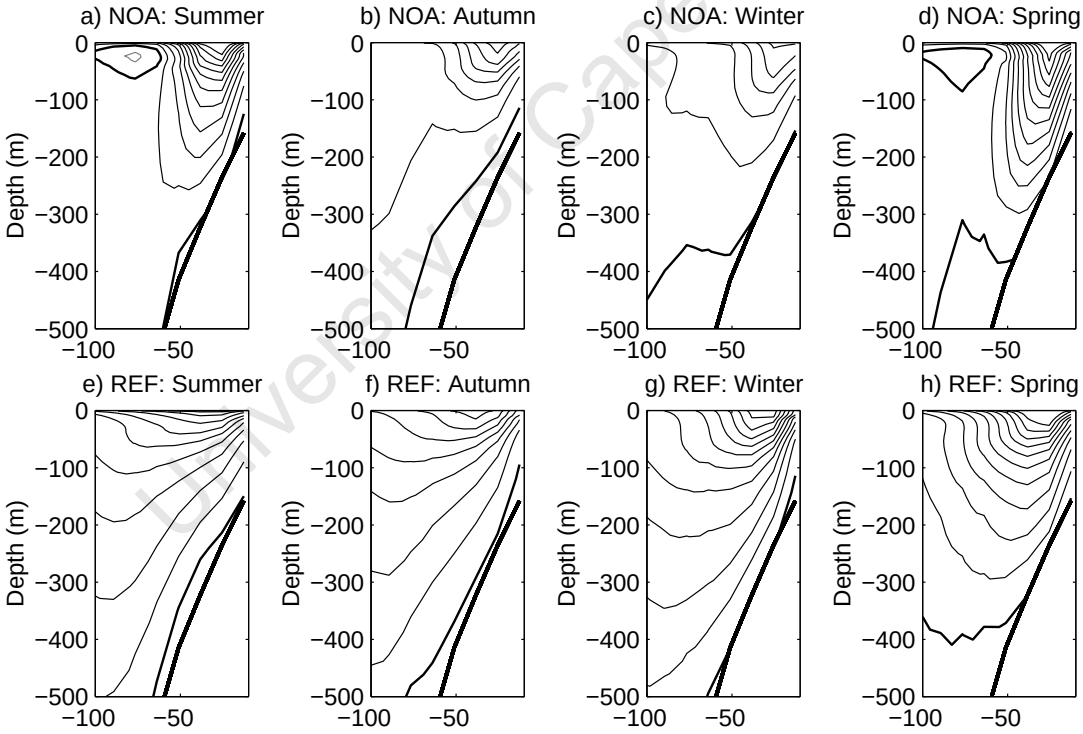

Figure 6.16: Seasonal mean alongshore currents across a section spanning the Goodhope Jet for the NOA (top) and REF (bottom) simulations: from 34°S, 18.3°E at the coast off the Cape Peninsula to 34.4°S, 17.3°E offshore. The grey shaded areas represent poleward flow, the dotted line represents the 0 cm.s^{-1}and the contour interval is 5 cm.s^{-1}.

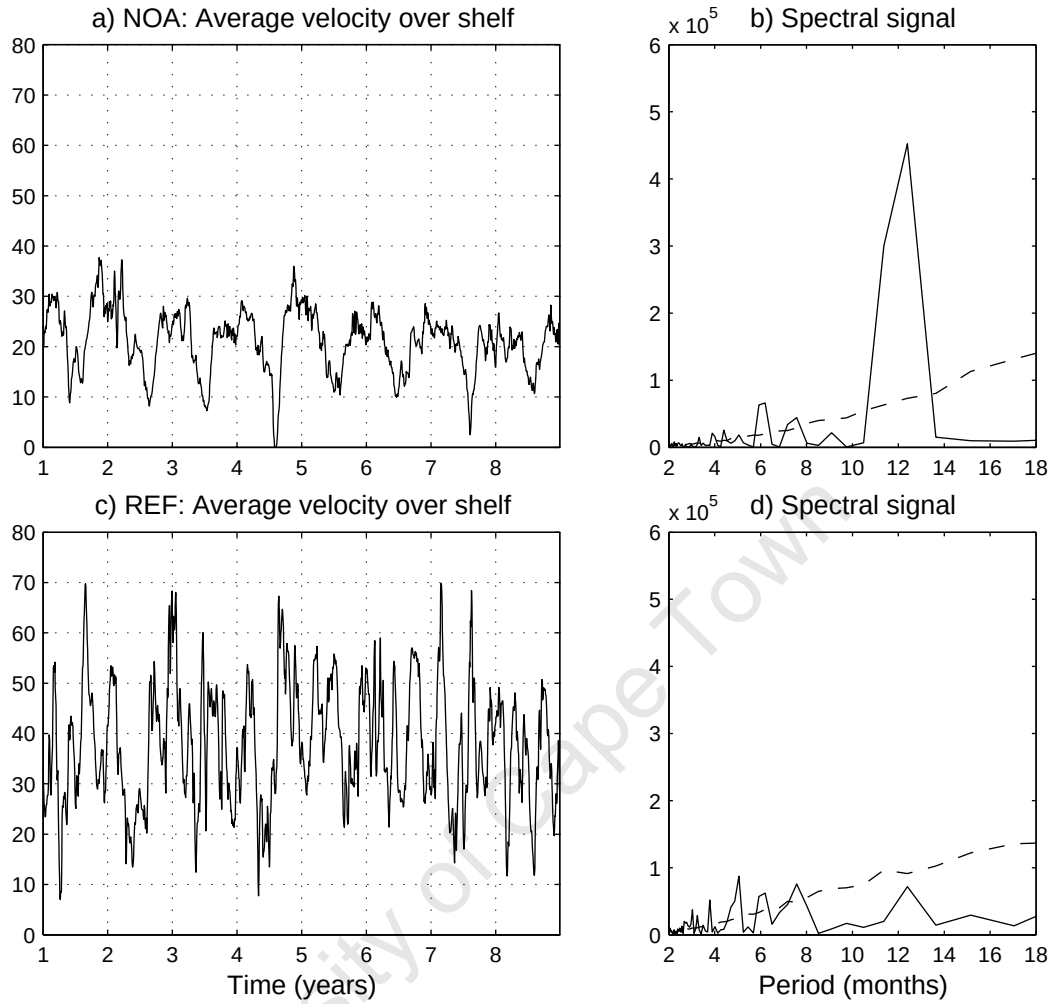

Figure 6.17: 2-daily mean velocities across a section spanning the Goodhope Jet: from 34°S, 18.3°E at the coast off the Cape Peninsula to 34.4°S, 17.3°E offshore for the NOA (a) and REF (c) simulations as well as their spectral signals (b and d respectively).

In order to directly test the inference that the Goodhope Jet is driven by the large offshore density gradient induced by the influx of the lower density waters of Agulhas/Indian Ocean origin, Figure 6.18 compares the alongshore model derived velocities (a and d) with alongshore geostrophic velocities (c and f) derived from the offshore gradient of density via the thermal wind relation (see equation (4.6)) with the surface geostrophic flow (as derived by SSHs) as the reference for both the NOA and REF simulations (top and bottom repectively). Also shown is the density field for both simulations (b and e). The offshore extent of the jet as well as its depth for the NOA experiment is well reproduced by the thermal wind relation (compare

Figure 6.18a and Figure 6.18c). For the REF simulation, while the velocities derived by the thermal wind relation (Figure 6.18f) are in line with that produced by the model (Figure 6.18d), the jet extends much deeper in the case of the former. This disparity could be related to the fact that the thermal wind relation does not take into account the effect of bottom friction, which is directly proportional to the speed of the overlying current.

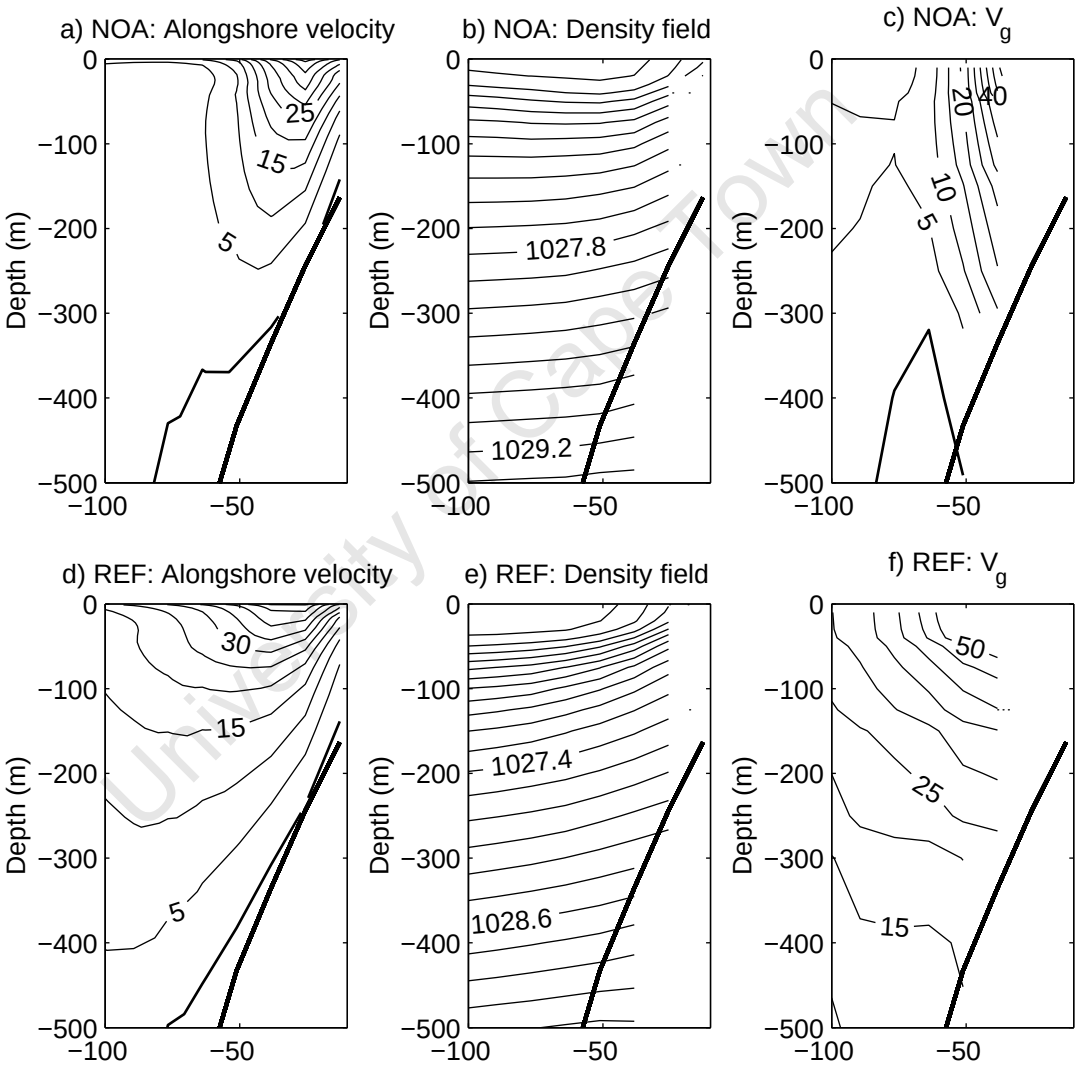

Figure 6.18: Annual mean model-derived alongshore velocity (a and d), density (b and e) and geostrophic flow (c and f) as derived by the thermal wind relation (see equation 4.6) using the density field shown in b) and e) spanning the Goodhope Jet (from 34°S, 18.3°E at the coast off the Cape Peninsula to 34.4°S, 17.3°E offshore) for the NOA and REF simulations respectively. The geostrophic velocity field is calculated using the surface geostrophic flow as reference.

6.3 Mesoscale variability

By removing Agulhas influx, the extremely high offshore mesoscale variability (or eddy kinetic energy: EKE) signal characteristic of the southern Benguela, disappears. Figures 6.19a and 6.19b show the surface EKE for the NOA and REF simulations respectively. Their difference as a percentage is shown in Figure 6.19c, so that blue (red) contours represent regions where the influence of the Agulhas is to increase (decrease) the surface EKE. The black contours in Figures 6.19a and 6.19b are lines of constant SSH and represent the surface geostrophic flow. While the REF simulation has a significantly stronger mean flow than the NOA experiment, both simulations exhibit peak EKEs in regions of most intense flow (represented by the most closely-spaced isolines). Specifically, the intense Goodhope Jet and the offshore stream of the Benguela Current correspond with high EKEs in both simulations. By removing the Agulhas it is clear that the distinct offshore transport separating the northern and southern Benguela systems (~25-28^{o}S) is a source of locally generated mesoscale variability, which could be related to the propensity for large upwelling filaments in this region (Lutjeharms et al. (1991); Shillington et al. (1990)). The termination of the surface manifestation of the poleward flow (~14-15^{o}S) at the ABFZ is also a local source of EKE as is the offshore flow associated with it (Mohrholz et al. (2001)) at ~17 ^{o}S. Figure 6.19c quantifies the extent to which Agulhas influx introduces and generates surface EKE in the Benguela system. It reveals that south of ~20^{o}S Agulhas influx accounts for more 60 % of the surface EKE and south of 30^{o}S its contribution exceeds 80 %.

The great depth of influence of Agulhas leakage on mesoscale variabiltiy in the southern Benguela is suggested by the vertical sections in Figure 6.20, which shows EKE in the upper 1000 m at 32^{o}S for the NOA, REF simulations and their percentage difference. While peak EKEs occur in the offshore domain for the REF simulation due to features associated with Agulhas influx, the peak EKE for the NOA experiment is locally generated at the shelf-edge equatorward jet. The percentage difference between the REF and NOA simulated EKEs at 32^{o}S (Figure 6.20c) strikingly shows that the shelf region of the southern Benguela is somewhat protected from variability induced by features associated with the Agulhas. Accord-

ing to Figure 6.20c, the Agulhas contributes no more than 50 % to the EKE on the shelf in the southern Benguela and the transition to a contribution of >80-90% in the offshore regions is represented as a sharp gradient (that spans < 100 km).

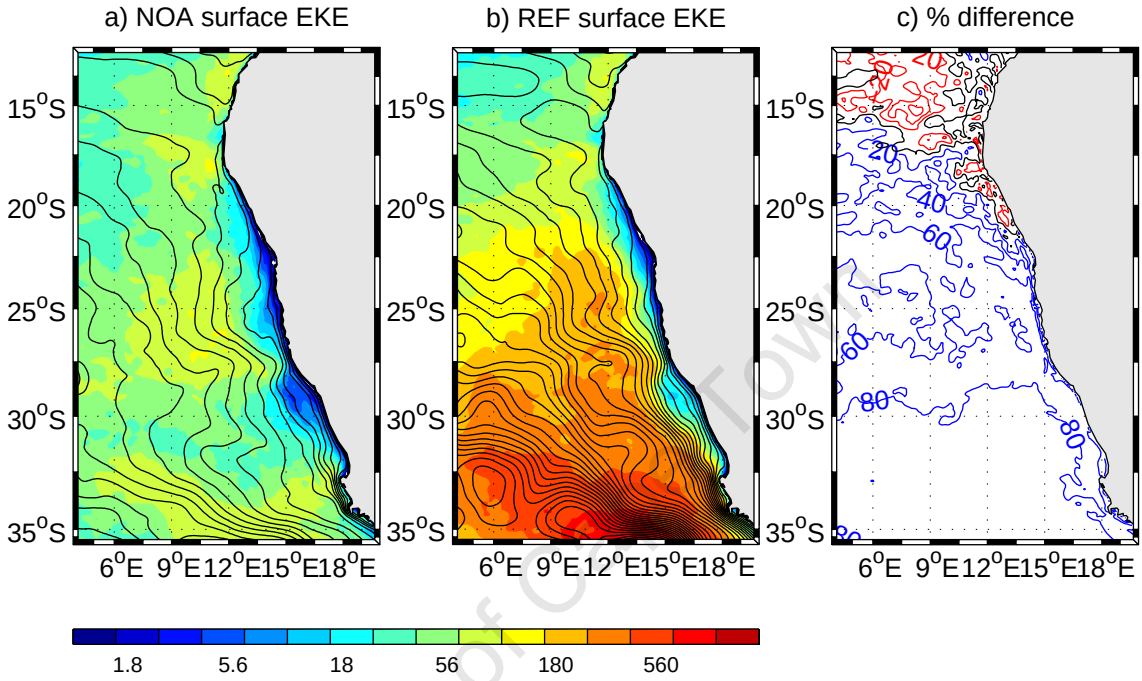

Figure 6.19: Surface non-seasonal (a) and seasonal (b) EKE for the NOA experiment. Units in $cm^2.s^{-2}$. Note that the colour bar is on a log scale.

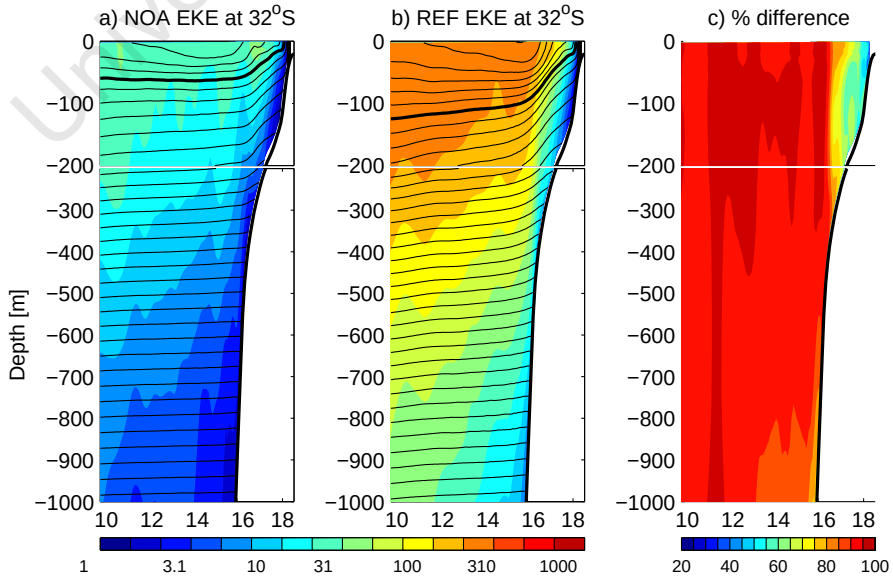

Figure 6.20: Seasonal (a) and non-seasonal (b) EKE section at 27.5°S for the NOA experiment.

6.4 The upwelling front

The offshore extent of the upwelling front in the Benguela system presents a distinct dichotomy between the northern and southern regions. Its strong topographical control in the southern Benguela does not extend into the northern Benguela region (refer to Figure 6.6b). In order to explicitly investigate the role of the Agulhas in the offshore extent and variability of the upwelling front, its location is extracted from each 2-daily averaged SST model output for both the REF and the NOA simulations. After several attempts at formulating the best method of extracting the location of the upwelling front, the most accurate and consistent proved to be the simplest. The upwelling front is identified as a the location of the isotherm defined by the addition of $\frac{3}{4}$ of the offhore SST (averaged between 500-1000 km from the coast) and $\frac{1}{4}$ of the coastal SST (averaged from the location of the 80 m isobath to the coast) at each latitude (see equation (6.1)).

$$T_{front} = 0.25T_{coast} + 0.75T_{offshore} \tag{6.1}$$

where T_{front} is the isotherm representative of the upwelling front, T_{coast} is the average SST between the coast and the location of the 80 m isobath and $T_{offshore}$ is the average offshore SST, averaged between 500-1000 km. While the model contains a surface SST restoring term (based on Pathfinder SSTs for both the REF and NOA simulations) in order to take into account the air-sea exchange feedback term, its effect is minimal and does not significantly affect the NOA SST results. Testament to the fact that the restoring SSTs do not effect the solution substantially is that the annual mean NOA experiment SSTs show significant deviations from the REF simulation (see Figure 6.6c).

Based on this method, the location of the summer mean upwelling front for the NOA and REF simulations is shown as a green line in Figures 6.21a and 6.21b respectively. In both simulations the mean upwelling front extends further offshore in the northern Benguela where the shelf is narrower (see dashed red line) than in the southern Benguela. Note the similarity of the nature of the summer upwelling front as resolved by the model (Figure 6.21b) with that resolved with satellite data

by Lutjeharms and Stockton (1987) that is shown in Figure 2.8 (bottom). The coherence between the location of the upwelling front and the shelf-edge is only distinct in the REF simulation, however the upwelling front in both simulations appears to be controlled by the discontinuity in the shelf-edge at ~28^{o}S.

The black dots in Figure 6.21 show the locations of the upwelling front, based on each 2-daily averaged summer SST from the NOA and REF simulations and give a good impression of intra-seasonal variation. The alongshore spread of the maximum offshore position of the front is extensive for the REF simulation (northward from ~28.5^{o}S) but significantly more confined for the NOA experiment (spanning ~27.5-25^{o}S). The alongshore region spanning maximum offshore excursions of the front in the NOA experiment corresponds with the location of the most vigorous and perennial upwelling cell in the Benguela system (Lüderitz: see Figure 4.24a), offshore surface geostrophic flow (see the streamlines in Figure 6.19a) and peak surface EKEs (see Figure 6.19a). Although the alongshore spread of the maximum offshore location of the upwelling front differs for the two simulations, the maximum offshore distance for both is of the order of 600-700 km. These model results suggest that large filaments are generated in the vicinity of Lüderitz due to the vigorous nature of the associated upwelling cell and the distinct offshore geostrophic flow, but that features linked to the Agulhas influx cause the maximum offshore position of the front to extend further north (Figure 6.22 gives a convincing impression of this). The mechanism may be related to the northward advection of the cooler, upwelled water at Lüderitz by the stronger equatorward surface geostrophic flow induced by Agulhas influence (see the streamlines in Figure 6.19b).

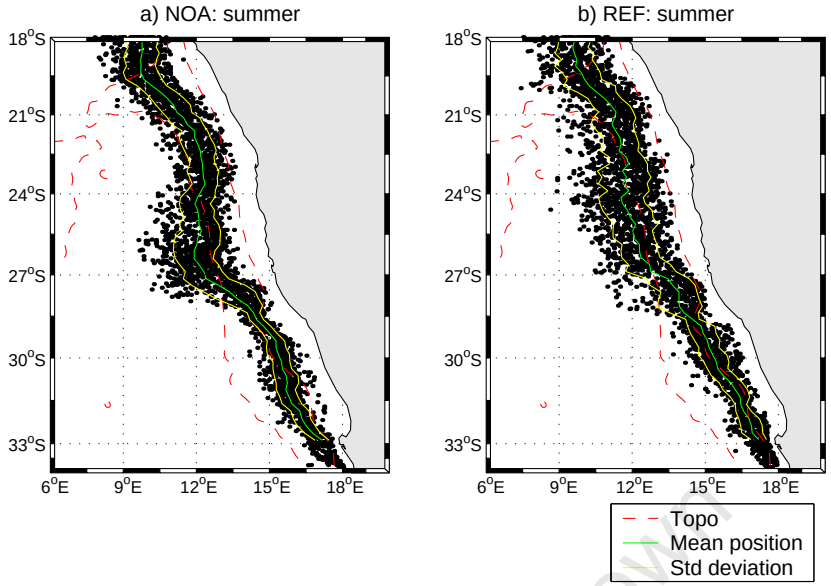

Figure 6.21: Summer upwelling front statistics for the, (a) NOA and (b) REF simulations. The black dots indicate the location of the upwelling front, based on the 2-daily averaged model SST for all summer months. The green line represents the mean summer position of the front and the yellow lines represent the standard deviation. The red dashed lines represent the 300 and 3000 m isobaths.

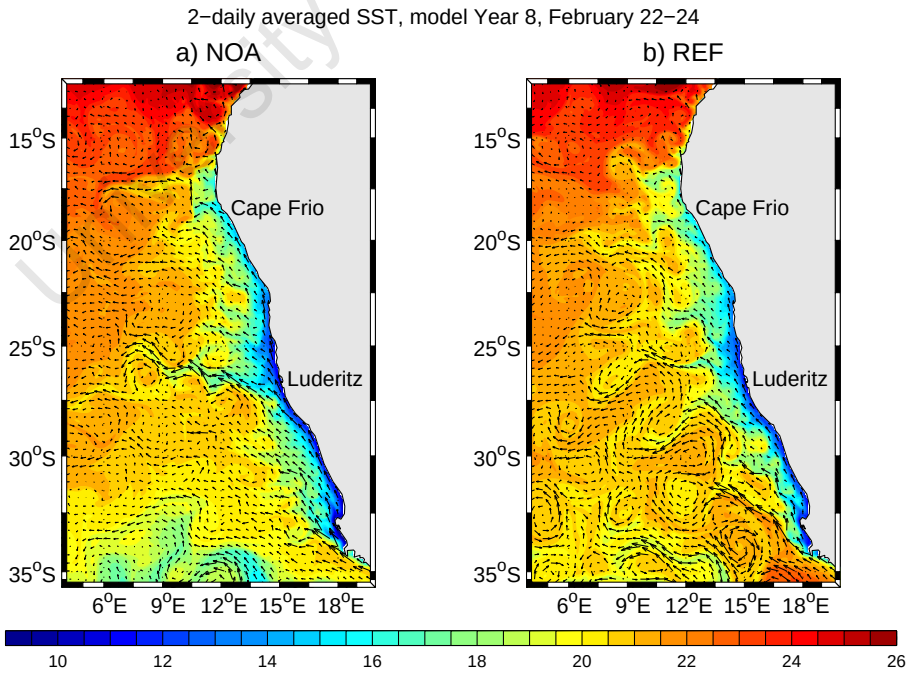

Figure 6.22: 2-daily averaged, 'snap-shot' of SST with surface current vectors overlaid for the (a) NOA and (b) REF simulations respectively for model year 8, 22-24 February.

While the mean upwelling front and its maximum offshore excursions south of 30°S are slightly further offshore for the NOA experiment than for the REF simulation, they remain relatively confined to the run of the shelf-edge, which is contrary to what we might expect. High SSTs introduced by Agulhas influx are likely to have a key role in the maintenance of the upwelling front at the shelf-edge in the southern Benguela (see Figure 6.6b), hence the unexpected result of a similar shelf-edge confinement of the front for the NOA experiment. We propose that the nearshore confinement of the front is the result of both the influx of warm offshore SSTs via Agulhas influx as well as the shelf-edge jet (i.e. the Goodhope Jet), which is present in both the NOA and REF simulations.

6.5 Cross-shelf volume fluxes

Features of importance to ecosystem functioning in the southern Benguela region are the Goodhope jet and the quiescent region of St Helena Bay. The former provides the vehicle of passage for eggs and larvae from their spawning ground on the Agulhas Bank to their nursery area and the latter provides the necessary environment for their retention. Cross-shelf fluxes of water mass characteristics are a key element of retention processes that are essential for successful productivity of upwelling ecosystems (Bakun (1996)). For example, Duncombe-Rae et al. (1992a) associated a poor year-class of anchovy with an Agulhas Ring that entrained an upwelling filament resulting in offshore losses of larvae. The role of Agulhas influx in driving cross-shelf volume fluxes is investigated by comparing results based on the NOA and REF simulations.

Figure 6.23a shows the volume flux across the shelf-edge, which is taken to be commensurate with the 500 m isobath, for the 0-50m layer in the southern part of the Benguela system (i.e. the region most affected by the Agulhas). Results based on the REF simulation are represented by black bars and the NOA experiment fluxes are shown as grey bars (averaged along 0.5° latitudinal domains). For both simulations the surface flux tends to be offshore, with peak offshore fluxes in the vicinity of the vigorous Lüderitz upwelling cell, suggesting an overall accordance with

surface offshore Ekman transport. Exceptions to the surface offshore flux occur in the REF simulation at ~33.5^{o}S and at 28^{o}S, where distinct onshore fluxes exist. The onshore flux at ~33.5^{o}S is related to the bifurcation of the Goodhope jet as it passes Cape Columbine (see Figure 6.15c) and is therefore an important factor in the transportation of fish larvae and eggs into St Helena Bay. At 28^{o}S, the sudden narrowing of the shelf guides an onshore flow that is enhanced by the presence of the Agulhas (e.g. refer to the streamlines in Figure 6.19). The standard deviation of the surface cross-shelf volume fluxes (calculated from the 2-daily averaged fluxes for the whole model time-series) is shown for the REF and NOA simulations in Figure 6.23c. The variability in NOA experiment is significantly lower than for the REF simulation and reveals peaks that are consistent with locations of upwelling cells and thus implies that the variability might be dominated by the seasonal upwelling cycle. The approximate monotonic decrease of variability of cross-shelf fluxes from the south to the north in the REF simulation does not appear in the NOA experiment, suggesting that the greater variability of fluxes in the south is directly related to Agulhas influx.

The volume fluxes in the bottom layer (i.e. 50-500 m) at the shelf (refer to Figure 6.23b) reveals the distinct meandering nature of the inshore stream of the Benguela Current south of ~30^{o}S for the REF simulation. The prominent standing meander feature that exists in the case of the REF simulation at (and flanking) the discontinuity of the shelf-edge at ~28^{o}S (see Figure 6.11b) is present as an alternating offshore-onshore-offshore flux pattern in Figure 6.23b. This feature exists, but is much weaker for the NOA experiment. A peak in variability (refer to Figure 6.23d) occurs in association with this feature for both simulations, suggesting that it is partially driven by locally generated instabilities however, its flux intensity as well as its variability is enhanced by Agulhas influence.

The fact that the intense offshore flux 30^{o}S at the 50-500 m layer resolved by the REF simulation is not captured in the NOA experiment (Figure6.23b) suggests that it is a direct result of Agulhas-derived features in the Benguela system.

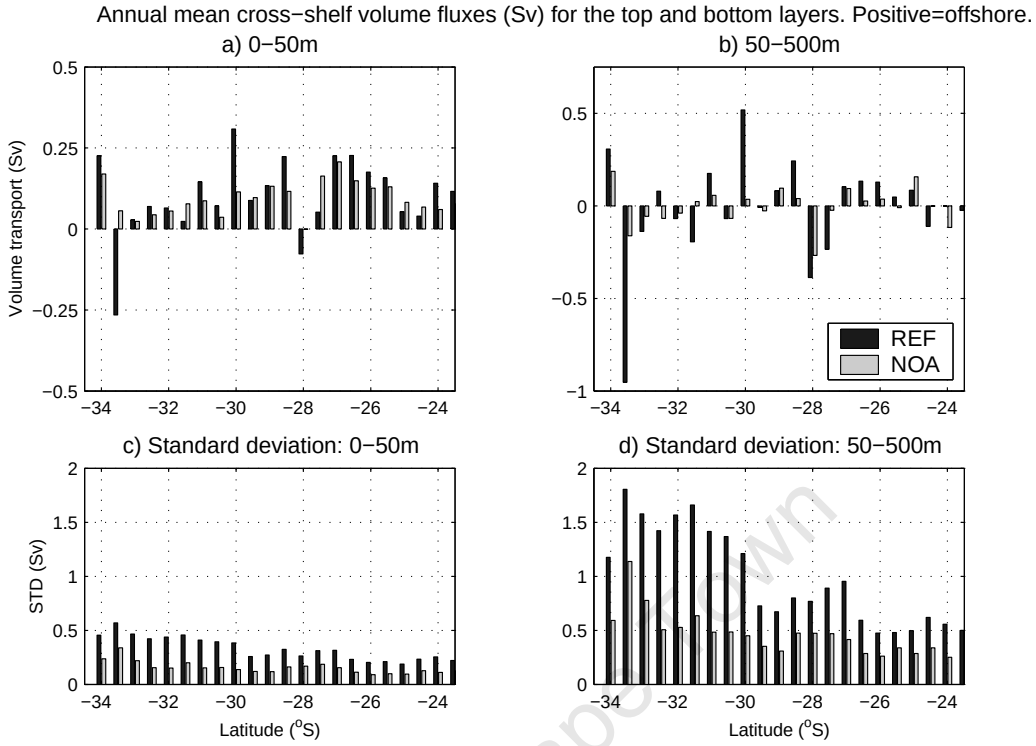

Figure 6.23: Annual mean cross-shelf volume fluxes for, (a) the surface (0-50 m) and (b) bottom (50-500 m) based on the REF and NOA simulations (black and grey bars respectively). c) and d) show the standard deviations (based on all 8 years of 2-daily averaged cross-shelf fluxes) for (a) and (b) respectively.

6.6 Synthesis and discussion

The difficulty of removing the signal of the Agulhas from the Benguela was demonstrated and discussed in the previous chapters. Unequivocal conclusions on the role of the Agulhas in the Benguela system are therefore similarly difficult to achieve. The use of numerical models allows us to purposefully create unrealistic scenarios in order to investigate the dominant driving forces of particular features. By introducing a dam at ~30^{o}S on the east coast in the model we cause an early retroflection of the Agulhas Current such that its influence on the Benguela system is minimal. Comparisons of this simulation (NOA) with the realistic one (REF), which has the same configuration and forcing, has allowed for some conclusions to be made on the role of the Agulhas Current in the Benguela system.

The most distinctive thermohaline effects of the Agulhas on the Benguela system occur south of ~30^{o}S in the case of SST and in the upwelling regime in the case of SSS. The presence of Agulhas influx increases the SSTs by as much as ~2.5^{o}C, at the southern boundary of the child domain and within the upwelling plume off Cape Columbine. The increased temperatures introduced by the Agulhas results in a thermocline (estimated by the depth of the 16^{o}C isotherm) that is deeper by about 50 m at 350 km offshore. Agulhas influx results in upwelled water that is more saline, particularly within and southward of the Lüderitz upwelling cells where it increases upwelled SSSs by ~0.1 psu. This is in line with the general increased salinity of the upwelling source water, namely the central water mass, by 0.05-0.1 psu in the presence of Agulhas leakage.

Comparisons of large-scale circulation features of the Benguela for the REF and NOA simulations reveal that the latter more closely corresponds with the Sverdrup relation and seasonal fluctuations associated with it, thereby implicating non-linear features associated with Agulhas influx in deviations from it. The results unequivocally reveal that two streams of the Benguela Current and the distinct meandering nature of the offshore stream are a result of features associated with Agulhas influence. The 0-1000 m depth integrated transport across 30^{o}S from 6^{o}E to the coast ranges from 5-15 Sv and 15-20 Sv for the NOA and REF simulations respectively, suggesting a 10 Sv contribution from the Agulhas, which is in accordance with the observational results of Gordon et al. (1987).

Depth-integrated transport streamlines and cross-shelf fluxes for the REF and NOA simulations show that while an anticyclonic meander exists in the vicinity of the sudden narrowing of the shelf-edge at ~28^{o}S, it is significantly more distinct for the REF simulation and results in far greater onshore fluxes of oceanic water. Therefore, although Agulhas influence is not the major driving force of this anticyclonic feature, it enhances cross-shelf exchanges at this location significantly. This can have implications for the productivity of the vigorous Lüderitz upwelling cell, which is situated at this feature.

The velocity structure at the shelf-edge reveals that the Agulhas has a role to play in inhibiting the southward penetration of the poleward flow that carries

water mass properties (e.g. low oxygen) of tropical Atlantic origin that can have detrimental effects on the Benguela ecosystem. Without influence from the Agulhas the equatorward flow in the southern Benguela at the shelf-edge is less meandering, much weaker and shallower, thereby giving way for a portion of the poleward flow to enter the southern Benguela at much shallower depths. Shelf-edge upwelling does not exist over the shelf-edge in the southern Benguela for the NOA experiment, which suggests that it is a result of the divergence of the shelf-edge current that is driven by Agulhas leakage.

The ecologically important Goodhope jet remains a feature of the NOA experiment, but is more intense and narrower, existing within 50-75 km of the coast. It does not have a robust seasonal signal in the REF simulation, but demonstrates a clear seasonal cycle in the NOA experiment such that is deepest and most intense during the upwelling seasons (spring and summer). Agulhas influx therefore modifies the Goodhope jet by by extending it over a broader region as well as removing its seasonal signal by the constant (seasonality of Agulhas leakage is small) enhancement of the cross-shelf steric height gradient.

Comparisons of surface EKE for the NOA and REF simulations show that Agulhas influx accounts for more than 80 % of the mesoscale variability south of 30^{o}S. A region of peak surface EKE in the NOA experiment is associated with the offshore flow at ~27^{o}S, which also corresponds to the region of the greatest offshore extent of the upwelling front. The high EKEs at this location suggest instabilities associated with the upwelling front, possibly in the form of filaments. The latitudinal domain across which largest offshore excursions (600-700 km) exist for the NOA is much smaller than for the REF simulation and spans the area of the Lüderitz upwellng cell and the shelf-edge discontinuity. Maximum offshore locations of the upwelling front extend northward from ~28.5^{o}S for the REF simulation and are also of the order of 600-700 km from the coast. The implications of these results is that the vigorous Lüderitz upwelling cell, the offshore surface geostrophic flow and the narrowing of the shelf in the vicinity of 27^{o}S generate large offshore filaments and that Agulhas leakage causes them to extend northward.

In the southern Benguela (south of 30^{o}S), the upwelling front remains topo-

graphically constrained by the shelf and does not extend far offshore for both the REF and the NOA simulations. While the high SSTs introduced by Agulhas influx may have a role to play, the fact that a similar shelf-edge confinement occurs in both simulations implies that it may also be related to northward advection by the Goodhope jet, which is present in both the NOA and REF simulations.

While this numerical modelling experiment does not remove the effect of the Agulhas entirely (i.e. the boundary conditions of the parent and the surface restoring term both retain Agulhas waters), it has allowed us to make some inferences on the effect of Agulhas leakage on the mean state of the Benguela system. It has shown that the Agulhas not only significantly affects the large scale flow regime and thermohaline characteristics but also nearshore features which can have critical ramifications for the health of the upwelling ecosystem.

Chapter 7

Conclusions

While research of the Benguela upwelling system goes far back, the model simulation on which this work is based, has provided the first opportunity to study salient features of the system in a spatially and temporally cohesive manner at a high enough resolution to capture nearshore dynamics. It has allowed us to characterise features definitive of the northern and southern regimes and to investigate the extent to which they can be regarded distinctly separate systems. Each of the preceeding chapters is somewhat 'stand-alone', such that they contain separate conclusions that collate results specific to them. In this final chapter we summarise the important findings of Chapter 4, 5 and 6 by addressing the key questions that were outlined in Chapter 2.

The questions in the final paragraph of Chapter 2 are highlighted in bold and are followed by a summary of pertinent results.

- **What characterises the dynamical disparity between the northern and southern Benguela regimes?**
  - **How do the regimes differ from each other, in terms of nearshore as well as offshore dynamics?**
  - **Is the transition between them defined by a distinct physical barrier? If so, what forces it?**

  The different characteristics of the northern and southern Benguela regimes and the very distinct nature of their divide presents a natural laboratory and

provides the opportunity for a systematic comparative study of different eastern boundary upwelling regimes within one system and within one simulation. Depth-integrated, large-scale circulation patterns of the Benguela system give a convincing impression of separate regimes. The poleward flow of the northern regime meets the stronger, more meandering equatorward flow of the southern regime in the vicinity of Lüderitz where the dominant transport is offshore and upwelling rates and fluxes are the highest and, for this reason, has long been considered the division between the northern and southern Benguela upwelling regimes. Greatest seasonal variability in upwelling intensities occur south of Lüderitz and particularly in the far south, with greatest fluxes during summer. Although seasonal variations decrease toward the north, upwelling intensifies somewhat during winter. A significant finding on the difference between the northern and southern Benguela upwelling regimes is that upwelling in the north (north of ~23°N) is inhibited by the convergence of geostrophic flow at the coast. The southern Benguela regime experiences shelf-edge upwelling due to the divergence of the inshore stream of the Benguela Current. Furthermore, the upwelling front in the southern Benguela displays a strong topographical control in the southern Benguela such that it follows the alongshore run of the shelf-edge.

Perhaps the most unique feature of the Benguela system is the fact that its southern boundary is one of the only places in the world that can be described as a meeting place of eastern and western boundary current systems, resulting in the very high offshore gradients of variability in this region. Though both the northern and southern Benguela regimes are rather unique in this regard, the offshore gradient in EKE is far more intense in the south, reflecting the influence of features associated with the termination of the Agulhas Current. Differences in the offshore EKE gradients of the two regimes is likely to have different implications for cross-shore exchanges of water properties in these regions. Coherent eddy structures are more prevalent in the southern Benguela region. Aside from the large anticyclonic Agulhas Rings that traverse the Cape Basin region, smaller-scale cyclonic eddies form off the Cape

Peninsula and Cape Columbine due to barotropic instability processes. They form preferentially during summer (i.e. the upwelling season) and either propagate westward or follow the shelf-edge northward until they reach the vicinity of Lüderitz where they are advected offshore.

The difference between the northern and southern systems in the offshore propagation of EKE, lies in the fact that a clear offshore propagating signal of ~3.5 cm.s^{-1} has been calculated for the nearshore source of EKE in the northern Benguela, but an offshore propagating signal only occurs from the location of the shelf-edge in the southern Benguela (no offshore propagating signal is present on the shelf area) and is a reflection of the northwestward translation of Agulhas rings. The EKE signal on the shelf in the southern Benguela instead propagates equatorward to ~30°S at a rate of ~12 cm.s^{-1} where it turns offshore. This signal is consistent with the trajectory of shelf-edge cyclonic eddies after their formation at the capes in the southern Benguela

- **What drives the large-scale flow regime in the Benguela system?**
  - **Why is the large-scale flow regime in the northern Benguela poleward, despite the prevailing southeasterly winds?**

A vorticity budget analysis reveals that the large-scale flow regime of the Benguela system is driven by the Sverdrup relation with significant (in places) departures due to the non-linear advection terms, which is similar to the finding of Marchesiello et al. (2003) for a similar analysis conducted for the California Current system. The Sverdrup balance (i.e. between the wind stress curl and the beta effect) is most valid, on the large-scale (with local contributions from the vorticity advection term) in the tropical Benguela region (13-18°S) and in the central Benguela region (25-30°S), which is characterised by distinct offshore transport. Both the northern and southern Benguela vorticity balances depend significantly on the advection and vortex stretching terms. The latter especially so, due to the passage of Agulhas rings and eddies and the general enhancement of mesoscale variability associated with Agulhas influence.

The depth-integrated, poleward flow in the northern Benguela and the offshore transport that has been identified as the transition between the northern and southern systems can therefore be explained by the approximate balance between wind stress curl and the beta effect. Local departures from the balance is accounted for by vorticity advection.

- **How do transient features, associated with Agulhas influx, influence the mean state of the Benguela system?**

  - **How does Agulhas influx affect the large-scale flow regime of the Benguela system?**

    The distinctly meandering path of the offshore stream of the Benguela Current is the mean state manifestation of the preferential path of Agulhas Rings. The dominant terms of the vorticity balance quantify the extent to which the eddy and mean vorticity advection terms drive the mean flow. The latter, in fact, being a remnant of the passage of the large-scale (i.e. ~100-200 km diameter) Agulhas Rings. The 0-1000 m depth integrated transport across 30^oS from 6^oE to the coast decreases to 5-15 Sv from 15-20 Sv for the experiment in which the Agulhas influx is removed, suggesting a 10 Sv contribution from the Agulhas, which is in accordance with the observational results of Gordon et al. (1987).

    Depth-integrated transport streamlines and cross-shelf fluxes show that a distinct anticyclonic meander that exists in the vicinity of the sudden narrowing of the shelf-edge at ~28^oS, it is significantly weaker for the experiment in which Agulhas influx has been removed. Therefore, while Agulhas influx is not the major driving force of this anticyclonic feature, it enhances cross-shelf exchanges at this location significantly, which can have implications for the productivity of the vigorous Lüderitz upwelling cell.

    The velocity structure at the shelf-edge reveals that the Agulhas inhibits the southward penetration of the poleward flow that carries water mass properties (e.g. low oxygen) of tropical Atlantic origin that can have

detrimental effects on the Benguela ecosystem.

– **Does Agulhas influx drive the Goodhope Jet?**

The ecologically important Goodhope jet remains a feature of the experiment in which Agulhas influx has been curtailed, but is more intense and narrower, existing within 50-75 km of the coast. While it does not have a robust seasonal signal in the reference simulation, it demonstrates a clear seasonal cycle in the no Agulhas experiment such that it is deepest and most intense during the upwelling seasons (spring and summer). Agulhas influx therefore modifies the Goodhope jet by by extending it over a broader region as well as removing its seasonal signal by the constant (seasonality of Agulhas leakage is small) enhancement of the cross-shelf steric height gradient.

– **To what extent is the nature of the upwelling front and mesoscale features associated with it (e.g. filaments) related to Agulhas features**

In the southern Benguela (south of 30°S), the upwelling front remains topographically constrained by the shelf and does not extend far offshore for either the reference or the no Agulhas simulations. While the high SSTs introduced by Agulhas influx may have a role to play, the fact that a similar shelf-edge confinement occurs in both simulations implies that it may also be related to northward advection by the Goodhope jet, which is present in both simulations.

The latitudinal domain across which largest offshore excursions (600-700 km) of the upwelling front exist is much smaller for the no Agulhas experiment than for the reference simulation and spans the area of the Lüderitz upwelling cell and the shelf-edge discontinuity. This region is also coincident with peak locally generated EKEs in the no Agulhas experiment. On the other hand, while the maximum offshore extent of the upwelling front is also of the order of 600-700 km, the location of the maximum spans over a greater region: northward of ~28.5°S. The implications of these results is that the vigorous Lüderitz upwelling cell, the offshore sur-

face geostrophic flow and the narrowing of the shelf in the vicinity of 27°S generate large offshore filaments and that Agulhas leakage causes them to extend northward.

A schematic of the salient dynamic features of the Benguela system is shown in Figure 7.1. Note the two streams of the Benguela Current: the offshore stream is the mean manifestation of the preferential path of the large-scale anticyclonic Agulhas rings (shown as red dashed circles) and the inshore stream is topographically controlled and follows the run of the shelf-edge until ~30°S, where it begins to veer offshore. The trajectory of the cyclonic eddies that form at Cape Colubine and at the Cape Peninsula is shown in a blue dashed line. Also note the shelf-edge upwelling in the southern Benguela that is associated with the divergence of the inshore stream of the Benguela Current. In the north, the depth-integrated flow regime is dominated by a poleward flow which veers offshore from ~25°S (these features being in approximte Sverdrup balance). The poleward flow converges against the coast between ~26-18°S, causing the inhibition of coastal upwelling.

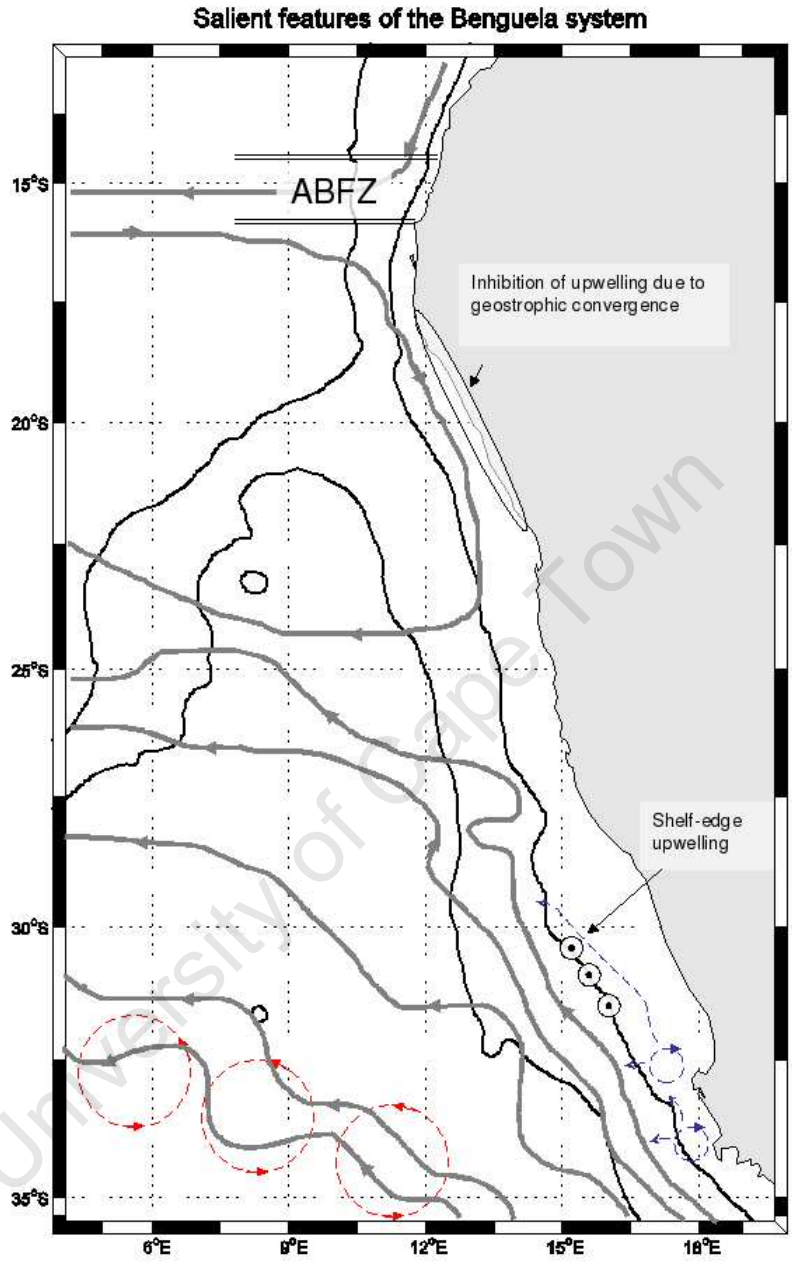

Figure 7.1: Schematic of the salient features of the Benguela system that have been discussed in this thesis.

This work has specifically been limited to equilibrium conditions in order to improve our understanding of the mean state and seasonal cycle of the Benguela Current system. Since the mean state is used as the bench-mark from which trends and episodic events (which are frequently catastrophic) are measured, it is imperative that we have a clear understanding of it. There are several avenues for exten-

sion/application of this work:

- Use a more realistic surface forcing (i.e. not a climatological product) and the bulk formulae for the air-sea feedback in order to investigate interannual variability within the system.

- The coupling of this simulation with an atmospheric model, such as MM5, would improve the solution, especially in coastal regions where the wind drop-off is under-estimated in satellite products and results in a cool coastal bias.

- An offline, submesoscale (i.e. <1.5 km-3 km) nesting could be carried out in order to investigate the importance of the large vertical velocities that occur at frontal zones (e.g. see Capet et al. (2008a)) as well as at the perimeter of Agulhas Rings.

- Idealised and simplified models could be run in order to more clearly understand, for example, the dynamics of the upwelling intensification downstream of capes.

- The results of this simulation have been thoroughly verified and are therefore ready to be used in biological modelling applications such as biogeochemistry and ecosystem models.

Bibliography

Agenbag, J. and L. Shannon, 1988: A suggested physical explanation for the existence of a biological boundary at 24.5^{o}S in the Benguela system. *S. Afr. J. Mar. Sci.*, **6**, 119–132.

Andrews, W. and L. Hutchings, 1980: Upwelling in the southern Benguela current. *Prog. Oceanogr.*, **9 (1)**.

Arakawa, A. and V. Lamb, 1977: Computational design of the basic dynamcial processes of the UCLA general circulation model. *Method Comput. Phys.*, **17**, 173–265.

Aristegui, J., P.Sangra, S. Hernandez-Leon, M.Canton, A. Hernandez-Guerra, and J. Kerling, 1994: Island-induced eddies in the Canary islands. *Deep Sea Res. I*, **41**, 1509–1525.

Armstrong, E. and J. Vazquez, 2001: A new global satellite-based sea surface temperature climatology. *Geophys. Res. Lett.*, **28 (22)**, 4199–4202.

Bakun, A., 1973: Coastal upwelling indices, west coast of North America. Tech. Rep. NMFS SSRF-671, NOAA, Seattle, WA.

Bakun, A., 1996: Patterns in the ocean: ocean processes and marine population dynamics. Tech. Rep. 323, University of California Sea Grant program, San Diego, California, USA, in cooperation with Centro de Investigaciones Biologicas de Noroeste, La Paz, Mexico.

Bakun, A. and C. Nelson, 1991: The seasonal cycle of wind-stress curl in subtropical eastern boundary current regions. *J. Phys. Oceanogr.*, **21**, 1815–1834.

Bang, N. and W. Andrews, 1974: Direct current measurements of a shelf-edge frontal jet in the southern Benguela system. *J. Mar. Res.*, **32**, 405–417.

Barnier, B., L. Siefridt, and P. Marchesiello, 1995: Thermal forcing for a global ocean circulation model using a three-year climatology of ECMWF analysis. *J. Mar. Syst.*, **6 (363-380)**.

Barth, J., 1989: Stability of a coastal upwelling front 2: Model results and comparison with observations. *J. Geophys. Res.*, **94 (C8)**, 10,857–10,883.

Barth, J., S. Pierce, and R. Smith, 2000: A separating coastal upwelling jet at Cape Blanco, Oregon and its connection to the California Current system. *Deep-Sea Res. II*, **47**, 783–810.

Biastoch, A., C. Boning, and J. Lutjeharms, 2008: Agulhas leakage dynamics affects decadal variability in Atlantic overturning circulation. *Nature*, **455**.

Biastoch, A. and W. Krauss, 1999: The role of mesoscale eddies in the surface regions of the Agulhas current. *J.Phys. Oceanogr.*, **29 (2303-2317)**.

Blanke, B., S. Speich, A. Bentamy, C. Roy, and B. Sow, 2005: Modeling the structure and variability of the southern Benguela upwelling using QuikSCAT wind forcing. *J. Geophys. Res.*, **110 (C7)**.

Boccaletti, G., R. Pacanowski, S. Philander, and A. Fedorov, 2003: The thermal structure of the upper ocean. *J. Phys. Oceanogr.*, **34**, 888–902.

Boebel, O., J. Lutjeharms, C. Schmid, W. Zenk, T. Rossby, and C. Barron, 2003: The Cape Cauldron: a regime of turbulent inter-ocean exchange. *Deep-Sea Res. II*, **50**, 57–86.

Boyd, A., J. Salat, and M. Maso, 1987: The seasonal intrusion of relatively saline water on the shelf of northern and central Namibia. *S. Afr. J. Mar. Sci.*, **5**, 107–120.

Boyd, A., J. Taunton-Clark and G. Oberholzer, 1992: Spatial features of the near-surface and midwater circulation patterns off western and southern South Africa

and their role in the life histories of various commercially fished species. *S. Afr. J. Mar. Sci*, **12**, 189–206.

Buchwald, V. and J. Adams, 1968: The propagation of continental shelf waves. *Proc. Roy. Soc. A.*, **305**, 235–250.

Byrne, D., A. Gordon, and W. Haxby, 1995: Agulhas eddies: a synoptic view using Geosat ERM data. *J. Phys. Oceanogr.*, **25**.

Capet, X., J.C. McWilliams, M.J.Molemaker and A.F. Shchepetkin, 2008a: Mesoscale to submesoscale transition in the California Current system. Part I: Flow structure, eddy flux and observational tests. *J. Phys. Oceanogr.*, **38**, 29–43.

Capet, X., F.Colas, P.Penven, P.Marchesiello, and J. McWilliams, 2008: *Ocean Modeling in an Eddying Regime*, Vol. 177, chap. Eddies in eastern boundary subtropical upwelling systems. AGU, Washington D.C.

Capet, X., P. Marchesiello, and J. McWilliams, 2004: Upwelling response to coastal wind profiles. *Geophy. Res. Lett.*, **31**, L13 311, doi: 10.1029/2004GL020 123.

Carr, M.-E. and E. Kearns, 2002: Estimation of potential productivity in eastern boundary currents using remote sensing. *Deep-Sea Res. II*, **49**, 59–80.

Chang, N., 2009: Numerical ocean model study of the Agulhas bank and the cool ridge. Ph.D. thesis, University of Cape Town, South Africa.

Chelton, D., 1984: Seasonal variability of alongshore geostrophic velocity off central California. *J. Geophys. Res.*, **89 (C3)**, 3473–3486.

Chelton, D., R. deSzoeke, and M. Schlax, 1998: Geograhical variability of the first rossby radius of deformation. *J. Phys. Oceanogr.*, **28**.

Chelton, D. and M. Schlax, 1996: Global observations of oceanic rossby waves. *Science*, **272 (234-238)**.

Colberg, F., 2006: An analysis of variability in the South Atlantic. Ph.D. thesis, University of Cape Town, Rondebosch, South Africa.

Colberg, F. and C. J. Reason, 2006: A model study of the Angola-Benguela frontal zone: sensitivity to atmospheric forcing. *Geophys. Res. Lett.*, **33**.

Conkright, M., R. Locarnini, H. Garcia, T. O'Brien, T. Boyer, C. Stephens, and J. Antonov, 2002: World Ocean Atlas 2001: objective analyses, data statistics and figures. CR-ROM documentation, Internal Report 17, National Oceanographic Centre, Silver Spring, Md.

Csanady, G., 1985: 'Pycnobathic' currents over the upper continental slope. *J. Phys. Oceanogr.*, **15**.

Da Silva, A., C. Young, and S. Levitus, 1994: Atlas of surface marine data 1994, vol. 1, algorithms and procedures, technical report. Tech. rep., National Oceanographic and Atmospheric Administration, Silver Spring, Md.

de Ruijter, W., A.Biastoch, S. Drijfhout, J. Lutjeharms, R. Matano, T. Pichevin, P. van Leeuwen, and W.Weijer, 1999: Indian-Atlantic interocean exchange: dynamics, estimation and impact. *J. Geophys. Res.*, **104 (C9)**, 20,885–20,910.

Debreu, L. and C. Mazauric, 2006: Adaptive grid refinement (AGRIF) in Fortran 90 users guide version 1.3. *Available at: http://www-lmc.imag.fr/IDOPT/AGRIF/index.html.*

Debreu, L., C. Voulard, and E. Blayo, 2008: AGRIF: Adaptive grid refinement in fortran. *Comput. Geosci.*, **34 (8-13)**.

Demarcq, H., R. Barlow, and L. Hutchings, 2007: Application of a chlorophyll index derived from satellite data to investigate the variability of phytoplankton in the Benguela system. *Afr. J. Mar. Sci.*, **29 (2)**, 271–282.

Demarcq, H., R. Barlow, and F. Shillington, 2003: Climatology and variability of sea surface temperature and surface chlorophyll in the Benguela and Agulhas ecosystems as observed by satellite. *Afr. J. Mar. Sci.*, **25**, 363–372.

Doglioli, A., B.Blanke, S. Speich, and G. Lapeyre, 2007: Tracking coherent structures in a regional ocean model with wavelet analysis: Application to Cape Basin eddies. *J. Geophys. Res.*, **112 (doi:10.1029/2006JC003952)**.

Ducet, N., P. L. Traon, and G. Reverdin, 2000: Global high-resolution mapping of ocean circulation from topex/poseidon and ers-1 and -2. *J. Geophys. Res.*, **105**, 19,477–19,498.

Duncombe Rae, C., 2004: A demonstration of the hydrographic partition of the Benguela upwelling ecosystem at 26.40°S. *S. Afr. J. Mar. Sci.*, **27 (3)**, 617–628.

Duncombe-Rae, C., A. Boyd, and R. Crawford, 1992a: 'Predation' of anchovy by an Agulhas ring: a possible contributory cause of the very poor year-class of 1989. *S. Afr. J. Mar. Sci*, **12**.

Duncombe-Rae, C., F. Shilington, J. Agenbag, J. Taunton-Clark, and M. Grundlingh, 1992b: An Agulhas ring in the South Atlantic ocean and its interaction with the Benguela upwelling frontal system. *Deep Sea Res.*, **39 (11/12)**, 2009–2027.

Enriquez, A. and C. Friehe, 1995: Effects of wind stress and wind stress curl variability on coastal upwelling. *J. Phys. Oceanogr.*, **25**, 1651–1671.

Estrade, P., P. Marchesiello, A. de Verdiere, and C. Roy, 2008: Cross-shelf structure of coastal upwelling: a two-dimensional expansion of Ekman's theory and a mechanism for innershelf upwelling shut down. *J. Mar. Res.*, **66**, 589–616.

Fennel, W., 1999: Theory of the Benguela upwelling system. *J. Phys. Oceanogr.*, **29**, 177–190.

Florenchie, P., J. Lutjeharms, C. Reason, S. Masson, and M. Rouault, 2003: The source of Benguela Niños in the South Atlantic ocean. *Geophys. Res. Lett.*, **30**, 121–124.

Florenchie, P., C. Reason, J. Lutjeharms, M. Rouault, C. Roy, and S. Masson, 2004: Evolution of interannual warm and cold events in the South-East Atlantic ocean. *J. Climate*, **17 (12)**, 2318–2334.

Freon, P., J.Alheit, E. Barton, S. Kifani, and P. Marchesiello, 2006: *Benguela: Predicting a Large Marine Ecosystem*, Large Marine Ecosystems, Vol. 14, chap.

Modeling, forecasting and scenarios in comparable upwelling ecosystems: California, Canary and Humboldt, 185–220. Elsevier B.V.

Gammelsrod, T., C. Bartholomae, D. Boyer, V. Filipe, and M. O'Toole, 1998: Intrusion of warm surface water along the Angolan-Namibian coast in February 1995: The 1995 Benguela Niño. *S. Afr. J. Mar. Sci.*, **19**, 41–56.

Gan, J. and J. Allen, 2002a: A modelling study of shelf circulation off northern California in the region of the coastal dynamics experiment: Response to relaxation of upwelling winds. *J. Geophys. Res.*, **107 (C9)**.

Garzoli, S., G. Goni, A. Mariano, and D. Olson, 1997: Monitoring the upper Southeastern Atlantic transports using altimeter data. *J Mar. Res.*, **55**, 453–481.

Garzoli, S. and A. Gordon, 1996: Origins and variability of the Benguela Current. *J. Geophys. Res.*, **101 (C1)**, 897–906.

Garzoli, S., A. Gordon, V. Kamenkovich, D. Pillsbury, and C. Duncombe-Rae, 1996: Variability and sources of the southeastern Atlantic circulation. *J. Mar. Res.*, **54**, 1029–1071.

Gordon, A., 2003: The brawniest retroflection. *Nature*, **421**, 904–905.

Gordon, A. and K. Bosley, 1991: Cyclonic gyre in the South Atlantic. *Deep-Sea Res.*, **38 [Supp.1]**, 323–343.

Gordon, A., K. Bosley, and F. Aikman, 1995: Tropical Atlantic water within the Benguela upwelling system at 27°S. *Deep-Sea Res.*, **42 (1)**, 1–12.

Gordon, A., J. Lutjeharms, and M. Grundlingh, 1987: Stratification and circulation at the Agulhas retroflection. *Deep-Sea Res.*, **34 (4)**, 565–599.

Gordon, A., R. Weiss, W. Smethie, and M. Warner, 1992: Thermocline and intermediate water communication between the south Atlantic and Indian oceans. *J. Geophys. Res.*, **97 (C5)**, 7223–7240.

Gruber, N., H. Frenzel, P. Marchesiello, J. McWilliams, T.Nagai, and G.-K. Plattner, 2007: On the role of eddies for coastal productivity and carbon export to the open-ocean. *Geophys. Res. Abs.*, **9 (07743)**.

Guo, X., H. Hukuda, Y. Miyazawa, and T. Yamagata, 2002: A triply nested ocean model for simulating the Kuroshio-roles of horizontal resolution on jebar. *J. Phys. Oceanogr.*, **33**.

Haney, R., R. Hale, and D. Dietrich, 2001: Offshore propagation of eddy kinetic energy in the California Current. *J. Geophys. Res.*, **106 (C6)**, 11,709–11,717.

Hardman-Mountford, A., A. Richardson., J. Agenbag, E. Hagen, L. Nykjaer, F.Shillington and C. Villacastin, 2003: Ocean climate of the south east atlantic observed from satellite data and wind models. *Prog. Oceanogr.*, **59**, 181–221.

Hart, T. and R. Currie, 1960: The Benguela Current. *Discovery Reports*, **31 (123-298)**.

Hedstrom, K., 1997: Users manual for an s-coordinate primitive equation ocean circulation model (SCRUM) version 3.0. Tech. rep., Institute of Marine and Coastal Sciences, Rutgers University.

Hutchings, L., 1992: Fish harvesting in a variable, productive environment-searching for rules or searching for exceptions? *S. Afr. J. Mar. Sci.*, **12**, 297–318.

Hutchings, L., 2004: A synthesis of the Lüderitz-Orange river cone area. Tech. rep., Benefit/BCLME LUCORC Workshop, Swakopmund, April 2004, Benefit/BCLME LUCORC Workshop, Swakopmund, April 2004. Benefit/BCLME LUCORC Workshop, Swakopmund, April 2004.

Huthnance, J., 1984: Slope currents and 'Jebar'. *J. Phys. Oceanogr.*, **14**.

John, H.-C., V. Mohrholz, and J. Lutjeharms, 2001: Cross-front hydrography and fish larval distribution at the Angola-Benguela front. *J. Mar. Syst.*, **28**, 91–111.

Johnson, A. and G. Nelson, 1999: Ekman estimates of upwelling at Cape Columbine based on measurements of longshore wind from a 35-year time-series. *S. Afr. J. Mar. Sci.*, **21**, 433–436.

Jury, M., 1985: *South African Ocean Colour Experiment*, chap. 3: Case studies of alongshore variations in wind-driven upwelling in the southern Benguela region, 29–46.

Jury, M., C. MacArthur, and G. Brundrit, 1990: Pulsing of the Benguela upwelling region: large-scale atmospheric controls. *S. Afr. J. Mar. Sci.*, **9**, 27–41.

Kamenkovich, V., Y. Leonov, D. Nechaev, D. Byrne, and A. Gordon, 1996: On the influence of bottom topography on an Agulhas eddy. *J. Phys. Oceanogr.*, **26**.

Kamstra, F., 1985: *South African Ocean Colour Experiment*, chap. Chapter 2: Environmental features of the southern Benguela with special reference to the wind stress, 13–27.

Kelly, K., R. Beardsley, R. Limeburner, K. Brink, J. Paduan, and T. Chereskin, 1998: Variability of the near-surface eddy kinetic energy in the California Current base on altimetric, drifter and moored current data. *J. Geophys. Res.*, **103 (C6)**.

Kliem, N. and J. Pietrzak, 1999: On the pressure gradient error in sigma coordinate ocean models: A comparison with a laboratory experiment. *J. Geophys. Res.*, **104 (C12)**.

Kone, V., E. Machu, P. Penven, V. Anderson, V. Garcon, P. Freon, and H. Demarcq, 2005: Modeling the primary and secondary productions of the southern Benguela upwelling system: A comparative study through two biogeochemical models. *Global Biogeochem. Cyc.*, **19**.

Kostianoy, A. and J. Lutjeharms, 1999: Atmospheric effects in the Angola-Benguela frontal zone. *J. Geophys. Res.*, **104**, 20 963–20 970.

Kundu, P., 1990: *Fluid Mechanics*. Academic Press.

Large, W., J. McWilliams, and S. Doney, 1994: Oceanic vertical mixing: a review and a model with a nonlocal boundary layer parameterization. *Rev. Geophys.*, **32**, 363–403.

Largier, J. and A. Boyd, 2001: Drifter observations of surface water transport in the Benguela Current during the winter of 1999. *S. Afr. J. Sci.*, **97**.

Lass, H., M. Schmidt, V. Mohrholz, and G. Nausch, 2000: Hydrographic and current measurements in the area of the Angola-Benguela front. *J. Phys. Oceanogr.*, **30**, 2 589–2 609.

Lett, C., J. Veitch, C. van der Lingen, and L. Hutchings, 2007: Assessment of an environmental barrier to transport of icthyoplankton from the southern to the northern Benguela ecosystems. *Mar. Ecol. Prog. Ser.*, **347**, 247–259.

Lorbacher, K., D. Dommenget, P. Niiler, and A. Kohl, 2006: Ocean mixed layer depth: A subsurface proxy for ocean-atmosphere variability. *J. Geophys. Res.*, **111 (C07010)**.

Lu, Y. and D. Stammer, 2004: Vorticity balance in coarse resolution global ocean simulations. *J. Phys. Oceanogr.*, **34**, 605–622.

Lutjeharms, J., 1996: The exchange of water between the South Indian and South Atlantic oceans. *The South Atlantic: Past and Present Circulation*, G. Wefer, W. Berger, G. Siedler, and D. Webb, Eds., Springer-Verlag, 125–162.

Lutjeharms, J., 2006: *The Agulhas Current*, 329. Springer-Verlag.

Lutjeharms, J. and C. Mathyssen, 1995: A recurrent eddy in the upwelling front off Cape Town. *S. Afr. J. Sci.*, **91 (7)**, 355–357.

Lutjeharms, J. and J. Meeuwis, 1987: The extent and variability of south-east Atlantic upwelling. *S. Afr. J. Mar. Sci.*, **5**, 51–62.

Lutjeharms, J., F. Shillington, and C. Duncombe-Rae, 1991: Observations of extreme upwelling filaments in the Southeast Atlantic Ocean. *Science*, **774 (3)**.

Lutjeharms, J. and P. Stockton, 1987: Kinematics of the upwelling front off southern Africa. *S. Afr. J. Mar. Sci.*, **5**, 35–49.

Lutjeharms, J. and R. van Ballegooyen, 1988: The retroflection of the Agulhas current. *J. Phys. Oceanogr.*, **18**, 1570–1583.

Lutjeharms, J., D. Webb, B. de Cuevas, and S. Thompson, 1995: Large-scale modelling of the south-east Atlantic upwelling system. *S. Afr. J. Mar. Sci.*, **16**, 205–225.

Marchesiello, P., B. Barnier, and A. de Miranda, 1998: A sigma-coordinate primitive equation model for studying the circulation in the south Atlantic part ii: Meridional transports and seasonal variability. *Deep-Sea Res. I*, **45**, 573–608.

Marchesiello, P., L. Debreu, and X. Couvelard, 2008a: Spurious diapycnal mixing in terrain-following coordinate models: advection problem and solutions. *Ocean Modelling*. **26**, 156–169.

Marchesiello, P. and P. Estrade, 2006: Eddy activity and mixing in upwelling systems: A comparative study of Northwest Africa and California regions. *Int. J. Earth Sci.*, **doi: 10.1007/s00531-007-0235-6**.

Marchesiello, P. and P. Estrade, 2009: Upwelling limitation by coastal geostrophic convergence. *Submitted to Journal of Physical Oceanography*.

Marchesiello, P., J. McWilliams, and A. Schepetkin, 2001: Open boundary conditions for long-term integration of regional oceanic models. *Ocean Modelling*, **3**, 1–20.

Marchesiello, P., J. McWilliams, and A. Schepetkin, 2003: Equilibrium structure and dynamics of the California current system. *J. Phys. Oceanogr.*, **33**, 753–783.

Matano, R. and E. Beier, 2003: A kinematic analysis of the Indian/Atlantic interocean exchange. *Deep-Sea Res.*, **50**, 229–249.

McCreary, J., 1981: A linear stratified model of the coastal undercurrent. *Philosophical Transcripts of the Royal Society of London*, **302**, 385–413.

McCreary, J., 1987: On the dynamics of the California Current system. *J. Mar. Res.*, **45**.

McCreary, J. and S.-Y. Chao, 1985: Three-dimensional shelf circulation along an eastern boundary. *J. Mar. Res.*, **43**, 13–36.

Meeuwis, J. and J. Lutjeharms, 1990: Surface thermal characteristics of the Angola-Benguela front. *S. Afr. J. Sci.*, **9**, 261–279.

Mercier, H., M. Arhan, and J. Lutjeharms, 2003: Upper-layer circulation in the eastern equatorial and south Atlantic ocean in January-March 1995. *Deep-Sea Res. I*, **50**, 863–887.

Mohrholz, V., C. Bartholomae, and A. van der Plas, 2007: The seasonal variability of the northern Benguela undercurrent and its relation to the oxygen budget on the shelf. *Cont. Shelf Res.*, **doi:10.1016/j.csr.2007.10.001**.

Mohrholz, V., M. Schmidt, J. Lutjeharms, and H.-C. John, 2001: The hydrography and dynamics of the Angola-Benguela frontal zone in April 1999. *S. Afr. J. Sci.*, **97**, 199–208.

Monteiro, P., G. Nelson, A. van der Plas, E. Mabille, G. Bailey, and E. Klingelhoeffer, 2005: Internal tide-shelf topography interactions as a forcing factor governing the large-scale distribution and burial fluxes of particulate organic matter (pom) in the Benguela upwelling system. *Cont. Shelf Res.*, **25**, 1864–1876.

Monteiro, P. and A. van der Plas, 2006: Low oxygen water (LOW) variability in the Benguela system: key processes and forcing scales relative to forecasting. *Benguela: predicting a large marine ecosystem*, V. Shannon, G. Hempel, P. Malanotte-Rizzoli, C. Moloney, and J. Woods, Eds., Elsevier, Large Marine Ecosystems, Vol. 14.

Monteiro, P., A. van der Plas, J.-L. Melice, and P. Florenchie, 2008: Interannual hypoxia variability in a coastal upwelling system: ocean-shelf exchange, climate and ecosystem-state implications. *Deep-Sea Res. I*, **55**, 435–450.

Myers, P., A. Fanning, and A. Weaver, 1996: Jebar, bottom pressure torque and Gulf stream separation. *J. Phys. Oceanogr.*, **26**.

Narimousa, S. and T. Maxworthy, 1986: Coastal upwelling on a sloping bottom: the formation of plumes, jets and pinched-off cyclones. *J. Fluid Mech.*, **176**, 169–190.

Nelson, G., 1989: *Poleward flows along eastern ocean boundaries*, Coastal and Estuarine Studies, Vol. 34, chap. Poleward motion in the Benguela area, 110–130. Springer, New York, New York.

Nelson, G., A. Boyd, J. Agenbag, and C. M. Duncombe-Rae, 1998: An upwelling filament north-west of Cape Town, South Africa. *S. Afr. J. Mar. Sci.*, **19**, 75–78.

Nelson, G. and L. Hutchings, 1983: The Benguela upwelling area. *Prog. Oceanogr.*, **12 (3)**.

O'Toole, M., 1980: Seasonal distribution of temperature and salinity in the surface waters off south west Africa from 1972-1974. *Investigational report of the division of Sea Fisheries*, **121**.

Parada, C., C. van der Lingen, C. Mullon, and P.Penven, 2003: Modelling the effect of buoyancy on the transport of anchovy (eugraulis capensis) eggs from spawning to nursery grounds in the southern Benguela: An IBM approach. *Fisheries Oceanogr.*, **12**, 170–184.

Pedlosky, J., 1974: Longshore currents and the onset of upwelling over bottom slope. *J. Phys. Oceanogr.*, **4**, 310–320.

Peffley, M. and J. O'Brien, 1976: A three-dimensional simulation of coastal upwelling off Oregon. *J. Phys. Oceanogr.*, **6**, 164–180.

Penven, P., 2000: A numerical study of the southern Benguela circulation with an application to fish recruitment. Ph.D. thesis, University of Brest.

Penven, P., N. Chang, and F. Shillington, 2006a: Modelling the Agulhas current using SAfE (Southern African Experiment). *Geophys. Res. Abstr.*, **8 (04225)**.

Penven, P., V. Echevin, J.Pasapera, F. Colas, and J. Tam, 2005: Average circulation, seasonal cycle, and mesoscale dynamics of the Peru current system: a modelling approach. *J. Geophys. Res.*, **110**, doi:10.1029/2005JC0029 452.

Penven, P., J. Lutjeharms, and P.Florenchie, 2006b: Madagascar: a pacemaker for the Agulhas current system? *Geophys. Res. Lett.*,**8 (04225)**, doi:10.1029/2006GLO26854.

Penven, P., C. Roy, G. Brundrit, A. D. Verdiere, P.Freon, A. Johnson, J. Lutjeharms, and F. Shillington, 2001: A regional hydrodynamic model of upwelling in the southern Benguela. *S. Afr. J. Sci.*, **97**, 472–475.

Penven, P., C. Roy, A. C. de Verdiere, and J. Largier, 2000: Simulation of a coastal jet retention process using a barotropic model. *Oceanologica Acta*, **23 (5)**, 615–634.

Penven, P. L. D., P. Marchesiello, and J. McWilliams, 2006c: Evaluation and application of the roms 1-way embedding procedure to the central California upwelling system. *Ocean Modelling*, **12**, 157–187.

Peterson, R. and L. Stramma, 1991: Upper-level circulation in the South Atlantic. *Progr. Oceanogr.*, **26**, 1–73.

Philander, G. and J.-H. Yoon, 1982: Eastern boundary currents and coastal upwelling. *J. Phys. Oceanogr.*, **12**, 862–879.

Pickett, M. and J. Paduan, 2003: Ekman transport and pumping in the California Current based on the U.S. navy's high resolution atmospheric model (coamps). *J. Geophys. Res.*, **108 (C10)**.

Poole, R. and M. Tomczak, 1999: Optimum multiparameter analysis of the water mass structure in the Atlantic ocean thermocline. *Deep-Sea Res.*, **46 (1)**, 1895–1921.

Preston-Whyte, R. and P. Tyson, 1993: *The atmosphere and weather of southern Africa*, chap. 11, 207–249. Oxford.

Reason, C., J. Lutjeharms, J. Hermes, A. Biastoch, and R. Roman, 2003: Inter-ocean fluxes south of Africa in an eddy-permitting model. *Deep Sea Res.*, **50 (2)**, 281–298.

Reid, J., 1989: Geostrophic circulation of the south Atlantic Ocean. *Progr. Oceanogr.*, **23**, 149–244.

Richardson, P., 2007: Agulhas leakage into the Atlantic estimated with subsurface floats and surface drifters. *Deep Sea Res. I*, **54 (8)**.

Richardson, P. and S. Garzoli, 2003: Characteristics of intermediate water flow in the Benguela current as measured with rafos floats. *Deep Sea Res. II*, **50**, 87–118.

Rio, M. and F. Hernanadez, 2004: A mean dynamic topography computed over the world ocean from altimetry, in situ measurements and a geoid model. *J. Geophys. Res.*, **109 (C1)**.

Rossi, V., C.Lopez, J.Sudre, E.Henandez-Garcia, and V.Garcon, 2008: Comparative study of mixing and biological activity of the Benguela and Canary upwelling systems. *Geophys. Res. Lett.*, **35**.

Sakamoto, T. and I. Umetsu, 2006: Seasonal energy cycle of wind-driven ocean circulation with particular emphasis on the role of bottom topography. *Deep Sea Res. I*, **53**, 154–168.

Sarkisyan, A. and V. Ivanov, 1971: The combined effect of baroclinicity and bottom relief as an important factor in the dynamics of ocean currents. *Izv. Acad. Sci. USSR, Atmosphere and Oceanic Physics, AGU translation*, **(173-188)**.

Schouten, M., W. de Ruijter, P. van Leeuwen, and J. Lutjeharms, 2000: Translation, decay and splitting of Agulhas rings in the southeastern Atlantic ocean. *J. Geophys. Res.*, **105 (C9)**, 21,913–21,925.

Scott, R. and F. Wang, 2005: Direct evidence of an oceanic inverse kinetic energy cascade from satellite altimetry. *J. Phys. Oceanogr.*, **35 (1650-1666)**.

Shannon, L., 1985: The Benguela ecosystem part 1: physical features and processes. *Oceanographic and Marine Biology Annual Review*, **23**, 105–182.

Shannon, L., J. Agenbag, and M. Buys, 1987: Large- and meso-scale features of the Angola-Benguela front. *S. Afr. J. Mar. Sci.*, **5**, 11–34.

Shannon, L., J. Agenbag, N. Walker, and J. Lutjeharms, 1990: A major perturbation in the Agulhas retroflection area in 1986. *Deep Sea Res.*, **37 (3)**, 493–512.

Shannon, L., A. Boyd, G. Brundrit, and J. Taunton-Clark, 1986: On the existence of an El niño-type phenomenon in the Benguela system. *J. Mar. Res.*, **44**, 495–520.

Shannon, L. and D. Hunter, 1988: Notes on Antarctic intermediate water around southern Africa. *S. Afr. J. Mar. Sci.*, **6**, 107–117.

Shannon, L. and G. Nelson, 1996: *The South Atlantic: Present and past circulation*, chap. The Benguela: Large-scale features and processes and system variability, 163–210. Springer.

Shaw, P.-T. and G. Csanady, 1983: Self-advection of density perturbations on a sloping continental shelf. *J. Phys. Oceanogr.*, **13**.

Shchepetkin, A. and J. McWilliams, 1998: Quasi-monotone advection schemes based on explicit locally adaptive dissipation. *Monthly Weather Review*, **126**, 1541–1580.

Shchepetkin, A. and J. McWilliams, 2003: A method for computing horizontal pressure-gradient force in an oceanic model with a nonaligned vertical coordinate. *J. Geophys. Res.*, **108 (C3)**.

Shchepetkin, A. and J. McWilliams, 2005: The Regional Oceanic Modeling System (ROMS): a split-explicit, free-surface, topography-following-coordinate oceanic model. *Ocean Modelling*, **9**, 347–404.

Shchepetkin, A. and J. McWilliams, 2008: *Handbook of numerical analysis: Computational methods for the ocean and atmosphere.*, chap. Computational kernel

algorithms for fine-scale, multi-process, long-term oceanic simulations, 119–181. Elsevier Science.

Shelton, P. and L. Hutchings, 1982: Transport of anchovy, engraulis capensis gilchrist, eggs and early larvae by a frontal jet current. *J.Cons.int.Explor.Mer*, **40**, 185–198.

Shillington, F., 1998: *The Global Coastal Ocean, Regional Studies and Syntheses*, The Sea, Vol. 11, chap. The Benguela upwelling system off southwestern Africa., 583–604. Wiley, New York.

Shillington, F., L. Hutchings, T. Probyn, H. Waldron, and W. Peterson, 1992: Filaments in the Benguela frontal zone: offshore advection or recirculation loops? *S. Afr. J. Mar. Sci.*, **12**, 207–218.

Shillington, F., W. Peterson, L. Hutchings, T. Probyn, H. Waldron, and J. Agenbag, 1990: A cool upwelling filament off Namibia, southwest Africa: preliminary measurements of physical and biological features. *Deep Sea Res.*, **37 (11)**, 1753–1772.

Shillington, F., C. Reason, C. Duncombe-Rae, P. Florenchie, and P. Penven, 2006: *Benguela: Predicting a Large Marine Ecosystem*, Large Marine Ecosystems, Vol. 14, chap. 4: Large scale variability of the Benguela Current Large Marine Ecosystem (BCLME), 49–70. Elsevier B.V.

Skogen, M., 1999: Numerical modelling of the Benguela system. some preliminary results. *S. Afr. J. Mar. Sci.*, **21**, 235–249.

Song, Y. and Y. Chao, 2004: A theoretical study of topographic effects on coastal upwelling and cross-shore exchange. *Ocean Modelling*, **6**, 151–176.

Song, Y. and D. Haidvogel, 1994: A semi-implicit ocean circulation model using a generalized topography following coordinate system. *J. Comput. Phys.*, **115**, 228–248.

Speich, S., J. Lutjeharms, P. Penven, and B.Blanke, 2006: Role of bathymetry in Agulhas current configuration and behaviour. *Geophys. Res. Lett.*, **33**, L23 611, doi:10.1029/2006GL027 157.

Stenevik, E., H. Verheye, M. Lipinski, M. Ostrowski, and T. Stromme, 2008: Drift routes of Cape hake eggs and larvae in the southern Benguela current system. *J. Plankton Res.*, **30 (10)**, 1147–1156.

Stramma, L. and R. Peterson, 1989: Geostrophic transport in the Benguela current region. *J. Phys. Oceanogr.*, **19**, 1440–1448.

Stramma, L. and R. Peterson, 1990: The south Atlantic current. *J. Phys. Oceanogr.*, **20**, 846–859.

Strub, P., F. Shillington, C. James, and S. Weeks, 1998: Satellite comparison of the seasonal circulation in the Benguela and California current systems. *S. Afr. J. Mar. Sci.*., **19**, 99–112.

Strub, T. and C. James, 2000: Altimeter-derived variability of surface velocities in the California Current system: 2. seasonal circulation and eddy statistics. *Deep Sea Res. II*, **47**, 831–870.

Suginohara, N., 1982: Coastal upwelling: onshore-offshore circulation, equatorward coastal jet and poleward undercurrent over a continental shelf slope. *J. Phys. Oceanogr.*, **12**.

Sverdrup, H., 1947: Wind-driven currents in a baroclinic ocean; with application to the equatorial currents of the eastern pacific. *Proc. N.A.S.*, 318–326.

Taunton-Clark, J., 1985: *South African Ocean Colour and Upwelling Experiment*, chap. The formation, growth and decay of upwelling tongues in response to the mesoscale wind field during summer.

Taunton-Clark, J. and L. Shannon, 1988: Annual and interannual variability in the south-east Atlantic during the 20th century. *S. Afr. J. Mar. Sci.*, **6**, 97–106.

Torrence, C. and G. Compo, 1998: A practical guide to wavelet analysis. *Bulletin of the American Meteorological Society*, **79 (1)**.

Treguier, A., O. Boebel, B.Barnier, and G.Madec, 2003: Agulhas eddy fluxes in a 1/6 degree Atlantic model. *Deep Sea Res. II*, **50**, 251–280.

Vallis, G., 2006: *Atmospheric and Ocean Fluid Dynamics*. Cambridge Universty Press.

van Aken, H., A. van Veldhoven, C. Veth, W. D. Ruitjer, P. van Leeuwen, S. S. Drijfhout, C. Whittle, and M. Rouault, 2000: Observations of a young Agulhas ring, Astrid, during MARE: the Mixing of Agulhas Rings Experiment, in March 2000. *Deep Sea Res. II*, **50 (1)**, 167–195.

van Ballegooyen, C., M. Grundlingh, and J. Lutjeharms, 1994: Eddy fluxes of heat and salt from the south west Indian Ocean into the south east Atlantic Ocean: a case study. *J. Geophys. Res.*, **99 (C7)**, 14,053–14,070.

van Foreest, D. and G. Brundrit, 1985: *South African Ocean Colour and Upwelling Experiment*, chap. Numerical modelling of the southern Benguela system, 111–123. Sea Fisheries Research Institute, Cape Town.

van Foreest, D., F. Shillington, and R. Legeckis, 1984: Large scale, stationary, frontal features in the Benguela current system. *Continental Shelf Research*, **3 (4)**, 465–474.

Veitch, J., 2007: The changing state of the Benguela Current Large Marine Ecosystem (BCLME): expert workshop on climate change and variability and impacts thereof in the bclme region. BCLME workshop report, 15-17 May 2007.

Veitch, J., P. Florenchie, and F. Shillington, 2006: Seasonal and interannual fluctuations of the Angola-Benguela frontal zone (ABFZ) using 4.5 km resolution satellite imagery from 1982 to 1999. *Int. J. Remote Sens.*, **27 (5)**, 987–998.

Veitch, J., P. Penven, and F. Shillington, 2009: The Benguela: a laboratory for comparative studies. *Prog. Oceanogr*,doi:10.1016/j.pocean.2009.08.008.

Viljoen, A., 2006: Investigation of the nearshore, episodic poleward current in the southern Benguela: a numerical modelling approach. M.S. thesis, University of Cape Town, South Africa.

Weeks, S., R. Barlow, C. Roy, and F. Shillington, 2006: Remotely sensed variability of temperature and chlorophyll in the southern Benguela: upwelling frequency and phytoplankton response. *Afr. J. Mar. Sci.*, **28 (3-4)**.

Wilkin, J. and D. Chapman, 1987: Scattering of continental shelf waves at a discontinuity in shelf width. *J. Phys. Oceanogr.*, **17**, 713–724.

Yoon, J.-H. and S. Philander, 1982: The generation of coastal undercurrents. *J. Oceanogr. Soc. Jap.*, **38**, 215–224.

APPENDIX A

Scaling the momentum equation

We begin with the Navier-Stokes equations for u- and v- horizontal momentum, based on the Boussinesq approximation (i.e. density variations are small except in their contribution to the buoyancy force):

$$\frac{\partial u}{\partial t} = fv - \frac{1}{\rho_0}\frac{\partial P}{\partial x} - u\frac{\partial u}{\partial x} - v\frac{\partial u}{\partial y} - w\frac{\partial u}{\partial z} + \frac{\partial}{\partial z}\left(A_v\frac{\partial u}{\partial z}\right) + A_H\left(\frac{\partial^2 u}{\partial x^2} + \frac{\partial^2 v}{\partial y^2}\right) \quad \text{(A.1)}$$

$$\frac{\partial v}{\partial t} = -fu - \frac{1}{\rho_0}\frac{\partial P}{\partial y} - v\frac{\partial v}{\partial y} - u\frac{\partial v}{\partial x} - w\frac{\partial v}{\partial z} + \frac{\partial}{\partial z}\left(A_v\frac{\partial v}{\partial z}\right) + A_H\left(\frac{\partial^2 u}{\partial x^2} + \frac{\partial^2 v}{\partial y^2}\right) \quad \text{(A.2)}$$

where:

- x, y and z are coordinates in the cartesian frame (in m)
- u,v and w are the zonal, meridional and vertical velocity vectors respectively (in $m.s^{-1}$)
- f is the coriolis parameter (in s^{-1})
- P is pressure (in $N.m^{-2}$ or $kg.m^{-1}.s^{-2}$)
- ρ_o is the reference density of seawater (1024 $kg.m^{-3}$)
- $A_v\frac{\partial u}{\partial z} = \frac{\tau_x^s}{\rho_o} - \frac{\tau_x^b}{\rho_o}$ and $A_v\frac{\partial v}{\partial z} = \frac{\tau_y^s}{\rho_o} - \frac{\tau_y^b}{\rho_o}$ where A_v is the vertical mixing parameter
- τ_x^s and τ_y^s are the zonal and meridional surface wind stress components (in $N.m^{-2}$ or $kg.m^{-1}.s^{-2}$)
- τ_x^b and τ_y^b are the zonal and meridional bottom stress components (in $N.m^{-2}$ or $kg.m^{-1}.s^{-2}$)
- A_h is the horizontal diffusivity (in $m^2.s^{-1}$)

The term on the left-hand side (LHS) of equations (A.1) and (A.2) represents the time rate of change, which is zero in a time-mean solution. The first two terms on the right-hand side (RHS) represent the Coriolis and pressure gradient terms. The third, fourth and fifth terms are the non-linear advection terms. The sixth term on the RHS is the vertical mixing term, which includes surface (i.e. wind stress) and bottom forcing. The seventh term on the RHS represents diffusion in the form of a laplacian operator.

Equations (A.1) and (A.2) can be simplifed in vector notation:

$$\frac{\partial \vec{u}}{\partial t} = -\vec{u}.\nabla\vec{u} - f\vec{k} \wedge \vec{u} - \frac{\nabla\vec{p}}{\rho_o} + \frac{\partial}{\partial z}\left(A_v \frac{\partial \vec{u}}{\partial z}\right) + A_H \nabla_H^2 \vec{u} \tag{A.3}$$

where:

- $\vec{\phi}$ denotes a vector of any variable (ϕ)
- ∇ is the gradient operator
- ∇_H^2 is the horizontal laplacian operator

In order to scale equation (A.3), we need to approximate velocity (U), length (L), depth (H), pressure (P) and time (T) scales relevant to the particular problem. We use these scales to normalize the terms of the momentum equation, forming dimensionless numbers that give the relative importance of each term.

$$\begin{aligned}
\vec{u}' &= \frac{\vec{u}}{U}, \quad \vec{u} = \vec{u}'U \\
x' &= \frac{x}{L}, \quad x = x'L \\
y' &= \frac{y}{L}, \quad y = y'L \\
z' &= \frac{z}{H}, \quad z = z'H \\
p' &= \frac{p}{P}, \quad p = p'P \\
t' &= \frac{t}{T}, \quad t = T'L
\end{aligned}$$

where $\vec{u}'$, x', y', z', p' and t' are of the order of 1 ($\mathcal{O}(1)$).

Each term is scaled separately:

1. The time rate of change term:

$$\frac{\partial \vec{u}}{\partial t} = \frac{\partial \vec{u}' U}{\partial t' T} = \frac{U}{T}\frac{\partial \vec{u}'}{\partial t'} \sim \mathcal{O}\left(\frac{U}{T}\right) \tag{A.4}$$

2. The nonlinear advection term:

$$\vec{u}.\nabla\vec{u} = \vec{u}'U.\nabla\vec{u}'U = \frac{U^2}{L}\vec{u}'.\nabla\vec{u}' \sim \mathcal{O}\left(\frac{U^2}{L}\right) \tag{A.5}$$

3. The coriolis term:

$$f\vec{k} \wedge \vec{u} = f\vec{k} \wedge \vec{u}'U \sim \mathcal{O}\left(fU\right) \tag{A.6}$$

4. The pressure pradient term:

$$-\frac{\nabla\vec{p}}{\rho_o} = -\frac{\vec{\nabla}'P}{\rho_o L} = -\frac{P}{\rho_o L}\vec{p}' \sim \mathcal{O}\left(-\frac{P}{\rho_0 L}\right) \tag{A.7}$$

5. The vertical mixing term:

$$\frac{\partial}{\partial z}A_V\frac{\partial \vec{u}}{\partial z} = \frac{U}{H^2}\frac{\partial}{\partial z'}A_V\frac{\partial \vec{u}'}{\partial z'} \sim \mathcal{O}\left(\frac{A_V U}{H^2}\right) \tag{A.8}$$

6. The horizontal turbulent mixing term:

$$\nabla_H\left(A_H\nabla_H\vec{u'}\right) \sim \mathcal{O}\left(\frac{A_H 2U}{L^2}\right) \tag{A.9}$$

The scaled-version of the momentum equation therefore becomes:

$$\begin{aligned}\left(\frac{U}{T}\right)\frac{\partial \vec{u}'}{\partial t'} = &-\left(\frac{U^2}{L}\right)\vec{u}'.\nabla\vec{u}' - \left(fU\right)\vec{k} \wedge \vec{u}' \\ &-\left(\frac{P}{\rho_o L}\right)\vec{p}' + \left(\frac{U}{H^2}\right)\frac{\partial}{\partial z'}A_V\frac{\partial \vec{u}'}{\partial z'} \\ &+\left(\frac{U}{L^2}\right)\nabla_H\left(A_H\nabla_H\vec{u'}\right)\end{aligned} \tag{A.10}$$

Dividing by the a characteristic magnitude of the Coriolis term (fU) so that the dimensionless terms are all relative to Coriolis:

$$\left(\frac{1}{fT}\right)\frac{\partial\vec{u}'}{\partial t'} = -\left(\frac{U}{fL}\right)\vec{u}'.\nabla\vec{u}' + 1 - \left(\frac{P}{\rho_o fUL}\right)\vec{p}' + \left(\frac{A_v}{fH^2}\right)\nabla_z^2\vec{u}' + \left(\frac{A_H}{fL^2}\right)\nabla_H^2\vec{u}' \tag{A.11}$$

The terms in paretheses in equation (A.11) represent dimensionless numbers that allow us to characterise flow regimes, based on simplified scales.

$\frac{U}{fL}$ is the Rossby Number (R_O), which is the ratio of the advective terms to the rotation terms. If is is large, then affects of planetary rotation are small and the nonlinear advection terms are important. If R_O is small, then we can make the geostrophic approximation as the Coriolis term is important and approximately balances the pressure gradient term as the nonlinear advection term is small.

$\frac{1}{fT}$ is the time-dependent form of the Rossby Number (R_{OT}). If the time-scale of interest is an advective one (i.e. $T\ \frac{L}{U}$) then $R_{OT} \sim R_O$. For phenomena with timescales greater than the inertial period (i.e. $T_i \sim \frac{1}{f}$), the effects of the Earths rotation are significant, but the converse is true for periods shorter than the inertial period

$\frac{A_H}{fL^2}$ is the horizontal Ekman number, which is the ratio of viscous forces in a fluid to the forces arising from planetary rotation. It is important in lateral viscous boundary layers.

$\frac{A_v}{fH^2}$ is the vertical Ekman number, which is significant in the surface and bottom boundary layers.

$\frac{P}{\rho_o fUL}$ is the pressure scale and should be of the order of one in a geostrophic flow regime.

APPENDIX B

The vorticity equation

The Sverdrup relation

We start with the momentum equations, based on a regime in which the time-dependant Rossby number, the Rossby number and the horizontal Ekman numbers are small (refer to Appendix A) so that we can neglect the first term on the LHS and the non-linear advection and horizontal diffusion terms on the RHS of equations (A.1) and (A.2):

$$0 = fv - \frac{1}{\rho_0}\frac{\partial P}{\partial x} + \frac{\partial}{\partial z}\left(A_v \frac{\partial u}{\partial z}\right) \tag{B.1}$$

$$0 = -fu - \frac{1}{\rho_0}\frac{\partial P}{\partial y} + \frac{\partial}{\partial z}\left(A_v \frac{\partial v}{\partial z}\right) \tag{B.2}$$

The curl of equations B.1 and B.2 (i.e. $-\frac{d}{dy}$ of equation (B.1) + $\frac{d}{dx}$ of equation (B.2)) is taken and the continuity equation ($\frac{\partial u}{\partial x} + \frac{\partial v}{\partial y} = -\frac{\partial w}{\partial z}$) is used to simplify the solution

$$0 = f\frac{\partial w}{\partial z} - v\beta + curl_z\left[\frac{\partial}{\partial z}\left(A_v \frac{\partial u}{\partial z}\right), \frac{\partial}{\partial z}\left(A_v \frac{\partial v}{\partial z}\right)\right] \tag{B.3}$$

where, $f\frac{\partial w}{\partial z}$ is the vortex stretching term, β is the meridional change of the Coriolis effect (i.e. $\frac{\partial f}{\partial y}$).

Equation B.3 can be integrated with depth to a chosen level of no motion (taken here to be 1000 m). Due to the large-scale climatological nature of this problem we make the rigid-lid assumption, so that $\frac{\partial w}{\partial z} = 0$ and the vortex stretching term can be neglected.We are left with the Sverdrup relation:

$$0 = -\beta \int_{-1000}^{0} v dz + \frac{1}{\rho_0}\left(\frac{\partial \tau_x^s}{\partial y} - \frac{\partial \tau_y^s}{\partial x}\right) \tag{B.4}$$

where $A_v \frac{\partial u}{\partial z} = \frac{\tau_x^s}{\rho_o}$ and $A_v \frac{\partial u}{\partial z} = \frac{\tau_y^s}{\rho_o}$ (we neglect the friction effects at the base of the layer). Equation (B.4) can equivalently be written as:

$$-\beta \frac{\partial \psi}{\partial x} = \frac{1}{\rho_0} \nabla \times \tau^s \tag{B.5}$$

where, ψ is the transport streamfunction: $M_y = -\frac{\partial \psi}{\partial x}$ and $M_y = \int_{-1000}^{0} v dz$

Mean and eddy vorticity advection terms

In a high Rossby-number regime, where non-linear processes are important, we cannot neglect the advection terms in the vorticity balance equation, nor do we make the rigid-lid assumption which suggests a negligable vortex stretching term. The depth-integrated (to 1000 m) vorticity balance therefore becomes:

$$\begin{aligned} 0 = \int_{-1000}^{\eta} \frac{\partial w}{\partial z} dz - \beta \int_{-1000}^{\eta} v dz \\ - \int_{-1000}^{\eta} curl_z \left[u \frac{\partial u}{\partial x} + v \frac{\partial u}{\partial y}, v \frac{\partial v}{\partial y} + u \frac{\partial v}{\partial x} \right] dz \\ + \frac{1}{\rho_0} \left(\frac{\partial \tau_x^s}{\partial y} - \frac{\partial \tau_y^s}{\partial x} \right) \end{aligned} \tag{B.6}$$

and written in vector notation:

$$0 = \int_{-1000}^{\eta} f \frac{\partial w}{\partial z} dz - \beta \int_{-1000}^{\eta} v dz - \int_{-1000}^{\eta} \overrightarrow{v} \nabla \xi dz + \nabla \wedge \frac{\vec{\tau}^{surf}}{\rho_0} \tag{B.7}$$

where ξ is relative vorticity $(-\frac{\partial u}{\partial y} + \frac{\partial v}{\partial x})$ and η is the free-surface.
In order to separate the vorticity advection term (i.e. the third therm on the RHS of equation B.6) into mean and eddy contributions, we begin with:

$$\phi = \bar{\phi} + \phi' \tag{B.8}$$

where $\bar{\phi}$ is the temporal mean of any variable (ϕ) and ϕ' is the deviation from the mean, or the transient component so that $\bar{\phi'} = 0$.

We separate the total non-linear advection terms that appear in the u- and v-horizontal momentum equations (equation (A.1) and (A.2) respectively and named *uadv* and *vadv* respectively) into their mean and eddy components as follows:

$$uadv = (\bar{u} + u') \frac{\partial (\bar{u} + u')}{\partial x} + (\bar{v} + v') \frac{\partial (\bar{u} + u')}{\partial y} \tag{B.9}$$

$$vadv = (\bar{v} + v') \frac{\partial (\bar{v} + v')}{\partial y} + (\bar{u} + u') \frac{\partial (\bar{v} + v')}{\partial x} \tag{B.10}$$

Expanding and in simplifying we use the product rule $\frac{\partial AB}{\partial x} = A\frac{\partial B}{\partial x} + B\frac{\partial A}{\partial x}$, the continuity equation and the fact that $\bar{\phi}' = 0$. Equations B.9 and B.10 become:

$$uadv = \frac{\partial \bar{u^2}}{\partial x} + \frac{\partial \bar{u}\bar{v}}{\partial y} + \frac{\partial u'^2}{\partial x} + \frac{\partial u'v'}{\partial y} \tag{B.11}$$

$$vadv = \frac{\partial \bar{v^2}}{\partial y} + \frac{\partial \bar{u}\bar{v}}{\partial x} + \frac{\partial v'^2}{\partial y} + \frac{\partial u'v'}{\partial x} \tag{B.12}$$

where the first two terms in equations B.11 and B.12 represent the mean advection terms in the u- and v- momentum equations respectively and the last two terms represent the transient eddy advection terms.

The mean (MADV) and eddy (EADV) vorticity advection terms therefore (i.e. third term on the RHS of equation B.7, separated into its mean and eddy/transient components) become:

$$MADV = -\int_{-1000}^{\eta} curl_z \left[\frac{\partial \bar{u}^2}{\partial x} + \frac{\partial \bar{u}\bar{v}}{\partial y}, \frac{\partial \bar{v}^2}{\partial y} + \frac{\partial \bar{u}\bar{v}}{\partial x} \right] dz$$

$$EADV = -\int_{-1000}^{\eta} curl_z \left[\frac{\partial u'^2}{\partial x} + \frac{\partial u'v'}{\partial y}, \frac{\partial v'^2}{\partial y} + \frac{\partial u'v'}{\partial x} \right] dz \tag{B.13}$$

APPENDIX C

The JEBAR (Joint Effect of Baroclinicity and Relief) term

The JEBAR term appears in the depth-integrated vorticity equation and describes a baroclinic flow over a sloping bottom and introduces a bottom torque. We derive the JEBAR term for a low Rossby number, low time-dependant Rossby number and low horizontal Ekman number regime (see Appendix A). Based on these assumptions we neglect the non-linear advection terms, the rate and the horizontal diffusion terms. We therefore begin our derivation with the following form of the momentum equations shown in Appendix A (equations (A.1) and (A.2)):

$$0 = fv - \frac{1}{\rho_o}\frac{\partial P}{\partial x} + \frac{\partial}{\partial z}\left(A_v \frac{\partial u}{\partial z}\right) \tag{C.1}$$

$$0 = -fu - \frac{1}{\rho_o}\frac{\partial P}{\partial y} + \frac{\partial}{\partial z}\left(A_v \frac{\partial v}{\partial z}\right) \tag{C.2}$$

Equations (C.1) and (C.2) are integrated from top to bottom and divided by the depth (H), replacing ϕ with the depth-integrated hydrostatic approximation: $P = \rho g z$.

$$M_y \frac{f}{H} = -\frac{1}{H}\left(\frac{\partial}{\partial x}\int_{-H}^{0} \frac{\rho g z dz}{\rho_0}\right) + \frac{1}{H}\frac{\tau_x^s}{\rho_o} - \frac{1}{H}\frac{\tau_x^b}{\rho_o} \tag{C.3}$$

$$M_x \frac{f}{H} = -\frac{1}{H}\left(\frac{\partial}{\partial y}\int_{-H}^{0} \frac{\rho g z dz}{\rho_0}\right) + \frac{1}{H}\frac{\tau_y^s}{\rho_o} - \frac{1}{H}\frac{\tau_y^b}{\rho_o} \tag{C.4}$$

where $M_x = \int_{-H}^{0} u dz$, $M_y = \int_{-H}^{0} v dz$, $A_v \frac{\partial u}{\partial z} = \frac{\tau_x^s}{\rho_o} - \frac{\tau_x^b}{\rho_o}$ and $A_v \frac{\partial v}{\partial z} = \frac{\tau_y^s}{\rho_o} - \frac{\tau_y^b}{\rho_o}$.

Simplify equations (C.3) and (C.4) by introducing the term for baroclinic poten-

tial energy: $\phi = \frac{g}{\rho_o}\int_{-H}^{0}\rho z dz$ and then take their curl (i.e. $-\frac{d}{dy}$ of equation (C.3) + $\frac{d}{dx}$ of equation (C.4)). Using the product rule and the fact that $\frac{\partial M_x}{\partial x} + \frac{\partial M_y}{\partial y} = 0$ in a rigid-lid approximation, this becomes:

$$\begin{aligned} M_y\frac{\partial}{\partial y}\left(\frac{f}{H}\right) + M_x\frac{\partial}{\partial x}\left(\frac{f}{H}\right) = \\ \frac{1}{\rho_o}\frac{\partial\phi}{\partial x}\frac{\partial H^{-1}}{\partial y} - \frac{1}{\rho_o}\frac{\partial\phi}{\partial y}\frac{\partial H^{-1}}{\partial x} \\ -\frac{\partial}{\partial y}\left(\frac{\tau_x^s}{\rho_o H}\right) + \frac{\partial}{\partial x}\left(\frac{\tau_y^s}{\rho_o H}\right) - \frac{\partial}{\partial y}\left(\frac{\tau_x^b}{\rho_o H}\right) + \frac{\partial}{\partial x}\left(\frac{\tau_y^b}{\rho_o H}\right) \end{aligned} \tag{C.5}$$

Which can also be written as follows:

$$\vec{M}.\nabla\frac{f}{H} = J\left(\phi, H^{-1}\right) + \nabla\wedge\frac{\tau^s}{\rho_o H} + \nabla\wedge\frac{\tau^b}{\rho_o H} \tag{C.6}$$

where:

- $\vec{M}.\nabla\frac{f}{H} = M_y\frac{\partial}{\partial y}\left(\frac{f}{H}\right) + M_x\frac{\partial}{\partial x}\left(\frac{f}{H}\right)$
- J is the Jacobian and represents: $\frac{\partial\phi}{\partial x}\frac{\partial H^{-1}}{\partial y} - \frac{\partial\phi}{\partial y}\frac{\partial H^{-1}}{\partial x}$
- $\nabla\wedge\frac{\tau^s}{\rho_o H} = -\frac{\partial}{\partial y}\left(\frac{\tau_x^s}{\rho_o H}\right) + \frac{\partial}{\partial x}\left(\frac{\tau_y^s}{\rho_o H}\right)$
- $\nabla\wedge\frac{\tau^b}{\rho_o H} = -\frac{\partial}{\partial y}\left(\frac{\tau_x^b}{\rho_o H}\right) + \frac{\partial}{\partial x}\left(\frac{\tau_y^b}{\rho_o H}\right)$

Shaw and Csanady (1983) and Csanady (1985) provide a succinct description of the dynamics of JEBAR. Horizontal density perturbations will result in a vertical shear in the flow due to the thermal wind relation. If the density perturbation occurs in the along-isobath sense over a sloping-bottom, the net transport in deeper regions will be more than in shallower regions resulting in a divergence. By the necessity of the conservation of mass, this divergence is compensated for by a barotopic transport field, which stretches the vortex lines, causing the water column to veer into deeper water. The steeper the slope and the more intense the along-isobath density gradient, the stronger this effect will be.

APPENDIX D

Cape and mean flow interaction

This model of the interaction between a cape and a mean flow to produce a standing shelf wave is derived based on the methods of Buchwald and Adams (1968), Wilkin and Chapman (1987) and Penven (2000).

We make the assumption of a barotropic ocean and the rigid-lid approximation. The rigid-lid approximation is justified due to the climatological nature of the problem and, more specifically, due to the fact that the external Rossby radius of deformation is much greater that the length scale of our problem, which is $O\,(100km)$. The external Rossby radius of deformation is $O\,(500km)$ and is defined as $R = \frac{\sqrt{gH}}{f}$, where g is the acceleration due to gravity $(9.8m.s^{-2})$, H is a characteristic depth-scale $O\,(200m)$ and f is the coriolis parameter, which is -0.8×10^{-4}.

Our interest is in standing waves at the shelf-edge that are generated by the interaction of a mean equatorward flow with a cape on the right of it. For this reason, we follow the method of Penven 2000 and assume that the cape is moving poleward with a mean velocity U_0 and is adjacent to an ocean at rest (which approximates the interaction of a mean equatorward flow with a cape on the right of it) so that we can rewrite the temporal derivations in a moving frame of reference. Given that (x, y, z, t) are the 'fixed' Eulerian co-ordinates of the mean flow and (x_1, y_1, z_1, t_1) are the reference co-ordinates attached to the moving cape, it follows that:

$$\frac{\partial}{\partial t} = \frac{\partial}{\partial x_1}\frac{\partial x_1}{\partial t} + \frac{\partial}{\partial t_1} \tag{D.1}$$

where: $\frac{\partial x_1}{\partial t} = U_0$ and U_0 is the magnitude of the mean flow.

For this problem, the time-dependant Rossby number, the Rossby number and horizontal Ekman numbers are small (see Appendix A for a description). Based on these assumptions and in the absence of wind-forcing and rewriting the temporal derivations in the moving frame (D.1), the shallow water, depth-integrated momentum

equations (see equations (A.1) and (A.2) in Appendix A) become:

$$U_0 \frac{\partial \bar{u}}{\partial x} = f\bar{v} - \frac{1}{\rho_o}\frac{\partial P}{\partial x} \tag{D.2}$$

$$U_0 \frac{\partial \bar{v}}{\partial x} = -f\bar{u} - \frac{1}{\rho_o}\frac{\partial P}{\partial y} \tag{D.3}$$

Due to the rigid-lid assumption, the depth-integrated continuity equation is two-dimensional:

$$\frac{\partial (hu)}{\partial x} + \frac{\partial (hv)}{\partial y} = 0 \tag{D.4}$$

and a streamfunction can be defined as follows:

$$hu = -\frac{\partial \psi}{\partial y} \tag{D.5}$$

$$hv = \frac{\partial \psi}{\partial x} \tag{D.6}$$

Subtracting the $\frac{\partial}{\partial y}$ of equation (D.2) from $\frac{\partial}{\partial x}$ of equation (D.3) we obtain a vorticity equation:

$$U_0 \frac{\partial}{\partial x}\left(\frac{\partial u}{\partial y} - \frac{\partial v}{\partial x}\right) = f\left(\frac{\partial v}{\partial y} + \frac{\partial u}{\partial x}\right) \tag{D.7}$$

Using the continuity equation (D.4) and the product rule, equation (D.7) becomes:

$$U_0 \frac{\partial}{\partial x}\left(\frac{\partial u}{\partial y} - \frac{\partial v}{\partial x}\right) = \frac{f}{h}\left(u\frac{\partial h}{\partial x} + v\frac{\partial h}{\partial y}\right) \tag{D.8}$$

Because there is no change of h in the alonghore direction, where y- is alongshore and x- is cross-shore, equation (D.8) becomes:

$$U_0 \frac{\partial}{\partial x}\left(\frac{\partial u}{\partial y} - \frac{\partial v}{\partial x}\right) = fu\frac{h'}{h} \tag{D.9}$$

Introducing the streamfunction relationships (D.5) and (D.6) into equation (D.9) gives:

$$U_0 \frac{\partial}{\partial x}\left(\frac{\partial^2 \psi}{\partial x^2} + \frac{\partial^2 \psi}{\partial y^2}\right) - \frac{h'}{h}\left(U_0 \frac{\partial^2 \psi}{\partial x \partial y} + f\frac{\partial \psi}{\partial x}\right) = 0 \tag{D.10}$$

Equation (D.10) can be simplified by linearizing it with respect to h, by introducing a linear function that approximates the geometry of the shelf:

$$h = h_{max} e^{-2\lambda(X_{max}-x)} \tag{D.11}$$

where λ is the shelf steepness and X_{max} and x are the maximum offshore distance and offshore distance respectively. Inserting the linearized shelf slope into equation (D.10) gives:

$$U_0 \frac{\partial}{\partial x}\left(\frac{\partial^2 \psi}{\partial x^2} + \frac{\partial^2 \psi}{\partial y^2}\right) - 2\lambda\left(U_0 \frac{\partial^2 \psi}{\partial x \partial y} + f\frac{\partial \psi}{\partial x}\right) = 0 \tag{D.12}$$

For a standing wave with alongshelf wavenumber k, ψ takes the form:

$$\psi = \psi_0 \phi\,(y)\, e^{ikx} \tag{D.13}$$

Substituting equation (D.13) into (D.12):

$$\frac{\partial^2 \phi}{\partial y^2} - 2\lambda \frac{\partial \phi}{\partial y} + \left(k^2 - \frac{2\lambda f}{U_0}\right)\phi = 0 \tag{D.14}$$

If, as in (Wilkin and Chapman, 1987), we make the assumption of boundary conditions of no flow through the walls, such that ψ is constant along $X = 0$ and $X = Xmax$ and $\phi(0) = \phi(Xmax) = 0$. Based on these assumptions, equation (D.14) can now accept solutions of the form:

$$\phi = e^{\lambda y} sin\left(\frac{n\pi x}{Y_{max}}\right) \tag{D.15}$$

where $\frac{n\pi}{Ymax} = k_n$ and n is the mode number. Substituting equation (D.15) into equation (D.14) yields the dispersion relationship:

$$L_n = \frac{2\pi}{\sqrt{-\frac{n^2\pi^2}{Y_{max}^2} - \lambda^2 - \frac{2\lambda f}{U_0}}} \tag{D.16}$$

where L_{n} is the wavelength.

APPENDIX E

The mean and eddy kinetic energy equations

We derive the mean and turbulent kinetic energy equations for the equilibrium state so that we may examine the terms that provide sources and sinks of kinetic energy within the Benguela system. Generic definitions of total, mean and eddy kinetic energy (TKE, MKE and EKE respectively) per unit of mass follow. This derivation approximately follows the method of [Kundu, 1990].

$$TKE = \frac{1}{2}\left(u^2 + v^2\right) \tag{E.1}$$

$$MKE = \frac{1}{2}\left(\bar{u}^2 + \bar{v}^2\right) \tag{E.2}$$

$$EKE = \frac{1}{2}\left(\overline{u'^2 + v'^2}\right) \tag{E.3}$$

where u is the total velocity, $\bar{u}$ is the mean velocity and u' is the eddy velocity, so that $u = \bar{u} + u'$. Our solution is derived for a regime of low time-dependant Rossby number (i.e. steady state) and low horizontal Ekman number (i.e. horizontal diffusion is negligable).

Mean kinetic energy equation

Kinetic energy equations are derived for the mean x-, y- and z- components of flow separately and are then added in order to obtain the full mean kinetic energy equation. We begin with the momentum equation (see equations (A.1) and (A.2) in Appendix A), based on a low time-dependant Rossby number and a low horizontal Ekman number, for the mean state for the x-component, which is derived by taking the mean of the total momentum equation, which can be separated into mean and

eddy parts: $\frac{\partial}{\partial t}(\bar{u}+u')$.

$$\overline{(\bar{u}+u')}\frac{\partial}{\partial x}\overline{(\bar{u}+u')}+\overline{(\bar{v}+v')}\frac{\partial}{\partial y}\overline{(\bar{u}+u')}+\overline{(\bar{w}+w')}\frac{\partial}{\partial z}\overline{(\bar{u}+u')}$$
$$=-\frac{1}{\rho_0}\frac{\partial}{\partial x}\overline{(\bar{p}+p')}+f\overline{(\bar{v}+v')}+\frac{\partial}{\partial z}A_v\overline{\left(\frac{\partial}{\partial z}(\bar{u}+u')\right)} \tag{E.4}$$

Because $\bar{\phi}'=0$, the last term on the RHS simplifies by losing its prime component (i.e. $\frac{\partial}{\partial z}A_v\left(\frac{\partial}{\partial z}\overline{(\bar{u}+u')}\right)=\frac{\partial}{\partial z}A_v\left(\overline{\frac{\partial\bar{u}}{\partial z}}\right)+\frac{\partial}{\partial z}A_v\left(\overline{\frac{\partial u'}{\partial z}}\right)=\frac{\partial}{\partial z}A_v\left(\frac{\partial\bar{u}}{\partial z}\right)+0$), as do all of the other terms on the RHS. The advection terms (i.e. the terms on the LHS) retain some primes by expansion and simplification using the product rule (i.e. $\frac{\partial}{\partial x}(ab)=b\left(\frac{\partial a}{\partial x}\right)+a\left(\frac{\partial b}{\partial x}\right)$) and the fact that $\bar{\phi}'=0$. As a demonstration, we develop only the 2nd term on the LHS of equation (E.4) (the 3rd and 4th terms expand similarly).

$$\overline{(\bar{u}+u')\frac{\partial}{\partial x}(\bar{u}+u')}=$$
$$\overline{(\bar{u}+u')\left(\frac{\partial\bar{u}}{\partial x}+\frac{\partial u'}{\partial x}\right)}=$$
$$\overline{u'\frac{\partial u'}{\partial x}+\bar{u}\frac{\partial u'}{\partial x}+u'\frac{\partial\bar{u}}{\partial\bar{x}}+\bar{u}\frac{\partial\bar{u}}{\partial x}}=$$
$$\overline{u'\frac{\partial u'}{\partial x}+\left(\frac{\partial\bar{u}u'}{\partial x}=0\right)+\bar{u}\frac{\partial\bar{u}}{\partial x}}=$$
$$\overline{u'\frac{\partial u'}{\partial x}}+\bar{u}\frac{\partial\bar{u}}{\partial x} \tag{E.5}$$

Using the same method to develop the mean v- and w- nonlinear advection terms, the final form of the mean u- momentum equation is therefore:

$$\bar{u}\frac{\partial\bar{u}}{\partial x}+\bar{v}\frac{\partial\bar{u}}{\partial y}+\bar{w}\frac{\partial\bar{u}}{\partial z}+\overline{u'\frac{\partial u'}{\partial x}}+\overline{v'\frac{\partial u'}{\partial y}}+\overline{w'\frac{\partial u'}{\partial z}}$$
$$=-\frac{1}{\rho_0}\frac{\partial\bar{p}}{\partial x}+f\bar{v}+\frac{\partial}{\partial z}A_v\left(\frac{\partial\bar{u}}{\partial z}\right) \tag{E.6}$$

The derivation will be continued in vector notation and in this form, equation (E.6)

appears as follows:

$$0 = -\frac{1}{\rho_0}\frac{\partial \bar{p}}{\partial x} + f\bar{v} - \vec{\bar{u}}.\nabla\bar{u} - \overline{\vec{u}'.\nabla u'} + \frac{\partial}{\partial z}\left(A_v\frac{\partial \vec{\bar{u}}}{\partial z}\right) \tag{E.7}$$

In order to calculate the kinetic energy equation of the mean u-momentum, equation (E.7) is multiplied by $\bar{u}$:

$$0 = -\frac{\bar{u}}{\rho_0}\frac{\partial \bar{p}}{\partial x} + \bar{u}f\bar{v} - \bar{u}\vec{\bar{u}}.\nabla\bar{u} - \overline{\bar{u}\vec{u}'.\nabla u'} + \bar{u}\frac{\partial}{\partial z}\left(A_v\frac{\partial \vec{\bar{u}}}{\partial z}\right) \tag{E.8}$$

we expand and re-arrange equation (E.8), using the following, which are based on the product rule and the identity that states $\frac{\partial}{\partial x}\left(a^b\right) = ba^{b-1}\frac{\partial a}{\partial x}$:

$$\bar{u}\left(\vec{\bar{u}}.\nabla\bar{u}\right) = \vec{\bar{u}}.\nabla\left(\frac{\bar{u}^2}{2}\right) \tag{E.9}$$

$$\bar{u}\overline{\left(\vec{u}'.\nabla u'\right)} = \nabla.\overline{\left(\vec{u}'u'\bar{u}\right)} - \overline{u'\vec{u}'}.\nabla\bar{u} \tag{E.10}$$

$$\bar{u}\frac{\partial \bar{p}}{\partial x} = \frac{\partial \bar{p}\bar{u}}{\partial x} - \bar{p}\frac{\partial \bar{u}}{\partial x} \tag{E.11}$$

Using (E.9), (E.10), (E.11), equation (E.8) can be rearranged as follows:

$$\begin{aligned}\vec{\bar{u}}.\nabla\left(\frac{\bar{u}^2}{2}\right) = &-\frac{1}{\rho_0}\frac{\partial}{\partial x}\left(\overline{pu}\right) - \nabla.\left(\overline{\vec{u}'u'u}\right) + \overline{\vec{u}'u'}.\nabla\bar{u} \\ &+f\overline{uv} + \frac{\bar{p}}{\rho_0}\frac{\partial \bar{u}}{\partial x} + \bar{u}\frac{\partial}{\partial z}\left(A_v\frac{\partial \vec{\bar{u}}}{\partial z}\right)\end{aligned} \tag{E.12}$$

The mean kinetic energy for the v-momentum is similarly derived and appears as follows:

$$\begin{aligned}\vec{\bar{v}}.\nabla\left(\frac{\bar{v}^2}{2}\right) = &-\frac{1}{\rho_0}\frac{\partial}{\partial y}\left(\overline{pv}\right) - \nabla.\left(\overline{\vec{v}'v'v}\right) + \overline{\vec{v}'v'}.\nabla\bar{v} \\ &-f\overline{uv} + \frac{\bar{p}}{\rho_0}\frac{\partial \bar{v}}{\partial y} + +\bar{v}\frac{\partial}{\partial z}\left(A_v\frac{\partial \vec{\bar{v}}}{\partial z}\right)\end{aligned} \tag{E.13}$$

Making the hydrostatic assumption, the mean momentum equation for the z-component of flow simplifies to:

$$\frac{1}{\rho_0}\frac{\partial \bar{p}}{\partial z} = -\frac{\bar{\rho} g}{\rho_0} \tag{E.14}$$

where g is the acceleration due to gravity ($9.8 m.s^{-2}$) and ρ is the local density. The mean kinetic energy equation for momentum in the z direction is calculated by multiplying equation (E.14) by $\bar{w}$:

$$\bar{w}\frac{1}{\rho_0}\frac{\partial \bar{p}}{\partial z} = -\bar{w}\frac{\bar{\rho} g}{\rho_0} \tag{E.15}$$

using the product rule, equation (E.15) can be re-written as:

$$0 = -\frac{1}{\rho_0}\frac{\partial}{\partial z}\left(\overline{pw}\right) - \frac{g}{\rho_0}\overline{(\rho w)} + \frac{\bar{p}}{\rho_0}\frac{\partial \bar{w}}{\partial z} \tag{E.16}$$

In order to obtain the total mean kinetic energy equation, equations (E.12), (E.13) and (E.16) are summed. For clarity, the solution is written in Einstein notation.

$$\bar{u}_j\frac{\partial \bar{K}}{\partial x_j} = \frac{\partial}{\partial x_j}\left(-\frac{\overline{pu_j}}{\rho_0} - \overline{u_j' u_i' \bar{u}_i}\right) + \overline{u_j' u_i}\frac{\partial}{\partial x_j}\bar{u}_i + \overline{wb} + \bar{u}_j\frac{\partial}{\partial z}\left(A_v\frac{\partial \bar{u}_j}{\partial z}\right) \tag{E.17}$$

where b is the buoyancy term and is defined as follows:

$$\bar{b} = -g\frac{\bar{\rho}}{\rho_0} \tag{E.18}$$

The term on the LHS is equivalent to the addition of the terms on the LHS of equations (E.12) and (E.13), where K is the total mean kinetic energy:

$$\bar{K} = \frac{\bar{u}^2 + \bar{v}^2}{2} \tag{E.19}$$

When adding the x-, y- and z- mean kinetic energy equations, the fifth term on the

RHS of equations (E.12), (E.13) and (E.16) fall away due to the continuity equation and the coriolis terms also disappear (they are only important in transferring within each of the $\bar{u}$ and $\bar{v}$ components).

The term on the LHS in equation (E.17) is the divergence of mean kinetic energy, which is brought about in varying contributions by the terms on the RHS. The first two terms on the RHS of equations (E.12) and (E.13) describe transport processes due to pressure and Reynolds stresses respectively and tends to zero when integrated over a large domain. The third term represents the transfer from mean kinetic energy to eddy kinetic energy. The fourth term (buoyancy) represents the transfer from mean available potential to kinetic energy and can be either positive or negative depending on the background density structure. Therefore, it can represent both the generation and destruction of kinetic energy due to buoyancy forcing. The last term on the RHS represents the work done by the mean surface and bottom forcing.

Eddy kinetic energy equation

The eddy kinetic energy equation is derived similarly to the mean kinetic energy equation such that each component of flow is separately derived and are then summed to get the full eddy kinetic energy equation. We begin with the turbulent momentum equation, which is derived by subtracting the mean momentum equation from the total momentum equation as follows:

$$\frac{\partial}{\partial t}\left(\bar{u}+u'\right)-\frac{\partial \bar{u}}{\partial t}=\frac{\partial u'}{\partial t} \tag{E.20}$$

However, in the mean state, the $\frac{\partial u}{\partial t}$ term tends to zero. Written in vector notation, the x-component of the turbulent momentum equation is therefore:

$$0=-\vec{\bar{u}}.\nabla u'-\vec{u'}.\nabla\bar{u}-\overline{\nabla u'\vec{u'}}-\overline{\vec{u'}.\nabla u'}-\frac{1}{\rho_0}\frac{\partial p'}{\partial x}+fv'+\frac{\partial}{\partial z}A_v\left(\frac{\partial u'}{\partial z}\right) \tag{E.21}$$

We multiply equation (E.21) by u' and take a spatial average in order to get the eddy kinetic equation:

$$0 = -\overline{u'\vec{u}.\nabla u'} - \overline{u'\vec{u'}.\nabla u} - \overline{u'.\nabla u'\vec{u'}} - \overline{u'\vec{u'}.\nabla u'} - \overline{\frac{u'}{\rho_0}\frac{\partial p'}{\partial x}} + \overline{fu'v'} + u'\frac{\partial}{\partial z}A_v\left(\frac{\partial u'}{\partial z}\right) \quad \text{(E.22)}$$

we expand and re-arrange equation (E.22), using the following, which are based on the product rule and the identity that states $\frac{\partial}{\partial x}\left(a^b\right) = ba^{b-1}\frac{\partial a}{\partial x}$:

$$\overline{u'\frac{\partial p'}{\partial x}} = \frac{\partial \overline{p'u'}}{\partial x} - \overline{p'\frac{\partial u'}{\partial x}} \quad \text{(E.23)}$$

$$-\overline{u'\vec{u}.\nabla u'} = -\vec{\bar{u}}.\nabla\left(\overline{\frac{u'^2}{2}}\right) \quad \text{(E.24)}$$

$$-\overline{u'\vec{u'}.\nabla u} = -\overline{u'\vec{u'}}.\nabla u \quad \text{(E.25)}$$

$$-\overline{u'.\nabla u'\vec{u'}} = -\bar{u}'.\overline{\nabla u'\vec{u'}} = 0 \quad \text{(E.26)}$$

$$-\overline{u'\vec{u}'.\nabla u'} = -\overline{\frac{1}{2}.\nabla\vec{u}'u'^2 + u'^2.\nabla\vec{u}'} = -\overline{\frac{1}{2}.\nabla\vec{u}'u'^2} \quad \text{(E.27)}$$

where $\overline{u'^2.\nabla\vec{u}'} = u'^2\left(\frac{\partial\vec{u}'}{\partial x} + \frac{\partial\vec{v}'}{\partial y} + \frac{\partial\vec{w}'}{\partial z}\right) = 0$ due to the continuity equation ($\nabla\vec{u}' = 0$). Using (E.23), (E.24), (E.25), (E.26), (E.27), equation (E.22) becomes:

$$\begin{aligned}\vec{\bar{u}}.\nabla\left(\overline{\frac{u'^2}{2}}\right) = &-\frac{1}{\rho_0}\frac{\partial}{\partial x}\left(\overline{p'u'}\right) - \overline{\frac{1}{2}.\nabla\vec{u}'u'^2} - \overline{\vec{u'}u'}.\nabla\bar{u} \\ &+f\overline{u'v'} + \overline{\frac{p'}{\rho_0}\frac{\partial u'}{\partial x}} + \overline{u'\frac{\partial}{\partial z}A_v\left(\frac{\partial u'}{\partial z}\right)}\end{aligned} \quad \text{(E.28)}$$

Similarly, we can derive equations for the y-component of the time-evolution of turbulent kinetic energy:

$$\begin{aligned}\vec{\bar{v}}.\nabla\left(\overline{\frac{v'^2}{2}}\right) = &-\frac{1}{\rho_0}\frac{\partial}{\partial y}\left(\overline{p'v'}\right) - \overline{\frac{1}{2}.\nabla\vec{v}'v'^2} - \overline{\vec{v'}v'}.\nabla\bar{v} \\ &+f\overline{u'v'} + \overline{\frac{p'}{\rho_0}\frac{\partial v'}{\partial y}} + \overline{v'\frac{\partial}{\partial z}A_v\left(\frac{\partial v'}{\partial z}\right)}\end{aligned} \quad \text{(E.29)}$$

The derivation of the turbulent kinetic energy equation for the z-component is similar to that of equations (E.28) and (E.29) except that we begin with the disturbance z-component momentum equation which, due to the hydrostatic assumption is as follows:

$$\frac{1}{\rho_0}\frac{\partial p'}{\partial z} = -\frac{\rho' g}{\rho_0} \tag{E.30}$$

The mean eddy kinetic energy of equation (E.30) is calculated by multiplying it by w' and take an average:

$$\bar{w}'\frac{1}{\rho_0}\overline{\frac{\partial p'}{\partial z}} = -\bar{w}'\frac{\bar{\rho}' g}{\rho_0} \tag{E.31}$$

Equation (E.31) can be rearranged to form the z-component of the turbulent kinetic energy:

$$0 = -\frac{1}{\rho_0}\frac{\partial}{\partial z}\left(\overline{p'w'}\right) - \frac{g}{\rho_0}\overline{(\rho' w')} + \frac{\bar{p}'}{\rho_0}\frac{\partial \bar{w}'}{\partial z} \tag{E.32}$$

To obtain the full time-evolution equation, we add the turbulent energy equations of each component and present the result in Einstein notation:

$$\bar{u}_j\frac{\partial \bar{K}'}{\partial x_j} = \frac{\partial}{\partial x_j}\left(-\frac{\overline{p'u_j'}}{\rho_0} - \overline{\frac{u_j' u_i' u_i'}{2}}\right) - \overline{u_j' u_i}\frac{\partial}{\partial x_j}\bar{u}_i + \overline{w'b'} + \overline{u_j'\frac{\partial}{\partial z}\left(A_v\frac{\partial u_j'}{\partial z}\right)} \tag{E.33}$$

where b' is the turbulent buoyancy forcing and is given by:

$$b' = -g\frac{\rho'}{\rho_0} \tag{E.34}$$

The term on the LHS is equivalent to the addition of the terms on the LHS of

equations (E.28) and (E.29), where K' is the total eddy kinetic energy:

$$\bar{K}' = \frac{\overline{u'^2 + v'^2}}{2} \tag{E.35}$$

Equation (E.33) contains transport terms for pressure and Reynolds stresses (first and second terms on RHS respectively), a term that describes the production of kinetic energy (third term on RHS), a term that represents the transfer of energy from eddy potential to eddy kinetic energy (the fourth term) and a term that describes the eddy surface and bottom stress work (last term on RHS).

The term that describes the conversion of mean kinetic energy to eddy kinetic energy (third term on LHS) is equivalent to the third term on the LHS of the mean kinetic energy equation (equation (E.17)), but of opposite sign (i.e. there is no net loss or gain of kinetic energy, just a transfer between mean kinetic energy to turbulent kinetic energy). The last term (buoyancy) can be either positive or negative, depending on the background density structure. Therefore, it can represent both the generation and destruction of kinetic energy due to buoyancy forcing.